Synthesis and functionalization of low-dimensional materials towards high-performance supercapacitors

Synteza i funkcjonalizacja materiałów niskowymiarowych oraz ich zastosowanie w wysokowydajnych superkondensatorach

A dissertation presented by

Włodzimierz Czepa

Supervisor: Prof. Artur Ciesielski

Faculty of Chemistry

A doctoral dissertation submitted in the form of a thematically
coherent series of scientific articles published in scientific journals,
prepared in the field of science, in the discipline of chemical science

Poznań 2023

Acknowledgement

I am extremely grateful to my supervisor Prof. Artur Ciesielski for offering his immerse knowledge and plentiful experience as well as open-minded approach.

I would like to express my sincere gratitude towards my very first supervisor Prof. Violetta Patroniak for personal guidance during my Bachelor and Master studies and boundless opportunities provided while my scientific maturate.

I would like to express my appreciation to Dr Marta A. Fik-Jaskółka for considering myself at the very beginning and introducing me into the laboratory work.

I would like to genuinely thank to Prof. Paolo Samorì for multiple possibilities and hospitality while my internships in Nanochemistry laboratory at the Institut de Science et d'Ingénierie Supramoléculaires (I.S.I.S.) in Strasbourg.

I would like to genuinely thank all my colleagues from Laboratory in WCAT AMU including Dr Samanta Witomska, Dr Iwona Janica, Dr Dawid Pakulski and Tomasz Chudziak.

I would like to thank my parents for their support throughout my entire education process.

Finally, I would like to thank to my fiancée Monika and my son Oliwier for unconditional support, love and waiting at home patiently.

The research included in presented thesis was supported by funds from National Science Centre (grant PRELUDIUM no. 2019/33/N/ST5/00052 and grant SONTA BIS 2015/18/E/ST5/00188) and by grant no. POWR POWR.03.02.00-00-I026/16 co-financed by the European Union through the European Social Fund under the Operational Program Knowledge Education Development.

Wielkopolska Centre for Advanced Technologies in Poznań and the Institut de Science et d'Ingenierie Supramoleculaires in Strasbourg provided the infrastructure facility for PhD research.

Contents

List of abbreviations

2D - two-dimensional

2DMs - two-dimensional materials

3D - three-dimensional

ACN - acetonitrile

CV - cyclic voltammetry

EDX - energy-dispersive X-ray spectroscopy

EIS - electrochemical Impedance Spectroscopy

FTIR - Fourier transform infrared spectroscopy

GCD - galvanostatic Charge-Discharge

GO - graphene oxide

h-BN - hexagonal boronitride

rGO - reduced graphene oxide

rGO-THA - reduced graphene oxide – thioamide composite

SEM - scanning electron microscopy

$TEABF_4$ - tetraethylammonium tetrafluoroborate

TEM – transmission electron microscopy

THA - thioamide-based polymer

TDMs - Transition metal dichalcogenides

WAXS - wide-angle X-ray scattering

XPS - X-ray photoelectron spectroscopy

XRD- X-ray diffraction

Abstract

Two-dimensional materials exhibit wide range of advantageous phisico-chemical properties making them great candidates for sensing, energy storage materials or (opto)electronics. Moreover, 2DMs provide great base for nano-composites considering the ease of their modification possibilities. The application of 2DMs and their hybrids or composites for modern electronic devices have enormous impact on development of novel synthetic methods, characterization of nanomaterials and interdisciplinary exploitation of unique properties. Currently scientific community is still seeking for new efficient sensory materials that will allow fabrication of chemical sensors with improved sensitivity and selectivity focusing especially on 2DMs based structures. The Review article (**P1**) highlights broad range of chemical sensors targeting gaseous analytes, metal ions and biologically active molecules where electrochemical sensors represent a major group. It includes current 2D materials and their composites including graphene, transition metal dichalocegenides, hexagonal boron nitride or black phosphorous, and considers several important parameters such as type of sensor, target analyte, limit of detection or linearity range. The article was inspiration for further research and exploiting electrochemical properties of modified 2DMs.

The research objectives of this dissertation entitled "Electrochemical investigations of modified two-dimensional materials and its application in supercapacitors" include synthesis of a new class of two-dimensional based materials by chemical functionalization of graphene oxide, the detailed characterization of synthesized materials and preparation of supercapacitors electrodes and electrochemical investigation in various conditions which was presented in articles **P2** and **P3** and electrochemical investigations of material provided by collaborators in **P4**.

The article **P2** describes the use of polyhedral oligosilsesquioxane (POSS) equipped with terminal -aminopropyl groups to modify graphene oxide (GO) to enhance porosity and extend interlayer space between the GO sheets, allowing efficient electrolyte transport. Additionally, the material was chemically reduced to restore electrical properties and to moderate oxidation degree. The rGO-POSS hybrid was used to prepare freestanding electrode which was investigated in three-electrode system demonstrating a high specific capacitance of 174 F g^{-1} in aqueous 1M H_2SO_4 electrolyte which surpasses over twice the

performance of reference material (rGO). Notably, the electrode exhibited great efficiency with no loose while charge-discharge investigations and very low resistance indicating fast charge transfer during the energy storage process, good conductivity, and excellent electrolyte ion transfer. The power density reached 2.25 W cm^{-3} and energy density was estimated at 41.4 mW h cm^{-3}. Additionally, the electrodes showed excellent durability with over 98% retention of initial capacitance after 5000 cycles.

Article **P3** deals with the synthesis of polymer with thioamide unit and covalent functionalization of graphene oxide towards introducing enhanced amount of heteroatoms (S,N) which are beneficial providing active redox centers and additional pseudocapacitance. Final oxygen content in GO-THA composite allowed to use material as prepared for further electrochemical experiments. The porous nanocomposite was used for preparation symmetric two electrodes coin-cell type device and investigated in aqueous and organic electrolytes. The experiments in aqueous electrolyte (1M H_2SO_4) revealed specific capacitance of 221 F g^{-1} at 1 A g^{-1}, while the use of organic media allows the specific capacitance to be boosted up to 340 F g^{-1}. Additionally, the wider operating window together with high porosity and mixed energy storage mechanism facilitates high energy densities up to 94.4 Wh kg^{-1}, exceeding most *state-of-the-art* GO-based materials for supercapacitors. Furthermore, the symmetric devices exhibit great robustness in both aqueous and organic electrolytes as evidenced by an excellent stability after 5000 working cycles (>98% in H_2SO_4 and>90% in $TEABF_4$/ACN).

The remarkable results obtained in **P3** have highlighted the importance of simple, yet effective functionalization of low-dimensional materials with thioamide-based polymer. To explore further such approach, we have decided to decorate conductive copper nanowires (CuNWs) with thiourea utilizing sulphidation reaction and present our finding in form of article **P4**. Well characterized compound in terms of composition, optical properties, structure and morphology was used to prepare symmetric supercapacitor in two-electrode cell. The use of organic electrolyte: 1-ethyl-3-methylimidazolium bis(trifluoromethylsulfonyl)imide in propylene carbonate allowed to extend the potential window up to 2.5 V. The circular voltammetry indicated significant presence of oxidation and reduction peaks suggesting minor co-participance of pseudocapacitance in energy storage mechanism. The highest specific capacitance was estimated at 324 F g^{-1}, while volumetric capacitance and energy density of the device reached 60.5 F cm^{-3} and 52.5 mWh cm^{-3}. The capacitance retention reached 70% after 5000 cycles, however it includes significant drop while first 1000 cycles when the protective layer of copper oxides is created on the surface preventing further degradation. Although, unlike articles **P1**-**P3** article **P4** deals with one-dimensional material, we believe that the approach presented there represents a natural extension of research describe in **P3**.

Streszczenie w języku polskim

Materiały dwuwymiarowe same w sobie stanowią związki wykazujące niezwykłe właściwości fizyko-chemiczne, co przekłada się na ich ogromny potencjał aplikacyjny w takich obszarach jak: sensory, materiały do przechowywania energii oraz elektronika. Ponadto, 2DMs stanowią doskonałą podstawę dla materiałów kompozytowych biorąc pod uwagę ogromne możliwości ich funkcjonalizacji. Zastosowanie 2DMs oraz ich związków hybrydowych w nowoczesnych technologiach z uwzględnieniem elektroniki ma wielki wpływ na dalszy rozwój metod syntezy materiałów hybrydowych, ich charakterystyki oraz badania aplikacyjne mające często charakter interdyscyplinarny. Obecnie naukowcy wciąż poszukują nowych wydajnych sensorów z polepszonymi parametrami dotyczącymi np. limitu wykrywalności, limitu oznaczalności czy specyficzności urządzenia skupiając się w szczególności na materiałach opartych o 2DMs. Artykuł przeglądowy (**P1**) porównuje szeroki zakres nowoczesnych sensorów chemicznych do wykrywania cząsteczek gazów, jonów metali oraz związków aktywnych biologicznie, z których większość oparta jest na sensorach elektrochemicznych. W pracy opisano wykorzystanie popularnych nanomateriałów dwuwymiarowych oraz ich materiałów kompozytowych z uwzględnieniem grafenu, dichalkogenków metali przejściowych, heksagonalnego azydku boru, czy czarny fosfor biorąc pod uwagę takie parametry jak rodzaj sensora, rodzaj analitu, limit wykrywalności czy zakres liniowy wykrywalności. Ten artykuł był inspiracją do dalszych badań oraz rozwijania niezwykłych właściwości elektrochemicznych modyfikowanych materiałów dwuwymiarowych.

Cele naukowe rozprawy doktorskiej zatytułowanej: „Elektrochemiczne badania modyfikowanych materiałów dwuwymiarowych i ich wykorzystanie w superkondensatorach" uwzględniają syntezę nowej klasy materiałów opartych na 2DMs poprzez chemiczną funkcjonalizację tlenku grafenu, szczegółową charakterystykę przygotowanych materiałów oraz skonstruowanie elektrod do superkondensatorów oraz badania elektrochemiczne w różnych warunkach co zawarto w artykułach **P2** i **P3**, a także elektrochemiczne badania materiału w ramach współpracy – nanorurek siarczku miedzi uwzględnione w artykule **P4**.

Artykuł **P2** obejmuje wykorzystanie oligomerycznego silseswioksanu (POSS) wyposażonego w terminalne grupy propyloaminowe do chemicznej modyfikacji tlenku grafenu (GO) celem zwiększenie porowatości oraz zwiększenia dystansu pomiędzy warstwami GO aby zapewnić lepszy transport jonów w trakcie procesów elektrochemicznych. Ponadto, po modyfikacji materiał został zredukowany chemicznie przy użyciu hydrazyny celem polepszenia właściwości elektrycznych oraz zapewnienia optymalnego poziomu zawartości grup tlenowych. Materiał hybrydowy rGO-POSS został użyty do przygotowania elektrody, która badana była w układzie trójelektrodowym wykazując pojemność właściwą równą 174 F g^{-1} w elektrolicie kwasowym – 1M H_2SO_4, co ponad dwukrotnie przewyższa wartości otrzymane dla materiału referencyjnego przygotowanego w analogiczny sposób (rGO). Na uwagę zasługuje fakt, że przygotowana elektroda cechuje się doskonałą wydajnością, efektywnym rozładowywaniem oraz niską rezystancją co świadczy o dobrej przewodności i sprawnym transferem ładunku. Gęstość mocy przygotowanej elektrody została oszacowana na 2.25 W cm^{-3} a gęstość energii wynosi 41.4 mWh cm^{-3}. Ponadto elektroda cechuje się wysoką stabilnością zachowując ponad 98% początkowej pojemności po 5000 cyklach.

Badania zawarte w artykule **P3** uwzględniają syntezę polimeru z jednostką tioamidową oraz kowalencyjną funkcjonalizację tlenku grafenu celem wprowadzenia znaczącej ilości heteroatomów, w tym siarki i azotu, co pozytywnie wpływa na wydajność urządzenia dzięki dodatkowemu współudziałowi mechanizmu pseudopojemnościowego. Ze względu na optymalną zawartość tlenu w próbce, użyto materiał do dalszych badań bez konieczności dodatkowej redukcji. Porowaty materiał GO-THA został użyty do przygotowania urządzenie w symetrycznym układzie dwuelektrodowym typu coin-cell i był badany przy zastosowaniu dwóch elektrolitów. Badania wykonane w 1M H_2SO_4 wykazały pojemność 221 F g^{-1} przy gęstości natężenia 1 A g^{-1}, natomiast użycie organicznego elektrolitu (1M $TEABF_4$ w ACN) pozwoliło na otrzymanie pojemności 340 F g^{-1}. Ponadto duże okno potencjału w drugim przypadku w połączeniu z porowatością materiału oraz hybrydowym mechanizmie przechowywania energii pozwoliło otrzymać wysoką wartość gęstości energii do 94.4 Wh kg^{-1}, co znacznie przewyższa wartości literaturowe dla materiałów bazujących na tlenku grafenu. Materiał wykazał się znakomitą stabilnością zachowując ponad 98% początkowej pojemności przy zastosowaniu 1M H_2SO_4 oraz ponad 90% przy zastosowaniu $TEABF_4$ w ACN po 5000 cykli.

Wyniki zaprezentowane w **P3** ukazały jak ważna może być stosunkowo łatwa funkcjonalizacja materiałów niskowymiarowych np. cząsteczkami polimerów. Dlatego też postanowiono zmodyfikować przewodzące nanorurki miedziowe przy pomocy tiomocznika, co zaprezentowano w artykule **P4**. Użycie elektrolitu 1-etylo-3-metyloimidazol bis(trifluorometylsulfonyl)imid w węglanie propylenu pozwoliło na zastosowanie dużego okna potencjałowego do 2.5 V. Podczas badań woltamperometrii cyklicznej zaobserwowano znaczący udział reakcji redox w trakcie procesów elektrodowych. Pojemność właściwą oszacowano na 324 F g^{-1} wówczas, gdy pojemność objętościowa oraz gęstość energii wyniosły odpowiednio 60.5 F cm^{-3} oraz 52.5 mWh cm^{-3}. Po 5000 cykli elektrody zachowały około 70% początkowej pojemności warto zauważyć, że znaczny spadek podczas pierwszych 1000 cyklów spowodowany jest zużywaniem się materiału jednak po tym okresie wytworzenie ochronnej warstwy pasywnej na powierzchni zapobiega dalszej degradacji.

Publications included in the dissertation

P1

Cosimi Anchini*, Włodzimierz Czepa*, Dawid Pakulski*, Alessandro Aliprandi, Artur Ciesielski, Paolo Samori
„Chemical sensing with 2D materials”
Chemical Society Reviews, 2018, 47, 4860.
IF_{2022}= 60.615 IF-5_{2022}= 48.957 Citations: 394

P2

Włodzimierz Czepa, Samanta Witomska, Artur Ciesielski, Paolo Samori
„Reduced graphene oxide-silsesquioxane hybrid as a novel supercapacitor electrode”
Nanoscale, 2020, 12. 18733.
IF_{2022}= 8.307 IF-5_{2022}= 7.481 Citations: 9

P3

Włodzimierz Czepa, Samanta Witomska, Artur Ciesielski, Paolo Samori
„ A graphene oxide – thioamide polymer hybrid for high performance supercapacitor electrodes „
Small Science, 2023,
IF_{2022}=N/A IF-5_{2022}= N/A Citations: 0

P4

Cosimo Anichini, Włodzimierz Czepa, Alessandro Aliprandi, Valentina Girelli Consolaro, Ovidiu Ersen, Artur Ciesielski, Paolo Samori
„Synthesis and characterization of ultralong copper sulfide nanowires and their electrical proprties”
Journal of Materials Chemistry C, 2021, 9, 12133.
IF_{2022}= 8.067 IF-5_{2022}= 7.481 Citations: 2

Summary:
IF: 76.989
Citations: 405

Scientific achievements

A. Publications not included in the dissertation

[1] Dawid Pakulski, Veronica Montes-Garcia, Adam Gorczyński, Włodzimierz Czepa, Tomasz Chudziak, Paolo Samori, Artur Ciesielski

„Thiol-decorated covalent organic framework as multifunctional materials for high-performance supercapacitors and heterogeneous catalysis"

Journal of Materials Chemistry A, 2022, 10, 16685-16696.

IF_{2022}= 14.511 $IF\text{-}5_{2022}$= 12.167 Citations: 8

[2] Dawid Pakulski, Adam Gorczyński, Dawid Marcinkowski, Włodzimierz Czepa, Tomasz Chudziak, Samanta Witomska, Yuta Nishina, Violetta Patroniak, Artur Ciesielski, Paolo Samori

„High-sorption terpyridine-graphene oxide hybrid for the efficient removal of heavy metal ions from wastewater"

Nanoscale, 2021, 13, 10490.

IF_{2022}= 8.307 $IF\text{-}5_{2022}$= 7.481 Citations: 9

[3] Włodzimierz Czepa, Dawid Pakulski, Samanta Witomska, Violetta Patroniak, Artur Ciesielski, Paolo Samori

"Graphene oxide – mesoporous SiO2 hybrid composite for fast and efficient removal of organic cationic contaminants"

Carbon, 2020, 158, 193.

IF_{2022}= 11.307 $IF\text{-}5_{2022}$= 7.481 Citations: 30

[4] Dawid Pakulski, Włodzimierz Czepa, Stefano del Buffa, Artur Ciesielski, Paolo Samori

„Thick Membranes for Water Purification and Blue Energy Harvesting"

Advanced Functional Materials, 2019, 1902394.

IF_{2022}= 19.924 $IF\text{-}5_{2022}$= 7.481 Citations: 43

[5] Martyna Szymańska, Włodzimierz Czepa, Cezary Hołubowicz, Renata Świsłocka, Teresa Łuczak, Maciej Kubicki, Joanna Karpińska, Marta A. Fik-Jaskółka, Violetta Patroniak

„Co(II/III) complexes with benzoxazole and benzothiazole ligands as efficient heterogenous photocatalysts for organic dyes degradation"

Catalyst, 2019, 9, 913.

IF_{2022}= 4.146 $IF\text{-}5_{2022}$= 7.481 Citations: 0

[6] Dawid Pakulski, Adam Gorczyński, Włodzimierz Czepa, Zhaoyang Liu, Luca Ortolani, Vittorio Morandi, Violetta Patroniak, Artur Ciesielski, Paolo Samori

„Novel Keplerate type polyoxometalate-surfactant-graphene hybrids as advanced electrode materials for supercapacitors"

Energy Storage Materials, 2019, 17, 186.

IF_{2022}= 20.831 $IF\text{-}5_{2022}$= 7.481 Citations: 27

[7] Samanta Witomska, Zhaoyang Liu, Włodzimierz Czepa, Alessandro Aliprandi, Dawid Pakulski, Piotr Pawluć, Artur Ciesielski, Paolo Samori

"Graphene Oxide Hybrid with Sulfur-Nitrogen Polymer for High-Performance Pseudocapacitors"

Journal of the American Chemical Society, 2019, 141, 482.

IF_{2022}= 16.383 $IF\text{-}5_{2022}$= 7.481 Citations: 49

[8] Włodzimierz Czepa, Marta A. Fik, Samanta Witomska, Maciej Kubicki, Giuseppe Consiglio, Piotr Pawluć, Violetta Patroniak

„Simple Schiff-Base Cu(II) Complexes as Efficient Catalysts for Benzyl Alcohol Oxidation"

ChemistrySelect, 2018, 3, 9504.

IF_{2022}= 2.24 $IF\text{-}5_{2022}$= 7.481 Citations: 11

[9] Dawid Pakulski, Włodzimierz Czepa, Samanta Witomska, Alessandro Aliprandi, Piotr Pawluć, Violetta Patroniak, Artur Ciesielki, Paolo Samori

„Graphene oxide-branched polyethylenimine foams for efficient removal of toxic cation from water"

Journal of the Materials Chemistry A, 2018, 6, 9384.

IF_{2022}= 14.511 IF-5_{2022}= 12.167 Citations: 74

[10] Marta A. Fik, Włodzimierz Czepa, Maciej Kubicki, Violetta Patroniak

„Formation of non-covalent porous framework with Fe ions and N_2O Schiff base ligand: structural and thermal studies"

Supramolecular Chemistry, 2017, 9, 643.

IF_{2022}= 2.23 IF-5_{2022}= 7.481 Citations: 6

Summary:

Total IF:	191.37
Total Citations:	662
h-index:	9

B. International internships

11.2020-03.2020	Institut de science et d'ingénierie supramoléculaires (ISIS) Nanochemistry Laboratory prof. Paolo Samori. Strasbourg, Francja
01.2019-02.2019	Institut de science et d'ingénierie supramoléculaires (ISIS) Nanochemistry Laboratory prof. Paolo Samori. Strasbourg, Francja
03.2017-05.2017	Dipartimento di Schienze Chimiche, Università degli Studi di Catania, Prof. Giuseppe Consiglio, Catania, Włochy
10.2016 -12.2016	Institut de science et d'ingénierie supramoléculaires (ISIS) Nanochemistry Laboratory prof. Paolo Samori. Strasbourg, Francja
20.04-8.05.2015	Institut de science et d'ingénierie supramoléculaires (ISIS) Nanochemistry Laboratory prof. Paolo Samori. Strasbourg, Francja

C. Scientific Conferences

[1] W. Czepa, S. Witomska, A. Ciesielski, P. Samori – „*Molecular approach for preparation of functional nanomaterials for high performance supercapacitors*" poster presentation.

35th Topical Meeting of the International Society of Electrochemistry, May 2023, Gold Coast – Australia.

[2] W. Czepa, S. Witomska, A. Ciesielki, P. Samori – „Supercapacitors based on graphene oxide enriched with thioamide based polymer" poster presentation.

7th Conference Graphene & 2D 2022, September 2022, Łódź – Poland.

[3] W. Czepa, S. Witomska, Z. Liu, A. Ciesielski, P. Samori – „*Graphene oxide modified with sulfur-nitrogen polimer for high performance pseudocapacitors*" poster presentation

GrapheneBrazil2019 International Conference, September 2019, Rio de Janeiro - Brazil.

Rio de Janeiro, Brazylia

[4] W. Czepa, D. Pakulski, S. Witomska, A. Ciesielski, P. Samori – „*Graphene oxide and its derrivatives for removal of inorganic and organic contaminants*" poster presentation.

Advanced Materials and Nanotechnology (AMN9), February 2019, Wellington, New Zealand.

[5] W. Czepa, A. Ciesielski, P. Samori – „*Graphene-oxide aminosilica hybrid for organic dyes adsorption*" poster presentation.

Graphene Week 2018, September 2018, San Sebastian - Spain.

[6] W. Czepa, P. Samori, A. Ciesielski – „Graohene oxide – aminosilica hybrid for removal of organic dyes from aqueous solutions" poster presentation.

NanoTech Poland , June 2018, Poznań – Poland.

[7] W. Czepa, D. Pakulski, A. Aliprandi, S. Witomska, P. Pawluć, V. Patroniak, A. Ciesielski, P. Samori – „*Graphene oxide modified with polyethyleneimine (PEI) as heavy metal ions adsorbent*" poster presentation

Chem2Dmat, August 2017, Strasbourg – France.

[8] W. Czepa, M. Fik, M. Kubicki, V. Patroniak – „*New tetranuclear Fe(II) complex with N_3-donor Schiff base type ligand as a supramolecular system based on noncovalent organic framework*" poster presentation

27th International Conference on Organometallic Chemistry (ICOMC2016), July 2016, Melbourne – Australia.

[9] W. Czepa, M. Fik, M. Kubicki, V. Patroniak – „*Schiff base ligands complexes with d^{10}-electron metals as luminophores with potential activity in Photodynamic Thrapy and OLEDs*" poster presentation

1st International Caparica Conference on Chromogenic and Emissive Materials (IC3EM), September 2014, Costa de Caparica, Portugal.

[10] W. Czepa, M. Fik, M. Kubicki, V. Patroniak – „ *Synteza, struktura oraz właściwości nowych związków kompleksowych zasad Schiffa z jonami Fe(III), Ni(II) i Cd(II)*" poster presentation

59 Zjazd Naukowy Polskiego Towarzystwa Chemicznego, September 2016, Poznań – Poland.

D. Research Projects

[1] „PRELUIUM 17" National Science Centre, project no: 2019/33/N/ST5/00052 „Three-dimensional heteroatoms enriched graphene based structures for pseudocapacitors" – principal investigator.

[2] „OPUS 18" National Science Centre, project no: 2019/35/B/ST5/01568 „Supramolecularly engineered sensors based on 2D materials for detection of gases and pressure" – investigator.

[3] „SONATINA 4" National Science Centre, project no: 2020/36/C/ST5/00247 „Metal/covalent organic frameworks (MOF/COF) hybrid materials for high performance supercapacitors application" – investigator.

[4] „SONATA BIS 5" National Science Centre, project no: 2015/18/E/ST5/00188 „New (supramolecular) approach to two-dimensional layered materials" – investigator.

E. Scholarships and awards

2021	Stypendium Ministra dla Wybitnych Młodych Naukowców
2020	Nagroda Rektora UAM za osiągnięcia naukowe
2020	Nagroda Miasta Poznania dla młodych badaczy poznańskiego środowiska naukowego
2019	Nagroda Rektora UAM I-go stopnia za osiągnięcia naukowe
2019	Jednorazowe Stypendium Rektora UAM za osiągnięcia naukowe

2018 - 2021	Stypendium projakościowe dla najlepszych doktorantów Wydziału Chemii UAM
2017	Stypendium Ministra za wybitne osiągnięcia dla najlepszych studentów
2013 –2019	Stypendium Rektora dla najlepszych studentów Wydziału Chemii UAM

Description of publications included in dissertation

1. General introduction and motivation

Nanomaterials are a category of materials characterized by having at least one dimension within the nanoscale range, usually between 1 and 100 nanometers. Due to their distinct size and the ratio of surface area to volume, they often exhibit unique properties that differ from those of larger bulk materials. The reduced dimensions of nanomaterials result in significantly larger surface areas and enhanced reactivity compared to their bulk counterparts, making them highly attractive in various scientific fields. Nanomaterials encompass a wide range of structures, including naturally occurring ones like spider webs, animal horns, or human bone matrix, as well as engineered structures such as nanoparticles, nanotubes, or layered materials. In recent times, there has been significant interest in two-dimensional (2D) materials, which belong to a distinct category of nanomaterials. These materials are composed of atomic or molecular layers and possess an extremely thin thickness, usually measuring less than 10 nanometers. Due to their structure, 2D materials exhibit exceptional properties in terms of electronics, optics, and mechanics, making them highly suitable for a wide range of applications. These applications encompass fields such as electronics, sensing, energy conversion and storage, biomedicine, optoelectronics, and numerous others..[1–5] Several examples of two-dimensional are in particular interest of science as a perfect candidates for emerging technology issues: Transition metal dichalcogenides (TMDs), hexagonal boron nitride (hBN), transition metal carbides/nitrides (MXenes), black phosphorous and graphene which became one of the most investigated nanomaterials since firstly isolated in 2004 by Andre Geim and Konstantin Novoselov.[6–9]

In general, there are two main approaches considering synthesis of modern nanomaterials: *bottom up* and *top down*. The *bottom up* method is a popular approach that involves assembling materials from smaller, molecular building blocks to create a larger, more complex structure. This method relies on the interactions between the building blocks, which can include atoms, molecules, and nanoscale particles, to self-assemble into the desired structure. There are several techniques used in the *bottom up* method of synthesis, *e.g.*, self-assembly, template synthesis, colloidal synthesis, or chemical vapor deposition. The nanomaterials obtained using this method benefit form high quality, minimal amount of defects and relatively more homogenous structure.[10,11] The *top down* method of synthesis involves starting with a larger material and breaking it down into smaller components to create the desired structure or material. This process involves various techniques that use mechanical, thermal, or chemical energy to reduce the size of the raw material. There are several *top down* methods used in materials science, including milling, lithography, chemical etching or wet methods which include the exfoliation with the use of solvents and sonication of electrochemical processes. Overall, the *top down* method of synthesis offers an effective method for creating relatively vast amount of materials at low cost.[12–14]

One of the most emerging nanomaterials is graphene which is a fascinating structure with unique chemical and physical properties. It is known as two-dimensional allotrope of carbon, consisting of a single layer of sp^2 hybridized carbon atoms arranged in honeycomb lattice. Graphene's chemical properties are remarkable, despite fact it is one of the thinnest material, it is incredibly strong, with a tensile strength of around 130 GPa, which is greater than steel. Moreover, graphene is also an excellent conductor of both heat and electricity due to its high electron mobility, which is approximately 100 times greater than that of traditional semiconductors such as silicon. Its high surface area which exceeds 2600 $m^2\ g^{-1}$ and high transparency also make it an attractive material for use in energy storage, supercapacitors, and solar cells.[15–17] The material also exhibits unique physical properties. It is an exceptional barrier to gases and liquids, making it potentially useful for applications such as water filtration, gas separation, and drug delivery.[18,19] Its mechanical flexibility and low density also make it desirable for use in flexible electronics and composite materials. The attractive alternative which offers wide range of functionalization properties is graphene oxide (GO) which is created by the chemical oxidation of graphene, resulting in the addition of oxygen-containing functional groups such as hydroxyl, epoxy, and carboxyl onto the graphene sheet.[20] The amount of oxygen present in graphene oxide can vary depending on the degree and duration of oxidation used during its production. Typically, the oxidation process results in a material containing between 20-30% oxygen by weight.[21] The presence of these functional groups has significant effects on the chemical and physical properties of graphene oxide. The functional groups on the surface of graphene oxide make the material hydrophilic, allowing it to easily disperse in polar solvents such as water and ethanol. Graphene oxide can also form stable suspensions in organic solvents, making it highly versatile and easy to work with.[22,23] In terms of its physical properties, graphene oxide is a highly heterogeneous material, with a highly disordered structure that contains regions of partially oxidized graphene, highly oxidized graphene, and fully oxidized graphene oxide.[24] This can result in variations in the properties of graphene oxide based on its synthesis process. Its mechanical properties, however, are significantly reduced due to the presence of oxygen-containing functional groups, resulting in a lower tensile strength compared to pure graphene.[25,26]

Functionalization of graphene oxide involves the modification of its surface chemistry by introducing new functional groups or attaching various molecules or nanoparticles to its surface.[27] This can change or enhance its properties and functionality, potentially leading to new applications. There are several approaches of modification methods considered in case of GO: i) covalent functionalization, which involves the attachment of a molecule to the surface of graphene oxide by forming a covalent bond. This method ensures a strong attachment, and the functional groups introduced on the surface of the graphene oxide can change its chemical stability, mechanical properties or chemical reactivity;[28,29] ii) non-covalent functionalization, where the weaker interactions such as van der Waals forces are used to attach molecules or nanoparticles to the surface of graphene oxide. This method is reversible, and the attachment of the molecules or nanoparticles can be easily controlled;[30–32] iii) hybrid functionalization, which involves combining graphene oxide with other materials such as semiconducting materials, metallic nanoparticles or carbon nanotubes or biomolecules such as DNA, proteins, and carbohydrates that allows the development of highly sensitive and specific biosensors.[33,34]

There are several important methods of characterization of porous nanomaterials which should be considered while planning synthesis and modification of nanomaterials with desired physico-chemical properties. X-ray diffraction (XRD) is a powerful characterization technique used to study the structural properties of materials. It is a widely used method in the research and development of nanomaterials including graphene.[35] XRD works by shining a beam of X-rays onto a material and then measuring the angles at which the X-rays are scattered. These scattered X-rays can provide valuable information about the atomic arrangement within a crystalline material. By analyzing the XRD patterns, scientists can determine the crystal structure, lattice parameters, and orientation of the sample. Therefore it is significant technique allowing to monitor the functionalization process.[36–38] Moreover, it can also be used to study the porosity of materials, which is an important parameter that affecting further properties and allow to calculate the pore size distribution, total pore volume, and specific surface area of a porous material. In addition to studying the porosity of porous materials, XRD can also be used to analyze the structural properties of non-porous materials such as ceramics, alloys, and polymers.[39–41] Especially it brings a valuable information about the degree of crystallinity as well as the size and shape of crystalline domains.[42] The other important measurement of modified nanomaterials is BET, which stands for Brunauer-Emmett-Teller, is a common technique used to characterize the specific surface area and porosity of nanomaterials. The BET method works by analyzing the adsorption of gas molecules on the surface of a solid material - typically nitrogen, at different pressure range, and the amount of gas adsorbed is measured. This data can then be analyzed using a mathematical model, known as the BET isotherm, which relates the amount of gas adsorbed to the pressure of the gas. From this analysis, the specific surface area of the nanomaterial can be determined. In addition, the pore size and pore volume of the nanomaterial can also be determined using the BET technique by incorporating other gas adsorption methods, such as the Barrett-Joyner-Halenda (BJH) or the Dollimer-Healy (DH) methods.[4,43] The adsorption and desorption isotherms obtained from BET analysis can exhibit different types of hysteresis, which can provide information about the pore structure and surface properties of the nanomaterials. Hysteresis refers to the differences between the adsorption and desorption curves, which can result from the formation of capillary condensation in mesopores or micropores, or from differences in the strength of adsorbate-substrate interaction. i) Type I hysteresis - the most common hysteresis pattern observed in nanomaterials with uniform and cylindrical pores, such as mesoporous silica nanoparticles. The adsorption and desorption isotherm curves overlap, forming a "loop" and indicating a narrow distribution of pore sizes; ii) type II hysteresis - where pattern is associated with non-cylindrical, mesoporous materials with irregular pore shapes, such as metal oxides. The adsorption and desorption curves do not overlap, and the hysteresis loop is an inverted "S" shape indicating a wide distribution of pore sizes; iii) type III hysteresis - this pattern is related to non-porous materials, such as amorphous silica, and indicates strong interactions between the adsorbate and the adsorbent. The adsorption and desorption curves do not overlap, and there is no hysteresis loop; iv) type IV hysteresis – which is observed in microporous materials, such as zeolites, and indicates capillary condensation. The adsorption and desorption curves overlap only slightly, and the hysteresis loop is a horizontal "L" shape.[44] Subsequently, X-ray photoelectron spectroscopy (XPS) is the next profitable technique for characterization of nanomaterials. It provides valuable information about the chemical composition, electronic structure, and surface chemistry of materials at the nanoscale. In XPS, a sample is bombarded with X-rays of a known energy, and the ejected photoelectrons are collected and measured as a function of their kinetic energy. By analyzing the kinetic energies of the photoelectrons and their intensities, it is possible to determine the elemental composition of a sample and the oxidation states of the elements.[45,46] XPS is particularly useful for the study of nanomaterials because their properties, including their high surface area and reactivity, can be strongly influenced by their surface chemistry. This information can be used to determine the presence of impurities, surface functionalization, and adsorbate interactions. For example, if graphene oxide, a significant changes in the C 1s and O 1s peaks in the XPS spectra can be observed reflecting the type of covalent attachment of functional molecules.[29,39,47] Another important tools for investigating functionalization of nanomaterials include microscopic techniques such as scanning electron microscopy (SEM) and transmission electron microscopy (TEM). SEM provides high-resolution images of the surface of a material by scanning it with an electron beam. SEM can be used for both elemental and structural analysis of materials, providing information about surface topography, morphology, particle size and shape, and elemental composition. By operating in different modes, SEM can also be used to provide information about the chemical bonding and electronic structure of functionalized materials. TEM, on the other hand, is a technique that provides high-resolution images of the internal structure of a material. In TEM, an electron beam is transmitted through a thin sample to produce magnified images of the structure. TEM can provide information about crystal structures, defects, particle size and shape, and other structural features.[48] It can also be used to study the functionalization of materials, by examining the distribution and location of functional groups within a material at a sub-nanometer scale. Together, SEM and TEM are powerful tools for the characterization of nanomaterials and functionalized materials, providing a wide range of complementary information on the structural, compositional, and electronic properties of the material.[49] Another example of beneficial technique for characterization of nanomaterials is Raman spectroscopy which bases on non-destructive measurement used to identify the unique vibrational energies of molecules in a sample. It works by measuring the scattered light from the sample when it is illuminated with a monochromatic light source, and the scattered light reveals information about the molecule’s vibrational energies, thus producing a Raman spectrum. This spectrum can provide precise information about the composition and structure of materials in solid, liquid, or gas phases. Conventional Raman spectroscopy is a sensitive technique that can identify and quantify chemical and biological substances in a sample.[50] Surface-enhanced Raman spectroscopy (SERS) amplifies the Raman signal by orders of magnitude and can be used to study analytes in extremely low concentrations. Resonant Raman spectroscopy, on the other hand, detects Raman scattering from molecules that are resonant with the laser frequency. Particularly this spectroscopy can be used to determine number of layers for nanomaterials, its electronic structure, doping level, functionalization degree as well as for mapping of morphology and determination of homogeneity.[51,52]

Energy storage devices are becoming increasingly important as the world transitions towards a more sustainable and renewable energy systems. These devices are designed to store energy that can be used later and are instrumental in providing a stable and reliable source of power for homes, businesses, and other energy-consuming devices. There are several types of energy storage devices, including batteries, supercapacitors, and others. At present batteries are perhaps the most used energy storage devices, and they are found in many consumer products such as smartphones and laptops, as well as in larger systems such as electric cars and grid-level storage solutions. Supercapacitors, also known as ultracapacitors, are another type of energy storage devices, which unlike batteries, supercapacitors can charge and discharge rapidly and have a long cycle life.[53–56] They are commonly used in applications where a burst of power is needed, such as in electric vehicles and regenerative braking systems. There are many different types of energy storage mechanisms, each with their own unique properties and applications. Electrochemical double layer capacitors store energy by separating the charge between two conductive surfaces, creating a double layer of charge at the interface. The separation of charge is maintained by an electrolyte, which allows ions to move between the two surfaces to maintain the electrostatic separation of charge. This mechanism results in a high-power density, fast charging/discharging cycles, and a long cycle life, making electrochemical double layer capacitors ideal for applications such as regenerative braking in electric vehicles, and smoothing out power-peaks in renewable energy systems.[57–60] On the other hand, pseudocapacitors store energy through reversible redox reactions that involve surface adsorption processes. The redox reactions enable the formation of metal oxide/hydroxide films on the electrode surfaces resulting in an increase in capacitance beyond the electrostatic double layer. Pseudocapacitors are characterized by high energy density compared to traditional capacitors, long cycle-life, and high charge/discharge rates. These properties make pseudocapacitors especially useful in applications such as portable electronics, power tools, and emergency power supplies.[61–63] A good candidate for supercapacitors application should be considered through the prism of several main issues: i) specific surface area: nanomaterials have a high surface area-to-volume ratio, which allows them to store more energy per unit of weight or volume which results in higher capacitance and energy density;[64,65] ii) faster charge and discharge rates possibility: the materials with shorter diffusion distances, provide quicker charge and discharge processes. This is particularly useful in high-power applications, such as electric vehicles and grid-level energy storage;[66] iii) improved durability: many nanomaterials are more durable and resistant to degradation compared to conventional materials. This means that they can maintain their performance over a longer period, which is important for long-term energy storage applications[67,68] iv) tunable properties, which are especially available in case of nanomaterials can be tuned by controlling their size, shape, and composition. This allows researchers to design materials with specific properties that are optimized for different applications;[69] v) compatibility with existing manufacturing processes.[70] The most important parameters determined while characterization of novel supercapacitors include: i) capacity which refers to the amount of energy that can be stored in the device; ii) cyclability that relates to the number of charge/discharge cycles that a device can undergo before its performance starts to degrade; iii) efficiency which describes the percentage of the energy input that is actually stored in the device; iv) power density reflecting the amount of power that can be supplied by the energy storage device over a given period of time. High power density devices are required for quick charging or powering devices with high peak loads; v) energy density which describes how much energy is stored within a given volume or mass of a materials.[71,72] Moreover, the safety and environmental impact of the potential material should be considered to provide non-hazardous use of the device and reduce or exclude potential pollution from electrical waste.[73]

2. Research objectives of dissertation

In conclusion modern nanomaterials, including graphene have a significant impact on the field of nanoscience and technology and its wide potential of functionalization offers multiple possibilities of application. The thesis entitled "Synthesis and functionalization of low-dimensional materials towards high performance supercapacitors" aligns with described assumptions. The dissertation focuses on following objectives: design and fabrication of new hybrid materials based on low-dimensional nanomaterials, multiscale characterization of prepared hybrids and electrochemical investigation of synthesized materials and its application in supercapacitors as electrodes. A schematic representation of these objectives is summarized in **Figure 1**. The research was motivated by wide review on modern nanomaterials and its application presented in **P1**, which considers graphene-based materials and other two-dimensional structures as highly efficient sensors.

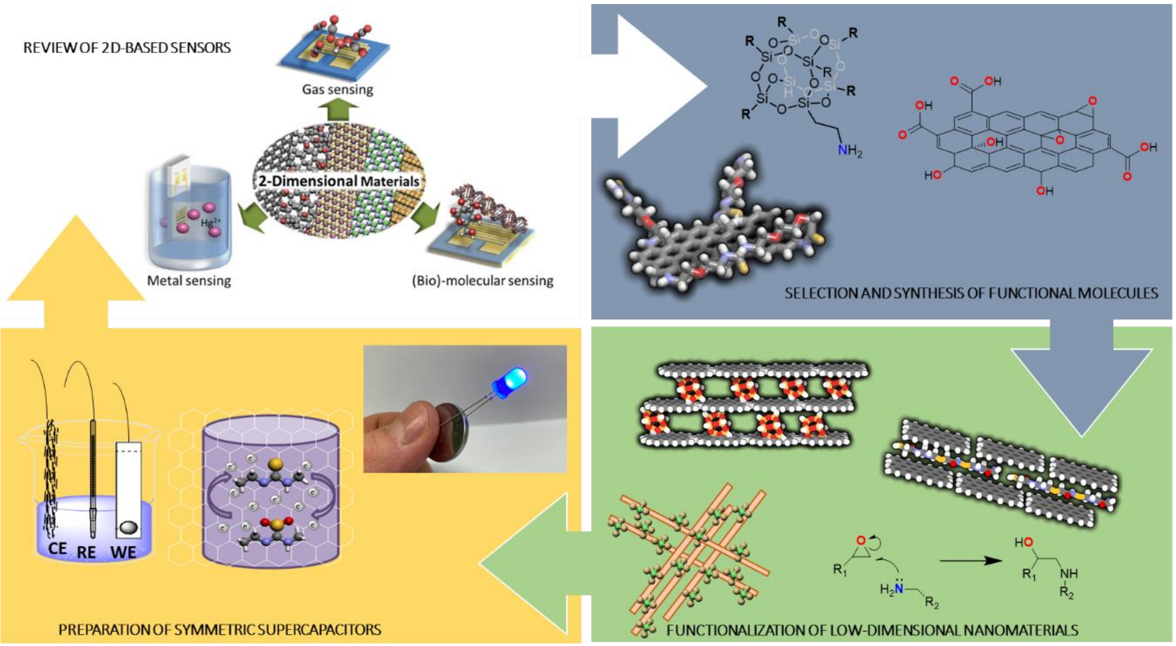

Figure 1 *Schematic representation of research objectives presented in dissertation.*

Objectives included in the dissertation represent a high level of innovation, presenting a unique opportunity to acquire significant information with potential for advancement in the field of nanotechnology. Through an innovative graphene composite design that incorporates functional molecules, novel composites were generated, and their properties were improved remarkably for tailor-made applications and wide spectrum of electrochemical investigations additionally affirm great potential of prepared materials for energy storage systems.

3. Results and discussion

3.1 Synthesis

The fabrication of novel porous nanostructures based on graphene with desired physicochemical properties is in the great interest of scientific community in recent years. Graphene oxide – based hybrid materials were prepared according to the *bottom up* method by introduction of synthesized and commercially available molecules into the GO structure.

[P2] rGO-POSS the synthesis of rGO-POSS was performed using commercially available aqueous suspension of graphene oxide (4 mg/mL) and octaammonium POSS (octa(3-aminopropyl)silsesquioxane hydrochloride) using simple nucleophilic ring opening reaction to provide covalent attachment of POSS molecules. A significant excess of POSS was applied to maximize functionalization degree and to avoid nonhomogeneous structure resulting from random attachment. Notably, we assume reaction of primary amines with epoxides while the terminal amines are present as hydrochloride salt. We compared the direct use of POSS in the form of the salt as well as the reaction with prior treatment with NaOH and no significant changes were observed as the $–NH_3^+Cl^-$ species undergo hydrolysis itself in the conditions of functionalization reaction. The functionalization was followed by chemical reduction with the use of hydrazine to provide optimal amount of oxygen in the final product (rGO-POSS), additionally the NH_2NH_2 treatment allowed to get rid of loosely connected excess of POSS, mainly interacting electrostatically.

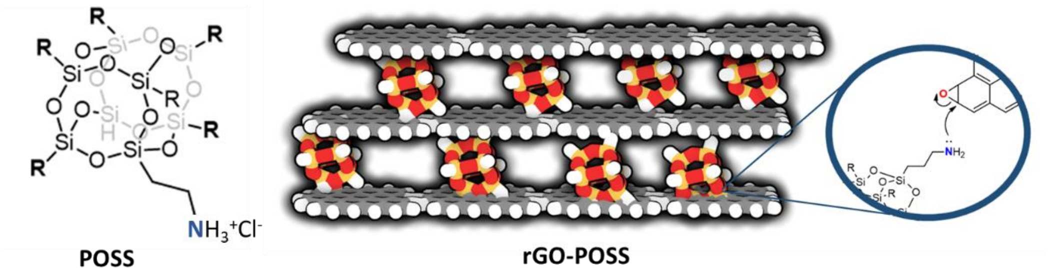

Figure 2 *Schematic representation of octaammonium POSS and rGO-POSS composite.*

[P3] GO-THA The synthesis of thioamide polymer (THA) involved a complex three-step process. Initially, the Hofmann rearrangement reaction was applied, wherein 2,2′-(ethylenedioxy)bis(ethylamine)'s terminal diamines underwent substitution with carbon disulfide, forming dithiocarbamid salt. This reaction was conducted under basic conditions. Subsequently, the dithiocarbamid salt was trnasformed into diisothiocyanate. Finally, the condensation between diisothiocyanate and 2,2′-(ethylenedioxy)bis(ethylamine) was performed to obtain the thioamide polymer (THA). The reaction time for this condensation process was limited to one hour to prevent complete polymerization and the concomitant precipitation of insoluble polymer (**Fig. 3**).

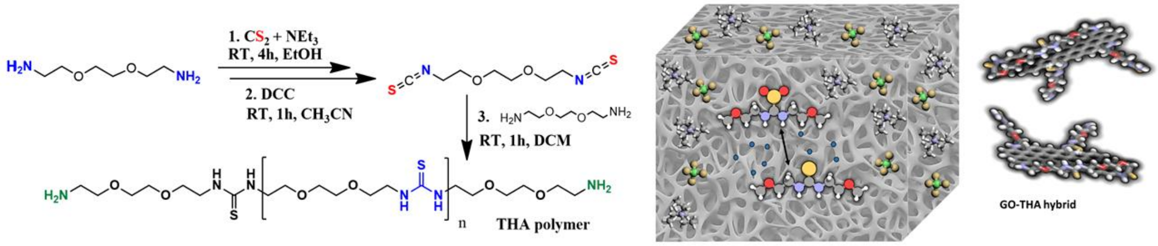

Figure 3 *Scheme representing synthesis of THA polymer and representation of porous GO-THA composite.*

Subsequently, the prepared polymer was used to modify GO. The functionalization relied on the condensation between the primary terminal amines of THA and the epoxide on the surface of GO. Notably, the minor esterification of carboxyl moieties present primarily on GO sheet edges was also observed. In like manner the functionalization was performed utilizing a significant excess of THA polymer with respect to GO to provide efficient functionalization (10:1 *m/m*). Naturally a vast amount of DMF was used to rinse prepared 3-

dimensional nanostructure to make sure that all unreacted polymer was removed from the precipitate.

[P4] The preparation of CuNWs was performed using controlled reduction of copper(II) chloride with glucose in the presence of octadecylamine. Final product of ultralong CuNWs was subsequently separated by centrifugation and transferred into organic phase (ethanol). The synthesis was followed by further modification of CuNWs surface taking advantage of the presence of thin layer of copper oxide, which was successfully functionalized with thiourea molecules at higher temperature (80° C). Interestingly, it was noticed that when the reaction was conducted in water instead of ethanol, the nanowires fragmented significantly. Finally, the mixture of two main crystalline phases was distinguished: a covellite (CuS) and roxbyite ($Cu_{1.8}S$) with the length in the range 20-200 μm and average diameter of 98±17 nm.

3.2 Characterization

The detailed multiscale characterization of modified low dimensional materials has been performed to get better insight into interactions between graphene oxide/CuNWs and functional molecules and provide explanation of its further electrochemical performance. The most important techniques were gently described in *General introduction and motivation* section and most important aspects are presented below.

The functionalized nanostructures included in **P2-P4** were thoroughly investigated in terms of porosity, homogenously and elemental composition and distribution. Powder X-ray diffraction measurement provided information about intercalation of POSS into the 3D structure and the orientation changes due to functionalization. Wide-angle X-ray scattering (WAXS) results revealed that characteristic sharp peak of pristine GO at approximately 10.01°, which corresponds to an interlayer spacing of 0.87 nm due to the (002) reflection of the stacked GO sheets[74], is significantly shifted due to the intercalation towards the lower angle values of 7.65° (**Fig. 4a**). Such shift corresponds to increased interlayer spacing of 1.15 nm, which was presumably due to the modification with POSS particles with sizes of approximately 0.5 nm. Further analysis revealed that after chemical reduction with hydrazine, a new peak appeared at 27.96°, suggesting the presence of new crystalline domains, which corresponded to the partially restored graphitic domains and π-π interactions with a significant shift compared to rGO that resulted from the presence of POSS species. Similarly, the functionalization of GO with THA polymer presented in **P3** was monitored by the shift of GO's peak towards 8.15°, suggesting an increased interlayer spacing between adjacent GO sheets up to 1.05 nm (**Fig. 4b**).[29] Moreover, due to functionalization a new broad peak at 23.4° originating from an amorphous THA phase can be identified. The functionalization was additionally confirmed by Raman spectroscopy as an increase in I_D/I_G ratio from 0.87 to 1.14 which is visible on **Fig. 4f**. On the other hand, in case of copper sulfide nanowires presented in **P4**,

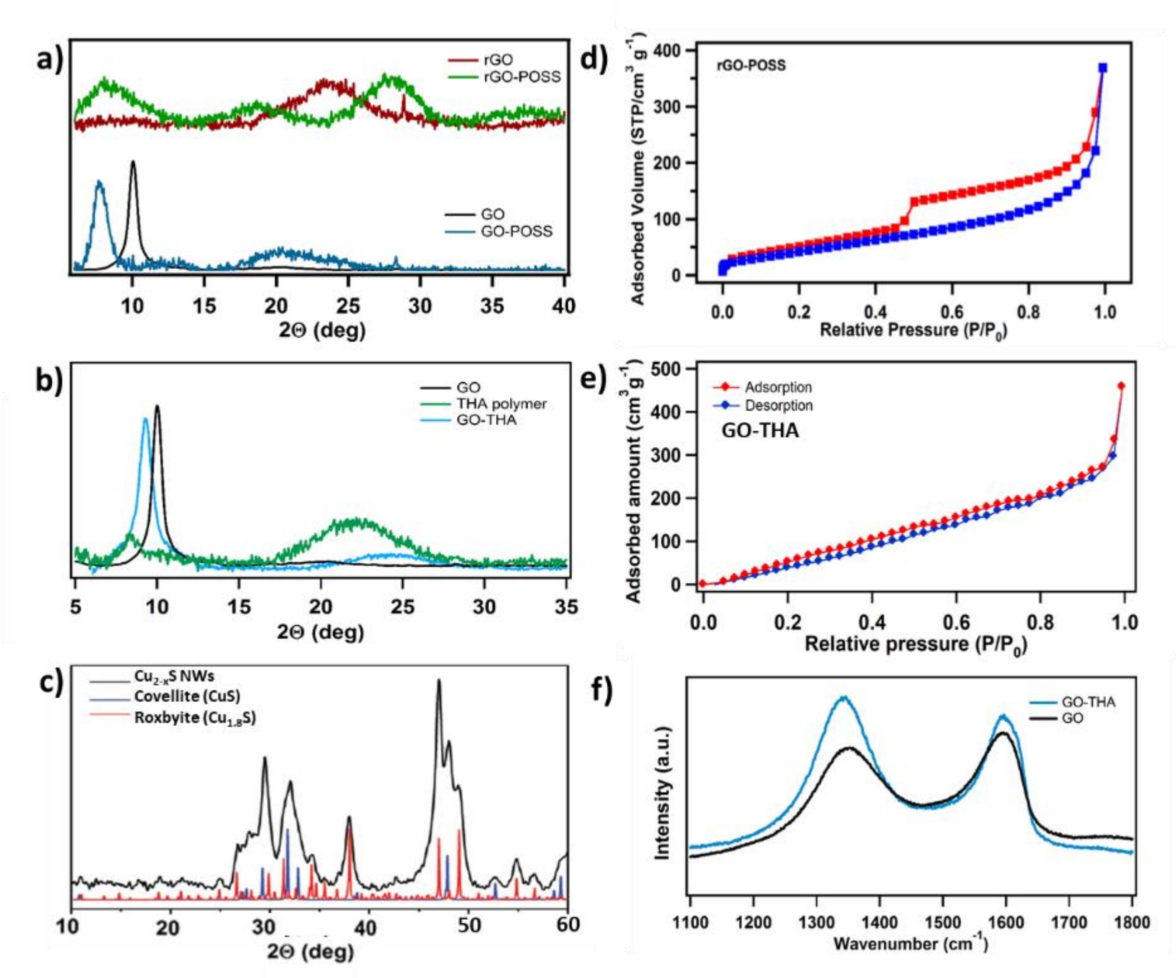

Figure 4 *a) XRD diffractograms of GO, GO-POSS, rGO and rGO-POSS presented in P2; b) XRD diffractograms of GO, THA polymer and GO-THA composite presented in P3; c) XRD diffractograms of Cu2-xS material and reference minerals; d) BET adsorption-desorption curve for rGO-POSS; e) BET adsorption-desorption curve for GO-THA; f) Raman spectroscopy spectra of GO and GO-THA composite.*

XRD was used to identify different crystalline phases. The diffractograms of the nanowires reveal the presence of two types of minerals: covellite (CuS) and roxbyite ($Cu_{1.8}S$).[75] Moreover, the absence of the Cu(111) peak at $2\Theta = 43.31$ and Cu(200) peak at 50.41, typical of metallic CuNWs, indicates a complete conversion of copper(0) to $Cu_{2-x}S$ (**Fig. 4c**).

Subsequently the specific surface area (SSA), pore size, and distribution were quantified using the Brunauer–Emmett–Teller (BET) model. The rGO-POSS hybrid material exhibited a high SSA reaching 180 $m^2\ g^{-1}$, roughly twice the accessible surface area of pristine rGO (**Fig. 4d**). During the functionalization, a new type of pores with the size of 4 nm and an average pore volume of 0.54 $cm^3\ g^{-1}$ were created, which facilitate effective electrolyte transport during electrochemical measurements. The functionalization of GO with THA yielded a threefold increase in specific surface area of 371 $m^2\ g^{-1}$ and slit-like mesopores present in the material with an average pore diameter of 3.1 nm according to BET (**Fig. 4e**). Notably, we can clearly observe that the reduction process, despite its positive influence on the electronic structure of GO-based materials, might result in lower SSA.

The presence of introduced functional molecules into the low-dimensional materials was monitored using XPS studies. Typically, GO itself represents a few characteristic peaks on high resolution C1s spectra corresponding to the C–C (284.6 eV), C–O (286.4 eV), C=O (287.5 eV), and COOH (288.3 eV) bonds (**Fig. 5a**).[76] Comparably, the functionalization of GO with POSS molecules result in appearance of peaks at 284.6 eV, 285.5 eV, 286.4 eV, and 287.5 eV, which can be assigned to C–C, C–N, C–O, and C=O bonds, respectively (**Fig. 5b**). Notably, the C 1s spectra of rGO–POSS exhibit a significant decrease of C–O bonds indicating the successful reduction of unreacted oxygen groups on the surface of GO-POSS (**Fig. 5c**). As expected, the high-resolution N 1s spectra of the GO sample does not show the presence of a nitrogen signal. Conversely, signals observed in the GO-POSS sample can be deconvoluted into two peaks, i.e. at 398.9 eV and 401.2 eV, which can be attributed to the secondary (N-sp^3 bonds) and $–NH_3^+$, respectively. Therefore we assume a major covalent functionalization process with a small amount of electrostatic interactions of protonated amine groups with carboxylic species present on GO' surface. In case of functionalization with THA polymer (**P3**) the analysis of high resolution C1s spectra reveals two new peaks: the C–N bond (287.3 eV) arising from the covalent attachment of terminal primary amines of THA to epoxides present on the surface of GO, additionally the band at 285.5 eV which is assigned to C–S bond present in thioamide polymer itself (**Fig. 5d**). On the other hand, the N 1s spectra of GO-THA provided valuable insight into the composition of obtained material. While the major peak at 399.5 eV can be ascribed to N–C bond of thioamide and secondary amine grouping, the existence of a peak at 398.1 eV is indicative of a resonance effect taking place in the thioamide moiety [R_1–NH–C(=S)–NH–R_2]↔[R_1–HN–C(SH)=N–R_2] (**Fig. 5e**). Interestingly, the sulfur–carbon bonds exposed in the S2p spectra of GO-THA indicated that partial oxidation of sulfides to sulfones occurred simultaneously during functionalization, beneficial for the measurable and reversible redox reactions (**Fig. 5f**). The functionalization of copper nanowires (**P4**) was confirmed by observing the Cu $2p_{3/2}$ peak on high resolution XPS spectra which indicated chemical shift of 932.4 eV, which is assigned to Cu(I) in both CuS and Cu_2S. There are also weak satellite peaks at 945 and 963 eV, while the pronounced tails of Cu $2p_{3/2}$ and $2p_{1/2}$ are due to the metallic properties of copper sulphides (**Fig. 5g**).

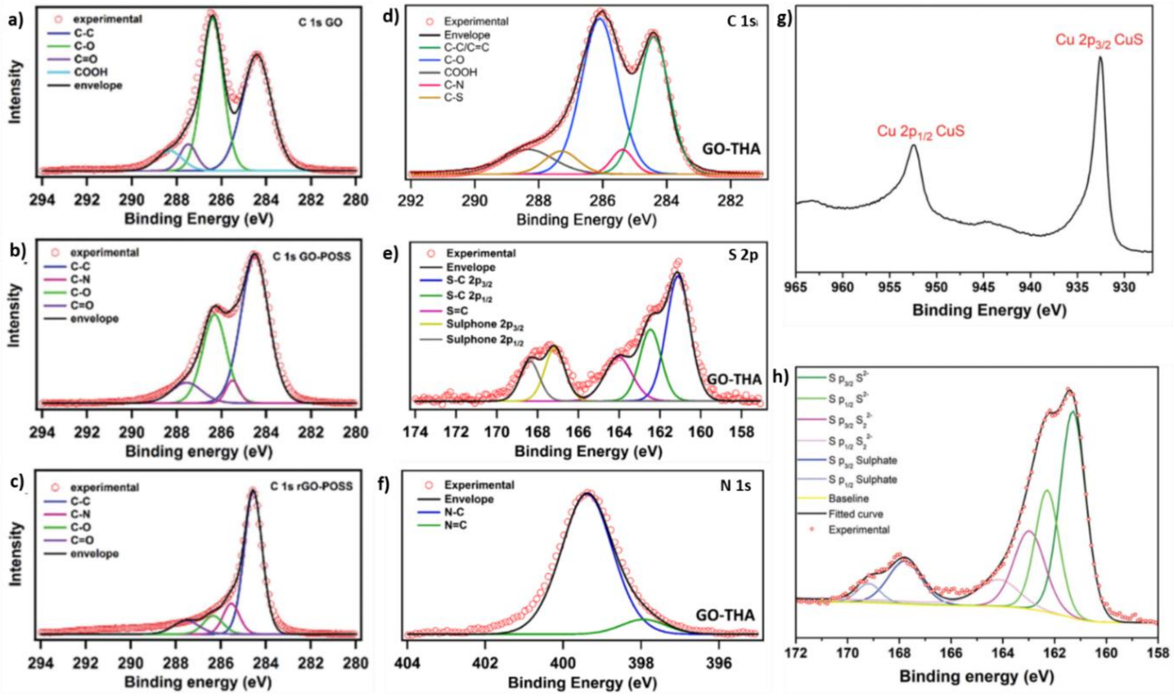

Figure 5 *XPS results, high resolution C1s spectra of a) GO; b) GO-POSS; c) rGO-POSS d) GO-THA; e) S 2p spectra of GO-THA; f) N 1s spectra of GO-THA; g) Cu 2p spectra and h) S p spectra of* $Cu_{2-X}S$ *NWs.*

The high resolution spectra of sulfur reveals components at 161.3 and 162.8 eV belong to the species S^{2-} and S_2^{2-}, which can be found in all copper sulphides. Another peak visible at 167.9 eV is due to the presence of sulfate, perhaps from the decomposition of thiourea, present on the nanowires' surface (**Fig. 5h**).

Subsequently, Interestingly**,** TEM, SEM and EDS analysis provided insights into the morphology and elemental distribution of the final material. In case of functionalized graphene oxide, we can clearly observe porous structure with corrugated nature (**Fig. 6a-b**). Notably, $Cu_{2\text{-}X}S$ NWs exhibit homogenous, long structure with smooth surface (**Fig. 6c**). All presented functionalized materials exhibit equal distribution of expected elements in the whole volume of the samples suggesting efficient functionalization utilizing all available active centers (**Fig. 6d-f**).

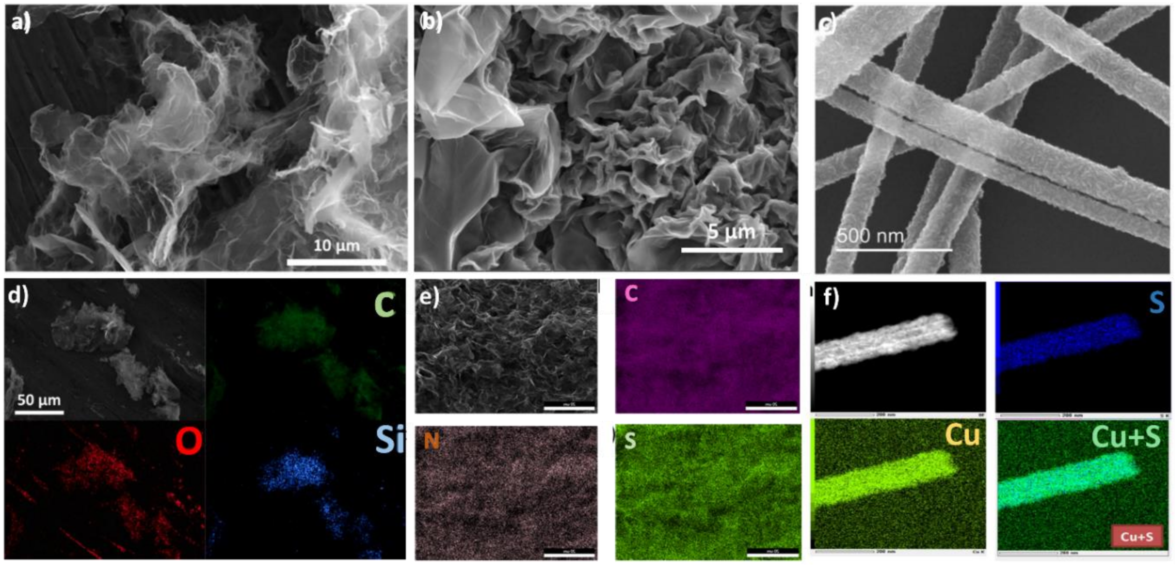

Figure 6 *SEM pictures of a) rGO-POSS; b) GO-THA and c)* $Cu_{2\text{-}x}S$ *NWs; with EDX mapping of the most important elements for each sample (d-f).*

Another important characterization method indicating presence of new types of bonds present in the samples and allowing more detailed determination of molecular interactions is FT-IR. The spectrum rGO-POSS revealed a strong absorption peak at 1573 cm^{-1} corresponding to N-H stretching vibration was observed, along with a broad peak at 3276 cm^{-1} corresponding to N-H vibration of secondary amines, suggesting that most of the $-NH_2$ groups took part in covalent bonding to the surface of graphene oxide. The formation of the rGO-POSS composite was further evidenced by the appearance of bands characteristic of siloxane groups (i.e., Si-O-Si at 1130 cm^{-1} and Si-C at 908 cm^{-1}) coming from the core of the POSS cage. The decreased intensity of peaks corresponding to the C-O bonds resulted from the functionalization and chemical reduction of the final material, and was previously reported while cross-linking GO with amine-based functional molecules. While the functionalization of GO with THA polymer resulted as a strong peak appeared at 1568 cm^{-1} that can be ascribed to C=N–H stretching vibrations which is characteristic for thiourea resonance structure. Moreover, we can observe typical $–CH_2–$ symmetric and asymmetric stretching at 2864 and 2923 cm^{-1}, arising from ethylene grouping present in the polymer.

3.3 Application in supercapacitors

There are several different approaches considering measurements of supercapacitors performance, *e.g.,* the electrode material can be investigated in 2- or 3-electerode setup, also there are symmetric and asymmetric configurations where both electrodes are constructed with the material or other type of materials is applied as a counter electrode. The 3-electrode system is beneficial in terms of more detailed signature of applied material and allows to minimalize the resistance due to presence of vast amount of electrolyte, while 2-electrode system represents more reliable approach in terms of practical applications.

The electrochemical performance of electrode rGO-POSS was investigated in the three electrode setup after deposition of the active material on Au-covered PET substrate with Pt counter electrode and Ag/AgCl reference electrode (**Fig. 7a**). Firstly, cyclic voltammetry was utilized to investigate the electrochemical performance of the rGO-POSS electrode in an aqueous H_2SO_4 (1 M) electrolyte over a potential window ranging from 0 to 1 V. The CV curves demonstrated a quasi-rectangular shape with slight peaks at lower scan rates (1-100 mV s^{-1}), displaying successful electrolyte ion transport and indicating effective electrochemical performance (**Fig. 7d-f**).

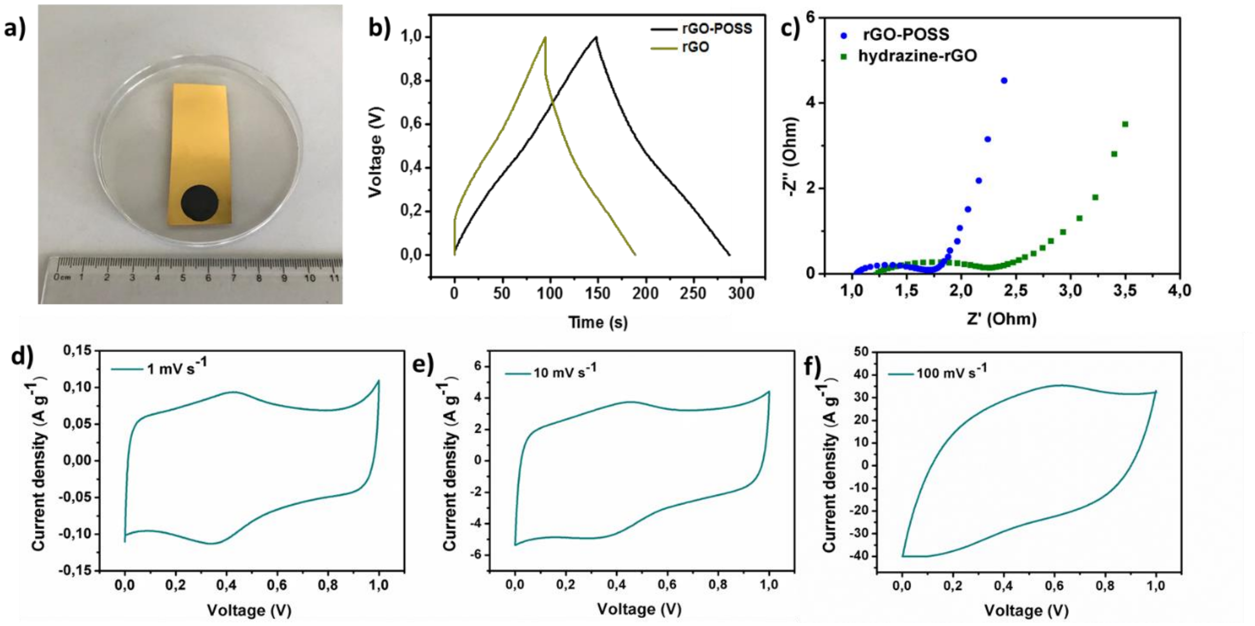

Figure 7 *a) prepared electrode for 3-electrode system; b) galvanostatic charge-discharge measurements for rGO-POSS and reference material at 1 A g^{-1}; c) electrochemical impedance spectroscopy of prepared electrode and reference material; d-f) cyclic voltammetry profiles of rGO-POSS at different scan rates.*

The presence of redox peaks also suggests presence of pseudocapacity phenomena in energy storage mechanism. In fact, the specific capacitance achieved at a scan rate of 1 mV s^{-1} was 179 F g^{-1}, which is relatively high compared to chemically reduced graphene oxide-based materials and significantly surpasses the reference material (rGO) performance which specific capacitance reaches 94 F g^{-1}. Additionally, experiments revealed that the prepared electrode demonstrated good areal capacitance of 350 mF cm^{-2} and volumetric capacitance reaching 115 F cm^{-3}, along with a power density of 2.25 W cm^{-3}. Furthermore, the electrode displayed excellent cyclability with over 98% initial capacitance remaining after 5000 cycles tested at a scan rate of 100 mV s^{-1}. The Warburg resistance of the rGO-POSS electrode was estimated at 1.75 Ohm, indicating fast charge transfer during the energy storage process, good conductivity, and better ion transfer between the electrolyte-electrode than that of hydrazine-reduced graphene oxide (**Fig. 7c**). The prepared electrode demonstrated a volumetric energy density of 41.4 mW h cm^{-3}, making it an important parameter for potential real-world applications in electric vehicles and mobile devices. Another approach was presented in **P3** for GO-THA composite which was investigated in symmetric two electrode device in coin cell type setup. Notably, the use of aqueous electrolyte (1M H_2SO_4)

improved the wettability due to the presence of electronegative atoms (O, N, S) in the GO-THA hybrid, which is confirmed by a good conductivity (reaching 140 S cm^{-1}). The electrode performance was showcased through cyclic voltammetry (CV) and galvanostatic charge-discharge (GCD) curves, indicating good reversibility and effective charging and discharging of the electrodes (**Fig. 8a-b**). Additionally, the electrode did not show any IR drop, confirming a negligible charge loss due to resistance effect. Moreover, the CV profiles represent peaks at 0.4 and 0.5 V indicating co-participation of redox reactions taking place on introduced heteroatoms while electrochemical performance. The GO-THA-based device exhibited high specific capacitance of 221 F g^{-1} at current density of 1 A g^{-1}, which decreases to 120 F g^{-1} at 20 A g^{-1}, presenting good capacitance retention. The performance after 5000 cycles, is almost sustained as the decrease of the initial capacitance reaches around 2%. The use of 1 M TEABF$_4$ in acetonitrile as the electrolyte widened the potential window up to 2 V and results in greater specific capacitance of 371 F g^{-1} as well as excellent energy density up to 94.4 Wh kg^{-1} and a power density reaching 333 mWh cm^{-3}, making this a standout performance among other GO-related materials (**Fig. 8d-e**). Moreover, the electrodes exhibited relatively low impedance in both electrolytes which confirms effective charge transfer while electrochemical processes (**Fig. 8c,f**).

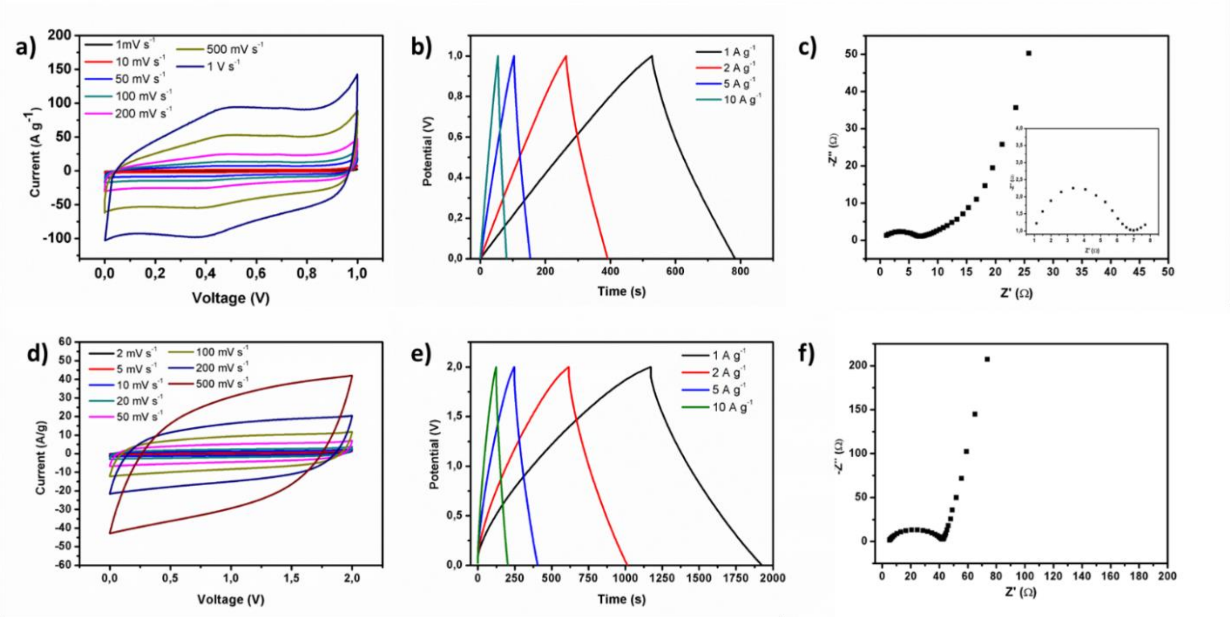

Figure 8 *The electrochemical measurements for GO-THA in 1 M* H_2SO_4*: a) cyclic voltammetry in the range 1-1000 mV* s^{-1}*; b) galvanostatic charge-discharge in the range 1-10 A* g^{-1}*; c) electrochemical impedance spectroscopy; and electrochemical measurements for GO-THA in organic electrolyte (1M* $TEABF_4$ *in ACN): d) cyclic voltammetry in the range 1-1000 mV* s^{-1}*; e) galvanostatic charge-discharge in the range 1-10 A* g^{-1}*; f) electrochemical impedance spectroscopy;*

Lastly, the electrochemical performance of $Cu_{2-x}S$ NWs was investigated in symmetric coin cell setup with ionic liquid type electrolyte. Cyclic voltammetry (CV) analyses were performed between 0 and 2.5 V at various scan rates, from 5 mV s^{-1} to 2000 mV s^{-1}, indicating pseudocapacitive behavior due to the significant contribution of faradaic reactions in the storage mechanism (**Fig. 9a-b**). The highest specific capacitance of 324 F g^{-1} was obtained at lower scan rates of 5 mV s^{-1}, which is similar to that of previously reported supercapacitors based on copper sulfide NWs. The volumetric capacitance and energy density of the electrode were estimated at 60.5 F cm^{-3} and 52.5 mWh cm^{-3}, respectively. The material showed moderate capacitance retention of 70% of initial capacitance after 5000 cycles at 100 mV s^{-1}, which suggests the formation of an irreversibly oxidized passivation layer protecting the rest of the active material over the first 1000 cycles. The GCD curves also confirmed this pseudocapacitive behavior showing disturbed shape, while the Nyquist plot revealed a relatively low resistance with the Warburg resistance corresponding to ion transfer on the electrolyte-Cu_{2-x}SNWs electrode interface, indicating good ion migration through the electrode (**Fig. 9c-d**).

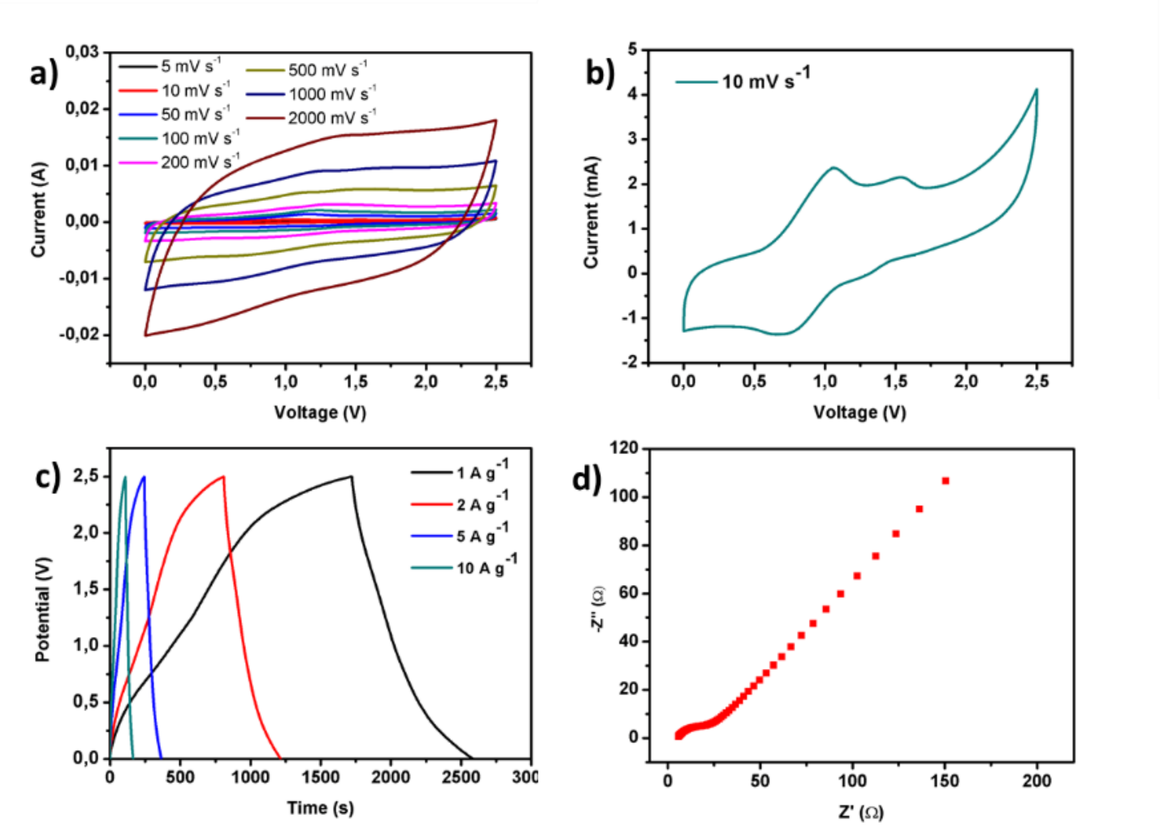

Figure 9 *Electrochemical measurements of $Cu_{2+x}S$ NWs in ionic liquid electrolyte a) cyclic voltammetry at 5-2000 mV s^{-1}; b) CV curve at 10 mV s^{-1}; c) galvanostatic charge-discharge at 1-10 A g^{-1}; d) Nyquist plot.*

4. Conclusions

This dissertation includes four thematically coherent scientific articles (**P1**-**P4**) representing innovative approach to the design and functionalization of low-dimensional materials (graphene oxide, copper nanowires) and application in supercapacitors.

The *bottom up* strategy was applied for functionalization of graphene oxide with octaammonium POSS (rGO-POSS) and thioamide-based polymer (GO-THA) and copper nanowires with thiourea ($Cu_{2-x}S$ NWs). The synthesis is based on simple reactions such as the use of primary amines towards nucleophilic epoxide ring opening and metallic surface modification. The use of commercially available raw materials represents low-cost and scalable process allowing fabrication of vast amounts of hybrid nanomaterials with well-defined structure and composition with excellent electrochemical properties.

The detailed characteristics of prepared materials provides information about the types of interaction between low-dimensional materials and functional molecules, as well as the degree of functionalization and confirms homogeneity of prepared nanomaterials. It was proven that high porosity, large specific surface area and optimal pore types and size and introduction of molecular spacers and heteroatoms provide excellent features for further electrochemical properties investigation.

Application in supercapacitors was investigated in vary device configurations and conditions such as applied electrolyte providing valuable information about electrochemical performance, good conductivity, and effective charge transfer while charge-discharge cycles. The rGO-POSS revealed capacitance of 174 F g^{-1} significantly exceeding value obtained for reference material. Morevoer, it exhibited power density of 2.25 W cm^{-3} and energy density was estimated at 41.4 mW h cm^{-3} as well as great capacitance retention after 5000 cycles (<98%) which can be attributed to increase of interlayer spaced provided by introduction of the POSS molecules. The porous GO-THA nanocomposite, which was investigated in symmetric two electrodes coin-cell revealed specific capacitance of 221 F g^{-1} at 1 A g^{-1} (1M H_2SO_4), while the use of organic media allows the specific capacitance to be boosted up to 340 F g^{-1}. As a result of wider operating window combined with high porosity and mixed energy storage mechanism facilitates high energy densities up to 94.4 Wh kg^{-1}. Lastly, copper sulfide nanowires were investigated in ionic liquid electrolyte, where significant pseudocapacitive behavior was observed reaching 324 F g^{-1} and volumetric capacitance of 60.5 F cm^{-3}, with stability limited to 70% of initial capacitance after 5000 cycles as a result of surface passivation while first electrochemical cycles.

Even though the high performance of energy storage devices was achieved in this dissertation, they are still far from real practical applications. There is plenty of room to explore new electrode composites for supercapacitors. In future works, it will be of interest to investigate low-cost high-performance novel low-dimensional based electrode materials and explore their electrochemical performance to construct hybrid batteries with higher energy and power densities, moreover, the strategies for improving the performance of low-dimensional material based electrodes should be demonstrated in full cells for practical applications

5. References

[1] N. Baig, I. Kammakakam, W. Falath, *Mater. Adv.* **2021**, *2*, 1821.

[2] F. Bonaccorso, L. Colombo, G. Yu, M. Stoller, V. Tozzini, A. C. Ferrari, R. S. Ruoff, V. Pellegrini, *Science* **2015**, *347*, 1246501.

[3] J. Ni, Y. Li, *Adv. Energy Mater.* **2016**, *6*, 1600278.

[4] N. Yousefi, X. Lu, M. Elimelech, N. Tufenkji, *Nat. Nanotechnol.* **2019**, *14*, 107.

[5] C. Anichini, W. Czepa, D. Pakulski, A. Aliprandi, A. Ciesielski, P. Samorì, *Chem Soc Rev* **2018**, *47*, 4860.

[6] K. S. Novoselov, D. Jiang, F. Schedin, T. J. Booth, V. V. Khotkevich, S. V. Morozov, A. K. Geim, *Proc. Natl. Acad. Sci.* **2005**, *102*, 10451.

[7] T. Chowdhury, E. C. Sadler, T. J. Kempa, *Chem. Rev.* **2020**, *120*, 12563.

[8] B. Anasori, M. R. Lukatskaya, Y. Gogotsi, *Nat. Rev. Mater.* **2017**, *2*, 16098.

[9] Q. Li, J.-T. Wu, Y. Liu, X.-M. Qi, H.-G. Jin, C. Yang, J. Liu, G.-L. Li, Q.-G. He, *Anal. Chim. Acta* **2021**, *1170*, 338480.

[10] D. X. Luong, K. V. Bets, W. A. Algozeeb, M. G. Stanford, C. Kittrell, W. Chen, R. V. Salvatierra, M. Ren, E. A. McHugh, P. A. Advincula, Z. Wang, M. Bhatt, H. Guo, V. Mancevski, R. Shahsavari, B. I. Yakobson, J. M. Tour, *Nature* **2020**, *577*, 647.

[11] M. Zhao, Y. Wang, Q. Ma, Y. Huang, X. Zhang, J. Ping, Z. Zhang, Q. Lu, Y. Yu, H. Xu, Y. Zhao, H. Zhang, *Adv. Mater.* **2015**, *27*, 7372.

[12] M. Yi, Z. Shen, *J Mater Chem A* **2015**, *3*, 11700.

[13] A. Gutiérrez-Cruz, A. R. Ruiz-Hernández, J. F. Vega-Clemente, D. G. Luna-Gazcón, J. Campos-Delgado, *J. Mater. Sci.* **2022**, *57*, 14543.

[14] S. Witomska, T. Leydecker, A. Ciesielski, P. Samorì, *Adv. Funct. Mater.* **2019**, *29*, 1901126.

[15] M. J. Allen, V. C. Tung, R. B. Kaner, *Chem. Rev.* **2010**, *110*, 132.

[16] B. L. Dasari, J. M. Nouri, D. Brabazon, S. Naher, *Energy* **2017**, *140*, 766.

[17] Y. Chen, B. Zhang, G. Liu, X. Zhuang, E.-T. Kang, *Chem Soc Rev* **2012**, *41*, 4688.

[18] P. Bhol, S. Yadav, A. Altaee, M. Saxena, P. K. Misra, A. K. Samal, *ACS Appl. Nano Mater.* **2021**, *4*, 3274.

[19] G. Liu, W. Jin, N. Xu, *Chem Soc Rev* **2015**, *44*, 5016.

[20] D. R. Dreyer, S. Park, C. W. Bielawski, R. S. Ruoff, *Chem Soc Rev* **2010**, *39*, 228.

[21] V. A. Nebol'sin, V. Galstyan, Y. E. Silina, *Surf. Interfaces* **2020**, *21*, 100763.

[22] A. T. Smith, A. M. LaChance, S. Zeng, B. Liu, L. Sun, *Nano Mater. Sci.* **2019**, *1*, 31.

[23] U. A. Méndez-Romero, M. A. Velasco-Soto, L. Licea-Jiménez, J. González-Hernández, S. A. Pérez-García, *Nano Sel.* **2021**, *2*, 2168.

[24] Z. Liu, T. Rios-Carvajal, M. Ceccato, T. Hassenkam, *J. Colloid Interface Sci.* **2019**, *556*, 458.

[25] D. G. Papageorgiou, I. A. Kinloch, R. J. Young, *Prog. Mater. Sci.* **2017**, *90*, 75.

[26] L. Liu, J. Zhang, J. Zhao, F. Liu, *Nanoscale* **2012**, *4*, 5910.

[27] A. Razaq, F. Bibi, X. Zheng, R. Papadakis, S. H. M. Jafri, H. Li, *Materials* **2022**, *15*.

[28] J. Park, M. Yan, *Acc. Chem. Res.* **2013**, *46*, 181.

[29] D. Pakulski, W. Czepa, S. Witomska, A. Aliprandi, P. Pawluć, V. Patroniak, A. Ciesielski, P. Samorì, *J Mater Chem A* **2018**, *6*, 9384.

[30] V. Georgakilas, J. N. Tiwari, K. C. Kemp, J. A. Perman, A. B. Bourlinos, K. S. Kim, R. Zboril, *Chem. Rev.* **2016**, *116*, 5464.

[31] S. Omidi, A. Kakanejadifard, F. Azarbani, *J. Mol. Liq.* **2017**, *242*, 812.

[32] S. Bouchareb, R. Doufnoune, F. Riahi, H. Cherif-Silini, L. Belbahri, *Mater. Chem. Phys.* **2020**, *243*, 122598.

[33] W. Czepa, D. Pakulski, S. Witomska, V. Patroniak, A. Ciesielski, P. Samorì, *Carbon* **2020**, *158*, 193.

[34] A. Lopez, J. Liu, *Adv. Intell. Syst.* **2020**, *2*, 2000123.
[35] C. F. Holder, R. E. Schaak, *ACS Nano* **2019**, *13*, 7359.
[36] H. Mahdavi, P. K. Kahriz, H. Gholipour-Ranjbar, T. Shahalizade, *J. Mater. Sci. Mater. Electron.* **2017**, *28*, 4295.
[37] S. Yu, J. Liu, W. Zhu, Z.-T. Hu, T.-T. Lim, X. Yan, *Sci. Rep.* **2015**, *5*, 16369.
[38] H. Zhang, X. Wang, Y. Li, C. Guo, C. Zhang, *Appl. Phys. A* **2019**, *125*, 86.
[39] S. Witomska, Z. Liu, W. Czepa, A. Aliprandi, D. Pakulski, P. Pawluć, A. Ciesielski, P. Samorì, *J. Am. Chem. Soc.* **2019**, *141*, 482.
[40] W. Tian, S. Li, B. Wang, X. Chen, J. Liu, M. Yu, *Int. J. Miner. Metall. Mater.* **2016**, *23*, 723.
[41] T. Batakliev, I. Petrova-Doycheva, V. Angelov, V. Georgiev, E. Ivanov, R. Kotsilkova, M. Casa, C. Cirillo, R. Adami, M. Sarno, P. Ciambelli, *Appl. Sci.* **2019**, *9*.
[42] S. Polizzi, G. Fagherazzi, A. Benedetti, M. Battagliarin, T. Asano, *Eur. Polym. J.* **1991**, *27*, 85.
[43] S. Varghese, J. P. Chaudhary, C. Ghoroi, *RSC Adv* **2020**, *10*, 13394.
[44] M. Thommes, K. Kaneko, A. V. Neimark, J. P. Olivier, F. Rodriguez-Reinoso, J. Rouquerol, K. S. W. Sing, *Pure Appl. Chem.* **2015**, *87*, 1051.
[45] E. Korin, N. Froumin, S. Cohen, *ACS Biomater. Sci. Eng.* **2017**, *3*, 882.
[46] R. Al-Gaashani, A. Najjar, Y. Zakaria, S. Mansour, M. A. Atieh, *Ceram. Int.* **2019**, *45*, 14439.
[47] M. J. Hortigüela, D. Machado, I. Bdikin, V. Neto, G. Otero-Irurueta, *Coatings* **2020**, *10*.
[48] Y.-Y. Chang, H. N. Han, M. Kim, *Appl. Microsc.* **2019**, *49*, 10.
[49] J. N. Coleman, M. Lotya, A. O'Neill, S. D. Bergin, P. J. King, U. Khan, K. Young, A. Gaucher, S. De, R. J. Smith, I. V. Shvets, S. K. Arora, G. Stanton, H.-Y. Kim, K. Lee, G. T. Kim, G. S. Duesberg, T. Hallam, J. J. Boland, J. J. Wang, J. F. Donegan, J. C. Grunlan, G. Moriarty, A. Shmeliov, R. J. Nicholls, J. M. Perkins, E. M. Grieveson, K. Theuwissen, D. W. McComb, P. D. Nellist, V. Nicolosi, *Science* **2011**, *331*, 568.
[50] A. C. Ferrari, D. M. Basko, *Nat. Nanotechnol.* **2013**, *8*, 235.
[51] G. Gouadec, P. Colomban, *Prog. Cryst. Growth Charact. Mater.* **2007**, *53*, 1.
[52] A. Sarycheva, Y. Gogotsi, *Chem. Mater.* **2020**, *32*, 3480.
[53] Q. Zhu, D. Zhao, M. Cheng, J. Zhou, K. A. Owusu, L. Mai, Y. Yu, *Adv. Energy Mater.* **2019**, *9*, 1901081.
[54] Q. Xue, J. Sun, Y. Huang, M. Zhu, Z. Pei, H. Li, Y. Wang, N. Li, H. Zhang, C. Zhi, *Small* **2017**, *13*, 1701827.
[55] L. Hao, X. Li, L. Zhi, *Adv. Mater.* **2013**, *25*, 3899.
[56] A. G. Olabi, Q. Abbas, A. Al Makky, M. A. Abdelkareem, *Energy* **2022**, *248*, 123617.
[57] G. Jeanmairet, B. Rotenberg, M. Salanne, *Chem. Rev.* **2022**, *122*, 10860.
[58] M. Favaro, B. Jeong, P. N. Ross, J. Yano, Z. Hussain, Z. Liu, E. J. Crumlin, *Nat. Commun.* **2016**, *7*, 12695.
[59] C. Li, X. Zhang, Z. Lv, K. Wang, X. Sun, X. Chen, Y. Ma, *Chem. Eng. J.* **2021**, *414*, 128781.
[60] C.-F. Liu, Y.-C. Liu, T.-Y. Yi, C.-C. Hu, *Carbon* **2019**, *145*, 529.
[61] Q. Lu, J. G. Chen, J. Q. Xiao, *Angew. Chem. Int. Ed.* **2013**, *52*, 1882.
[62] N. R. Chodankar, H. D. Pham, A. K. Nanjundan, J. F. S. Fernando, K. Jayaramulu, D. Golberg, Y.-K. Han, D. P. Dubal, *Small* **2020**, *16*, 2002806.
[63] K. Zhang, X. Han, Z. Hu, X. Zhang, Z. Tao, J. Chen, *Chem Soc Rev* **2015**, *44*, 699.
[64] Y. Liu, N. Xin, Q. Yang, W. Shi, *J. Colloid Interface Sci.* **2021**, *583*, 288.
[65] K. Li, B. Zhao, H. Zhang, H. Lv, J. Bai, H. Ma, P. Wang, W. Li, J. Si, X. Zhu, Y. Sun, *Adv. Funct. Mater.* **2021**, *31*, 2103073.
[66] M. Hepel, *Electrochem. Sci. Adv.* **2022**, *n/a*, e2100222.
[67] H. Wang, M. Wang, Y. Tang, *Energy Storage Mater.* **2018**, *13*, 1.
[68] C. Guan, J. Liu, Y. Wang, L. Mao, Z. Fan, Z. Shen, H. Zhang, J. Wang, *ACS Nano* **2015**, *9*, 5198.
[69] I. Mukkatt, A. P. Mohanachandran, A. Nirmala, D. Patra, P. A. Sukumaran, R. S. Pillai, R. B. Rakhi, S. Shankar, A. Ajayaghosh, *ACS Appl. Mater. Interfaces* **2022**, *14*, 31900.

[70] V. Vignesh, R. Divya, M. Sundararajan, S. Yuvaraj, In *Smart Supercapacitors* (Eds.: Hussain, C. M.; Ahamed, M. B.), Elsevier, **2023**, pp. 631–650.

[71] Y. Zhang, H. Mei, Y. Cao, X. Yan, J. Yan, H. Gao, H. Luo, S. Wang, X. Jia, L. Kachalova, J. Yang, S. Xue, C. Zhou, L. Wang, Y. Gui, *Coord. Chem. Rev.* **2021**, *438*, 213910.

[72] Y. Zhao, C. Liu, Q. Lu, O. Ahmad, X. Pan, M. Daria, *New Carbon Mater.* **2022**, *37*, 875.

[73] A. Dutta, J. Mahanta, T. Banerjee, *Adv. Sustain. Syst.* **2020**, *4*, 2000182.

[74] X. Jiao, Y. Qiu, L. Zhang, X. Zhang, *RSC Adv.* **2017**, *7*, 52337.

[75] K. Tezuka, W. C. Sheets, R. Kurihara, Y. J. Shan, H. Imoto, T. J. Marks, K. R. Poeppelmeier, *Solid State Sci.* **2007**, *9*, 95.

[76] J. Zhang, Y. Xu, Z. Liu, W. Yang, J. Liu, *RSC Adv.* **2015**, *5*, 54275.

Author contribution

Włodzimierz Czepa
Wydział Chemii UAM

Poznań, 01.06.2023

Author Contribution Form

I hereby declare that in the following publications:

1. Cosimi Anchini*, Włodzimierz Czepa*, Dawid Pakulski*, Alessandro Aliprandi, Artur Ciesielski, Paolo Samori - „Chemical sensing with 2D materials" **Chemical Society Reviews**, 2018, 47, 4860.

My own contribution to above article includes:
- planning of the study;
- discussion results and interpretation of data;
- writing chapter "(Bio)molecular sensors";
- revision of the manuscript.

2. Włodzimierz Czepa, Samanta Witomska, Artur Ciesielski, Paolo Samori - „Reduced graphene oxide-silsesquioxane hybrid as a novel supercapacitor electrode" **Nanoscale**, 2020, 12. 18733.

My own contribution to above article includes:
- planning of the study;
- Synthesis of rGO-POSS material;
- Characterization of the materials including XRD, XPS, BET, EDX, SEM, TEM.
- Preparation of electrodes and electrochemical measurements;
- discussion results and interpretation of data;
- writing and editing the manuscript;
- revision of the manuscript.

3. Włodzimierz Czepa, Samanta Witomska, Artur Ciesielski, Paolo Samori - „ A graphene oxide – thioamide polymer hybrid for high performance supercapacitor electrodes" **Small Science**, 2023,

My own contribution to above article includes:
- planning of the study;
- Synthesis of GO-THA material;
- Characterization of GO-THA material including: EDX, SEM, TEM, XPS, XRD, FT-IR, Raman, BET, TGA;

- Preparation of the electrodes and electrochemical measurements;
- discussion results and interpretation of data;
- writing and editing the manuscript;
- revision of the manuscript.

4. Cosimo Anichini, Włodzimierz Czepa, Alessandro Aliprandi, Valentina Girelli Consolaro, Ovidiu Ersen, Artur Ciesielski, Paolo Samori - „Synthesis and characterization of ultralong copper sulfide nanowires and their electrical proprties” **Journal of Materials Chemistry C**, 2021, 9, 12133.

My own contribution to above article includes:
- discussion results and interpretation of data;
- characterization of copper sulfide nanowires including XRD analysis;
- preparation of the electrodes and electrochemical measurements;
- writing and editing the manuscript;
- revision of the manuscript.

Czepa Włodzimierz

Artur Ciesielski (HDR, Research Associate)
Institut de Science et d'Ingénierie Supramoléculaires (I.S.I.S.)
University of Strasbourg & CNRS,
Adam Mickiewicz University

Strasbourg, 25.05.2023

Author Contribution Form

I hereby declare that in the following publications:

1. Cosimi Anchini*, Włodzimierz Czepa*, Dawid Pakulski*, Alessandro Aliprandi, Artur Ciesielski, Paolo Samori - „Chemical sensing with 2D materials" **Chemical Society Reviews**, 2018, 47, 4860.

My own contribution to above article includes:
- planning of the study;
- discussion results and interpretation of data;
- writing and editing the manuscript;
- revision of the manuscript.

2. Włodzimierz Czepa, Samanta Witomska, Artur Ciesielski, Paolo Samori - „Reduced graphene oxide-silsesquioxane hybrid as a novel supercapacitor electrode" **Nanoscale**, 2020, 12. 18733.

My own contribution to above article includes:
- planning of the study;
- discussion results and interpretation of data;
- writing and editing the manuscript;
- revision of the manuscript.

3. Włodzimierz Czepa, Samanta Witomska, Artur Ciesielski, Paolo Samori - „ A graphene oxide – thioamide polymer hybrid for high performance supercapacitor electrodes" **Small Science**, 2023,

My own contribution to above article includes:
- planning of the study;
- discussion results and interpretation of data;
- writing and editing the manuscript;
- revision of the manuscript.

4. Cosimo Anichini, Włodzimierz Czepa, Alessandro Aliprandi, Valentina Girelli Consolaro, Ovidiu Ersen, Artur Ciesielski, Paolo Samori - „Synthesis and characterization of ultralong copper sulfide nanowires and their electrical proprties" **Journal of Materials Chemistry C**, 2021, 9, 12133.

My own contribution to above article includes:
- planning of the study;
- discussion results and interpretation of data;
- writing and editing the manuscript;
- revision of the manuscript.

Ciesielski

Strasbourg, 29.05.2023

Prof. Paolo Samorì
Membre de l'Académie des technologies
FRSC
Fellow of the European Academy of Sciences (EURASC)
Member of the Academia Europaea (MAE)
Institut Universitaire de France (IUF)

Director
Institut de Science et d'Ingénierie Supramoléculaires (I.S.I.S.)
Université de Strasbourg & CNRS
8, allée Gaspard Monge
F-67000 Strasbourg (France)
Tel: +33-(0)3-68855160
Tel secretary: +33-(0)3-68855204
Fax: +33-(0)3-68855236

Author Contribution Form

I hereby declare that in the following publications:

1. Cosimi Anchini*, Włodzimierz Czepa*, Dawid Pakulski*, Alessandro Aliprandi, Artur Ciesielski, Paolo Samori - „Chemical sensing with 2D materials" **Chemical Society Reviews**, 2018, 47, 4860.

My own contribution to above article includes:
- discussion results and interpretation of data;
- writing and editing the manuscript;
- revision of the manuscript.

2. Włodzimierz Czepa, Samanta Witomska, Artur Ciesielski, Paolo Samori - „Reduced graphene oxide-silsesquioxane hybrid as a novel supercapacitor electrode" **Nanoscale**, 2020, 12. 18733.

My own contribution to above article includes:
- discussion results and interpretation of data;
- revision of the manuscript.

3. Włodzimierz Czepa, Samanta Witomska, Artur Ciesielski, Paolo Samori - „ A graphene oxide – thioamide polymer hybrid for high performance supercapacitor electrodes" **Small Science**, 2023,

My own contribution to above article includes:
- writing and editing the manuscript;
- revision of the manuscript.

4. Cosimo Anichini, Włodzimierz Czepa, Alessandro Aliprandi, Valentina Girelli Consolaro, Ovidiu Ersen, Artur Ciesielski, Paolo Samori - „Synthesis and characterization of ultralong copper sulfide nanowires and their electrical proprties” **Journal of Materials Chemistry C**, 2021, 9, 12133.

My own contribution to above article includes:
- planning of the study;
- discussion results and interpretation of data;
- writing and editing the manuscript;

Paolo Samorì

Samanta Witomska (PhD)
Centre for Advanced Technologies UAM

Strasbourg, 29.05.2023

Author Contribution Form

I hereby declare that in the following publications:

1. Włodzimierz Czepa, Samanta Witomska, Artur Ciesielski, Paolo Samori - „Reduced graphene oxide-silsesquioxane hybrid as a novel supercapacitor electrode" **Nanoscale**, 2020, 12. 18733.

My own contribution to above article includes:
- characterization of rGO-POSS composite including: FT-IR, TGA analysis;
- discussion results and interpretation of data;
- writing and editing the manuscript;

2. Włodzimierz Czepa, Samanta Witomska, Artur Ciesielski, Paolo Samori - „ A graphene oxide – thioamide polymer hybrid for high performance supercapacitor electrodes" **Small Science**, 2023,

My own contribution to above article includes:
- planning of the study;
- Synthesis of THA polymer,
- Characterization of THA polymer including NMR analysis;
- writing and editing the manuscript;

Witomska

Dawid Pakulski (PhD)
Adam Mickiewicz University Foundation

Poznań , 29.05.2023

Author Contribution Form

I hereby declare that in the following publications:

1. Cosimi Anchini*, Włodzimierz Czepa*, Dawid Pakulski*, Alessandro Aliprandi, Artur Ciesielski, Paolo Samori - „Chemical sensing with 2D materials" **Chemical Society Reviews**, 2018, 47, 4860.

My own contribution to above article includes:
- planning of the study;
- discussion results and interpretation of data;
- writing the chapter "Applications in metal sensing";
- revision of the manuscript.

Pakulski Dawid

Cosimo Anchini (PhD)
Institut de Science et d'Ingénierie Supramoléculaires (I.S.I.S.)

Strasbourg, 09.05.2022

Author Contribution Form

I hereby declare that in the following publications:

1. Cosimi Anchini*, Włodzimierz Czepa*, Dawid Pakulski*, Alessandro Aliprandi, Artur Ciesielski, Paolo Samori - „Chemical sensing with 2D materials” **Chemical Society Reviews**, 2018, 47, 4860.

My own contribution to above article includes:

- Planning and discussion of the study;
- Writing the chapter „Application in gas sensing”
- Editing and revision of the manuscript.

2. Cosimo Anichini, Włodzimierz Czepa, Alessandro Aliprandi, Valentina Girelli Consolaro, Ovidiu Ersen, Artur Ciesielski, Paolo Samori - „Synthesis and characterization of ultralong copper sulfide nanowires and their electrical proprties” **Journal of Materials Chemistry C**, 2021, 9, 12133.

My own contribution to above article includes:

- Synthesis of functionalized copper-based nanowires;
- Characterization of $Cu_{2-x}S$ NWs including: XPS, FT-IR, EDX, Raman, SEM, TEM, resistance and bending tests;
- Writing and editing the manuscript;

Anchini
Cosimo

Alessandro Aliprandi (Associate Professor)
Department of Chemical Sciences
University of Padua

Padua, 25.05.2023

Author Contribution Form

I hereby declare that in the following publications:

1. Cosimi Anchini*, Włodzimierz Czepa*, Dawid Pakulski*, Alessandro Aliprandi, Artur Ciesielski, Paolo Samori - „Chemical sensing with 2D materials" **Chemical Society Reviews**, 2018, 47, 4860.

My own contribution to above article includes:

- Planning and discussion of the study;
- Writing the introduction section and editing the manuscript;

2. Cosimo Anichini, Włodzimierz Czepa, Alessandro Aliprandi, Valentina Girelli Consolaro, Ovidiu Ersen, Artur Ciesielski, Paolo Samori - „Synthesis and characterization of ultralong copper sulfide nanowires and their electrical proprties" **Journal of Materials Chemistry C**, 2021, 9, 12133.

My own contribution to above article includes:

- Planning and discussion of the study;
- UV-Vis experiments;
- Writing and editing the manuscript;

Valentina Girelli Consolaro (PhD)
Universite´ de Strasbourg, CNRS, IPCMS

Strasbourg, 09.05.2022

Author Contribution Form

I hereby declare that in the following publications:

1. Cosimo Anichini, Włodzimierz Czepa, Alessandro Aliprandi, Valentina Girelli Consolaro, Ovidiu Ersen, Artur Ciesielski, Paolo Samori - „Synthesis and characterization of ultralong copper sulfide nanowires and their electrical proprties” **Journal of Materials Chemistry C**, 2021, 9, 12133.

My own contribution to above article includes:

- TGA and DSC analysis of copper sulfide nanowires;
- Measurements of ionization energy of $Cu_{2-x}S$ NWs.

V.G. Consolaro

Ovidiu Ersen (Professor)
Institut de Science et d'Ingénierie Supramoléculaires (I.S.I.S.)

Strasbourg, 25.05.2023

Author Contribution Form

I hereby declare that in the following publications:

1. Cosimo Anichini, Włodzimierz Czepa, Alessandro Aliprandi, Valentina Girelli Consolaro, Ovidiu Ersen, Artur Ciesielski, Paolo Samori - „Synthesis and characterization of ultralong copper sulfide nanowires and their electrical proprties" **Journal of Materials Chemistry C**, 2021, 9, 12133.

My own contribution to above article includes:

- Optical microscopy characterization of the Cu-nanowires material;

Ersen O.

Copy of publications included in dissertation

Chem Soc Rev

REVIEW ARTICLE

View Article Online
View Journal | View Issue

Cite this: *Chem. Soc. Rev.*, 2018, **47**, 4860

Chemical sensing with 2D materials

Cosimo Anichini,†[a] Włodzimierz Czepa,†[bc] Dawid Pakulski,†[abc] Alessandro Aliprandi,[a] Artur Ciesielski *[a] and Paolo Samorì *[a]

Received 21st May 2018

DOI: 10.1039/c8cs00417j

rsc.li/chem-soc-rev

During the last decade, two-dimensional materials (2DMs) have attracted great attention due to their unique chemical and physical properties, which make them appealing platforms for diverse applications in opto-electronic devices, energy generation and storage, and sensing. Among their various extraordinary properties, 2DMs possess high surface area-to-volume ratios and ultra-high surface sensitivity to the environment, which are key characteristics for applications in chemical sensing. Furthermore, 2DMs' superior electrical and optical properties, combined with their excellent mechanical characteristics such as robustness and flexibility, make these materials ideal components for the fabrication of a new generation of high-performance chemical sensors. Depending on the specific device, 2DMs can be tailored to interact with various chemical species at the non-covalent level, making them powerful platforms for fabricating devices exhibiting a high sensitivity towards detection of various analytes including gases, ions and small biomolecules. Here, we will review the most enlightening recent advances in the field of chemical sensors based on atomically-thin 2DMs and we will discuss the opportunities and the challenges towards the realization of novel hybrid materials and sensing devices.

1 Introduction

Since the ground-breaking experiments by Geim and Novoselov on the isolation and study of the outstanding physical properties of graphene in 2004,[1] the research endeavour on two-dimensional materials (2DMs) has grown exponentially, becoming a flagship in many classical fields of research such as chemistry and condensed matter physics, and it is particularly blooming in the inter-disciplinary realms of nanoscience and materials science. One-atom thick graphene is arguably the most glorified material

Cosimo Anichini

Cosimo Anichini obtained his MSc degree from the University of Bologna in 2016 under the supervision of Prof. Alberto Credi. After a research internship in the group of Prof. Paolo Samorì when he worked on the development of transparent and flexible electrodes for (opto)electronic devices, he joined the group as a PhD candidate in 2017. His current research interest is focused on the development of novel devices for sensing and (opto)electronics based on the hybrid assembly of 2D and organic/inorganic materials.

Włodzimierz Czepa

Włodzimierz Czepa received his MSc degree in Chemistry from Adam Mickiewicz University (AMU) in Poznań, Poland (2017), under the supervision of Prof. Violetta Patroniak. He is currently a PhD student at the Centre for Advanced Technologies of AMU, working on the chemical modification of two-dimensional layered materials and their applications in adsorption systems and sensing devices under the supervision of Dr Artur Ciesielski.

---

[a] *Université de Strasbourg, CNRS, ISIS, 8 alleé Gaspard Monge, 67000 Strasbourg, France. E-mail: samori@unistra.fr, ciesielski@unistra.fr*
[b] *Faculty of Chemistry, Adam Mickiewicz University, Umultowska 89b, 61614 Poznań, Poland*
[c] *Centre for Advanced Technologies, Adam Mickiewicz University, Umultowska 89c, 61614 Poznań, Poland*

† These authors contributed equally to this work.

of the last decade; its fascinating physico-chemical properties have spread beyond the academic community and drawn the attention of world-leading chemical and materials oriented companies as well as public institutions, especially since graphene-based products are going on sale.[2] This so-called 'graphene rush' has triggered the pursuit of atomically thin sheets of other layered materials, such as semiconducting transition metal dichalcogenides (TMDs),[3] boron nitride and, more recently, MXenes, which include transition metal carbides, nitrides and carbonitrides,[4] and phosphorene.[5–7] The chemical and structural diversities of these 2DMs, whose properties are indeed dictated by their dimensionality,[8] offer immense opportunities for fundamental and applied research. Different optical and electronic properties may be achieved ranging from the exceptional semi-metallic conductivity of graphene[9,10] to the semiconducting characteristics of some TMDs that possess

Dawid Pakulski

Dawid Pakulski received his MSc degree from Adam Mickiewicz University in Poznań, Poland (2015). He is currently a PhD student in the frame of the "cotutelle" program at Adam Mickiewicz University in Poznań (Poland) and the University of Strasbourg (France). His current research focuses on the design and synthesis of graphene-based materials, with particular emphasis on membranes and foams for water purification and detection of heavy metal ions.

Alessandro Aliprandi

Dr Alessandro Aliprandi received his master's degree from the University of Ferrara. After a short stay at the University of Münster, he received his PhD degree in Chemistry from the University of Strasbourg at the Institut de Science et d'Ingénierie Supramoléculaires (I.S.I.S.), under the supervision of Prof. Luisa De Cola. His thesis was awarded with the "Prix de these de la Fondation Université de Strasbourg" in 2016. Then he carried out postdoctoral research in the group of Prof. Paolo Samorì in the same institute. In 2018 he became a CNRS research associate (IR) in the group of Prof. Luisa De Cola. His research focuses on self-assembling (electro)-luminescent transition-metal complexes as well as 2D materials for electronic applications.

Artur Ciesielski

Artur Ciesielski got his master's degree from Adam Mickiewicz University (Poland), followed by his PhD degree from the University of Strasbourg (France). In 2016 he became a research associate (IR) working at the Institut de Science et d'Ingénierie Supramoléculaires and Centre National de la Recherche Scientifique. More recently, he has been appointed as visiting professor at the Centre for Advanced Technologies of Adam Mickiewicz University (Poland). His current research interests include the design of supramolecular systems, the self-assembly of nanopatterns and the production and chemical modification of 2D materials by exploiting supramolecular approaches.

Paolo Samorì

Paolo Samorì obtained a Laurea degree in Industrial Chemistry from the University of Bologna in 1995 and a PhD in Chemistry from the Humboldt University of Berlin in 2000. After being a research scientist at the National Research Council of Bologna, he was appointed Professor of Physical Chemistry at the Université de Strasbourg. He is now Distinguished Professor and Director of the Institut de Science et d'Ingénierie Supramoléculaires (ISIS) of the Université de Strasbourg. He is a Fellow of the Royal Society of Chemistry (FRSC), a Fellow of the European Academy of Sciences (EURASC), a Member of the Academia Europaea and a Junior Member of the Institut Universitaire de France (IUF). His research interests encompass supramolecular sciences, nanochemistry and materials chemistry, with a specific focus on graphene and other 2D materials as well as functional organic/polymeric and hybrid nanomaterials for applications in opto-electronics, energy and sensing. His work has been awarded various prestigious prizes and honorary professorships.

sizeable and tuneable bandgaps, which change from indirect (bulk material) to direct (single layer form).[11] This also results in unique photoluminescence properties,[12] thus making such materials suitable for diverse applications such as transistors, photodetectors, electroluminescent devices and luminescent probes. The richness of their electronic and optical properties, which can also be engineered by chemical functionalization, combined with their 2D nature, *i.e.* their extremely high surface area-to-volume ratios, makes such materials extremely appealing in the field of sensing, ranging from the quantitative detection of gases and metals (alkali and heavy metals) to biologically relevant molecules (*e.g.* glucose and DNA). Noteworthily, unlike classical digital sensors, 2DM-based sensors do not possess physical gates for selectively reacting with the targeted species (gas molecules,[13,14] metal ions or biomolecules[15,16]).

The interaction between 2DMs' sheets and molecules/ions is accompanied by the adjustment of the properties of both the initial components. Such interaction can occur *via* the physical adsorption, *i.e.* physisorption, of molecular units onto the basal planes of 2DMs' sheets through non-covalent interactions, or through the chemical adsorption, *i.e.* chemisorption, of reactive species undergoing chemical reactions with 2DMs to form covalent bonds onto their basal planes. In the field of sensing, non-covalent interactions may be preferred when a quick response and a fast recovery rate are required (*i.e.* real-time monitoring), yet the weakness of the supramolecular forces can be disadvantageous when biomolecules (*i.e.* enzymes) need to be immobilized on the surface and to be stable during the assay (*i.e.* in buffered saline solution), thus making covalent linkages more suitable.

The physisorption of molecules onto a surface depends on the nature of both the analyte and surface; for example, graphene is an extended honeycomb network of sp^2 hybridized carbon atoms characterized by a long-range π-conjugation. Consequently, non-covalent intermolecular interactions involving π-systems are pivotal in the recognition events since subtle changes in the electronic characteristics of the π systems can lead to modifications of the structure and properties,[17,18] as well as they may enhance the stability of the physisorbed compounds as observed for proteins, and enzyme–drug and DNA–protein complexes.[19,20] The understanding of the nature of π-complexes has indeed high importance for graphene based sensors since the gas–π interaction,[21] H–π interaction,[22–25] π–π interaction,[26–31] cation–π interaction,[32–39] and anion–π interaction[26,40–50] possess different strengths, which are determined by a combination of attractive and repulsive forces. Compared to graphene, the family of TMDs, which includes molybdenum disulfide (MoS_2), tungsten disulfide (WS_2), molybdenum diselenide ($MoSe_2$) and tungsten diselenide (WSe_2) as the most studied, has not been investigated extensively from this point of view. However, in the case of MoS_2 it has been demonstrated that the physisorption onto its basal plane is mainly driven by electromagnetic interactions (*e.g.* electrostatic and van der Waals).[51,52] More generally, 2DMs produced by means of different methods can be very different due to the presence of structural defects, which leads to different behaviours, and consequently different performances in the final sensing device. In the past years the term "defects"[53–57] has become a keyword in the field of 2DMs since the presence of defects plays a major role in modifying the properties of 2DMs. Although defects might have a negative implication when one targets applications in fast opto-electronics, well-designed defects might lead to new and tuneable properties, opening a wide range of interesting applications that pristine materials cannot afford such as enhanced electron transfer rates and electrochemical activity as observed for graphene based electrochemical sensors.[58] Lattice vacancies affect the electronic properties of the TMD sheets, by lowering their charge carrier mobility and density[59,60] as well as triggering photoluminescence[61,62] and modifying chemical reactivity.[63] In graphene the defects within the honeycomb network of C=C, whose number depends mainly on the protocol employed for its fabrication, typically consists of point defects, *i.e.* the absence of some sp^2 carbon atoms, and/or the presence of carbon atoms with sp^3 hybridization. The carbon atoms surrounding these defects are electronically perturbed; thus they exhibit different electronic structures; therefore, they are chemically activated for further chemical reactions. In other words, the presence of point defects enhances the chemical reactivity of graphene.[64] The sp^2 carbon atoms of graphene can react with highly reactive free radicals, such as those produced by diazonium salts[65–67] or benzoyl peroxide;[68] as well as dienophiles which react with the C=C of graphene through a 1,3-dipolar cycloaddition.[69] However, a massive introduction of defects can be achieved by exposing graphite to strong oxidizing agents,[70] resulting in the formation of graphite oxide (GO). The latter when immersed in water tends to spontaneously exfoliate into single layers of graphene oxide due to the negative charged oxygen functionalities decorating both the basal plane and edges.[71] Such material is probably the most investigated 2DM in the field of sensing[72–76] because of its ease of functionalization. The negative charges on its surface can interact non-covalently with a wide range of positively charged molecules; for example, outstanding sorption properties for heavy metal cations have been reported.[77,78] Moreover, the oxygen functionalities, which consist mostly of hydroxyl and epoxy groups exposed on the basal plane and carboxy and carbonyl functionalities located at the sheet edges,[79,80] are extremely reactive, thus allowing further modification of GO.[81,82] Importantly, the electrical conductivity can be to a great extent restored and tuned during the reduction step of the functionalized graphene oxide (fGO),[83] making it an extremely versatile material for sensing with electrical readouts. The use of defects to introduce functionalities has also been successfully extended to the family of TMDs, where the presence of chalcogen deficiency can be used to decorate the surface of the 2DM with different functionalities. For example, reactive sulphur vacancies in MoS_2 may simply arise during the exfoliation process[59,84] or be introduced on purpose electrochemically[85] or by ion-beam irradiation.[86] These reactive sites can readily react with sulphur-containing moieties such as alkanethiol molecules, resulting in the formation of covalent bonds.[86–88] Alternatively, defects can be further expanded into (sub)-nanometre sized pores, transforming the 2DMs into permselective membranes[89] or ultrasensitive sensors even able to sequence DNA.[90,91] Such a property can be further tuned and harnessed to achieve enhanced permselectivity by controlled chemical functionalization of both pore edges and the surface in a post-process chemical treatment.[89] As already anticipated, the 2D nature of such materials offers several advantages in the field of sensing since the atomic thickness provides a direct interaction of all the atoms with the analyte, while the large lateral size not only guarantees a large active surface for the sensing event, but also facilitates the assembly of the device, as demonstrated for field-effect transistors (FETs), *i.e.* by enabling better contact with metal electrodes and better control over the channel structures.[92] Obviously, the architecture of the sensing device depends on which properties of the 2DMs the analytes affect mostly as well as on the nature of both the 2DM and the analyte. Electrochemical sensors based on graphene have been probably the most investigated so far since they provide a direct electrical response. Graphene[93] offers indeed a large electrochemical window (up to 2.5 V),[72] thus enabling the detection of molecules with high reduction or oxidation potentials (*e.g.* nucleic acids), and good electrocatalytic activities for many redox reactions.[94] Furthermore, due to its ambipolar character, the functionalization with both electron withdrawing and donating groups can lead to chemical gating, resulting in a change in the conductivity of the material.[95] The combination of the atomic thickness of the 2DMs with the chemical gating that results when the surface potential is changed due to the binding of molecules has led to the generation of new FET sensors based on 2DMs, as recently reviewed by Mao *et al.*[92] Interestingly, in such kinds of sensors, 2D semiconducting materials outperform their conducting counterparts since the presence of a finite band gap decreases the initial conductance inside the channel, thus improving the signal-to-noise ratio. Consequently, the performance of the device is mainly dictated by the band gap, which can be tuned by defect engineering and doping, as well as by playing with the thickness of the material, opening a wide range of opportunities, as recently demonstrated by Cui *et al.*[96] in a phosphorene-based FET gas sensor.

While a direct electrical response is generally preferred for practical applications, the interactions of 2DMs with analytes give rise to interesting optical phenomena such as the modulation of their photoluminescence properties, opening up a wide range of opportunities. Graphene and GO are known to be highly efficient fluorescence quenchers compared to organic compounds; thus Förster resonance energy transfer (FRET) sensors have attracted increasing interest in the past few years especially for biomedical applications since they can be used to measure precisely nanometre-scale distance and changes both *in vivo* and *in vitro*,[97] resulting in nanobiosensors with excellent sensitivity, selectivity, and biostability.[98] Even a single-layer MoS_2 nanosheet possesses high fluorescence quenching efficiency, and by taking advantage of such a characteristic, it has been exploited as a sensing platform for the detection of DNA and small molecules.[99] However, the use of 2DMs in FRET is not limited to energy acceptors since an appropriate functionalization may result in photoluminescent flakes, which can act as energy donors and be quenched by more electron deficient molecules such as nitro compounds, which are common constituents to prepare powerful explosives.[100]

The use of 2DMs as substrates for enhancing the Raman signals of adsorbed molecules represented a major breakthrough in the field of sensing.[101,102] Different Raman vibrational modes can be enhanced depending on which layered material the molecule is adsorbed onto. Surface enhanced Raman spectroscopy (SERS) is mainly employed to explore the detection of chemical and biological species[103–106] due its high sensitivity (even down to single molecules)[107,108] and the bar-code like reading that comes from the narrow vibrational bands in the Raman spectrum. Different Raman enhancement mechanisms have been proposed for different 2DMs; however, like in the previous examples, surface modification[109] and the thickness[110] play fundamental roles in terms of selectivity and Raman signal enhancement.

The intensive research on 2DMs for sensing application has been further motivated by their intrinsic mechanical properties such as robustness, flexibility, and lightweight, which make the realization of portable and wearable sensors with tremendous impact on our society possible, enabling the monitoring of wearers' health, fitness, and their surroundings.[111] The development of wearable chemical sensors faces multiple challenges on various fronts such as power, analytical procedures, communication, data acquisition, processing and security. Nevertheless, several examples of flexible graphene-based wearable gas and chemical sensors have been recently reviewed,[112] and a wearable patch for sweat-based diabetes monitoring and feedback therapy has also been reported,[113] which combines a heater and temperature, humidity, glucose and pH sensors.

Looking forward to the emergence of portable and ultrasensitive sensors based on 2DMs, in this Review article we discuss the recent advances in gas, alkali and heavy metal sensing as well as relevant chemical entities, emphasizing the performances of the different sensor devices based on 2DMs in terms of sensitivity, selectivity, robustness and response times, by focusing on the device preparation and their suitability as wearable sensors. Each section will start with a general introduction to the sensing towards a specific analyte (gases, metals or chemically relevant molecules), and will be followed by a detailed discussion on the smartest approached strategies and the best recent achievements obtained for various 2DMs ranging from graphene to MXenes. For each 2DM we classify the sensors on the basis of the type of signal transduction; in particular, we focus on electrochemical, FET, fluorescent and SERS sensors. While presenting remarkable examples of chemical sensors, we will pay specific attention to the most important figures of merit such as their sensitivity, selectivity, robustness, and response time, and to the use of strategies to minimize and ideally exclude the effects of interfering analytes, with the final aim of developing flexible sensors for wearable technology (Fig. 1).

1.1 Overview on the properties of 2DMs

Graphene is an atomically thin, planar membrane of carbon atoms arranged in a honeycomb lattice whose unique properties

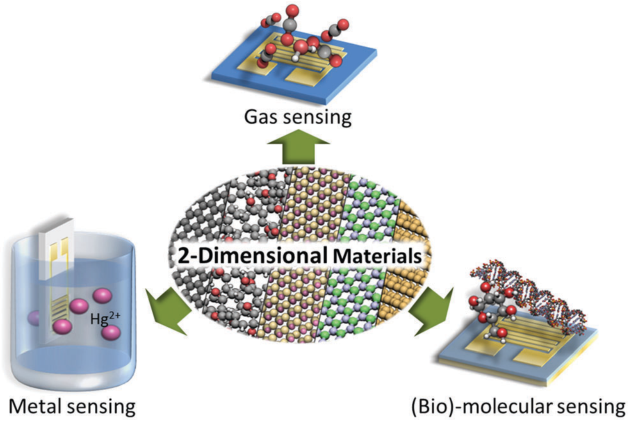

Fig. 1 Schematic representation of the different molecular chemical sensors based on 2DM approaches that have been explored over the past few years.

were first investigated by Geim and Novoselov in 2004.[1] Graphene can be seen as a single layer of graphite, and while the latter behaves metallically, graphene is a semi-metal featuring a unique zero band gap.[114] In addition, graphene exhibits remarkable thermal and electrical conductivity and an impressive mechanical strength superior to steel.[2] Graphene is particularly promising for sensing by virtue of its extremely high conductivity, and its large surface area. Despite being only one atom thick, graphene is impermeable in its pristine form, effectively blocking the passage of even the smallest molecules.[115] The impermeable nature of graphene has triggered extensive studies on its application as a barrier for liquid and gas permeation,[116,117] as well as on its use as a shielding material protecting metallic surfaces against corrosion.[118] Such a unique property of graphene has triggered extensive efforts towards the use of graphene and other 2DMs for the design of ultrathin water-separation membranes and as platforms to absorb (heavy) metal ions. Hitherto the highest quality graphene flakes have been obtained using a top-down approach relying on mechanical exfoliation. The graphene layers are most commonly exfoliated from the bulk graphite *via* the ''Scotch tape'' method.[119] Unfortunately, the flakes produced with such a method have high quality, yet very limited lateral size. Large area and high-quality mono- and few-layer thick graphene sheets can be obtained by two bottom-up approaches: chemical vapour deposition (CVD) and epitaxial growth. CVD graphene is usually obtained through a catalytic decomposition of hydrocarbons (usually methane) on a hot ($\sim$1000 °C) metal surface (Cu, Ni and Co) under vacuum.[120] Since the graphene grows directly onto the metal surface, different techniques have been developed to transfer it onto dielectric substrates.[121] Epitaxial growth is another method to obtain large and uniform high-quality graphene films.[122] Typically, SiC is heated under high vacuum at high temperature ($>$1200 °C); this allows the surface silicon atoms to evaporate, yielding the rearrangement of the carbon atoms to form a graphene layer. Mechanical exfoliation makes it possible to obtain high quality graphene monolayers, but the very low throughput and yield of the so-obtained graphene flakes hinder any industrial application, while CVD and epitaxial growth allow obtaining large-area graphene monolayers, although the production costs remain high. The production of GO followed by its reduction is a high throughput, easily scalable and cheap method to obtain a large amount of graphene.[123] It is, however, fair to note that reduced graphene oxide (rGO) is less conductive and has numerous structural defects and residual functional groups compared to pristine graphene, yet its presence could offer a clear route for improvement of the sensing capabilities as already discussed.[124] Similarly, GO has a higher number of oxygen functional groups, but it is an electrical insulator.[123] A compromise in terms of the quality of the flakes and yield is offered by the liquid-phase exfoliation (LPE) of graphite: graphene flakes dispersed in water/surfactants or organic solvents can be obtained with the aid of ultrasonication,[125,126] shear mixing[127] or an electrochemical approach.[128]

Alongside graphene, transition metal dichalcogenides are the most studied 2DMs. TMDs are semiconductors of the type MX_2, where M is a transition metal atom (such as Mo, W, Re and others belonging to groups 4, 5 and 10) and X is a chalcogen atom (such as S, Se or Te); these materials that exist in the bulk form can be exfoliated, yielding 2D monolayers in which one atomic layer of the metal is sandwiched between two layers of X atoms. TMDs are promising materials for use in electronic devices,[129,130] energy storage[131] and sensors[132–134] due to their unique chemical and physical properties, including semiconducting properties, high surface area-to-volume ratios and absorption coefficients, adjustable and direct band gaps and availability of reactive sites for redox reactions.[135] The chemical versatility of TMDs and their reactivity together with their natural abundance result in the ever growing interest in those materials.[135] Although a majority of TMDs exhibit similar structures, their opto-electronic properties are diverse. In particular, the band gaps of TMDs range from insulating HfS_2 to conductive VSe_2.[135] Noteworthily, 2D TMDs exhibit two different crystal phases: a trigonal prismatic and an octahedral phase, usually denoted as 2H and 1T phases, respectively. In Mo- and W-based TMDs the 2H phase is thermodynamically stable and has semiconductive properties, while the 1T phase displays metallic properties. Other TMDs present a stable distorted octahedral phase, usually referred to as a 1T' phase.[136] The most investigated TMDs are MoS_2, $MoSe_2$, WS_2, WSe_2, ReS_2 and $ReSe_2$. Among them, MoS_2 is considered as the most promising material as it exhibits various physico-chemical properties including fast electron transfer, good conductivity and a quenching ability and it is abundant in nature as molybdenite. Multiple preparation techniques have been reported to obtain nanosized MoS_2 including LPE,[137] chemical vapour deposition,[138,139] and lithium intercalation.[99,140,141] LPE makes it possible to obtain dispersions of MoS_2 nanosheets and other TMDs in higher yield and low cost. However, the obtained materials are usually quite thick and feature limited lateral dimensions.[142] Larger mono- and few layers thick MoS_2 of good quality can be produced by CVD[143] directly on various substrates, including Si/SiO_2.[144–147] Semiconducting MoS_2 exhibits a thickness-dependent band gap, ranging from 1.3 eV for bulk MoS_2 to 1.9 eV for isolated monolayers,[148] good conductivity and fast electron transfer. MoS_2 is currently considered as one of the most preferable materials for chemical sensing applications, predominantly due to available edges that facilitate electron transfer.[3,149] Moreover, it can be easily produced on a large scale and dispersed in numerous solvents to obtain desired structures.[137,150] Layered tungsten disulphide (WS_2) nanosheets are one among the newly emerging TMDs, which consist of S–W–S sandwich structures. WS_2 nanosheets have been the focus of intense research effort as a catalyst, a semiconducting material for field-effect transistors, an active material in lithium-ion batteries, *etc.* Ambipolar WSe_2 has a similar trigonal lattice and a 1.6 eV band gap (in the monolayer). Finally, ReS_2, $ReSe_2$ and $PtSe_2$ are recently explored TMDs, characterized by a highly distorted triclinic structure which endows them with extremely anisotropic optical, mechanical and electrical properties.[151] Mono- and few-layer ReS_2 and $ReSe_2$ can be obtained by mechanical exfoliation and CVD.[152]

Similar in structure to TMDs, SnS_2 is a layered material possessing a triclinic structure, which can be exfoliated into mono- and few-layers with semiconducting properties.[135] Compared to TMDs, SnS_2 exhibits a higher electronegativity, which can potentially enhance the absorption sites and the sensing capabilities.

Among the emerging 2DMs, black phosphorus (BP) has been recently re-discovered as a 2DM under the commonly used name of phosphorene. This material, which is, in analogy to graphene, a single honeycomb layer of the layered phosphorus allotrope can be obtained *via* mechanical or liquid exfoliation and presents remarkable electrical properties of a tuneable direct band gap and high mobility.[153] BP exhibits a relatively low energy band gap, which depends on the number of layers and ranges from 0.3 to 1.5 eV.[154,155] BP exhibits fascinating optical and electronic properties such as size dependent optical response and anisotropic electrical conductivity, which simplifies characterization and segregation methods and makes BP a promising material for various electrical applications.[156,157] BP has already found several applications as FETs, photodetectors, solar cells and gas sensors.[158–161] However, its application in devices is limited by the very low material's stability when exposed to air or water.[162] Such a negative characteristic can become an advantage when fabricating chemical sensors.

Hexagonal boron nitride (hBN) is a synthetic polymorph of boron nitride with a layered structure analogous to graphite. Similarly to graphene, hBN WS_2 exhibits a two-dimensional honeycomb-like structure with strong covalent bonds in the plane. It is characterized by a relatively high band gap ranging from 3.6 to 7.1 eV, which determines its insulating properties.[163,164] This feature provides transparency in the visible and near-IR regions, extending its application potential.[165] The weakly bonded layers can be exfoliated down to monolayer hBN, which has not only electrical insulating properties, but also high thermal conductivity, mechanical strength, hardness and chemical stability.[166] The production method strictly determines the 2D hBN nanosheets' crystallinity, structure and other physical and chemical properties. Multiple methods have been exploited for hBN production including mechanical exfoliation,[167,168] liquid exfoliation[137,169–171] and chemical vapour deposition.[172–174] Features such as good thermal conductivity, low toxicity, high mechanical strength, and atomically smooth surface makes BN a good candidate for sensing applications.

The large family of 2DMs also includes early transition metal carbides/nitrides (MXenes). This novel class of 2DMs shows promising properties toward a range of applications. MXene nanosheets originate from the MAX phases which constitute a class of nitrides and carbides, in which M is an early transition metal, A is an element from group 13 or 14 of the periodic table, X is C and/or N. The MXene layers are obtained from the MAX phase by the removal of the element A, which is intercalated between MXene layers of the crystal, by treatment with HF and further sonication.[175] MXenes display good electronic conductivity and a unique morphology, making them suitable for energy storage,[176] electrochemical capacitors[177] and chemical sensors.[178,179]

In the field of sensing it is generally preferred to make use of non-covalent interactions between the sorbent, *i.e.* the active material, and the analyte to ensure a quick response and a fast recovery rate (*i.e.* real-time monitoring). The use of pristine 2DM nanosheets has some drawbacks. A major limitation is their poor porosity, which limits the number of available recognition sites. In particular, 2DM nanosheets produced *via* LPE exhibit a strong tendency to self-aggregate and form even micron-sized stacked structures. Moreover, nanosheets produced *via* LPE exhibit low charge carrier as well as low field-effect mobility.

Alongside the capacity of pristine 2DMs to detect various analytes, extensive efforts have been devoted towards the development of 2DM-based sensors through the non-covalent functionalization of 2DMs with both inorganic and organic moieties which act as spacers/pillars imposing a certain distance between adjacent sheets. This results in an enhanced porosity of 2DM-based composites, which determines a greater sensitivity for the analyte of choice. Such an approach enables the tailoring of the properties of 2DM-based sensors, which could preserve many of the unique characteristics of the individual 2DM sheets and benefit from the presence of (in)organic moieties. Such moieties, besides acting as separators, can by design incorporate the receptor of the analyte of choice, endowing the highest selectivity in the recognition and sensing process. In this context, the fabrication of 2DM-based sensors through non-covalent interactions between individual 2DM sheets is extremely appealing, as it could result in structures exhibiting a remarkable enhancement of sensitivity towards specific analytes.

2 Applications in gas sensing

A gas sensor is a device that can detect the presence and quantify the concentration of a specific gas in the atmosphere such as water vapour (humidity), organic vapours and hazardous gases.[180] Gas sensors have attracted strong interest and are widely employed in environmental monitoring and emission control,[181] personal and military safety,[182] production control in agriculture and industry and medical diagnostics.[183–185]

Among the variety of materials used for gas sensing devices, metal oxides have been largely considered for their high sensitivity and low cost; however, their crucial drawbacks such as high temperature operation and large energy consumption, as well as poor selectivity, have hindered their practical application.[186] Therefore, many efforts have been devoted towards developing new gas sensors with high sensitivities and low operating temperatures. Numerous active materials have been considered including conducting polymers[187] and carbon nanotubes (CNTs),[188] which possess interestingly low operating temperatures but suffer from long response and recovery times, poor stability, degradation and difficult processing.

In the past few years 2DMs have emerged as new materials for gas sensing by virtue of their unique properties, which promise to largely improve the sensitivity of the sensors. Among 2DMs, graphene is particularly appealing, because of its low resistivity and electrical noise.[189] Such characteristics enable the detection of small changes in the intrinsic resistance resulting from the interaction of graphene with gaseous species. Alongside graphene, its analogues such as TMDs (MoS_2,[190–193] WS_2,[194,195] $MoSe_2$, *etc.*), layered metal oxides (MoO_3,[196] SnO_2[197,198]), phosphorene,[158] h-BN,[199] *etc.*, have also been employed for gas sensing by exploiting their thickness dependent characteristics and semiconducting properties. Indeed, the presence of a band gap that can be modulated by the interaction with gases is a tool that enables enhanced sensitivity. Furthermore, the semiconducting properties of these materials render them suitable for integration as active components in FETs, allowing realization of low power consumption and miniaturized devices.[199] In these devices, the adsorption of gases on the semiconducting material determines a change in their conductivity, which can be measured as a variation in the drain current.[144] Other common gas sensing devices are chemiresistors[185] and chemi-capacitors,[200] in which the sensing material is interposed between two electrodes, and the gas molecules adsorbed on the surface of the material induce a change in the resistance or capacitance, which can be directly quantified.

The performances of gas sensors are usually characterized by various figures of merit, with the most important being sensitivity, selectivity, stability, response and recovery times, cost, dimensions and flexibility. In this section we will define the response $R(\%)$ of a given device as the ratio between the difference in resistance (or another output) when it is operating in the presence and in the absence of the sensed gas, and the resistance in the absence of the sensed gas:

$$R(\%) = \frac{R(i) - R_0}{R_0} \times 100 \tag{1}$$

In this part of review we will provide an overview of the gas sensing mechanism for devices containing active 2DMs, and we will present the most interesting and up-to-date gas sensing applications of graphene, its derivatives, TMDs and other 2DMs.

2.1 Graphene-based gas sensing

2.1.1 Gas sensing with pristine graphene. A graphene sheet exhibits two exposed surfaces without a bulk separation; thus it has all its atoms exposed to the environment; such a structure makes it an ideal building block for the detection of gas molecules.[201] Furthermore, the high variability of its resistance and the low electrical noise of some devices make it possible to detect even extremely small changes in the number of carriers generated by the interaction with gas molecules.[124] The most frequent detection mechanism of graphene, as well as many other 2DMs, is based on the charge transfer process, in which the sensing material and the gas molecules behave as charge donors or acceptors.[202] In particular, Leenaerts *et al.*[203] used density functional theory (DFT) calculations to demonstrate that gas molecules adsorbed on the surface of graphene act as dopants changing the carrier density of graphene. The interaction energies of H_2O, CO, NO, NO_2 and NH_3 with graphene were calculated, which shows that H_2O and NO_2 molecules behave as strong electron acceptors for graphene, thereby resulting in a decrease of charge carriers in the latter, while NH_3, NO and CO behave as electron donors, enhancing the concentration of charge carriers. Upon exposure of the graphene surface to air or to an inert gas the sensed gas molecules are promptly desorbed and the initial conductivity of graphene is recovered.

The first application of graphene as a gas sensor was reported in 2007 by Novoselov *et al.*[201] A micromechanically exfoliated graphene flake supported on a Si/SiO_2 substrate was first etched in a bar shape and patterned with top gold contacts exploiting electron-beam lithography (EBL) (Fig. 2a) and later exposed to H_2O, NO_2, NH_3 and CO gases. It was shown that the presence of gas molecules causes a doping in the graphene, changing the concentration of charge carriers. In particular, it was demonstrated that H_2O and NO_2 decrease the charge carrier concentration, while an increase of the carrier concentration was observed when NH_3 or CO was employed (Fig. 2b). Furthermore, exploiting the Hall resistivity, changes in the number of carriers of just a single electron were investigated in the vicinity of the Dirac point. In this way, by exposing the device to very diluted NO_2 gas, it was possible to sense the adsorption of a single NO_2 molecule. In fact, it can be seen that the Hall resistivity varies in a step-like manner, because each NO_2 molecule adsorbed/desorbed produces a variation of one electron in the number of carriers (Fig. 2c). This outstanding performance was attributed to the high carrier mobility and extremely low noise of the so patterned graphene device.

In 2009 Dan *et al.*[204] demonstrated that the outstanding sensing performances of Novoselov's device could not only be ascribed to the use of pristine graphene, whose inert surface is not optimal for adsorbing molecules, but also be attributed to the lithographic process employed for device fabrication. Towards this end, a miniaturized FET based on mechanically exfoliated graphene on a Si/SiO_2 substrate was fabricated by EBL and used to detect various gas vapours, including H_2O, nonanal, octanoic acid, and trimethylamine, down to the ppm level. It was claimed that the sensitivity of the device was enhanced by the presence of a contamination layer on the graphene surface induced by the EBL process. This layer consists of residues such as the photoresist, acting as an absorbent layer that concentrates

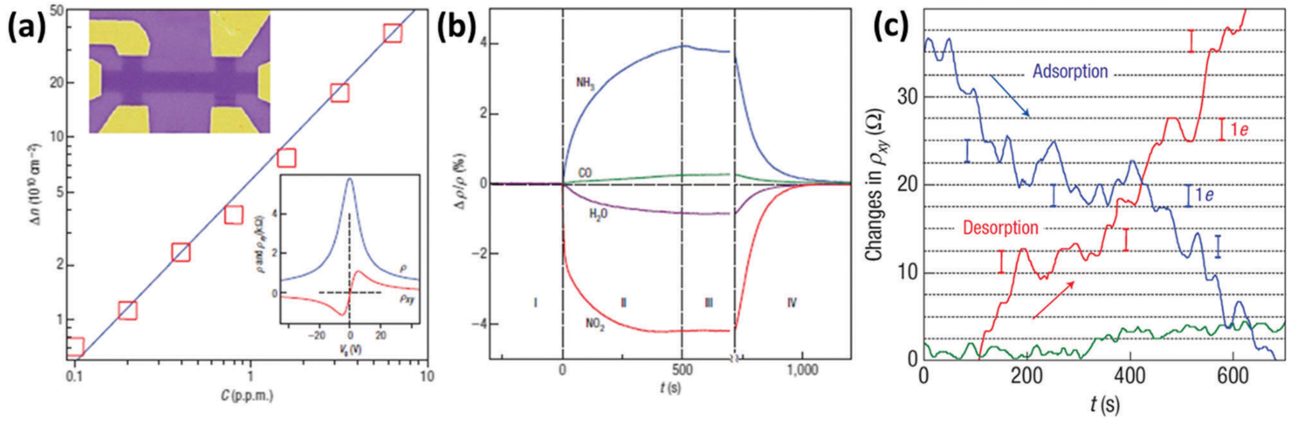

Fig. 2 (a) Dependence of the concentration of charge carriers (Δn) in single-layer graphene when exposed to different concentrations (C) of NO_2. Upper inset: Scanning electron microscopy (SEM) image in false colours of this device (the device is 1 μm wide). Lower inset: Characterization of the graphene device using the electrical field-effect. (b) Changes in resistivity caused by graphene's exposure to 1 ppm of various gases, highlighting the positive or negative doping effects. (c) Changes in Hall resistivity observed near the Dirac point during the adsorption (blue curve) and desorption (red curve) of strongly diluted NO_2. The green curve is a reference of the same device exposed to pure He. The grid lines correspond to changes in ρ_{xy} caused by adding one electron charge. Adapted from ref. 201 with permission from Springer Nature.

analyte molecules onto the graphene surface. In fact once this layer was removed by Ar/H_2 etching, the device became almost completely insensitive to the analysed vapours. A similar device based on mechanically exfoliated graphene patterned through EBL was developed by Ko *et al.* to detect NO_2, with a response of 9% to 100 ppm of NO_2.[80]

EBL was also employed by Balandin *et al.*[205] to fabricate a FET that can selectively detect different organic vapours through analysis of the low frequency noise of the device. In particular, it was shown that the gas molecules act as trap centres, leading to fluctuation in the carrier concentration and thus noise. In addition, the different kinetics of the adsorption/desorption of the different vapours lead to different characteristic noises and made it possible to selectively distinguish the presence of tetrahydrofuran (THF), methanol (MeOH), acetonitrile (MeCN) and chloroform in the environment.

Graphene obtained by mechanical exfoliation was also employed by Yoon *et al.*[206] as a sensor of CO_2. In order to minimize the number of residues resulting from the traditional "Scotch tape" cleavage method and from the EBL process, a monolayer of graphene was exfoliated from the bulk by employing a polydimethylsiloxane (PDMS) stamp and transferred on top of gold electrodes pre-patterned on a Si/SiO_2 substrate. Such a device showed moderately fast (~10 s), reversible, high and linear response to a concentration of CO_2 ranging between 10 and 100 ppm at room temperature.

Larger and high-quality graphene sheets can be obtained by chemical vapour deposition:[121] such a graphene type has been used to detect NO_2,[207–210] NH_3,[210–212] CO_2 and humidity.[213] CVD graphene devices showed in fact good sensitivity towards the detected gases, yet they suffered from difficult desorption of the sensed gases and exhibited slow and incomplete recovery at low temperatures. CVD graphene monolayers transferred onto Si/SiO_2 substrates were used by Gautam *et al.* to sense NH_3, CH_4 and H_2.[211] The best performance of the device in terms of sensitivity was observed when operated at 150–200 °C, yet the use of such extreme experimental conditions was not accompanied by an improvement in the response time. Choi *et al.*[209] realized a transparent and flexible NO_2 detector, in which single layer graphene (SLG) was employed as a sensing active component and bi-layer graphene (BLG) was used as an internal heater: by applying an electrical power of 1.7 W to the device, it was possible to heat the device itself up to 200 °C for the Joule effect. Such a device showed a response of 39% to 40 ppm of NO_2 and the presence of the heater was found to accelerate the recovery time of the device, reaching values of a few seconds. Kim *et al.*[210] in 2015 presented a similar self-heated, transparent, flexible NO_2 sensor. CVD SLG was patterned on Cu foil to obtain a conductive channel of 5 μm width between two graphene electrodes and then transferred onto a flexible polyimide (PI) substrate (Fig. 3a). Also in this case, the SLG microchannel was self-heated up to 73 °C by applying a bias of 60 V, yielding an increase in the sensitivity and recovery time of the device ($\Delta R/R_0$ = 12% and a recovery time of 82 s to 5 ppm of NO_2 at 60 V) (Fig. 3b and c). This device also exhibited good selectivity, reversibility and durability even under mechanical bending and a negligible influence of humidity. Yavari *et al.*[212] in 2011 realized a sensor based on unconventional CVD graphene. In particular, graphene foam was produced by growing CVD graphene onto a porous nickel template, which was dissolved afterwards to obtain the self-standing foam. After contacting the foam with two electrodes, a 30% response to 1000 ppm of NH_3 was measured, yet the response and the recovery time were both found to be slow (~1000 s).

The sensing performance can be tailored by the choice of the substrate in epitaxially grown graphene.[214] In fact SiC possesses a wide number of different polymorphs, and each one of them, as well as diverse crystal faces, can have doping effects on graphene.[215] As an example, Pearce *et al.*[216] realised a NO_2 sensor based on epitaxially grown SLG on the atomically flat Si face of 4H-SiC. This sensor displayed an extremely high response to 2.5 ppm of NO_2 ($\Delta R/R_0 \approx$ 120%). Interestingly, the response

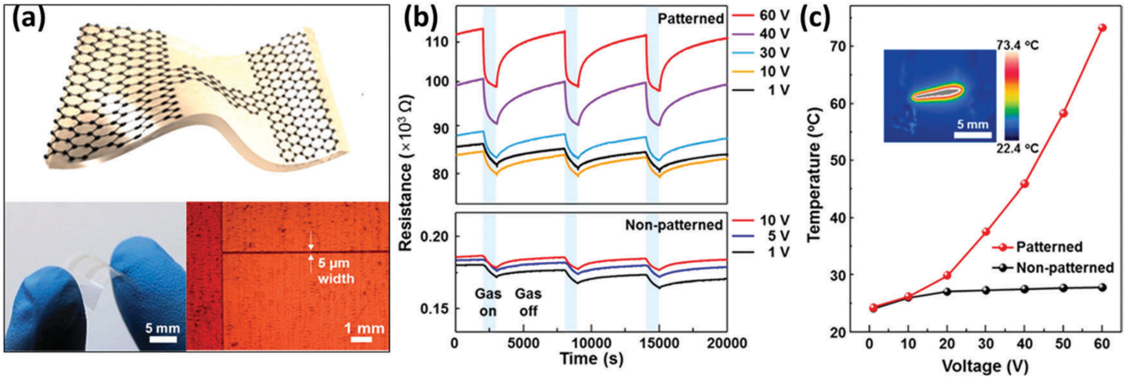

Fig. 3 (a) Scheme (top) and photograph (bottom left) of the all-graphene flexible, transparent gas sensor and micrograph of patterned graphene (bottom right). (b) Response curves, *i.e.* resistance changes, recorded in patterned and non-patterned graphene sensors when exposed to three pulses of 5 ppm of NO_2. (c) Thermographic image and thermal characteristics at different bias voltages. Adapted from ref. 210 with permission from the American Chemical Society.

switched from n-type to p-type upon increasing the NO_2 concentration because of the intrinsic n-doped nature of graphene grown on 4H-SiC. This behaviour was also demonstrated by Nomani *et al.*[214] In their work graphene grown on the C face of 6H-SiC and on the Si face had opposite behaviour when exposed to 18 ppm of NO_2: the one grown on the C face was n-type and exhibited a 4.5% increase of the conductance, while the other was p-type and exhibited a 10% decrease of the conductance.

In order to enhance the performance of a graphene-based gas sensor, a promising solution consists of introducing defects and functional groups. In fact, the absence of dangling groups on graphene's surface renders it inert to the chemisorption of gas molecules. For example, the ozone treatment of graphene sheets is a viable approach to introduce oxygen functional groups uniformly on the surface. Such defects can act as recognition sites and promote the interaction with gaseous molecules through hydrogen bonds and van der Waals forces.[217] Chung *et al.*[208] treated CVD SLG with ozone and demonstrated that the so-treated graphene features better performances in terms of sensitivity and response time for detecting NO_2 compared to pristine CVD graphene. Along the same line, Masel *et al.*[218] proved that the CVD polycrystalline graphene was much more sensitive to various organic vapours than monocrystalline pristine graphene because of the presence of structural defects.

2.1.2 Gas sensing with graphene oxide and reduced graphene oxide. The key role played by the oxygen containing functional groups in graphene oxide is perfectly highlighted by its sensing capabilities. The sensing performances of GO can be easily tailored by varying the amount of its oxygen containing functional groups *via* reduction (thermal or chemical) to rGO. These unique characteristics make pristine and reduced GO the most studied platforms for gas sensing.[124] Numerous articles on GO,[200,219] rGO[220,221] and functionalized GO (fGO)[222,223] based gas sensors have been published. The first application of rGO as a gas sensor was developed by Robinson *et al.* in 2008.[73] GO was spin-coated on the top of a Si/SiO_2 substrate and Ti/Au pads were evaporated as top electrodes (Fig. 4a). The device was exposed to hydrazine vapours at 100 °C to trigger the reduction of GO to rGO. Fig. 4b portrays the response of the device when exposed to pulses of acetone vapours for 5 s. The response (*e.g.* electrical) of the device varies depending on the duration of the reduction treatment. In particular, it is possible to observe two response components: a fast response, which increases with the reduction time due to the decrease of the number of oxygen functional groups, and a slow response, which decreases with increasing reduction time. It was explained that the fast response is the result of the gas adsorption onto low-energy binding sites, such as sp^2-bonded carbon, while the slow response occurs due to the interaction of gases with higher-energy binding sites,

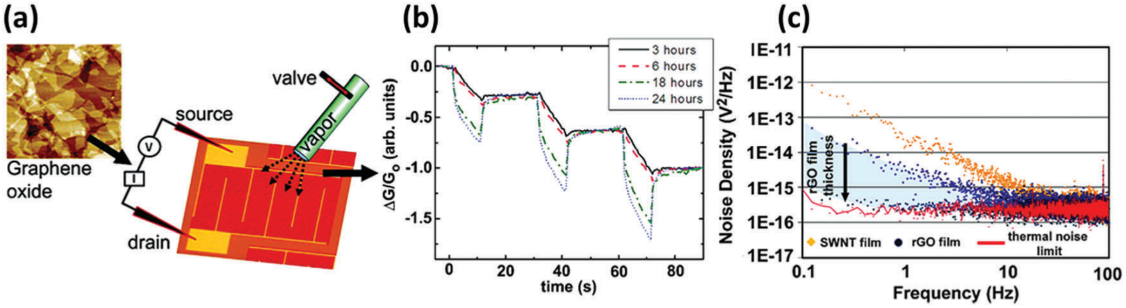

Fig. 4 (a) AFM image of the GO film and scheme of the device. (b) Plot of the response to 5 s pulses of acetone for GO devices reduced with hydrazine for 3, 6, 18, and 24 h. (c) Noise density spectra for SWNT and rGO devices. Adapted from ref. 73 with permission from American Chemical Society.

such as structural defects, and oxygen bearing functional groups. Furthermore, the electrical noise of the device can be pushed to the thermal noise limit (Fig. 4c) for very thin films and long reduction treatment, which is much lower than that of the CNT network. Thanks to the low electrical noise, the limits of detection of various vapours were found to be extremely low. For example, it was possible to sense 70 ppb of HCN and 5 ppb of dimethyl methylphosphonate (DMMP).

A flexible all printed gas sensor based on rGO reduced with ascorbic acid was realized by Manohar *et al.*[224] This was done by preparing a dispersion of rGO in water in the presence of a surfactant, followed by its ink-jet printing onto a PET substrate. The device displayed a response with a detection limit in the tens of ppm range; such a response is positive, *i.e.* displaying increasing resistances, for NH_3, dichloromethane and various alcohols, whereas it was found to provide negative response for Cl_2 and NO_2. Such a phenomenon has been attributed to the electron withdrawing character of Cl_2 and NO_2, which enhances the conductivity of semiconducting p-type rGO.[212] In another case,[225] a NO_2 gas sensor was fabricated by reducing and patterning *via* laser irradiation the GO on various flexible substrates. The device exhibited a good sensitivity, which could allow the detection of 20 ppm of NO_2, with complete, yet slow recovery. Another chemiresistive NO_2 sensor was developed by Prezioso *et al.*[219] using pristine GO; this device yielded the best performance when heated at 150 °C, with a response of 60% to 5 ppm of NO_2, yet accompanied by the response and recovery times close to an hour. In another study[226] the authors improved this GO based NO_2 sensor, which reached a detection limit of just 20 ppb. Furthermore, this sensor had a response to NO_2 unaffected by the humidity level and was able to detect also the presence of ethanol, acetone and ammonia. Sinitskii *et al.*[222] fabricated a highly selective gas sensor able to discern three different alcohols such as methanol, ethanol and isopropanol with a high success rate using a 20-channel array integrated sensor of thermally reduced GO, in which each channel had a unique response due to the structural/morphological irregularity of the rGO film.

Among the various gas sensing applications, GO and rGO have been extensively used also as humidity sensors.[227–230] Humidity is the presence of water vapour in air and is normally measured as relative humidity (RH), which is the ratio between the partial pressure of water and the equilibrium vapour pressure at a given temperature. It is worth reminding that having good control over the humidity in the environment is key to numerous industrial and technological processes and most importantly to ensure the comfort of human beings, improving the quality of life in living and working places.

The presence of numerous oxygen-bearing functional groups as hydroxyl, epoxy and carboxylic groups renders GO's surface highly hydrophilic, thus being a perfect candidate for sensing moisture.[71] Ruoff *et al.*[231] in 2008 demonstrated that the interaction of water molecules with these functional groups of GO determines changes in the conductivity of GO; the authors therefore concluded that highly reduced GO is not suitable for humidity sensing. Water interacts with GO mainly by increasing its conductivity because of the formation of charge carriers as hydronium and hydroxide ions as demonstrated by Yao *et al.* in 2012.[230] In their work, GO was drop-cast on an interdigitated electrode (IDE); when a potential <2 V was applied, a 10-fold change in the GO's conductivity was observed upon varying the RH between 15 and 95%. Such a conductivity change was found to be even larger when higher potentials were applied and has been attributed to the favoured ionization of the water molecules. Similarly, Borini *et al.*[227] spray-cast a solution of GO on top of interdigitated electrodes (IDEs) screen-printed on a flexible and transparent polyacrylonitrile (PAN) substrate. Thin films of spray-coated GO can be essentially reduced to a simple resistor–capacitor (RC) equivalent circuit in which a resistor and a capacitor are in parallel. It was found that resistance displayed an impressive exponential dependence on RH, with a 10-fold decrease when increasing the RH from 40 to 70% (Fig. 5a). Furthermore, this device showed an ultra-fast response and recovery to pulses of humid air of just 20 ms (Fig. 5b). Another GO based flexible humidity sensor was prepared by Guo *et al.*[220] *via* spin-coating on PET substrates. The GO film was micro-patterned using two-beam-laser interference to create alternating lines of GO and rGO. By tuning the laser power, it was possible to control the conductivity as well as the response/recovery time. The best results were obtained at 0.2 W laser power, with response and recovery times of a few seconds and a change in the resistance of 1 order of magnitude between 11 and 95% RH. In a very recent study, Tai *et al.*[229] underlined the effect of the degree of reduction on the humidity sensing properties of GO. While GO showed a decrease in the resistance for increasing humidity, rGO displayed the opposite behaviour. By annealing GO at 150 °C for different times, integrating the so-obtained material into humidity sensors, and studying them

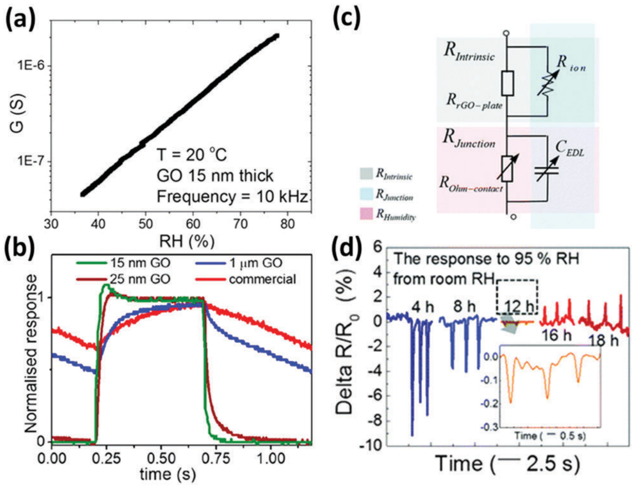

Fig. 5 (a) Conductance dependence of an ultrathin GO film to the RH of the environment. (b) Normalized responses of the different sensors to a modulated humid air flow at 1 Hz. Adapted from ref. 227 with permission of American Chemical Society. (c) Equivalent electrical circuitry model of rGO representing intrinsic and junction-dependent resistances. (d) Responses of rGO films with different thermal reduction times to humidity pulses. Adapted from ref. 229 with permission from the Royal Society of Chemistry.

with electrochemical impedance spectroscopy (EIS), they concluded that the resulting resistance of a macroscopic film of GO is essentially composed of two resistances in series: an intrinsic resistance within the flake (R_{int}) and a junction resistance between flakes (R_{junct}). Both these terms are humidity dependent; in particular, the first can be expressed as two resistors in parallel – the in-plate resistance dependent only on the reduction grade and the ionic resistance, which decreases with increasing humidity. The second term (R_{junct}) can also be expressed as two elements in parallel, a capacitor (C_{EDL}) and a resistor ($R_{\mathrm{Ohm\text{-}contact}}$), both humidity dependent: when the humidity increases and the GO film adsorbs water molecules, the distance between flakes increases, thus yielding an increase in both the C_{EDL} and $R_{\mathrm{Ohm\text{-}contact}}$ values. As a result, with increase of humidity, R_{int} decreases (negative response) and R_{junct} increases (positive response). For GO R_{int} is greater than R_{junct}, thus leading to a negative response to the increased humidity, while for rGO $R_{\mathrm{int}} < R_{\mathrm{junct}}$, thus yielding a positive response to the increased humidity (Fig. 5d).

In order to target more specific types of gases, GO and rGO have been functionalized with (macro)molecules bearing specific functional groups acting as selective active sites. The molecules can be chemisorbed on the surface of graphene or physisorbed on its surface. For example, Al-Mashat *et al.*[232] reported a hydrogen sensor based on an assembly of polyaniline (PANI) adsorbed on the rGO surface. The material was synthetized *via* ultrasonication of an alcoholic mixture of rGO, aniline and the polymerization initiators, which promoted the polymerization of PANI selectively on the rGO surface. Then, the mixture was spray coated on a quartz substrate with a gold IDE. This functionalized rGO showed a better sensitivity to H_2 compared to pure rGO and PANI with a 16.6% response to 1% H_2 gas. The improved sensitivity was attributed to the higher porosity of the hybrid structure with respect to the bare PANI. In another case, a PANI–rGO assembly was used for NH_3 sensing.[233] Shi *et al.*[234] fabricated a NO_2 chemiresistive-type gas sensor based on sulfonated rGO (S-rGO) and rGO functionalized with ethylenediamine (EDA–rGO). In particular, S-rGO displayed a response to NO_2 10 times greater than rGO and 3 times larger than EDA–rGO. Furthermore, the S-rGO also exhibited faster response and recovery and good selectivity towards NO_2. The superior sensitivity of the S-rGO sensors can be attributed to the electron withdrawing characteristics of sulfophenyl groups, which enhance the hole doping in p-type rGO. After the absorption of NO_2 the p-doping is further boosted, thus harnessing the material's conductivity. Hu *et al.*[223] developed a DMMP sensor based on rGO functionalized with *p*-phenylenediamine, which was deposited from solution on an IDE. The response of this device to DMMP vapours was much higher than that of hydrazine reduced GO ($\Delta R/R_0$ to 30 ppm of DMMP = 11% for f-rGO and 1.5% for rGO); however, the response and recovery times were on the scale of several minutes. The chemical functionalization of GO can be used to build sensor arrays in order to recognize different gases. In a very recent study Jelinek *et al.*[200] assembled a capacitive-type porous graphene oxide (pGO) vapour sensor in which the GO was deposited on an IDE through a freeze-drying technique in order to maximize the area exposed to the gas. In parallel, the GO was also chemically functionalized with aniline (phenyl-GO), dodecylamine (dodecyl-GO) and ethanolamine (ethanol-GO) by exploiting the amidation reaction between the amines and the carboxylic groups present on the GO surface – yet, the functionalization of epoxy groups may also occur. These three differently functionalized GOs were deposited on an IDE similarly to pGO, and by combining them in an array, it was possible to selectively detect the presence of water, NH_3, toluene, EtOH, phenol and cyclohexane (Fig. 6). Additionally, the sensitivities of these devices towards the target gases were high, with high reproducibility and both response and recovery times on the time scale of few seconds.

The doping of GO and rGO has also been used to improve the performance of humidity sensors. Rathi and Pal[228] demonstrated that GO doped with Li and B have higher sensitivity to humidity compared to GO. The Li–GO and B–GO were prepared through reaction of GO with LiOH and boric acid, then these doped GO water solutions were drop-cast on a glass with two copper electrodes on top. The Li doped GO in particular showed a response to humidity 4 times higher than un-doped GO. Also in this case the higher performances can be attributed to the increased p-doping of Li–GO.

2.1.3 Gas sensing with graphene based composites. Hybrid composites made by combining graphene with functional materials (such as metals, metal oxides, polymers, *etc.*) can exhibit significantly increased porosity compared to films of

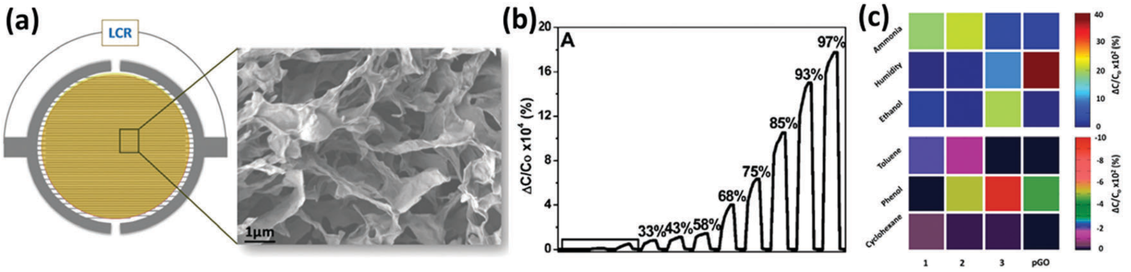

Fig. 6 (a) Schematic structure of the device and a SEM image of the p-GO. (b) Response of the p-GO device to different values of humidity (RH%). (c) Array-based colour code identification of different vapours (180 ppm) using the functionalized pGO capacitive sensor: phenyl-GO (1); dodecyl-GO (2); and ethanol-GO (3). The colours indicated in the diagram correspond to the percentage capacitance response, according to the colour keys shown on the right. Adapted from ref. 200 with permission from Royal Society of Chemistry.

pristine 2DMs, thus resulting in increased accessible surface area. Furthermore, such an approach harnesses the sensing performances of 2DMs due to the combination of different functionalities and their synergistic effects.[75] Metallic nanoparticles (NPs) and films (especially those of noble metals) can enhance the sensitivity and selectivity due to specific catalytic effects.[235]

For example, it is well-known that metals such as palladium and platinum exhibit a catalytic activity towards the adsorption of hydrogen.[236] With this in mind, palladium– and platinum–graphene composites have been extensively explored to target H_2 gas;[182,235,237–241] hydrogen is colourless and odourless but when mixed with air forms an explosive mixture; thus, its detection is of paramount importance for safety. Kaniyoor *et al.*[235] produced a hydrogen sensor based on GO decorated with Pt NPs: the Pt NPs were grown *in situ* on the GO surface and then the so decorated GO was drop-cast on an alumina substrate with pre-patterned Cu electrodes. This device showed a 16% increased electrical resistance when exposed to 4% H_2 yet accompanied by a slow responsivity. Similarly, Wu *et al.*[237] fabricated a H_2 sensor based on a Pd thin film (1 nm) evaporated over CVD graphene with 12% sensitivity towards the exposure to 1% H_2. Chung *et al.*[238] realized a flexible hydrogen sensor composed of CVD graphene decorated with Pd NPs, exhibiting an impressive sensitivity of 30% to 1% H_2. Reduced GO decorated with Pd NPs has also been used to sense NO gas for medical applications by Li *et al.*[185] The rGO with physically absorbed Pd NPs on its surface was deposited on CVD graphene-coated Ni electrodes (Fig. 7a). This device exhibited high sensitivity with an impressive limit of detection of 2 ppb, which is notably higher than that of the reference device assembled without decorated rGO or without graphene-coated electrodes (Fig. 7b). In this case, Pd NPs may act as absorption sites of NO molecules, promoting the donation of electrons from NO to rGO. Furthermore, the interaction of the hybrid with NO can lower the Schottky barriers between rGO and Pd NPs, leading to a further increase in the conductance.

Interestingly, the modification of rGO with functional groups capable of boosting the p-doping can be combined with the catalytic activity of metal NPs. For example, Huang *et al.*[242] assembled a flexible, all-printed NO_2 sensor based on sulfonated rGO/Ag NPs. The rGO was first sulfonated and then Ag NPs were grown *in situ* on the rGO surface *via* hydrazine reduction of $AgNO_3$ (Fig. 7c). Then Ag electrodes and the rGO/Ag NP based ink were printed on a PI substrate. This sensor displayed a 74.6% fast response to 50 ppm of NO_2. Besides, the sensor was quite robust: it exhibited good stability over time and tolerance to humidity (Fig. 7d). The sensor could also detect NH_3, with a similar, yet negative response.

Hybrid materials composed of graphene and metal oxide nanostructures[184,243–249] or quantum dots[250,251] have also proved to enhance the sensing performances of graphene to NO_2, ethanol, H_2S and other gases. In fact, semiconducting metal oxides such as ZnO, SnO_2, In_2O_3, and Cu_2O have been already employed in gas sensing,[252,253] yet the high operating temperature and low conductivity represented a severe limit towards their application. Deng *et al.*[243] synthetized hybrid rGO/Cu_2O nanowire mesocrystals under hydrothermal conditions and integrated them into a NO_2 gas sensor. The hybrid sensor displayed a higher sensitivity compared to those of the single components alone, with an impressive detection limit of 64 ppb (Fig. 8a and b). Also, in this case, the response resulted from the electron withdrawing effect of NO_2 towards the p-type rGO and Cu_2O semiconducting mesocrystals, and it took further advantage of the higher porosity of the hybrid material. An ethanol sensor was assembled by Yi *et al.*[244] by growing semiconductive vertically aligned ZnO nanorods on a metal bottom electrode and depositing CVD few-layer graphene on top as the top contact. This sensor, with a geometry similar to those of metal–insulator–metal devices, offered a 900%

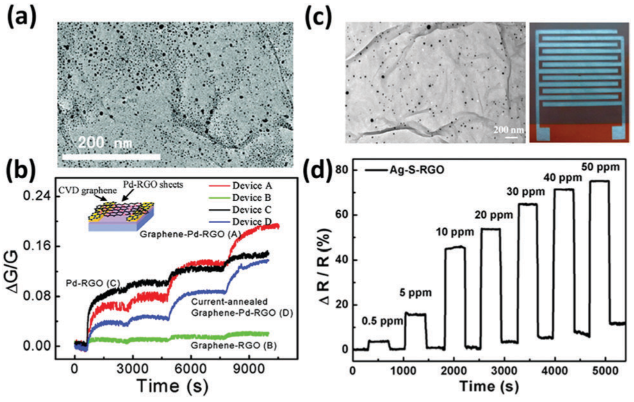

Fig. 7 (a) Transmission electron microscopy (TEM) image of Pd–rGO sheets. (b) Relative changes in the conductances of the various devices *versus* time when exposed to 1, 10, 60, and 120 s pulses of NO gas. Inset: Scheme of the device. Adapted from ref. 185 with permission from American Chemical Society. (c) TEM image of Ag–S–rGO and photograph of the sensing device printed on PI. (d) Response of the Ag–S–rGO sensor as a function of time in various concentrations of NO_2 gas. Adapted from ref. 242 with permission from American Chemical Society.

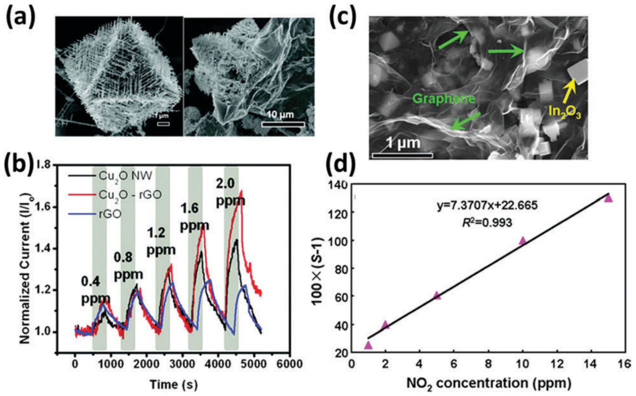

Fig. 8 (a) SEM images of rGO–Cu_2O mesocrystal composites, and (b) dynamic responses of Cu_2O NW, rGO–Cu_2O, and rGO devices under increasing NO_2 exposure. Adapted from ref. 243 with permission from American Chemical Society. (c) SEM image of the In_2O_3 cubes/rGO composites at a 1 : 1 mass ratio. (d) Linear fitting curve of the sensor response *versus* NO_2 concentration. Adapted from ref. 254 with permission from American Chemical Society.

sensitivity to 10 ppm of ethanol and a good flexibility. However, an operating temperature as high as 300 °C was required to leverage the n-type characteristic of semiconductive ZnO nanorods and obtain a good sensitivity to the electron donor EtOH. In another study[245] GO decorated with ZnO NPs was used to sense CO and NH_3 gases. ZnO NPs were grown in solution on the GO surface; such a decorated GO was spin-coated on ITO patterned glass substrates. This device, when operated at room temperature, revealed a much higher sensitivity towards CO and NH_3 compared with the two components alone. In particular, the change in conductivity was $\sim$24% to 1 ppm of NH_3 and 22 ppm of CO. Similarly, Cuong *et al.*[246] reported a H_2S sensor based on vertically aligned ZnO nanorods hydrothermally grown on the surface of spray-coated rGO, which showed high sensitivity in oxygen, but long response and recovery times. Another H_2S sensor was developed by Zhou *et al.*[247] by hydrothermally growing Cu_2O nanocrystals on a GO surface and drop-casting the suspension onto a gold IDE on a Si/SiO_2 substrate. The GO/Cu_2O assembly was demonstrated to have better performances compared to the isolated components, with a high 11% sensitivity to 5 ppb of H_2S at room temperature and response and recovery times on the few minutes time scale. rGO/In_2O_3 assemblies have been used to detect NO_2[249,254] for environmental monitoring. Feng *et al.*[254] were able to embed In_2O_3 nanocubes in rGO networks using InN NWs and GO as precursors. Depending on the ratio between the two components, different morphologies were obtained: the best sensing performances were found when a 1 : 1 InN : GO ratio was used (Fig. 8c). Such a sensor exhibited a 61% change in the resistance when exposed to 5 ppm of NO_2 and a markedly high selectivity towards interfering gases (Fig. 8d). In 2017 Liu *et al.*[249] overtook these performances by combining flower-shaped In_2O_3 nanocrystals with rGO, thereby obtaining a sensor with an impressive 3 orders of magnitude increase in the resistance when exposed to 1 ppm of NO_2 combined with a detection limit lower than 10 ppb.

The sensing of simple alkanes, such as methane and ethane, is important because of the industrial relevance of these molecules. However, very few examples of sensing of these gases can be found in the literature because of the weak doping nature of these apolar molecules.[255–257] For example, a hydrogen and liquid petroleum gas (LPG) sensor based on rGO decorated with SnO_2 quantum dots was developed by Lee *et al.*,[251] showing an impressive response of 89% to 500 ppm of H_2 and 92% to 500 ppm of LPG. Zhang *et al.*[255] produced a methane sensor based on a nanocomposite of rGO and ZnO nanocrystals that displayed a decent and fast response to 100 ppm of CH_4 and a good selectivity towards interfering gases; unfortunately, a high operating temperature of 190 °C is necessary for proper functioning of this sensor.

Polymers and semiconducting polymers coupled with graphene, GO and rGO constitute the third large family of hybrid assemblies. Some of these assemblies with conducting polymers, like the polyaniline/GO assembly, have already been discussed in the previous paragraph[232] as the boundary between polymer functionalized GO/rGO and polymer–GO/rGO assemblies is blurred. In a typical example, in 2014 Zhang *et al.*[221] developed a resistive-type, flexible humidity sensor based on the assembly of GO and a polyelectrolyte, *i.e.* poly(diallyldimethyammonium chloride) (PDDA), using the layer-by-layer (LbL) deposition method. The nanostructured film was fabricated on a Cu/Ni IDE on a PI substrate. In the first instance, a bi-layer of PDDA and an ionic polymer was self-assembled on the substrate as precursor layers for charge enhancement, and then 5 GO/PDDA layers were deposited by alternating immersions into PDDA and GO suspensions for five repetitive cycles. Following that, the GO was chemically reduced by soaking the film in a solution of HBr acid. Such an assembled device exhibited a 37% increase in the resistance when passing from 0% RH to 97% RH, with response and recovery times of a few minutes, an excellent linearity of the response and long-term stability over time. The superior sensor performances were attributed to the high surface area of the assembly, the p-type semiconducting properties of rGO at low RH, and the interlayer swelling of the PDDA/RGO film at high RH, which contributes to the resistance increase. In another study Shi *et al.*[258] synthetized GO/conducting polymer composite hydrogels, including GO/polypyrrole (PPy) and GO/PANI, by chemical polymerization *in situ* of the corresponding monomers in aqueous dispersions of GO, where GO sheets acted as 2D templates. These gels showed many interesting properties, including electrical conductivity and electrochemical activity. In particular, the GO/PPy gel, once lyophilized, exhibited a good sensitivity to NH_3 gas. In this case, the improved response was attributed to the high surface area of the conductive gel compared to that of the bare polymer film.

A nanocomposite thin film of chemically exfoliated graphene and PANI was used by Wu *et al.*[257] to sense methane at room temperature, with a decent 10% response to 10 ppm of gas. Shi *et al.*[259] prepared a highly sensitive NO_2 sensor based on electrospun PVA/PEI nanofibers coated with a thin GO layer, which self-assembled on the surfaces of the nanofibers for charge interaction. The nanofibers were deposited on an IDE and then exposed to hydrazine vapours to reduce the GO. This sensor displayed an impressive sensitivity, with a 16% response to 150 ppb of NO_2 and good linearity until 1 ppm; furthermore, the stability and the selectivity towards NO_2 were high, and the response and recovery times were around 5 minutes.

The combination of graphene with ionic liquids is a similar route to achieve high sensitivity and selectivity in gas sensing. Within this framework, Ariga *et al.*[260] developed a sensor capable of discriminating between various organic vapours based on a multi-layered rGO/ionic liquid film assembled in solution *via* the LbL method on a quartz microbalance. Assemblies of CNTs and graphene have also been employed for gas sensing. In 2010 Jeong *et al.*[261] produced a flexible NO_2 sensor using a CNTs/rGO hybrid film. A rGO film was deposited on a plastic substrate with a gold IDE followed by the CVD deposition of vertically aligned CNTs on top. The so-fabricated sensor revealed a sensitivity of 20% after 60 min exposure to 10 ppm of NO_2 at room temperature.

The most important performance parameters of all the graphene based gas sensors described in this section, including

Table 1 Comparison of the sensing performances of different graphene based gas sensors

Material	Sensed gases	Response/recovery time	Limit of detection	Sensitivity (response × ppm^{-1})	Ref.
SLG (ME)	NO_2	500 s	ppb	4%	201
	H_2O, nonanal, octanoic acid		0.5 ppm	0.6–1%	204
	CO_2	10 min/10 min		0.26%	206
	NO_2	4 min/4 min	100 ppm	0.08%	80
SLG/BLG (ME)	THF, MeOH, MeCN, $CHCl_3$				205
SLG (CVD)	CH_4, NH_3, H_2	9 min/9 min		0.046% (NH_3)	211
SLG/BLG (CVD)	NO_2	95 s/11 s		0.98%	209
SLG (CVD) oxidized with O_3	NO_2	15 min/30 min		0.0085%	208
SLG (CVD) patterned	NO_2, NH_3	89 s/579 s		2.6% (NO_2)	210
CVD graphene foam	NH_3	800 s/1200 s		0.03%	212
SLG (epitaxially grown)	NO_2	1 h/3 h		48%	216
	NO_2	250 s/150 s at 300 °C		0.55%	214
GO	H_2O	20 ms/20 ms		30%/RH	227
	NO_2, H_2O	40 min/40 min		12%	219
	NO_2	40 min/40 min	20 ppb	250%	226
	H_2O			12.5%	230
rGO	Acetone, DMMP, HCN	5 s		100%	73
	NO_2, Cl_2, NH_3	10 min/10 min		0.25% (NH_3)	224
	H_2O				231
	NO_2	10 min/30 min		0.05%	225
	H_2O	20 s/30 s		10.7%/RH	148
Li and B doped GO	H_2O	4 s		35.3%	228
Sulfonated-GO and EDA–GO	NO_2			50%	234
Phenyl-GO, dodecyl-GO; ethanol-GO	Various gases	15 s/10 s		200% (NH_3)	200
p-Phenylenediamine/GO	DMMP	1080 s/360 s		0.4%	223
PANI/rGO	H_2	2 min/3 min		0.0016%	232
PANI/graphene flakes	CH_4	1 min/1 min	10 ppm	2.5%	257
PDDA/GO LbL assembly	H_2O	2 min/3 min		0.38%/RH	221
Microfiber PVA–PEI/rGO	NO_2	4 min/10 min		110%	259
CNTs/GO	NO_2	1 h/3 h	0.5 ppm	2%	261
Ag NPs/sulfonated-GO	NO_2, NH_3	12 s/20 s		1.49% (NO_2)	242
Pd film/CVD SLG	H_2	>10 min		0.0012%	237
Pd NPs/CVD SLG	H_2	15 min/20 min		0.003%	238
Pd/rGO	NO	265 s		35%	185
Pt NPs/GO	H_2	9 min/20 min		0.004%	235
Cu_2O NPs/rGO	H_2S	5 min/5 min		2200%	247
Cu_2O/rGO	N_2O	5 min/10 min		34%	243
In_2O_3/rGO	NO_2	4 min/1 min		109 800%	249
In_2O_3/rGO	NO_2	3 min/4 min		12.2%	254
ZnO NPs/rGO	CO, NH_3	5 min		24% (NH_3)	245
ZnO Nrods/rGO	H_2S	>30 min			246
ZnO Nrods/CVD SLG	EtOH			90%	244
ZnO NCryst/rGO	CH_4	1 min/10 s	100 ppm	0.05%	255

List of abbreviations. SLG: single layer graphene, ME: mechanically exfoliated, BLG: bi-layer graphene, CVD: chemical vapour deposition, GO: graphene oxide, rGO: reduced graphene oxide, $CHCl_3$: chloroform, THF: tetrahydrofuran, MeOH: methanol, MeCN: acetonitrile, DMMP: dimethyl methylphosphonate, HCN: hydrogen cyanide, EDA: ethylenediamine, PANI: polyaniline, PDDA: poly(diallyldimethyammonium chloride), LbL: layer-by-layer, PVA: polyvinyl alcohol, PEI: polyethylenimine, CNTs: carbon nanotubes, NPs: nanoparticles, Nrods: nanorods, NCryst: nanocrystals.

the response time and the sensitivity (calculated as the ratio between the response % and the corresponding gas concentration expressed in ppm), are summarized in Table 1.

2.2 Gas sensing with transition metal dichalcogenides

The sensing properties of TMDs are based on the already discussed charge-transfer mechanism. Yue *et al.*[191] gained deep insight into such a mechanism by focusing on n-type MoS_2 as an exemplary system. In this article, the charge transfer mechanism between different gas molecules including O_2, H_2O, NH_3, NO, NO_2, CO, *etc.*, and monolayer MoS_2 was explained with the aid of DFT calculations. The authors showed that the conduction band (CB) of pristine n-type MoS_2 monolayers is already populated by some electrons at room temperature. When the monolayer is exposed to electron–acceptor gases such as O_2, H_2O, NO, NO_2, and CO, electrons are transferred from MoS_2 to the sensitive gases, leading to a decrease of carrier density in MoS_2, which ultimately yields an increased resistance. In contrast, NH_3, which behaves as an electron-donor, transfers electrons to the MoS_2 monolayer, thereby reducing its resistance.

The charge transfer between TMD monolayers and gases can also be evidenced by changes in the photoluminescence (PL), which is due to the direct band gap properties of TMD monolayers. Tongay *et al.*[262] showed that the light emission efficiency of these TMDs can be modulated by physisorption of gas molecules such as O_2 and H_2O, as a result of a molecular gating effect. The charge depletion in n-type materials such as MoS_2 and $MoSe_2$ caused by the charge transfer to molecules such as O_2 and H_2O leads to a drastic enhancement in photoluminescence for the stabilization of neutral excitons X_0.

Among the various TMDs, MoS_2 is the most studied material. Mechanically exfoliated MoS_2 has been successfully used to detect a wide range of gases.[14,190,193,263] For instance, Zhang *et al.*[190] fabricated miniaturized FETs based on mechanically exfoliated MoS_2 for the detection of NO. Single, bi-, tri- and quadri-layers of MoS_2 transferred onto Si/SiO_2 substrates were investigated in this work. The sensitivities of these devices to NO were high and the responses were fast; however, the current passing through a single-layer thick MoS_2 FET was unstable, while the devices based on 2-, 3- and 4-layer MoS_2 showed both high sensitivity and stability with a detection limit of 0.8 ppm of NO. In a similar study Late *et al.*[14] prepared transistors by depositing mechanically exfoliated MoS_2 flakes on Si/SiO_2 substrates and contacting them with gold top electrodes through electron beam lithography, and they employed them to sense NO_2, NH_3 and humidity (Fig. 9a). From the analysis of flakes consisting of 1, 2 and 5-layers it was observed that the signal was unstable for monolayers, while among 2 and 5-layers the latter exhibited the highest response to the sensed gases. As expected from the charge transfer mechanism, NO_2 produced a negative resistance response, while NH_3 had the opposite behaviour (Fig. 9b and c). For the same reason, the applied gate voltage had opposite effects in NH_3 and NO_2 in increasing or decreasing the sensitivity, and these effects were larger for the 5-layer device. In addition, the effects of green light irradiation on the sensitivity and response time of the device were also explored. The reason for the increased and stable response in the devices based on few-layers compared to the single-layer thick device remains unclear, yet the authors showed with DFT calculations that the adsorption of NO_2 was slightly favoured in the few-layer thick devices. In another example Perkins *et al.*[193] measured the conductance changes in a device based on mechanically exfoliated MoS_2 after exposing it to various organic vapours. They found that the device had high selectivity towards triethylamine (TEA) and acetone with a detection limit of 1 ppm over the last analyte.

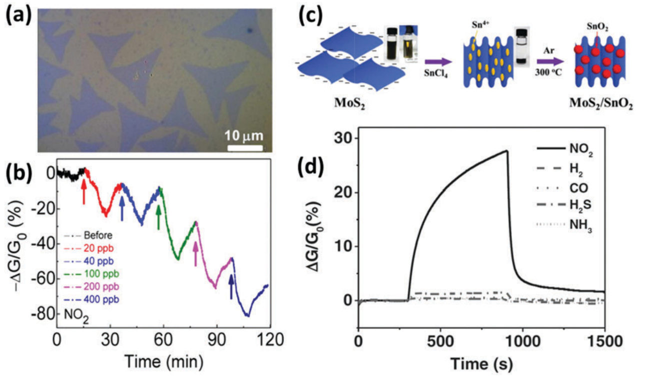

Fig. 10 (a) Micrograph of triangular shaped CVD grown MoS_2 monolayers supported on a Si/SiO_2 substrate. (b) Response of the device upon exposure to increasing NO_2 concentration. Adapted from ref. 144 with permission from American Chemical Society. (c) Schematic illustration of the preparation of a SnO_2/MoS_2 hybrid. (d) Response of the device to 10 ppm of various gases, highlighting the selectivity towards NO_2, the sensitivity and the response time. Adapted from ref. 270 with permission from Wiley-VHC.

Dispersions of MoS_2 sheets in solution can be obtained with a relatively high yield and low cost by liquid-phase exfoliation. These dispersions can be processed to generate films of overlapping flakes, which have been used as active materials to detect different gases.[192,264,265] For example, Yao *et al.*[265] prepared a water dispersion of MoS_2 flakes combining grinding and sonication of the bulk material. The dispersion was deposited with an inject printer onto pre-patterned microelectrodes and the so-obtained device was used to detect NH_3 gas up to a few ppm. A similar method that relies on the intercalation of Li ions within the MoS_2 layers and their subsequent exfoliation in water solution through ultrasonication was used by Zhang *et al.*[141] to sense NO. The dispersion of MoS_2 flakes was deposited by drop-casting on a Si/SiO_2 substrate pre-patterned with gold electrodes to form a thin-film transistor (TFT), which was found to be sensitive to NO at concentrations down to 0.4 ppm.

Similarly to graphene, MoS_2 can also be produced by CVD.[143] In 2014 Liu *et al.*[144] fabricated FETs by contacting through EBL small triangular-shaped monolayers of MoS_2 grown by CVD on Si/SiO_2 substrates (Fig. 10a). These devices exhibited a high Schottky barrier (ΔSB) between the Ti/Au contacts and the monolayer, which can be modulated by exposing the devices to NO_2 and NH_3 gases. In particular, NO_2 adsorption increases the ΔSB and thus the contact resistance, whereas NH_3 adsorption decreases both of them. The effect of the Schottky barrier modulation, together with the charge transfer mechanism, yielded an increase in the sensitivity of the device to both the analytes, with changes in the conductance up to 3 orders of magnitude and detection limits down to 20 ppb of NO_2

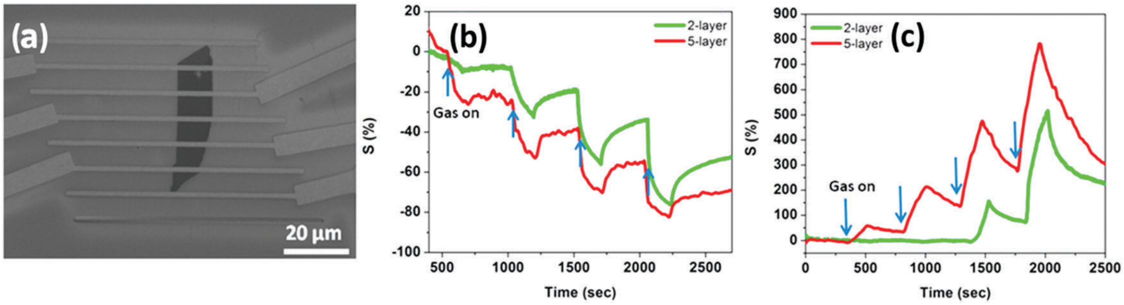

Fig. 9 (a) SEM image of a two-layer MoS_2 transistor device. Sensing performances of the 2 and 5-layer devices when exposed to 100, 200, 500, and 1000 ppm of (b) NH_3 and (c) NO_2. Adapted from ref. 14 with permission from the American Chemical Society.

and 1 ppm of NH_3 (Fig. 10b). Cho *et al.*[146] produced a gas and photo-detector based on a wafer-scale film of 3-layer MoS_2 deposited on sapphire substrates *via* CVD with IDE gold electrodes on top. This sensor exhibited good sensitivity and selectivity to NO_2, with a response around 40% to 120 ppb combined with a stable cycling behaviour. Furthermore, the response time was fast, yet the recovery at room temperature was not complete even after 30 minutes. Similarly, a 3-layer MoS_2 film produced by CVD on sapphire substrates was developed by Cho *et al.*[266] for the sensing of NO_2 and NH_3. The device exhibited an increased resistance when exposed to NO_2 and a decreased resistance when interacting with NH_3, as expected from the charge-transfer mechanism.

The sensitivity of MoS_2 to gases could be improved by increasing the number of active sites that can interact with the analyte of interest through processes of molecular absorption on sulphur vacancies and edges. For example, Jung *et al.*[147] showed that sensors based on MoS_2 layers vertically aligned, thus exposing their edges to the environment, exhibited a higher response to NO_2 and EtOH gases. The films of horizontally and vertically aligned MoS_2 layers were produced *via* CVD. By increasing the thickness of the films, the number of vertically aligned layers increased, and at a thickness of 15 nm almost all the surface was covered by vertically aligned layers, as revealed by TEM mapping. These films exhibited a response 5 times greater than the 1 nm thick film, because of the increased edge sites exposed to the environment.

The surface functionalization of MoS_2 with molecules or nanomaterials as metal and metal oxide NPs represents an alternative viable method to increase the interactions with the gas molecules, and thus to harness the device sensitivity.[267,268] For example, Zhang *et al.*[267] fabricated a flexible TFT depositing a film of MoS_2 obtained with a method previously described[141] on a rGO electrode array on polyethylene terephthalate (PET). Successively, Pt NPs were deposited on the surface of the MoS_2 film and the device was employed to detect NO_2. The device functionalized with the Pt NPs showed a response to NO_2 3 times faster than the non-functionalized device, with detection limits as low as 2 ppb. The reason for such an improved sensitivity was attributed to the formation of a Schottky barrier between the MoS_2 and the Pt NPs. In a similar study Sarkar and co-workers[269] functionalized MoS_2 with various metallic NPs, including Ag, Pd, Pt, Sc and Y, and examined their doping effects. The Pt NPs functionalized MoS_2 device revealed an improved sensitivity to H_2 gas compared to the pristine MoS_2 device. A H_2 sensor based on Pd NPs functionalized MoS_2 was also assembled by Jin *et al.*[268] by drop-casting a water suspension of MoS_2 flakes obtained by liquid-phase exfoliation and Pd NPs. This sensor displayed a fast response and good recovery upon exposure to H_2 (0.5–5%) and a decent cross-sensitivity. Metal oxide NPs have also been used to improve the sensitivity; in particular, semiconducting SnO_2 has been employed to sense humidity,[198] NO_2[270] and EtOH.[271] For example, Chen *et al.*[270] prepared a NO_2 sensor based on SnO_2 nanocrystal decorated MoS_2 nanosheets. The material was prepared as depicted in Fig. 10c. A MoS_2 flake suspension was produced by lithiation of MoS_2 followed by liquid exfoliation, then SnCl was added to the suspension and Sn^{4+} ions got absorbed on the negatively charged flakes' surfaces. Finally, the SnO_2/MoS_2 hybrid was obtained by annealing the filtered suspension at 300 °C in argon. Interestingly, this material showed p-type behaviour because of the p-doping effect of the SnO_2 nanocrystals. The sensor based on the hybrid showed a decent sensitivity to NO_2, with a 30% response to 10 ppm and a detection limit of 0.5 ppm combined with good reversibility and selectivity (Fig. 10d).

MoS_2 can also be functionalized with dangling molecules, especially through the covalent attachment of thiolated molecules on the sulphur vacancies of the MoS_2 surface.[272] By applying such a strategy, Jung *et al.*[13] developed a volatile organic compound (VOC) sensor for breath analysis based on MoS_2 nanosheets obtained *via* liquid-exfoliation functionalized with mercaptoundecanoic acid (MUA). This sensor exhibited a good sensitivity down to 1 ppm to various VOCs including toluene, hexane, acetone, propanal and ethanol. Furthermore, while the resistance of a pristine MoS_2 based device increased upon exposure to all the sensed gases, the MUA–MoS_2 sensor once exposed to the molecules with oxygen functionalities displayed a decrease in the resistance. These differences originated from the diverse interaction of the oxygen containing molecules with the dangling MUA. In particular, the oxygen-bearing gas molecules can interact *via* hydrogen bonding with the exposed carboxyl group in MUA and then form an electron-rich region able to transfer the charge to the MoS_2 sensing channel.

Among the other TMDs, $MoSe_2$, WS_2, WSe_2, ReS_2 and $PtSe_2$ have also been employed for fabricating gas sensing devices by exploiting their diverse semiconducting characteristics and their unique high surface area-to-volume ratios. For example, $MoSe_2$ has found application as an NH_3 sensor in a study of Late *et al.*[273] The device was based on a single-layer $MoSe_2$ flake obtained *via* mechanical exfoliation deposited on a Si/SiO_2 substrate and contacted with gold electrodes by EBL. The device showed a sensitivity to NH_3 in concentration from 50 to 500 ppm and a response time of 2.5 min. The doping effect of NH_3 was also confirmed by the shift in the Raman spectrum after the absorption of NH_3.

WS_2 has been used in recent years as a sensor for NH_3,[52,194] humidity[195,274] and alcohols.[52,195] Li *et al.*[52] developed a transistor based on a mechanically exfoliated multilayer WS_2 flake and measured the current change and the photoresponse of the transistor when exposed to different gases including NH_3, ethanol and O_2. In particular, NH_3 and ethanol behaved as electron-donors, yielding an increase in current and photoresponsivity in the n-type WS_2 device, while O_2 extracted electrons from the device, resulting in a current decrease and a lower photo-response. The device showed the highest sensitivity toward NH_3 and really fast response and recovery to all the sensed gases. Pumera *et al.*[195] prepared a chemiresistive device depositing metallic 1T-WS_2 flakes obtained through liquid exfoliation on an IDE. The selective vapour sensing capabilities of the device were studied with impedance spectroscopy. When exposed to methanol, the device presented an impedance phase spectrum with a resonant frequency maximum around 1 Hz, while with water the maximum shifted to 1 kHz. Therefore, the device was able to discern methanol and water isolated and mixed together by simply selecting specific frequencies, even when high concentrations of interfering gases were present. Duesberg *et al.*[194] reported an NH_3 sensor based on CVD WS_2 thin films. The films with thicknesses ranging from 1 to 50 nm were grown on Si/SiO_2 substrates with gold IDEs using H_2S plasma to sulphurise WO_3 films at 500 °C. The so-achieved devices demonstrated good sensitivity to NH_3, with a detection limit of 1.4 ppm.

WSe_2 is another TMD semiconductor which has been used to detect toxic gases. Javey *et al.*[275] assembled a p-type FET based on mechanically exfoliated WSe_2 monolayers for NO_2 detection. A high work function metal such as Pd was used as source and drain electrodes to lower the contact resistance for hole injection. Upon exposure to 0.05% of NO_2 the source–drain current increased 5 orders of magnitude as a result of the decrease of the Schottky barrier and increase of p-doping. Furthermore, in devices with a top-contact gate the on–off ratio was also greatly improved after NO_2 exposure.

Recently, ReS_2, $ReSe_2$ and $PtSe_2$ have also been employed for gas sensing.[276–279] Yang *et al.* reported the photoresponse of monolayer ReS_2[276] and $ReSe_2$[278] based FETs under red light illumination in NH_3 and O_2 gases. The increase in current that was observed under illumination was higher in an NH_3 atmosphere for ReS_2, while for $ReSe_2$ it was higher in an O_2 atmosphere. With the aid of DFT spin-polarized calculations, the reason for the different photoresponse behaviours of single-layer ReS_2 and $ReSe_2$ FETs in O_2 and NH_3 was attributed to the different transfer directions and quantities of electrons in n-type ReS_2 and p-type $ReSe_2$. Yim *et al.*[279] prepared a FET by depositing a thin layer $PtSe_2$ film by CVD on a Si/SiO_2 substrate and tested it as a photodetector and gas sensor. The FET exhibited a fast detection of NO_2, with a resistance decrease of 0.25% to 1 ppm of gas and response and recovery times of 30 and 10 s respectively.

2.3 Gas sensing with other 2DMs

SnS_2 is a layered material similar to TMDs exhibiting a higher electronegativity, which can potentially enhance the gas sensing capabilities. Ou *et al.*[280] developed a sensitive and selective NO_2 sensor based on few-layer SnS_2 flakes obtained by a wet chemical synthesis technique. The flakes, with lateral sizes ranging between 80 and 200 nm, were synthetized from a solution of $SnCl_4$ and sulphur and then drop-cast on an IDE. The device displayed a linear response from 0.6 to 10 ppm of NO_2, with an extremely high sensitivity of 3500% to 10 ppm of NO_2 and response and recovery times of 170 and 140 s, respectively, at an operating temperature of 120 °C. Furthermore, the device showed high selectivity to NO_2 among high concentrations of various interfering gases; these results were attributed to the strong affinity of SnS_2 for NO_2 as well as the favourable Fermi level of SnS_2 to the energy of the partially occupied NO_2 molecular orbitals.

In another example, Shi *et al.*[281] developed an NH_3 sensor operating at room temperature based on flower-shaped nanoflakes of SnS_2 prepared by a solution method. The sensing device was produced depositing a paste made of the interconnected flakes on an IDE. The sensor, when exposed to concentrations of NH_3 ranging between 5 and 150 ppm, presented a 21% sensitivity to 5 ppm of gas with response and recovery times of 40 and 100 s, respectively. Another NH_3 sensor based on SnO_2/SnS_2 hybrid flakes was fabricated more recently by Xu *et al.*[197] To form the hybrid structure, SnS_2 flakes were first produced by a solution method and deposited on a gold IDE, then the device was heated to 300 °C in air in order to partially oxidise the surface to SnO_2. This device showed good sensitivity to NH_3, with a 16% response to 10 ppm of NH_3, which was much higher compared to the sample with non-oxidized SnS_2 or with the completely oxidized SnO_2. The device also exhibited a good dynamic range from 10 to 500 ppm of NH_3, high reproducibility and a response time of just 11 s.

Black phosphorus is a promising candidate as a platform for gas sensing for its electrical properties and its sensitivity to the environment, which is usually considered as a drawback.[153] First-principles calculations[159] made it possible to shed light on the interaction of many gases with phosphorene. The gas molecules can get physisorbed on the phosphorene surface and interact *via* van der Waals forces, yielding a modification of the electronic properties of phosphorene. O_2, NO_2 and NO act as strong electron acceptors, whereas CO, H_2, H_2O and NH_3 act as electron donors. Abbas *et al.* first reported on the chemical sensing of NO_2 using a FET based on mechanically exfoliated multilayer phosphorene.[158] The FET was produced by exfoliating the black phosphorus with the Scotch-tape method on a Si/SiO_2 substrate and patterning gold electrodes by EBL. The sensor displayed increased conductivity upon NO_2 exposure with a 3% response to 5 ppb of the gas. Moreover, when the device was exposed to NO_2 concentration ranging from 5 to 40 ppb, its response complied with the Langmuir isotherm for molecules adsorbed on a surface, confirming the charge transfer as a sensing mechanism. Cui *et al.*[96] reported a similar FET based on phosphorene nanosheets exfoliated with the Scotch-tape method for NO_2 sensing. The sensor showed thickness dependent performance with sensitivities up to 190% to 20 ppb of NO_2, excellent stability and high selectivity in the presence of interfering gases.

Phosphorene also demonstrated good sensitivity to organic vapors[160] and humidity.[282] Pumera *et al.*[160] developed a highly selective methanol sensor based on black phosphorus plates deposited on a gold IDE. The device was studied with EIS: when exposed to methanol, a strong signal at a resonance frequency of 1 kHz appeared in the impedance phase spectrum and its intensity was proportional to the methanol concentration in the 380–1900 ppm range. High reproducibility, long-term stability and excellent selectivity in the presence of interfering gases were also established. Yasaei *et al.*[282] explored the possibility of employing of phosphorene films as humidity sensors. Phosphorene flakes were produced by ultrasonication in liquid and then filtered to obtain thick films of stacked flakes that were used as chemiresistors. When the humidity was increased from 10 to 85% RH, the conductivity increased by 4 orders of magnitude. From EIS measurements, a sensing mechanism based on the formation of ionic charge carriers caused by ionization of the water molecules and solvation of the phosphorus oxoacids was hypothesized.

Hexagonal boron nitride also exhibits promising properties, which make it an interesting material for gas sensing as was assessed in few first-principles calculations.[283,284] However, the only example of the application of hBN as a gas sensor was reported by Feng *et al.*[199] In particular, an O_2 and CH_4 sensor based on wafer-scale hBN nanosheets (1.7 nm thick) obtained using the CO_2-pulsed laser deposition technique was developed. Such a sensor revealed a sensitivity to 100 ppm of O_2 of 150% with response and recovery times around 70 s and 100 s, respectively. The sensitivity to 100 ppm of CH_4 was even greater (around 780% with response and recovery times reduced to 15 s and 20 s, respectively). The highest sensitivity towards CH_4 could be caused by the higher polarizability compared to O_2, which promotes its adsorption on the surface and at grain boundaries of hBN, thereby changing its conductivity.

The properties and the performances of the gas sensing devices based on TMDs and other layered 2DMs are summarized in Table 2.

By and large, in this first part of this Review article we have provided an overview on the recent developments in the application of the most common 2DMs as gas sensors. From the results highlighted, it is possible to affirm that 2DMs are fully competitive materials for the production of high-performance gas sensors with low operating temperature, thanks to their peculiar properties. Among the 2DMs, pristine graphene does not appear to be ideal for assembling sensing devices because of its chemical inertness and zero-band gap, and thus lack of semiconducting properties. In fact, the modulation of the semiconductivity is a key characteristic to harness the performances of gas sensors. Furthermore, in pristine graphene the absence of dangling groups on its surface that act as bonding sites for the analytes hampers the gas absorption and the sensing performances. Towards this end, doping and modifying graphene with functional atoms and groups and assembly of hybrid structures of graphene and functional nanomaterials have been proven to be the winning strategies for the enhancement of gas sensing performance. A different approach relies on exploiting other 2DMs, which possess intrinsic functionality as TMDs (MoS_2, $MoSe_2$, WS_2, *etc.*). Unlike graphene, TMDs exhibit remarkable semiconducting properties with a tuneable band gap, which depends on their thickness and on the doping effect of *ad hoc* molecules as the sensed gases. Therefore, TMDs are overall promising materials for the fabrication of gas sensors. Nevertheless, to date, their (production) costs and the hurdle in the control over the thickness hinder their application in competitive gas sensing devices.

A few challenges still need to be tackled in order to make 2DMs competitive for the industrial sensing market. In particular, while the sensitivity has evidenced great improvement, an enhancement of response and recovery characteristics is necessary. In fact, in most of the reported examples 2DM based gas sensors exhibit slow response and incomplete recovery when operating at room temperature. Additional performance parameters that require improvements are selectivity and stability. Most of these materials show a poor selectivity for a cross-response to different sensed gases, and in many cases the response signals are unstable. Such a modest selectivity can hardly find a definitive solution because of the major hurdle of

Table 2 Comparison of the sensing performances of different graphene based gas sensors

Material	Sensed gases	Response/ recovery time	Limit of detection	Sensitivity (response × ppm^{-1})	Ref.
MoS_2 (ME)	NO		0.8 ppm		190
	NO_2, NH_3, H_2O			1.372% (NO_2)	14
	TEA, acetone	15 s, 30 s	1 ppm of TEA	5% (TEA)	193
MoS_2 (CVD)	NO_2, NH_3	>10 min	5 ppm	2.5% (NO_2)	266
	NO_2	1 min, 30 min	120 ppb	333%	146
MoS_2 (CVD-Schottky contact)	NO_2, NH_3	10–20 min	20 ppb of NO_2, 1 ppm of NH_3	1000% (NO_2)	144
MoS_2 (CVD – vertically align)	EtOH, NO_2	10 min, 1 h		0.1% (NO_2)	147
MoS_2 (LPE)	NH_3		ppm	5%	265
MoS_2 (LPE in the presence of mercaptoundecanoic acid)	VOCs (toluene, EtOH, hexane, acetone)			0.003–0.0015%	13
MoS_2 – array of devices (LPE)	NO_2	1 h, 1 h	2 ppb	10%	267
MoS_2/graphene electrodes	NH_3, NO_2		1.2 ppm of NO_2	0.06% (NH_3), 1.4% (NO_2)	263
SnO_2/MoS_2	NO_2	5 min, 1 min	0.5 ppm	3%	270
	H_2O			34 883%/RH	198
Pd/MoS_2	H_2	40 s, 83 s		0.0032%	268
WS_2	H_2O, MeOH		5.6 ppm of MeOH, 10% RH		195
	NH_3	~10 min	1.4 ppm	0.005%	194
WSe_2	NO_2			200%	275
$PtSe_2$	NO_2	30 s, 10 s		0.25%	279
SnS_2	NO_2	170 s, 140 s	30 ppb	350%	280
	NH_3	11 s	10 ppm	1.6%	197
	NH_3	40 s, 100 s		4.2%	281
Phosphorene	NO_2	30 s, 840 s		600%	158
	H_2O			135%/RH	282
hBN	O_2, CH_4	15 s, 20 s		7.8% (CH_4)	199

List of abbreviations. ME: mechanically exfoliated, TEA: triethylamine, CVD: chemical vapour deposition, align.: aligned, EtOH: ethanol, LPE: liquid phase exfoliation, MeOH: methanol.

supramolecular chemistry to develop highly selective receptors for volatile gas molecules. Finally, the fabrication methods often used as microfabrication and drop casting are not suitable for the industrial scale up for their complexity and time-demand.

3 Applications in metal sensing

The rapid escalation of agricultural and industrial activities as a result of population growth is yielding a dramatic proliferation of the amount of pollutants released daily worldwide into the environment.[285–287] Metal ions in aqueous environments have caused various diseases and have been a serious threat to ecosystems and public health with the rapid development of industry in recent years.[288,289] Great efforts have been made towards fabricating portable sensors for monitoring heavy metals in the environment. Within this framework also 2DM-based materials have been integrated into different types of sensors capable of detecting heavy and alkali metal ions *via* electrical[92,290–305] and optical outputs.[306–317] The interactions between 2DMs and metal ions have been extensively explored in the past few years, and as a result, outstanding adsorption capabilities have been achieved, opening new avenues in the fields of wastewater purification and sensing.[89] Several excellent reviews have been published on the desalination of water using neat or functionalized GO;[318–321] these reports discuss a variety of approaches to separate alkali metal ions from either seawater or wastewater through incorporation of GO or functionalized GO in membranes. Yet, those review articles do not discuss the use of 2DMs as platforms for sensing devices and in particular for detection of (heavy) metal ions. Many efforts have been made towards developing new robust technologies for low-cost and effective portable sensors for monitoring heavy metals in the environment. Among various approaches, those based on physisorption or chemisorption, relying on the capturing of the pollutant (*i.e.* analyte) by an adsorbent (*i.e.* receptor), are chemically programmable as they exploit supramolecular recognition events. Understanding the dynamic adsorption capabilities of metal ions on the surfaces of 2DMs is therefore extremely important and will be discussed prior to the use of 2DMs in sensing devices for heavy metal ions.

3.1 The adsorption process

The development of *ad hoc* receptors of metal ions makes it possible to exploit the reversible processes of adsorption and desorption as extremely versatile strategies towards sensing in a variety of environments. Moreover, by relying on the reversible nature of non-covalent interactions, the sensor can exhibit a quick response, a fast recovery rate (*i.e.* real-time monitoring) and a facile regeneration to enable its use multiple times. 2DMs are atomically thick and possess two planar surfaces available for metal ion adsorption, thus featuring extremely high surface area-to-volume ratios. In particular, GO is very interesting for the removal of metal ions due to its unique hydrophilic nature and the presence of functional groups containing oxygen atoms, which can efficiently bind the metal ions to form strong surface complexes.[78,322] On the other hand, TMDs intrinsically possess numerous chalcogen atoms, which can act as potential coordination sites for certain heavy metal ions. The adsorption capabilities of 2DMs will be evaluated through the maximum adsorption capacity ($q_{\max}$) defined as the ratio between the maximum loaded mass of the analyte expressed in milligrams and the mass of the absorbent expressed in grams.

3.1.1 Metal sensing with graphene, graphene oxide and related composites. Graphene-based materials are being considered as the most promising absorbents for capturing various heavy metal ions.[323–325] Remarkably, graphene can be easily produced in the form of GO, which displays numerous oxygen-rich functional groups such as carbonyls, epoxides, and hydroxides that both act as reactive sites for further covalent functionalization, and can interact *via* dipole–dipole or strong electrostatic interactions with metal ions, enhancing the occurrence of adsorption events. While several excellent reviews have been published on the desalination of water using neat or functionalized GO,[318–321] these reports discuss a variety of approaches to separate alkali metal ions from either sea-water or wastewater and do not discuss the abilities of other 2DMs as platforms to adsorb (heavy) metal ions. Conventional methods for the quantification of heavy metal ions include plasma mass spectrometry (ICP-AES), atomic absorption/emission spectroscopy (*e.g.* F-AAS, UV-Vis), and polarography. To define the concentration of the remaining heavy metal ions after adsorption, we should calculate the difference between the initial (C_0; mg L^{-1}) and the equilibrium (C_e; mg L^{-1}) concentration. The equilibrium sorption capacity and time-dependent capacity were determined using eqn (2):

$$q_e = \frac{(C_0 - C_e) \times V}{m_{\text{adsorbent}}} \tag{2}$$

where q_e is the equilibrium amount of heavy metal ions adsorbed per unit mass (m) of adsorbent (mg g^{-1}), and V is the volume of the metal ion solution.

Among various adsorption isotherm models, the Freundlich and Langmuir models are most commonly used to estimate the maximum adsorption capacity ($q_{\max}$) of metal ions on both 2D and 3D carbon-based adsorbents.[322,324,326,327] GO and chemically modified graphene oxide (CMGO) are considered as promising adsorbents for the removal of heavy metal ions such as Pb(II),[78,322,326–356] Cu(II),[78,327,335,337,339,347,349,351,356–366] Cr(VI),[262,286,337,355,367–377] Cd(II),[78,327,340,349,355] Hg(II),[335,349,355,378,379] Ni(II),[355,380] Co(II),[381] Mn(II),[327] Pd(II),[382] Sr(II),[383] Au(III),[382] As(V),[384] and U(VI).[385–387] Moreover, in order to increase the adsorption capacity and simplify the separation of the GO from water, numerous hybrid materials have been investigated and include combinations of GO/CMGO with poly(acrylamide) (PAM),[328,331] poly(*N*-vinyl-carbazole) (PVK),[329] hyperbranched polyamine (HPA),[330] iron oxide (Fe_3O_4),[333,334,338] polyamidoamine dendrimers (PAMAMs),[327] ethylenediaminetetraacetic acid (EDTA),[335,336] chitosan (CS),[337,339,350,374,382] *etc.* Hybrids of GO with other polymers have also been used to remove organic contaminants from water.[388]

Among numerous factors affecting the adsorption capacity, the initial concentration of the solution, phase contact time, temperature and pH are found to play crucial roles in the process of adsorption of metal ions on GO.

The adsorption properties of neat GO towards divalent metal ions (copper, zinc, cadmium and lead) were investigated by Sitko *et al.*[78] In this seminal work, it was shown that GO prepared *via* the oxidation of synthetic graphite flakes using potassium dichromate possesses impressive maximum adsorption capacities (q_{max}) for Cu(II) (223 mg g^{-1}), Zn(II) (345 mg g^{-1}), Cd(II) (530 mg g^{-1}), and Pb(II) ions (1120 mg g^{-1}). The single and competitive adsorption of Cu(II), Zn(II), Cd(II) and Pb(II) shows that the affinities of GO for these metal ions follow the order of Pb(II) > Cu(II) ≫ Cd(II) > Zn(II). Since then, many groups have investigated the impact of GO functionalization (with chemical groups and inorganic compounds) on its maximum adsorption capacity. The most relevant results reported so far are listed in Table 3.

Table 3 Maximum adsorption capacities of CMGO composites used in the Pb(II) removal process

Adsorbent	q_{max} (mg g^{-1})	Conditions	Ref.
Few layer GO	1850[a]	pH = 6, T = 333 K	322
	758[a]	pH = 5.5, T = 333 K	332
GO	1119[a]	pH = 5, T = 298 K	78
rGO/PAM	1000[a]	pH = 6, T = 298 K	328
PVK–EGO	888[a]	pH = 7, T = 298 K	329
HPA–GO	820[a]	pH = 5.9, T = 318 K	330
PAM–G	820[a]	pH = 6, T = 288 K	331
$MnFe_2O_4$/GO	673[a]	pH = 5, T = 298 K	333
GO/Fe_3O_4	588[a]	pH = 5, T = 303 K	334
GO/PAMAMs	568[b]	pH = 6, T = 283 K	327
EDTA/CMGO	508[a]	pH = 4.2, T = 298 K	335
EDTA/GO	479[a]	pH = 6.8, T = 298 K	336
CS/GO	461[c]	pH = 6, T = 318 K	337
	99[a]	pH = 6, T = 298 K	352
Fe_3O_4/cysteine	459[a]	pH = 6, T = 298 K	338
CS/GO-SH	447[b]	pH = 5, T = 293 K	339
Polydopamine/GO	365[a]	pH = NA, T = 298 K	340
NH_2–SiO_2/GO	345[a]	pH = 5, T = 313 K	341
Mesoporous silica/GO	333[a]	pH = 7.1, T = 298 K	342
Ag/GO	313[a]	pH = 5.3, T = 298 K	343
Hydroxyapatite/GO	278[a]	pH = 4.5, T = 308 K	344
Polysiloxane/GO	256[a]	pH = 5, T = 313 K	345
Phenylenediamine/rGO	228[a]	pH = 7, T = 298 K	346
Tryptophan/GO	222[a]	pH = 4, T = 293 K	347
GO/polyaniline	217[a]	pH = 5, T = 303 K	348
CS/FeOOH/GO	111[a]	pH = 5.5, T = 313 K	350
GO–SH	108[a]	pH = 4–10, T = 298 K	351
GO–NH_2	96[a]	pH = 6, T = 298 K	326
MHCGO	79[a]	pH = 5.5, T = 298 K	353
CMGO	77[a]	pH = 5, T = 298 K	354
Fe_3O_4–G	28[b]	pH = 6, T = 293 K	355
NH_2–SiO_2/GO	14[a]	pH = 5.5, T = 298 K	356

List of abbreviations. rGO: reduced graphene oxide, PAM: poly(acrylamide), PVK: poly(*N*-vinylcarbazole), HPA: hyperbranched polyamine, $MnFe_2O_4$: manganese iron oxide, Fe_3O_4: iron oxide, PAMAM: polyamidoamine, EDTA: ethylenediaminetetraacetic acid, CMGO: chemically modified graphene oxide, CS: chitosan, GO–SH: sulfhydryl-functionalized graphene oxide, NH_2–SiO_2: amino-siloxane, FeOOH: iron(III) oxide-hydroxide, GO–NH_2: aminosilanized graphene oxide, MHCGO: magnetic carboxymethyl chitosan.[a] Q_{max} values were calculated using Langmuir isotherms. [b] Q_{max} values were calculated using Freundlich isotherms. [c] Q_{max} values were calculated using Redlich–Peterson isotherms.

Zhao *et al.* demonstrated that the q_{max} values of two- or three-layer thick GO nanosheets synthesized from flake-graphite through modified Hummers' method can be tuned with temperature.[322] Interestingly, it has been shown that the adsorption of Pb(II) ions on few-layer thick GO nanosheets was independent of the ionic strength, *i.e.* not affected by concentrations of background electrolyte ($NaClO_4$) at pHs ranging from 1 to 13. In particular, the q_{max} values of Pb(II) ions calculated using the Langmuir model are 842, 1150, and 1850 mg g^{-1} at 293, 313, and 333 K, respectively. Yang *et al.* proposed a different approach which relies on the functionalization of rGO with water-soluble poly(acrylamide) (PAM).[328] The GO prepared following the Staudenmaier method was thermally reduced, yielding rGO. PAM is a polymer with a large number of acetylamine groups in its macromolecular chains, which can interact with metal ions *via* coordination. In particular, the carboxyl groups at the peripheries of the rGO sheets were converted to amine groups by reaction with *N*-hydroxysuccinimide and 1,3-diaminopropane, and a free-radical polymerization initiator was anchored to the rGO sheets. The highest adsorption capacity of rGO/PAM for Pb(II) was 1000 mg g^{-1} (298 K), which is comparable to that of the neat rGO.

Aqueous solutions containing copper ions have been exploited for technological applications in the fields of mechanical manufacturing, electroplating, the light industry and architecture. Yet, these solutions may cause serious diseases in the human central nervous system.[361] According to EPA regulations, the copper concentration in drinking water should not exceed 1300 ng mL^{-1}.[351] Tan *et al.* prepared a hybrid composite including L-tryptophan (L-Trp) and GO by nucleophilic substitution reaction in order to increase the hydrophobicity of GO and to promote the sorption.[347] It was found that such chemical modification of GO increases its sorption capacity from 223 to 588 mg g^{-1}. It has been shown that that high removal efficiencies can be obtained, reaching values exceeding 95% at pH 5 and 4 for Cu(II) and Pb(II), respectively.

Several examples of CMGO-based adsorbents rely on the use of chitosan as a molecule possessing a high affinity for heavy metal ions.[337,339,350,374,382] Chitosan reacts with the carboxyl groups of GO and forms amide bonds.[262,354] In particular, chitosan modified GO has been prepared *via* covalent modification and electrostatic self-assembly by Li *et al.*[339] The introduction of GO–SH sheets as an interlayer can offer extra space into the chitosan structure and further increase the specific surface area. The results indicated that a new type of sorbent material, with functional groups such as –OH, –COOH, –SH and –NH_2, has a high adsorption capacity of copper ions (425 mg g^{-1}, see Table 4). Furthermore, the recyclability of the sorbent has been studied by treating it with HNO_3 and EDTA solutions. The chitosan (CS)/GO–SH hybrid revealed a decrease of the adsorption capacity over three cycles by 23% for Cu, 25% for Pb and 26% for Cd ions. The chitosan/GO hybrid in the form of a nanofibrous composite has been studied by Najafabadi *et al.*[337] The nanofibrous morphology of the hybrid material has been achieved through the use of an electrospinning process. The maximum Cu(II) adsorption capacity was estimated

Table 4 Maximum adsorption capacities of CMGO composites used in the Cu(II) removal process

Adsorbent	$q_{\max}$ (mg g^{-1})	Conditions	Ref.
Trp/GO	588[a]	pH = 5, T = 293 K	347
CS/GO	425[a]	pH = 5, T = 293 K	339
	424[c]	pH = 6, T = 318 K	337
	203[b]	pH = 5, T = 293 K	358
	162[a]	pH = 5.5, T = 303 K	359
	54[a]	pH = 5, T = 293 K	366
Polyallylamine/GO	349[a]	pH = 6, T = 293 K	357
EDTA/CMGO	301[a]	pH = 5, T = 298 K	335
GO	294[a]	pH = 5, T = 298 K	78
	117[b]	pH = 5.3, T = 293 K	361
GO/CdS	137[a]	pH = 6, T = 298 K	360
GO–EDTA	109[a]	pH = 5, T = 293 K	362
GO–NH_2	103[a]	pH = 6, T = 298 K	363
GO–SH	100[a]	pH = 6, T = 298 K	363
	42[a]	pH = 5–10, T = 293 K	351
GO/PAMAMs	69[a]	pH = 4.5, T = 298 K	327
SMGO	63[a]	pH = 4.7, T = 323 K	364
Alginate/GO	60[a]	pH = NA, T = 293 K	365
NH_2–SiO_2/GO	6[a]	pH = 5.5, T = 293 K	356

List of abbreviations. Trp: tryptophan, CS: chitosan, EDTA: ethylenediaminetetraacetic acid, CMGO: chemically modified graphene oxide, CdS: cadmium sulfide, GO–NH_2: aminosilanized graphene oxide, GO–SH: sulfhydryl-functionalized graphene oxide, PAMAM: polyamidoamine, SMGO: sulfonated magnetic graphene oxide, NH_2–SiO_2: aminosiloxane.[a] $Q_{\max}$ values were calculated using Langmuir isotherms. [b] $Q_{\max}$ values were calculated using Freundlich isotherms. [c] $Q_{\max}$ values were calculated using Redlich–Peterson isotherms.

Table 5 Maximum adsorption capacities of CMGO composites used in the Cr(VI) removal process

Adsorbent	$q_{\max}$ (mg g^{-1})	Conditions	Ref.
PPy/cyclodextrin/GO	667[a]	pH = 2, T = 318 K	367
PPy/GO	497[a]	pH = 3, T = 293 K	368
CS/GO	310[c]	pH = 3, T = 318 K	337
	219[a]	pH = 2, T = 293 K	371
	145[a]	pH = 3–4, T = 303 K	374
	108[a]	pH = 2, T = 303 K	376
Fe_3O_4/GO	259[b]	pH = 2, T = 298 K	369
Trioctylamine/GO	232[a]	pH = 2.5–3, T = 293 K	370
G–MgAl-LDH	172[b]	pH = 2, T = 293 K	372
Fe/G	162[a]	pH = 4.5, T = 293 K	373
Cyclodextrin/GO	120[a]	pH = 3, T = 293 K	286
Fe_3O_4/TiO_2/GO	118[b]	pH = 2, T = 303 K	375
DCTA/GO	84[b]	pH = 2, T = 303 K	377
Fe_3O_4/G	17[b]	pH = 1–3, T = 293 K	355

List of abbreviations. PPy: polypyrrole, CS: chitosan, Fe_3O_4: iron oxide, TiO_2: titanium dioxide, G–MgAl-LDH: graphene–magnesium/aluminum-layered double hydroxide, DCTA: 1,2-diaminocyclohexanetetraacetic acid.[a] $Q_{\max}$ values were calculated using Langmuir isotherms. [b] $Q_{\max}$ values were calculated using Freundlich isotherms. [c] $Q_{\max}$ values were calculated using Redlich–Peterson isotherms.

to be 423.8 mg g^{-1}. It was shown that the $q_{\max}$ decreased slowly with increasing cycle number; such behaviour was attributed to the decrease in the availability of active sites of adsorbent for metal ions. CS/GO–SH nanofibers could be used up to the fifth cycle of regeneration using HNO_3 solution by retaining 91.5% of the initial adsorption capacity for Cu(II) ion sorption.

Chromium, which exists most frequently as Cr(III) and Cr(VI),[377] is commonly used in metallurgy, tanning, military, dyes and pigments.[368,369] Generally, Cr(VI) compounds are considered to be more toxic than Cr(III) because of their toxicity to humans, animals, plants and microorganisms.[377,389] A variety of chemical approaches has been employed in order to increase the affinity of GO towards chromium ions. For example, functionalization of GO with polypyrrole (PPy), a widely studied conductive polymer, has been exploited by Li *et al.*[368] The PPy/GO composite nanosheets prepared by the sacrificial template polymerization method exhibit an adsorption capacity for Cr(VI) ions as high as 497 mg g^{-1}. Moreover, the adsorption capacity of the PPy/GO composite nanosheets is about twice as large as that of conventional PPy nanoparticles.[390,391] Supplementary studies showed that subsequent covalent functionalization of PPy/GO with α-cyclodextrin[367] leads to maximum adsorption capacities of 606 mg g^{-1} at 25 °C and 667 mg g^{-1} at 45 °C (Table 5).

Numerous organic and inorganic compounds have been used to functionalize GO and form composites in order to detect and capture other heavy metal ions like Cd(II),[78,327,340,349,355] Hg(II),[335,349,378,379] Ni(II),[355,380] Co(II),[381] Mn(II),[327] Pd(II),[382] Sr(II),[383] Au(III),[382] As(II)[384] and U(III)[385–387] efficiently from aqueous solutions. Zhang *et al.* demonstrated that efficient CMGO-based sorbents could be achieved by decorating GO with polyamidoamine dendrimers (GO/PAMAMs).[327] The adsorption behaviour of GO/PAMAMs for heavy metal ions in water solution was studied by changing the concentration of heavy metal ions, pH values, and temperature. The maximum adsorption capacities of GO/PAMAMs were found to be 568.18, 253.81, 68.68, and 18.29 mg g^{-1} for Pb(II), Cd(II), Cu(II), and Mn(II), respectively. Noteworthily, it was also found that the adsorption capacities of the GO/PAMAMs for the heavy metal ions were highly pH dependent. In particular, at pH < 3, the hydronium ions of higher concentration compete with M(II) to grasp the adsorption sites. With an increase of pH, the protonation degree of the amino groups weakened, and the coordination and chelating ability of PAMAM's amino groups toward Pb(II), Cd(II), Cu(II), and Mn(II) was reinforced.

Conducting polymers interfaced with carbon and carbon-based derivatives have displayed an enhanced removal of mercury and other toxic materials from water. A facile chemical route was reported by Chandra *et al.*[378] In particular, they showed that polypyrrole (PPy)–rGO composites possess a highly selective Hg^{2+} removal capacity. rGO sheets cross-linked with polypyrrole exhibited an increased surface area of 166 m^2 g^{-1}. The uptake of Hg^{2+} by PPy/rGO has been estimated to be as high as 980 mg g^{-1}. Furthermore, PPy/rGO possesses an extremely high desorption capacity of up to 92.3%. Chitosan/GO (CSGO) composites with three different loadings of GO, *i.e.* 5, 10 and 15 wt%, were prepared for the adsorption of Au(III) and Pd(II) by Liu *et al.*[382] The adsorption capacities of Au(III) and Pd(II) onto the CSGO composites were high at pH 3.0–5.0 for Au(III) and pH 3.0–4.0 for Pd(II). It was found that the composite with 5 wt% of GO had the largest adsorption capacity for Au(III) and Pd(II) compared with the other prepared adsorbents, where the maximum adsorption capacities were 1076.6 mg g^{-1} and 216.9 mg g^{-1} for Au(III) and Pd(II), respectively.

Noteworthily, GO-based composites can also be used in the adsorption process of radioactive ions.[385–387] Chen *et al.* reported on the amino functionalized magnetic graphene oxide composite (AMGO) synthesized by a facile, one-step solvothermal method, tailor made for the removal of U(VI) from aqueous solutions.[387] It was shown that the sorption of U(VI) on AMGO occurs *via* the formation of coordination complexes with the nitrogen- and oxygen-containing functional groups. It was concluded that the chemical affinity of the U(VI) for the nitrogen containing functional groups is stronger than that for the oxygen containing functional groups. Interestingly, the AMGO composite could be recovered from the solution with magnetic separation within one minute. The same group demonstrated that the adsorption capacity of CMGO towards uranium can be improved by functionalizing GO with activated carbon felt (ACF) through electrophoretic deposition and subsequent thermal annealing.[385] The q_{max} of GO-ACF for U(VI) was 298 mg g^{-1} at pH 5.5, which is much higher than that of ACF (173 mg g^{-1}), thus suggesting that the carboxyl functional groups of GO-ACF play a salient role in the sorption process, yielding a high efficiency for the removal of U(VI) (Table 6).

Table 6 Maximum adsorption capacities of CMGO composites used in the removal process of various metal ions

Adsorbent	Contaminant	q_{max} (mg g^{-1})	Conditions	Ref.
GO	Cd(II)	530^a	pH = 5, T = 298 K	78
GO/PAMAMs		253^b	pH = 5, T = 298 K	327
PDA/GO		210^a	pH = NA, T = 298 K	340
Fe_3O_4/G		28^b	pH = 6–7, T = 293 K	355
PPy–rGO	Hg(II)	980^a	pH = 3, T = 293 K	378
Ferrite/CS/G		361^a	pH = 7, T = 323 K	379
EDTA–GO		268^b	pH = 4.1, T = 298 K	335
Fe_3O_4–G		23^b	pH = 6–7, T = 293 K	355
GO–G	Ni(II)	37^a	pH = 6, T = 293 K	380
Fe_3O_4–G		22^b	pH = 6–7, T = 293K	355
GO–NH_2	Co(II)	116^a	pH = 6, T = 298 K	381
GO/PAMAMs	Mn(II)	18^a	pH = 4, T = 298 K	327
CS/GO	Pd(II)	216^a	pH = 3, T = 323 K	382
PAM/GO	Sr(II)	185^a	pH = 8.5, T = 303 K	383
CS/GO	Au(III)	1076^a	pH = 4, T = 303 K	382
GO–FeOOH	As(V)	73^a	pH = 7, T = 298 K	384
GO/AC	U(VI)	298^a	pH = 5, T = 298 K	385
GO-sepiolite		161^a	pH = 5, T = 298 K	386
GO–NH_2		141^a	pH = 6, T = 298 K	387

List of abbreviations. PAMAM: polyamidoamine, PDA: polydopamine, Fe_3O_4: iron oxide, PPy: polypyrrole, CS: chitosan, EDTA: ethylenediaminetetraacetic acid, GO–NH_2: aminosilanized graphene oxide, PAM: poly(acrylamide), FeOOH: iron(III) oxide-hydroxide, AC: activated carbon. [a] Q_{max} values were calculated using Langmuir isotherms. [b] Q_{max} values were calculated using Freundlich isotherms.

3.1.2 Metal sensing with transition metal dichalcogenides.

TMDs are characterized by an abundance of intrinsic chalcogen atoms, which are suitable coordination sites for certain heavy metal ions. For this reason, TMDs are now being considered as promising sorbents. In particular, due to the strong non-covalent sulphur–mercury and sulphur–lead interactions, MoS_2 has been recently investigated for the efficient purification of wastewater. The thickness of the S–Mo–S triple layer in MoS_2 amounts to 3.17 Å, resulting in a distance of 2.98 Å between two neighbouring layers.[140] Such a distance is too narrow to allow the penetration of hydrated chalcogen ions into the interior spaces where the vast majority of potential coordination sites are located.[392] Therefore, maximizing the number of accessible sulphur atoms is a crucial step in using layered TMDs in the high-efficiency removal of heavy metal ions from contaminated water. Numerous papers have been published on the control over the interlayer spacing of MoS_2, by either post-treatment of bulk MoS_2 or *in situ* synthesis. For example, Gao *et al.* reported the preparation of MoS_2 with an interlayer spacing of 9.4 Å *via* the intercalation of oxidized DMF species.[393] Zheng *et al.* demonstrated that the interlayer spacing of MoS_2 could be increased to 7.08 Å, 8.99 Å, and 11.61 Å by intercalation with Li^+, K^+ and Na^+, respectively.[394] Recently, Ai *et al.* showed that the interlayer spacing of MoS_2 can also be controlled by the synthesis temperatures.[395] In particular, the interlayer spacing of the obtained MoS_2 was greatly increased (9.5 Å) in the 140–200 °C temperature range; upon further increase of the temperature up to 220 °C, the interlayer spacing of the obtained MoS_2 was found to be almost identical to that of bulk MoS_2. Additionally, due to extremely fast adsorption kinetics the reduction of mercury ions concentration has been observed (Fig. 11a). In brief, 20 mg of widened defect-rich nano MoS_2 (W-DR-N-MoS_2) was added to 200 mL of an aqueous solution containing 10 000 ppb of Hg^{2+}. The concentration of Hg^{2+} drastically decreased to 16.9 ppb after 5 min of treatment, indicating a removal efficiency of 99.83%. The structural features of W-DR-N-MoS_2 were systematically investigated (Fig. 11b–e). They revealed for the first time that such widened defect-rich MoS_2 (W-DR-N-MoS_2) nanosheets are capable of capturing Hg(II) ions, with an extremely high q_{max} (2563 mg g^{-1}) (Fig. 11f) closely matching the theoretically predicted value of 2506 mg g^{-1} (assuming a stoichiometric S/Hg ratio of 1 : 1), which is higher than the q_{max} values of the best adsorbents reported to date.[396–398] The selectivity of W-DR-N-MoS_2 exhibited negligible capturing capability for various competitive ions, such as Na^+, K^+, Ca^{2+}, Mg^{2+}, Al^{3+}, Cr^{3+}, Mn^{2+}, Zn^{2+} and Cd^{2+}, and even inferior capturing capacity for Fe^{3+}, Cu^{2+} and Pb^{2+}.

Liu *et al.* showed that MoS_2 exhibits a superior ability to adsorb lead ions.[399] MoS_2 nanosheets were prepared with an ultrasound assisted electrochemical exfoliation method. As in the case of Hg(II) ions the adsorption capacity of MoS_2 towards Pb(II) can be attributed to the coordination of Pb(II) with the S atoms of MoS_2. Moreover, the strength of such non-covalent interactions is reinforced by electrostatic adsorption. The experimental Pb(II) uptake capacity of MoS_2 was estimated to be as high as 1479 mg g^{-1}. The adsorption followed the Freundlich isotherm model and fitted well with both the pseudo-first-order and pseudo-second-order kinetic models. The adsorption of Pb(II) on MoS_2 materials was further confirmed by SEM-EDS (Fig. 12a–d) and XPS measurements (Fig. 12e). The immobilization of heavy metal ions on 2DMs is depicted in Fig. 12f. The adsorption might be attributed to the chemical adsorption due to the complexation of Pb(II) with intrinsic S or O atoms exposed on the MoS_2 surfaces, together with electrostatic adsorption.

Other studies showed that the modification or the use of MoS_2 as a component of a hybrid material does not increase the q_{max} towards Pb(II)[399,400] and Hg(II)[395,401,402] (see Table 7).

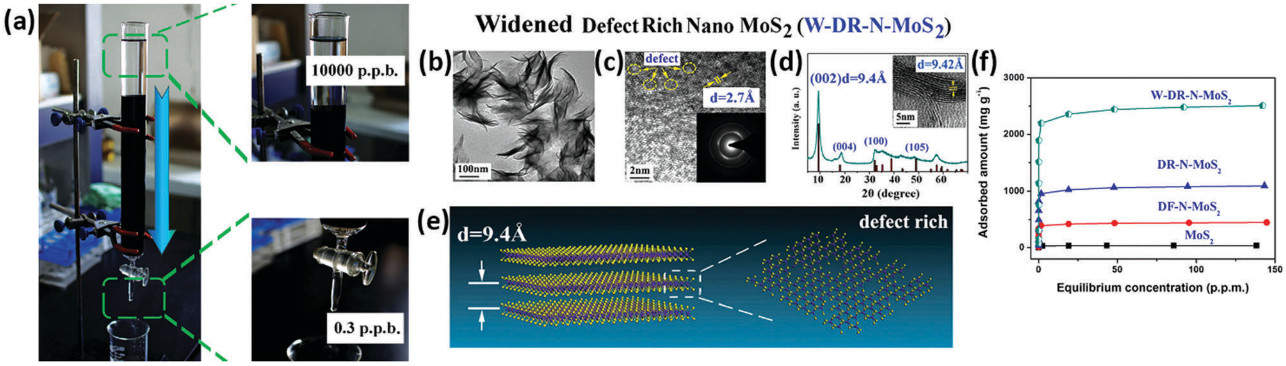

Fig. 11 (a) Purification of a natural water sample. The mercury-contaminated water was passed through a purification column filled with W-DR-N-MoS_2: (b) TEM image of W-DR-N-MoS_2. (c) HRTEM image of the basal plane of W-DR-N-MoS_2; the inset shows the corresponding SAED pattern. (d) XRD pattern and the cross-sectional HRTEM image of W-DR-N-MoS_2. (e) Structural model of W-DR-N-MoS_2 with an enlarged interlayer spacing and multiple defects on the basal planes (the sulphur atoms are yellow and the Mo atoms are purple). (f) Mercury adsorption isotherm, compared with commercial MoS_2 powder, DF-N-MoS_2 and DR-N-MoS_2. Adapted from ref. 395 with permission of Wiley-VCH.

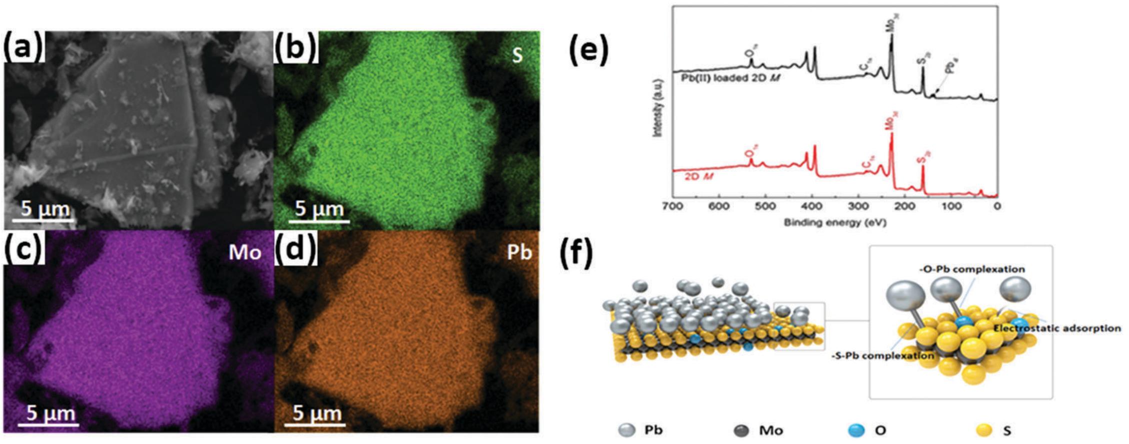

Fig. 12 (a) SEM image of a Pb(II) loaded 2DM. (b–d) SEM-EDS elemental mapping images of S, Mo, and Pb, respectively. (e) XPS survey spectra of 2DM before and after Pb(II) adsorption. (f) Diagrammatic illustration of the mechanism for Pb(II) adsorption on the 2DM. Adapted from ref. 399 with permission of Elsevier Ltd.

Table 7 Maximum adsorption capacities of TMD composites used in the removal process of Hg^{2+} and Pb^{2+} metal ions

Adsorbent	Contaminant	q_{max} (mg g^{-1})	Conditions	Ref.
W-DR-N-MoS_2	Hg(II)	2563[a]	pH = NA, T = NA	395
Au/Fe_3O_4/MoS_2		1527[a]	pH = 5, T = 293 K	402
MoS_2		305[b]	pH = 6, T = 308 K	401
MoS_2	Pb(II)	1479[b]	pH = 5, T = 308 K	399
Co–MoS_2		660[a]	pH = 1–6, T = 293 K	400
Mn–MoS_2		588[a]	pH = 1–6, T = 293 K	400

List of abbreviations. W-DR-N-MoS_2: widened defect rich nano molybdenum disulfide, Au: gold.[a] Q_{max} values were calculated using Langmuir isotherms. [b] Q_{max} values were calculated using Freundlich isotherms.

3.2 Fluorescence-based metal sensors

Colorimetric sensors for metal ions comprise two key features, *i.e.* a metal chelating or binding (coordination) pocket and at least one fluorophore capable of absorbing and/or emitting light. Fluorescence sensing is based on analyte-induced changes in the physicochemical properties of fluorophores, including fluorescence intensity, lifetimes, and anisotropy, which are related to charge transfer or energy transfer processes.[403] To function as a sensor, the electronic structure of the sensor must be altered upon metal binding. Changes in the electronic structure of the sensor can lead to the changes in the intensity or wavelength of light absorption or emission, while changes in the molecular structure can modify the distance or alignment between a pair of fluorophores that serve as a donor–acceptor pair.

3.2.1 Graphene-based fluorescent metal sensors. Graphene oxide has superb fluorescence quenching capability.[404,405] For example, a fluorescent quantum dot (QD)–aptamer–GO sensor based on the nanometal surface energy transfer (NSET) mechanism was designed by Qian *et al.* in order to detect Pb^{2+} ions.[306] In particular, photoinduced electron transfer between graphene quantum dots and GO was employed to achieve the controllable fluorescence turn-on process. The capability of the QD–aptamer–GO nanosensor to detect Pb(II) and other ions with high sensitivity and good reproducibility is demonstrated in Fig. 13.

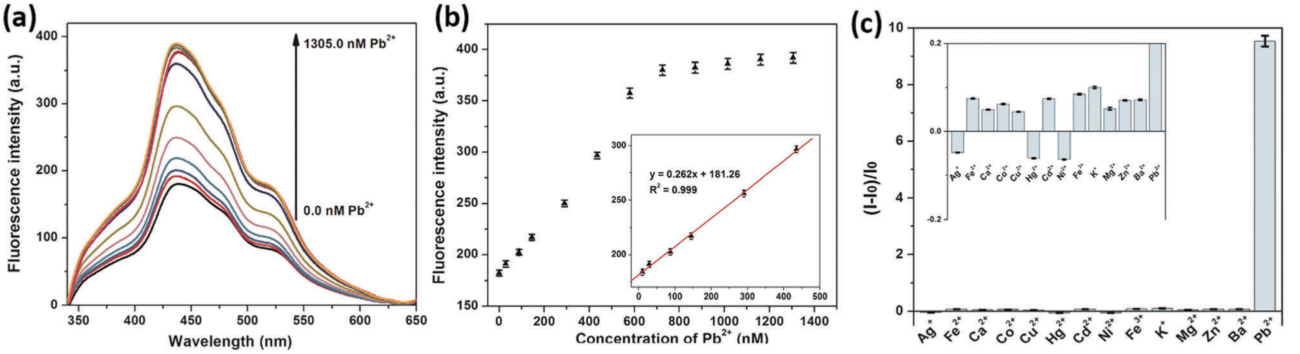

Fig. 13 (a) Fluorescence recovery of the aptamer–rGQD/GO system after incubation with various concentrations of Pb^{2+} (0.0, 29.0, 87.0, 145.0, 290.0, 435.0, 580.0, 725.0, 870.0, 1015.0, 1160.0, 1305.0 nM). (b) Linear relationship between the fluorescence intensity and the concentration of Pb^{2+}. (c) Fluorescence intensity changes ($I - I_0/I_0$) of the sensor in the presence of various metal ions. Adapted from ref. 306 with permission of Elsevier Ltd.

Li *et al.* demonstrated that the single-stranded DNA (ssDNA) aptamer attached on GO can specifically bind to the mercury ions, leading to the formation of a hairpin-shaped double-stranded DNA (dsDNA) structure.[307] The water-dispersible GO sheets, which are functionalized with the ssDNA aptamer, exhibit strong fluorescence emission at 600 nm under excitation at 488 nm in the absence of Hg(II) ions. When Hg^{2+} ions appear in the aqueous solution, they are sandwiched between the hairpin-shaped dsDNA due to the formation of the thymine–Hg(II)–thymine complex, which grasps the Hg^{2+} ions in proximity to the surface of GO. As a result, the fluorescence emission of GO is quenched. Such a sensor shows a limit of detection as low as 0.92 nM and excellent selectivity towards Hg(II) over a wide range of metal ions including K^+, Ag^+, Ca^{2+}, Cd^{2+}, Cu^{2+}, Pb^{2+}, Ni^{2+}, Co^{2+} and Fe^{3+}. Recently, Wen *et al.* reported a FRET sensor based on a cytosine rich DNA probe and GO.[308] In the presence of Ag^+, a DNA–Ag^+ complex was formed, and the conformation of the probe changed to straight stiff, resulting in the desorption of DNA from the surface of GO and fluorescence recovery (Fig. 14a). Fluorescence spectra of the cytosine-rich oligonucleotide (SSO) probe upon incubation with a series of concentrations of Ag^+ and then mixed with GO are portrayed in Fig. 14b. This assay is based on the interaction between the target-induced conformational change of the SSO fluorogenic probe and graphene oxide quenching effects. The use of a simple mix-and-detect analysis revealed a high selectivity toward Ag^+ as determined in the presence of ten times higher concentrations of 12 different interference metal ions (Fig. 14c).

3.2.2 Transition metal dichalcogenide based fluorescent metal sensors. As a result of their finite band gaps, TMDs exhibit interesting optical properties. By mastering the selective recognition capabilities of TMDs toward specific heavy metal ions, several fluorescent sensors for metal ion detection have been developed recently, highlighting the promise of using TMD-based materials to construct novel nanoprobes for chemical sensing and in particular for detection of metal ions.[309–314] For heavy metal ion sensors, TMDs are either non-covalently functionalized with molecules, which are used as sensing probes – because of their high binding affinity to heavy metal ions,[314] or covalently modified, *e.g.* through N- or B-doping.[311] Mao *et al.* reported a seminal study on the use of single layer MoS_2 as the fluorescence quencher to design a probe for detection of Ag^{I}

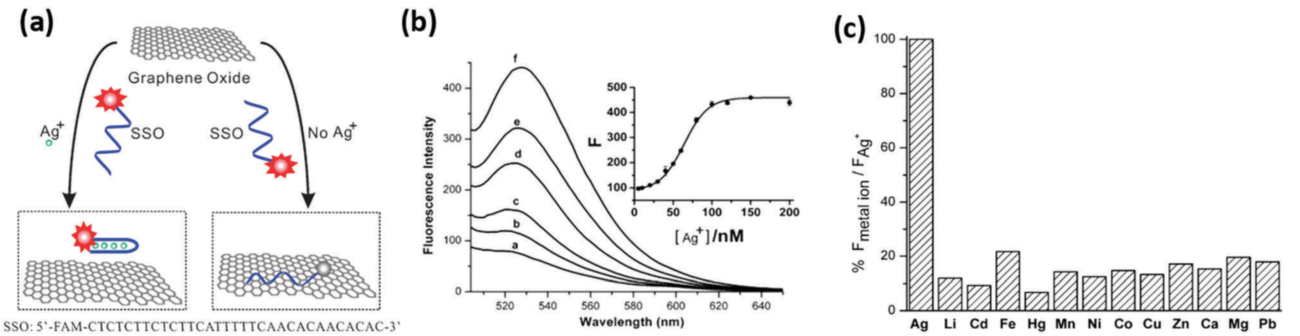

Fig. 14 Schematic illustration of the fluorescence sensor for Ag(I) ions based on the target-induced conformational change of a silver specific cytosine-rich oligonucleotide (SSO) and the interactions between the fluorogenic SSO probe and graphene oxide: (a) FAM-labelled silver-specific oligonucleotide probe. (b) Fluorescence spectra of the SSO probe upon incubation with a series of concentrations of Ag^+ and then mixed with GO: a 0 M, b 20 nM, c 40 nM, d 60 nM, e 80 nM and f 150 nM. All experiments were carried out in MOPS buffer (10 mM, pH 7.0) containing 50 mM $NaNO_3$ and 10 nM SSO. Ag^+ of different concentrations were incubated in this solution for 5 min at 23 °C and then the fluorescence spectra were recorded 2 min after GO (10 mg) was added to this mixture. λ_{ex} = 494 nm. (c) Selectivity of the analysis of Ag^+ ions in the presence of different metal ions. The concentration of Ag^+ was 100 nM, whereas all other interference metal ions were 1 μM. Adapted from ref. 308 with permission of the Royal Society of Chemistry.

Table 8 Comparison of the sensing properties of different TMD based fluorescent sensors

Material	Analyte	Linear range	Detection limit	Ref.
MoS_2	Ag(I)	10–500 nM	1 nM	309
WS_2		5.0–1000 nM	1.2 nM	313
	Hg(II)	6.0–650 nM	3.3 nM	313
B,N-MoS_2		0.01–3 μM	1 nM	311
BP-TPPS		1–60 nM	0.39 nM	317
MoS_2	Pb(II)	0.5–12 μM	0.22 μM	312
BP-fibres		$0.1–1.5 \times 10^7$ ppb	0.25 ppb	315

List of abbreviations. TPPS: tetraphenylporphyrin tetrasulfonic acid.

with excellent sensitivity and selectivity. The detection limit in this assay was found to be as low as 1 nM for Ag^+.[309]

Recently, a fluorescent nanoprobe based on MoS_2 nanosheets for selective and ultrasensitive detection of Ag^+ (down to 10 nM) ions alike in aqueous solutions and biological cells (*Escherichia coli*) was developed by Yang *et al.*[310] In this study Ag^I ions were reduced to Ag^0, which led to the detachment of rhodamine B isothiocyanate (RhoBS) non-covalently interacting with MoS_2 nanosheets, which resulted in the quenching of its fluorescence (see Table 8 for details).

An interesting approach for enhancing the fluorescence of MoS_2 was proposed by Liu *et al.*[311] and it relies on covalent modification of MoS_2 nanosheets with either boron or nitrogen atoms. Boron and nitrogen doping results in changes in the band gap of MoS_2, which increases from 1.20 eV to 1.61 eV. The as-prepared B- and N-doped MoS_2 nanosheets were used as facile, green, label-free and effective sensing platforms for Hg^{2+} ions. The modified nanosheets exhibit enhanced fluorescence properties compared with the undoped MoS_2, which were highly quenched after selective absorption of Hg^{2+}. Wang *et al.* found that after the doping with Pb^{2+} ions the fluorescence of MoS_2 nanosheets was enhanced, which was subsequently quenched by the addition of sulphide ions.[312] The fluorescence quantum yield measurements of the single layer MoS_2 was estimated to be ∼0.28%. The quantum yield of the doped MoS_2 nanosheets was calculated to be ∼0.73%, thereby indicating that molecular doping of MoS_2 nanosheets with lead(II) metal ions strengthened their fluorescence.

To date, little has been done on the application of WS_2 nanosheets in biological and chemical sensing. For example, Zuo *et al.* developed a novel dual-colour fluorescence biosensing platform based on WS_2 nanosheets.[313] The sensor could achieve simultaneous detection of Hg^{2+} and Ag^+ in a high sensitivity and wide linear range by monitoring fluorescence intensity changes at 525 nm and 583 nm, respectively. Hg^{2+} and Ag^+ were selectively detected in the concentration range from 6.0 to 650.0 nM and from 5.0 to 1000.0 nM, with detection limits of 3.3 nM and 1.2 nM, respectively. The fluorescence intensities in the presence of other heavy metal ions changed by ∼5% when the cation concentrations were 10-fold greater than those of Hg^{2+} and Ag^+ ions, indicating that the developed biosensor is highly selective for mercury and lead ions.

3.2.3 Other 2DM based fluorescent metal sensors.

Liu *et al.* showed an integrated black phosphorus–tilted fibre grating (TFG) configuration as an enhanced light–matter interaction platform for heavy metal sensing.[315] BP nanosheets were produced by liquid-phase exfoliation and deposited through an *in situ* layer-by-layer technique. The BP–TFG composite was exploited as the optic probe for Pb^{2+} ion detection, and the results showed an ultrahigh sensitivity of up to 0.5×10^{-3} dB ppb^{-1}, a limit of detection down to 0.25 ppb, and an extremely wide concentration range from 0.1 ppb to 1.5×10^7 ppb. The achievable limit of detection was estimated to be 40 times lower than the World Health Organization permissible limit for lead in drinking water. The wide detection range is 4-orders of magnitude larger than that of a BP-FET based lead sensor.[316]

Gu *et al.* presented a novel ratiometric fluorescence sensor based on the inner filter effect (IFE) of tetraphenylporphyrin tetrasulfonic acid (TPPS) toward black phosphorus quantum dots (BP QDs), developed for the selective and sensitive detection of Hg^{2+}.[317] Highly fluorescent BP QDs were successfully synthesized from bulk BP by a sonication-assisted solvothermal method. In the presence of Hg^{2+}, the IFE originating from the spectral overlap between the excitation of BP QDs and the absorption of TPPS is inhibited, resulting in the recovery of the fluorescence of BP QDs. The constructed sensor revealed a good linear response to Hg^{2+} ranging from 1 to 60 nM with a detection limit of 0.39 nM. Interestingly, this strategy could also be applied in the determination of Hg^{2+} in real water samples with satisfactory results. Sensing properties for all 2DM-based fluorescent sensors are presented in Table 8.

3.3 Field-effect transistor based metal sensors

2DM nanosheets integrated into FETs have recently revealed their enormous potential for detection of heavy metals. The working principle of a 2DM-based FET sensor is based on the changes in the critical parameters of a FET containing 2DM nanosheets upon adsorption of targeted heavy metal ions. This includes primarily the field-effect mobility, threshold voltage and I_{on}/I_{off} ratio. 2D semiconducting sheets are of particular interest because of their high charge carrier mobility and very high surface-to-volume ratio, leading to high sensitivity. Chemical sensors based on FETs can overcome the obstacles of previous detection methods. For example, the aforementioned optical methods have some limitations such as multiple sensing steps, the need for using chemical agents, a higher cost, and a longer detection time. In contrast, the use of 2DM-based FET sensors enables the rapid label-free detection of metal ions in real-time by monitoring the resistance or the Dirac point shift caused by the adsorption of target analytes. Such devices can be characterized also by low power consumption and can be miniaturized for the development of portable sensors, eventually supported on flexible foils.

3.3.1 Graphene-based FET metal sensors.

In a typical graphene field-effect transistor (GFET) based sensor, graphene is used as a conducting material in the channel between drain and source electrodes. The gate potential is applied through the back-gate (typical thin SiO_2 layer)[406] or top-gate (electrical double layer in electrolyte).[114] The absorption of analyte molecules or change in the local environment leads to a change in graphene

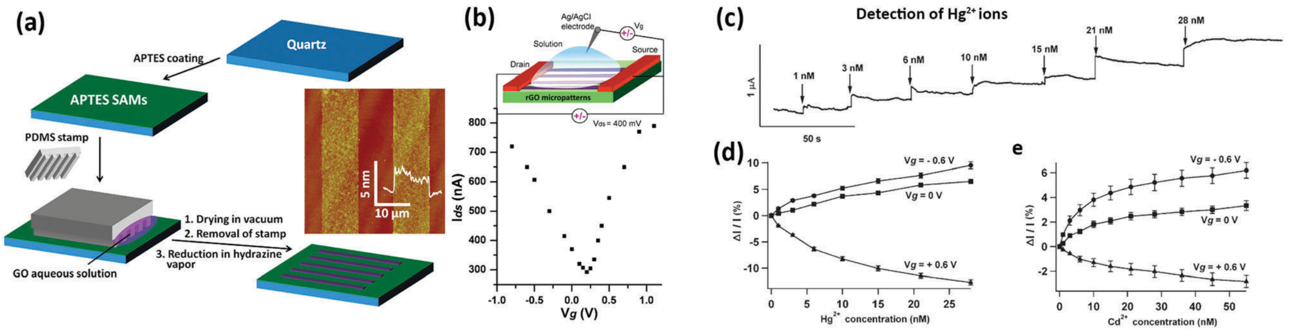

Fig. 15 (a) Schematic illustration for the fabrication of patterned rGO thin films on APTES-coated quartz. Inset: AFM image of the obtained rGO micropatterns on APTES-coated quartz. (b) Ambipolar characteristics of the rGO-FET measured in 0.1 M phosphate buffer saline (PBS) solution. Inset: Schematic of a solution-gated configuration of rGO-FET. (c) Typical real-time recording of I_{ds} with the addition of Hg^{2+} ions. (d and e) Change in I_{ds} in rGO-FETs (number of tested samples, $n = 6$) with the addition of (d) Hg^{2+} and (e) Cd^{2+} ions at $V_{ds} = 0.4$ V and $V_g = -0.6$ (circles), 0 (squares), and +0.6 V (triangles). Adapted from ref. 291 with permission of American Chemical Society.

electrical conductance. Zhang *et al.* reported the functionalization of mechanically exfoliated graphene with a self-assembled monolayer of 1-octadecanethiol and its application in Hg^{2+} sensing.[290] Substituted alkane derivatives were found to self-assemble into large-scale highly-ordered physisorbed monolayers on single-layer graphene supported by a SiO_2 dielectric substrate. According to AFM imaging, the height of graphene increased to 1.6 nm when exposed to Hg^{2+}, indicating the successful uptake of mercury ions by the thiol groups exposed on the graphene surface. Such a graphene-FET sensor revealed a detection limit for Hg^{2+} as low as 10 ppm.

Alternative approaches based on solution processable rGO,[291,292] and G functionalization[92,293–295] are being pursued with the ultimate goal of developing low-cost, scalable fabrication of graphene-FET sensors. Recently, Sudibya *et al.* presented a FET sensor using micropatterned, metallothionein type II protein (MT II)-functionalized rGO films, which bind with both physiological (*e.g.*, Cu^{2+}, Zn^{2+}) and xenobiotic (*e.g.*, Hg^{2+}, Cd^{2+}) metal ions with high affinity (see the schematic illustration in Fig. 15a).[291] A typical plot of drain-to-source current (I_{ds}) *versus* solution-gate voltage (V_g) of a rGO-FET sensor is displayed in Fig. 15b. Such a nanoelectronic sensor is capable of detecting various metal ions in real-time with high sensitivity. The addition of mercury (Hg^{2+}), at a concentration as low as 1 nM, caused an obvious current increase in the rGO-FET which was biased at V_{ds} = 400 mV and $V_g = -0.6$ V (Fig. 15c). The magnitude of the device response scales with the Hg^{2+} concentration, and its polarity depends on the gate voltage (V_g). The detection limit for Hg^{2+} was estimated to be as low as ~1 nM with a signal-to-noise ratio of 25–30 (Fig. 15d). The very same device exhibited also Cd^{2+} detection at 1 nM with a slightly smaller change in the current signal-to-noise ratio of 15–20 (Fig. 15e).

For heavy metal ion GFET sensors, biomolecules are frequently used as sensing nanoprobes due to their high binding affinity to inorganic contaminants.[92] An *et al.* reported a high-performance flexible graphene aptasensor for Hg^{2+} detection.[293] 1,5-Diaminonaphthalene (DAN) and glutaraldehyde (GA) were employed as cross-linking agents, while the aptamer (3′-amine-TTC TTT CTT CCC CTT GTT TGT-C10-carboxylic acid-5′) was non-covalently linked onto the graphene surface as a probe for Hg^{2+}. The field-induced responses from the graphene aptasensor showed excellent sensing performance: Hg^{2+} ions with a very low concentration of 10 pM could be detected (Fig. 16a), which is 2–3 orders of magnitude higher than previously reported mercury sensors using electrochemical devices.[406,407] A GFET-sensor was characterized with the experimental setup presented schematically in Fig. 16b. The sensor response time was rapid, with values below 1 s. Noteworthily, the pristine graphene devices showed no significant current changes upon exposure to Hg^{2+}. It was concluded that the origin of current changes in the sensor relies on the p-doping effect

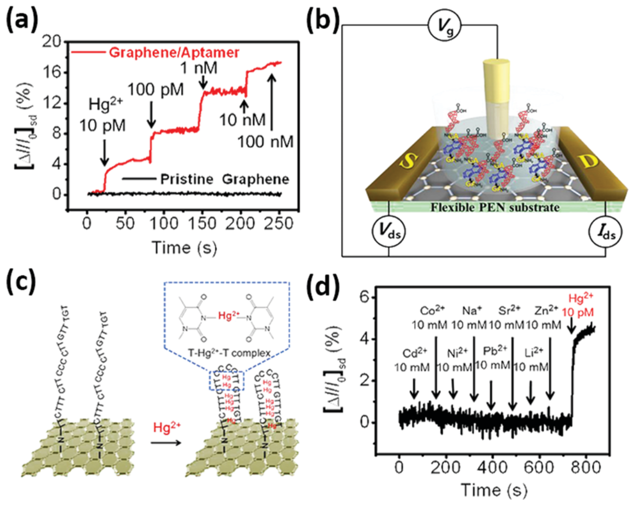

Fig. 16 (a) Real-time response curve of the aptasensor with various Hg^{2+} concentrations (10 pM to 100 nM). Graphene substrate without the aptamer was introduced as a control sample. (b) Schematic diagram of a liquid-ion gated FET using graphene conjugated with the aptamer (V_g, S and D indicate the gating voltage and source/drain electrodes). (c) Interaction of Hg^{2+} ions with thymine base pairs in the aptamer immobilized on the surface of the modified graphene layer. (d) Selective responses of the aptasensor toward the target metal ions (Hg^{2+}, 10 pM) and nontarget metal ions (Cd^{2+}, Co^{2+}, Ni^{2+}, Na^{+}, Pb^{2+}, Sr^{2+} and Zn^{2+}, 10 mM). Adapted from ref. 293 with permission of American Chemical Society.

resulting from the thymine–Hg–thymine complex formed between Hg^{2+} ions and thymine base pairs in the aptamer (Fig. 16c).

Noteworthily, graphene-based FET sensors can be exploited for the detection of not only heavy metal ions (*e.g.* Hg^{2+} and Pb^{2+}) but also alkali metal ions in water including K^{+}[294] and Na^{+}.[295]

3.3.2 Transition metal dichalcogenide FET metal sensors. The semiconducting properties of MoS_2 make this 2DM particularly suitable as an electroactive material for application in transistors.[408] Also for this reason, MoS_2 has been employed in FET sensors for detecting heavy metal ions.[296,297]

Jiang *et al.* demonstrated a FET based on mechanically exfoliated few-layer MoS_2 nanosheets for sensing Hg^{2+} ions.[296] The interaction between Hg^{2+} ions and few-layer MoS_2 was studied using FET measurements and photoluminescence. Due to the high binding affinity between the sulphur sites on the MoS_2 surface and Hg^{2+} ions, the latter can strongly bind to MoS_2. Remarkably, it was shown that the binding of Hg^{2+} results in a p-type doping and reduces the electron concentration in n-type few-layer MoS_2. Upon binding Hg^{2+} ions the electron transport and photoluminescence properties in few-layer MoS_2 are effectively modulated. It was also demonstrated that by monitoring the changes in the conductance of few-layer MoS_2 and varying the concentration of Hg^{2+} solutions, few-layer MoS_2 transistors can function as highly sensitive sensors for rapid electrical detection of Hg^{2+} with a detection limit as low as 30 pM.

Zhou *et al.* reported on a DNA-functionalized MoS_2 nanosheet/gold nanoparticle hybrid FET sensor for the ultrasensitive detection of Hg^{2+} in an aqueous environment (Fig. 17a).[297] A thin film was formed by filtration of MoS_2 nanosheets produced by liquid-phase exfoliation, followed by transfer onto the Au electrodes and thermal annealing. Then Au NPs were sputtered onto the MoS_2 film, and finally the DNA molecules were grafted onto Au NPs by immersing the device in a DNA solution. In the hybrid structure, the MoS_2 thin film acts as the conducting channel with the homogeneously dispersed Au NPs operating as anchoring sites for DNA probes chosen to specifically target Hg^{2+} ions. Upon addition of Hg^{2+} to the sensor, the formation of metal complexes between the thymidine bases present in the DNA molecules and mercury ions takes place, resulting in the changes in the MoS_2 conductance. The detection of metal ions was enabled by monitoring the change in the source–drain current in the FET device as a function of Hg^{2+} concentration. The detection limit of the sensor can reach values down to the concentration of 0.1 nM (Fig. 17b). It was shown that the rate of the increase in the conductance or source–drain current is dependent on the Hg^{2+} concentration (Fig. 17c). The sensor was also tested with a series addition of Hg^{2+} and the dynamic responses indicated that the sensor responded to Hg^{2+} within a few seconds, which is much faster than the conventional optical methods. The output characteristics of three types of sensors, *i.e.* MoS_2, MoS_2–Au NPs, MoS_2/DNA–Au NPs, are shown in Fig. 17d. Because of the work function difference between the Au NPs (3.6 eV in air for D = 8 nm) and the MoS_2 film (∼5.23 eV after annealing), electron transfer occurs from the Au NPs to the MoS_2 film, leading to a decreased concentration of holes in the MoS_2 film and thus the decreased conductivity.

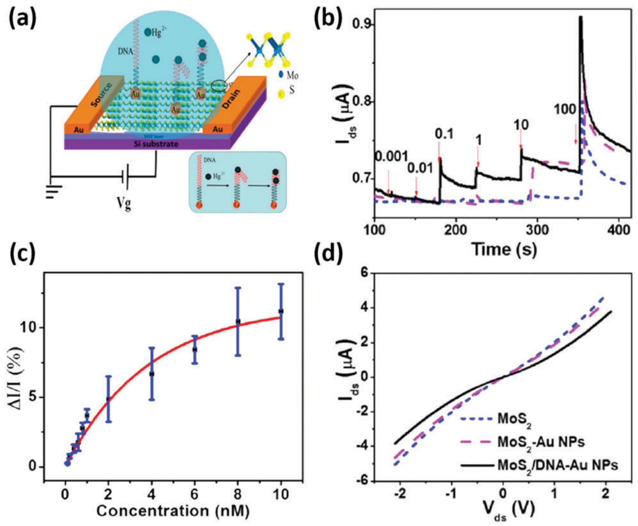

Fig. 17 (a) FET sensor platform based on the hybrid structure. The formation of T–(Hg^{2+})–T chelates, through reaction between Hg^{2+} and the thymidine bases exposed on the DNA molecules grafted onto the Au NPs, leading to the change in the MoS_2 electrical conductivity as a sensor signal. (b) Real-time detection of Hg^{2+} (nM) in water (V_{ds} = 0.1 V) with platforms of MoS_2/DNA–Au NPs (black, solid), MoS_2–Au NPs (purple, dashed), and MoS_2 (blue, short dashed), respectively. (c) Sensitivity variation and exponential fitting of sensitivity as a function of Hg^{2+} concentration for the MoS_2/DNA–Au NP hybrid sensor. (d) Evolution of the I_{ds}–V_{ds} characteristics during the MoS_2/DNA–Au NP hybrid sensor fabrication process (V_{ds} = −2.1 V to 2.1 V, step = 0.1 V) at room temperature. Adapted from ref. 297 with permission of American Chemical Society.

Despite the examples discussed in this Review, little knowledge has been gathered on the sorption capacities of other metal ions on 2D MoS_2. Therefore, it is of significant importance to extend in the future the application of such 2DM for the detection or removal of other heavy metals considering its markedly high metal capture capacity.

3.3.3 Other 2DM based FET metal sensors. Li *et al.* for the first time presented an ultra-sensitive suspended black phosphorus FET sensor for detection of mercury ions operated in the sub-threshold regime.[298] Thin BP nanosheets were mechanically exfoliated by a Scotch tape based method and transferred onto a low resistance Si substrate covered with a 300 nm thick layer of SiO_2. A BP FET is a transducer, which converts the adsorption of ions into conductivity/current shift by the gating effect. Free-standing BP FET sensors gated into the sub-threshold regime demonstrated ultrahigh sensitivity, which was almost two orders of magnitude larger than that of non-suspended BP in the linear regime. The proposed BP sensors were able to realize rapid (3 s) label-free detection of Hg^{2+} down to 0.01 ppb, and superb selectivity was achieved by functionalizing the BP surface with mercury ionophores. BP sensors tested with different thicknesses revealed that the response ($\Delta R/R_0$) to 10 ppb of Hg^{2+} decreased approximately 30% when the BP channel thickness varied from 8 nm to 20 nm.

The same group also demonstrated air stable high-performance BP chemical sensors encapsulated with ionophores (Fig. 18a, inset).[316] Without protection, BP samples once exposed to air

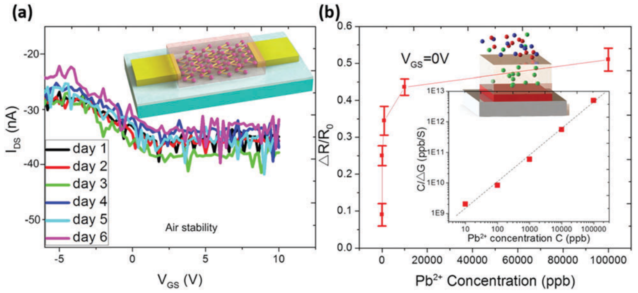

Fig. 18 (a) Schematic view of a BP sensor with I_{ds} *vs.* V_{gs} curves of BP with ionophore protection. I_{ds} variation is less than 10%, suggesting significantly improved air stability. (b) $\Delta R/R_0$ *versus* Pb^{2+} concentration (experimental results from 7 sensors) and a schematic view of BP sensors with lead ionophores. The resistance of BP becomes saturated at higher concentrations. Experimental results demonstrate a good linear relation between $C/\Delta G$ and C, fitting well the Langmuir adsorption isotherm, as shown in the inset. Adapted from ref. 316 with permission of American Chemical Society.

start to degrade and oxygenated phosphorus (PO_X) is shortly formed, with degradation of its electrical properties and device performances. The ionophore film effectively reduces negative factors from the ambient environment; meanwhile, it displays selective permeability towards certain types of molecules. The ionophore-encapsulated BP devices were found to be still in good shape after 1 week of ambient exposure, with source–drain current I_{ds} variation less than 10% (Fig. 18a). The methodology of the preparation of thin BP nanosheets is the same as the one shown above (*i.e.* mechanical exfoliation with Scotch tape). The BP sensors were sensitive to the detection of multiplex ions such as AsO^{2-}, Hg^{2+}, Cd^{2+}, and Pb^{2+} with detection limits down to 10, 1, 3 and 1 ppb, respectively. Moreover, Pb^{2+} ions can be effectively detected over a wide concentration range, from 10 ppb to 100 000 ppb (Fig. 18b). The detection limit and response rate of BP are both better than those reported for graphene based sensors.

Although only a few biosensors and water sensors with BP FETs were reported due to the inherent instability of BP in a moisture rich environment, BP sensors have attracted increasing interest across the sensing community due to the 2D structure, tuneable band gap, and high carrier mobility of BP. From a practical application standpoint, the thickness, uniform control, and stability of BP limit its application in ultrasensitive sensor technology. With further understanding of interactions between BP and oxygen/water and the improvement of sensor fabrication techniques, BP-based FET sensors can be foreseen to provide a robust sensing method for a wide variety of target analytes in the near future.

3.4 Electrochemical based metal sensors

Electrochemical sensing of heavy metal ions relies on the use of sensing electrodes that are employed for passing the current to an aqueous solution and generate an electrical signal that corresponds to the electrochemical reaction within the solution due to the presence of metal ions. Common experimental setups for electrochemical detection of heavy metal ions consist of an electrolytic cell containing an electrolyte, *i.e.* a solution of heavy metal ions, in contact with an electrode. The cell potential is measured at the interface of the electrode with the electrolyte solution. Noteworthily, because heavy metal ions have defined redox potentials, the selectivity toward specific heavy metal ions can be achieved using bare electrodes without the need for a molecular recognition probe. Numerous techniques have been employed in electrochemical sensing, including potentiometry, voltammetry, impedimetry, amperometry and conductometry. In particular, the anodic stripping voltammetry (ASV) method is widely explored for detection of heavy metals. ASV analysis typically involves two steps, *i.e.* deposition of heavy metals onto the electrode surface, and stripping or dissolution of the deposited analyte from the electrode surface. Recent advances in the field have revealed the potential of 2DMs in electroanalysis. Several electrochemical sensors based on 2DMs for bioanalysis and environmental analyses have been developed. In particular, Zhao *et al.* presented for the first time that Hg^{2+} can be selectively identified using a PPy–rGO nanocomposite-modified glassy carbon electrode (GCE).[299] Such selectivity was achieved using square wave anodic stripping voltammetry (SWASV), which determines a reduction of adsorbed Hg^{2+} to Hg^0 at a certain potential. The anodic stripping current was obtained in a potential range for the identification of Hg^{2+}. In addition, excellent sensitivity (0.124 μA nM^{-1}) and limit of detection (LOD) (15 nM) results were achieved. The measured stripping current toward Hg^{2+} at the PPy modified electrode was found to be 3–9 times higher than those towards other ions, indicating that rGO in the nanocomposite plays an important role in highly selective detection.

Sahhoo *et al.* reported a facile *in situ* approach for the fabrication of a rGO/bismuth (Bi) nanocomposite by employing modified Hummers' method without the use of any surfactants. Bi nanoparticles were uniformly anchored onto the surfaces of individual graphene nanosheets, which prevent restacking of rGO, resulting in good dispersion in solvents. The rGO/Bi nanocomposite was used as an electrode material for the stripping voltammetric determination of heavy metal ions in water. The detection limits of the proposed electrochemical sensor for Cd^{2+}, Pb^{2+}, Zn^{2+} and Cu^{2+} were found to be 2.8, 0.55, 17 and 26 ppb, respectively.[300] Wei *et al.* developed a SnO_2/rGO-based electrochemical sensor, which could simultaneously and selectively analyse four heavy metal ions such as Cd(II), Pb(II), Cu(II) and Hg(II).[301] SWASV has been employed for the detection of heavy metal ions (Fig. 19a). The SnO_2/rGO nanocomposite modified glass carbon electrode synthesized by a simple wet chemical method showed enhanced sensing performance compared with single SnO_2 and single rGO (Fig. 19b).

Li *et.al.* used Nafion and rGO for anodic stripping voltammetric analysis of cadmium with a detection limit 0.005 ppb.[302] Willemse *et al.* reported on the determination of Cd^{2+}, Pb^{2+}, Zn^{2+} and Cu^{2+} by making use of a platform based on a Nafion–graphene nanocomposite film.[409] LODs of 0.07–0.08 ppb have been achieved for the individual ions, which are comparable to those determined with ICP-MS, and ascribed to a combination of the enhanced electron conduction of rGO and the cation exchange capacity of Nafion. Similarly, Chaiyo *et al.* constructed

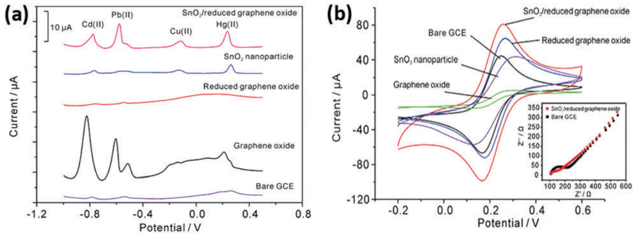

Fig. 19 (a) Square wave anodic stripping voltammetry (SWASV) curves for 0.5 μM each of Cd(II), Pb(II), Cu(II), and Hg(II) on bare (violet line), graphene oxide (black line), reduced graphene oxide (red line), SnO_2 nanoparticle (blue line), and SnO_2/reduced graphene oxide nanocomposite (pink line) modified GCEs in 0.1 M acetate buffer (pH 5.0). Deposition potential = −1.0 V; deposition time = 120 s; amplitude = 25 mV; incremental potential = 4 mV; frequency = 15 Hz; *vs.* Ag/AgCl. (b) Cyclic voltammograms measured with bare, GO, rGO, SnO_2 nanoparticle, and SnO_2/reduced graphene oxide nanocomposite modified GCEs in a solution of 5 mM $Fe(CN)_6^{3-/4-}$ containing 0.1 M KCl. Inset: Nyquist diagram of electrochemical impedance spectra for bare and SnO_2/reduced graphene oxide nanocomposite modified GCEs in the solution of 5 mM $Fe(CN)_6^{3-/4-}$ containing 0.1 M KCl. Adapted from ref. 301 with permission of American Chemical Society.

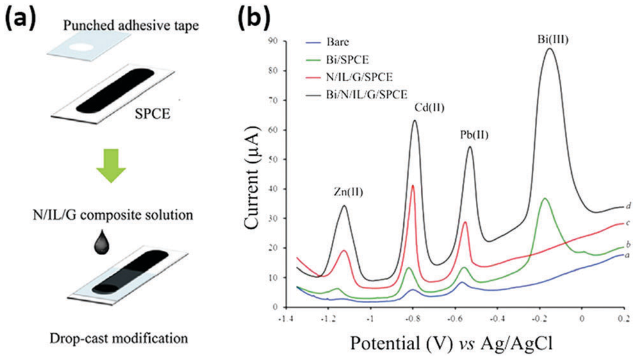

Fig. 20 (a) Schematic drawing of the electrochemical sensor fabrication. (b) Square wave anodic stripping voltammetry (SWASV) curves of 50 ng mL^{-1} Zn(II), Cd(II) and Pb(II) in 0.1 M acetate buffer solution (pH 4.5). Adapted from ref. 303 with permission of Elsevier B.V.

a Nafion/ionic liquid/graphene electrochemical sensor for simultaneous determination of zinc, cadmium and lead using screen-printed carbon (Fig. 20a).[303] The functionalized graphene-based nanocomposite modified electrode showed better detection performance for Zn(II), Cd(II) and Pb(II) compared to the bare electrode by SWASV (Fig. 20b). The detection limits of such sensors for Zn(II), Cd(II) and Pb(II) detection were 0.09 ng mL^{-1}, 0.06 ng L^{-1} and 0.08 ng L^{-1}, respectively.

Gong *et al.* reported an ultrasensitive Hg(II) electrochemical sensor using monodispersed Au nanoparticles onto the graphene nanosheet matrix as the enhanced sensing platform.[410] The detection limit was found to be as low as 6 ppt. The interference from other heavy metal ions such as Cu^{2+}, Cr^{3+}, Co^{2+}, Fe^{3+}, $Zn^{2+}$and I^- ions associated with Hg^{2+} analysis could be effectively inhibited. Another example relies on the use of cysteine-functionalized GO (sGO) and carbonyldiimidazole as a cross-linker *via* the formation of amide and carbamate bonds. A sGO/polypyrrole (PPy) nanocomposite film was grown on the working electrode surface of a screen-printed electrode (SPE) *via* controlled one-step electrochemical deposition.[304] The sGO/PPy-SPE was used to detect lead ions in water by differential pulse voltammetry (DPV). The DPV signals were linear in the range of 1.4–14 000 ppb of Pb^{2+}. The measurable detection limit of the sensor is 0.07 ppb, which is 2 orders of magnitude below the threshold value for drinking water set by the World Health Organization. The average removal efficiency of Pb^{2+} deposited on the electrode amounted to 99.2%, with a relative standard deviation (RSD) of 3.8%. The selective detection of the GO/PPy composites was investigated by mixing GO/PPy with various metal ions such as Pb^{2+}, Na^+, Mg^{2+}, Cd^{2+}, Cu^{2+}, Hg^{2+} and Ag^+. The results clearly show that the GO/PPy composite film can selectively detect Pb^{2+} and remains unresponsive in the presence of other metal ions. In addition, the developed device can be used multiple times.

TMD nanostructures were mainly utilized as sensing platforms for the development of electronic and fluorescent sensors, while their electrochemically sensing applications are still limited. Cui *et al.* synthesized a monolayer MoS_2 supported Cu_7S_4–Au nanocomposite as a sensing platform to detect Hg(II) using an anodic stripping voltammetric technique.[305] They found that the synergistic effects of both Au domains and active edge sites of monolayer MoS_2 played a vital role in the high-performance detection of Hg(II) with a limit of detection of 190 nM.

In this part of the Review article, we have provided an overview on the recent advances in metal ion sensing. Different types of 2DMs employed for specific and selective recognition of heavy metals have been discussed in this section. By taking advantage of their unique properties, 2DMs can be successfully explored to construct a wide range of optical and electrical sensing platforms for the detection of various heavy metal ions. Chemical modification of GO and TMDs has proven to provide a promising solution for improving the sensing performance with high specificity, enhanced sensitivity and a low detection limit. Chemical metal sensors based on 2DMs have demonstrated high sensitivity detection of a wide variety of heavy metal ions at low concentrations, due to the maximum sensor surface area per unit volume. Their favourable structural and compositional synergy allows them to be excellent electrode materials for fabricating various fluorescent and electrochemical sensing platforms, such as FET-based sensors. Moreover, electrochemical measurements have shown numerous advantages for trace heavy-metal detection, including rapid analysis, good selectivity, and sensitivity. Optical detection systems are other alternatives to the electrochemical detection methods. They represent attractive analytical tools whenever continuous monitoring and real-time information are desired.

4 (Bio)molecular sensors

4.1 (Bio)molecular sensing with graphene, graphene oxide and related composites

Ultrafast sensing of chemically and biologically active molecules at low concentrations is critical in a wide range of research fields

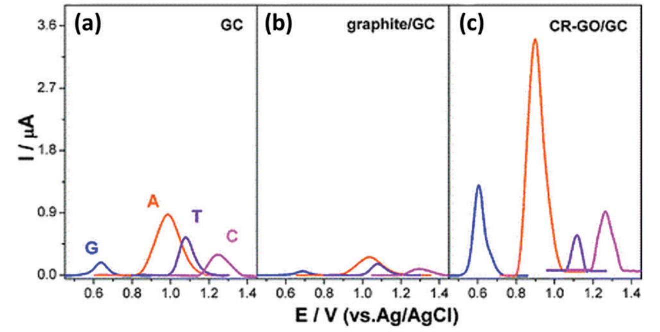

Fig. 21 Differential pulse voltammograms (DPVs) recorded using (a) a GC electrode, (b) a graphite/GC electrode, and (c) a CR-GO/GC electrode, for guanine (blue), adenine (orange), thymine (violet), and cytosine (magenta), respectively. Adapted from ref. 72 with permission of American Chemical Society.

and in particular for applications, such as chemical analysis,[411] healthcare,[412,413] and monitoring the environment or diagnostic diseases.[414] Because of their particular physico-chemical properties, graphene-based materials have been used to fabricate various types of chemical sensors including electrochemical,[72,413,415–444] FET,[445–449] fluorescent[450–457] and surface enhanced Raman spectroscopy-based sensors.[411,458–460] Graphene based materials have been used to develop various types of sensors to detect molecules such as glucose,[72,415–423,425,427,445,461–465] DNA,[72,428,430,447,449,451,452,455,457,466–469] hydrazine,[431,470–473] dopamine,[72,413,424,432–439,441,454,474,475] ascorbic acid,[72,413,434,441,476,477] H_2O_2,[72,443,478–480] and other aromatic molecules (Fig. 21).[411,453,456,458,459,478] Graphene-based materials offer various advantages, when compared to other carbon-based nanomaterials like CNTs or fullerenes. In particular, graphene can be easily produced from bulk graphite *via* exfoliation.[126,481–483] Moreover, the particular strength of graphene, the quality of its crystal structure, and its band structure and high conductivity allow the preparation of devices with extremely low noise levels and relatively low 1/*f* noise.[448]

4.1.1 Electrochemical (bio)molecular sensors. Electrochemical sensing is an effective and powerful technique used for qualitative and quantitative determination of bioactive and functional molecules.[427,465,475] Numerous advantages including low limits of detection, high selectivity and detection in the presence of interferents made graphene-based materials appealing for fabrication of electrochemical sensors. Those properties determine graphene-based electrochemical sensors as the most explored group of sensors in recent years. The most common approach relies on the use of electrodes based on graphene[442,477] or modified graphene-based nanostructures.[441,474,478] Fast electron transfer and effective electrocatalytic activity of graphene allow the effective detection of target molecules during oxidation.[484] Among its numerous physico-chemical properties, graphene has a wide electrochemical potential window (∼2.5 V in phosphate buffer),[72] lower charge transfer resistance (compared with a glass electrode)[72] and well characterized redox potentials against most common redox couples.[485] Keeley *et al.* developed an electrochemical sensor based on graphene exfoliated in DMF for ascorbic acid (AA) detection.[477] The electrode was prepared by drop-casting a centrifuged graphene supernatant solution onto a pyrolysed photoresist film. Cyclic voltammetry investigation revealed a wide linearity range and a limit of detection of up to 0.12 mM. Another effective electrode was prepared by mixing platinum nanoparticles and graphene nanosheets.[478] Such a hybrid system displayed the capacity to detect traces of trinitrotoluene (TNT), a typical explosive compound, with detection limits as low as 0.3 ppm and satisfactory reproducibility. Luo *et al.* presented an electrochemical glucose sensor based on Cu decorated graphene sheets.[421] The as prepared electrode exhibited a low detection limit of 0.5 μM and very fast response (<2 s) with its response linearity up to 4.5 mM. Additionally, a synergistic effect of copper and graphene on glucose oxidation was observed.

As mentioned above, the majority of graphene-based sensors rely on the chemical modification of GO, which exhibits numerous oxygen-rich functional groups that can interact *via* dipole–dipole or strong electrostatic interactions with (charged) molecules, or it can be covalently functionalized with functional molecules, enhancing the occurrence of adsorption events. In particular, covalent grafting of organic molecules onto GO offers the flexibility for various functionalizations to enhance the sensor performance. Moreover, the combination of its abundant structural defects and chemical groups facilitates the charge transfer and thus ensure high electrochemical activity. Noteworthily, the chemical and electrical properties of rGO are highly tuneable and can be engineered through control of the reduction process.

Zhou *et al.* exploited a chemically reduced GO modified glassy carbon electrode (CR-GO/GC) for electrochemical sensing of free purine and pyrimidine acids and several other biologically active molecules.[72] It was demonstrated that the CR-GO/GC electrode provides greater electrocatalytic activity to guanine (G), adenine (A), thymine (T) and cytosine (C) oxidation than commonly used glassy carbon (GC) and graphite/glassy carbon graphite/GC electrodes (Fig. 21). Moreover, presented electrode exhibited enhanced analytical performance toward detection of glucose, ethanol, dopamine and other biological molecules. In particular, while the amperometric measurement of reduced nicotinamide adenine dinucleotide (NADH) exhibited a faster response time, a wider linear range (40–800 μM), a lower detection limit (10.00 μM) and higher sensitivity (2.68 μA mM^{-1} cm^{-1}). Gao and co-workers carried out the chemical reduction of GO, obtaining a hydroxyapatite/rGO composite, used as an effective electrochemical sensor of hydrazine.[472] The composite dispersed in 1% acetic acid was applied on a GCE and dried, resulting in a high-performance electrode with outstanding performance of the electrocatalytic oxidation of N_2H_4. The as-prepared electrode exhibited a synergistic effect of the components during detection of hydrazine, which is greater than those of the electrodes fabricated with rGO and hydroxyapatite separately. Wang and co-workers devised a facile approach relying on the efficient preparation of nitrogen-doped graphene *via* nitrogen plasma treatment of chemically synthesized graphene, which exhibits excellent electrocatalytic activity toward hydrogen peroxide reduction.[415] Detection of H_2O_2 as one of the products of catalytic glucose oxidation can be applied for selective and sensitive glucose determination during enzymatic processes. Noteworthily, a N-doped graphene electrode exhibited high concentration-dependent response and was able to detect up to 0.01 mM glucose in the presence of interferents. N-Doped electrodes can also find their use in detection of important biomolecules such as ascorbic acid (AA), dopamine (DA) and uric acid (UA).[413] Efficient oxidation and large peak separation provide simultaneous determination of those three biomolecules with detection limits up to 2.2×10^{-6}, 2.5×10^{-7} and 4.5×10^{-8} M for AA, DA and UA, respectively. Furthermore, a differential pulse voltammetry (DPV) experiment revealed that the electrochemical response of target biomolecules increases linearly with increase of molecule concentration.

4.1.2 Field-effect transistors for (bio)molecular sensors. Due to their high selectivity, fast response and excellent limit of detection, graphene-based FET-based sensors became very popular for label-free ultrasensitive biomolecule sensing. By and large, graphene-based materials are used as conducting components in the channel between drain and source electrodes, and subsequently a gate potential is applied.[446] Two different approaches are being pursued for the construction of FET sensors, *i.e.*, back gating (usually a Si/SiO_2 thin layer)[445,446] or top gating (an electrical double layer in electrolyte)[449,465] also known as solution gated graphene transistors (SGGTs). Both methods are schematically presented in Fig. 22. In general, charged molecules can induce an effective gating field, which influences the conductance of the channel by balancing the charge transfer and gating effect. The change in current as measured allows the analyte determination.

Huang and co-workers presented a CVD-grown graphene FET sensor functionalized with specific redox mediators for glucose and glutamate detection.[445] Glucose sensing is usually based on an enzymatic reaction catalysed by glucose oxidase. Since the products of the oxidation process are H_2O_2 and gluconic acid, direct measurement of H_2O_2 is useful for glucose detection. The detection limits were found to be 0.1 mM and 5 μM for glucose and glutamate, respectively. Another CVD-grown glucose sensor was assembled by Kwak *et al.*[446] A solution-gated field-effect transistor (SGFET) was constructed utilizing a graphene channel modulated by the gate potential applied from the top gate electrode and transmitted through the solution. Such a SGFET sensor was exploited to detect glucose in the 3.3–10.9 mM range. Moreover, it provided high resolution and continuous real-time monitoring. To reach the largest sensing response, graphene transistors are operated at the point of maximum transconductance, which leads to large noise that influences the device sensitivity. To avoid such a phenomenon, Fu and co-workers exploited the sensing properties of single layered graphene near its neutrality point.[447] This approach led to a significant decrease of the signal-to-noise ratio, thereby making it possible to observe positive signals coming from single stranded DNA (ssDNA) at levels of picomolar concentrations (pM). Moreover, to target specific hybridization corresponding to HIV-virus related ssDNA, functionalization of a GFET surface with pyrene-linked peptide nucleic acid (pPNA) was performed. Noteworthily, the 1/*f* noise in graphene based FET sensors was found to vary with the number of graphene layers; therefore subsequent optimization of this class of sensors is anticipated.[448] Another approach in which hydrazine-reduced GO was used to fabricate a FET sensor on a SiO_2/Si substrate was proposed by Cai *et al.*[449] A DNA sensor was prepared by drop-casting a rGO suspension onto a sensing channel as the conducting material. 1-Pyrenebutanoic acid succinimidyl ester (PASE) used as a molecular linker was fixed on the graphene surface *via* π–π stacking interactions and peptide nucleic acid (PNA) molecules were covalently anchored. Subsequently, a complementary DNA was applied onto the device and specific hybridization caused a shift of the I_{ds}–V_g curves and allowed the measurement. The detection limit was estimated to be as low as 100 fM.

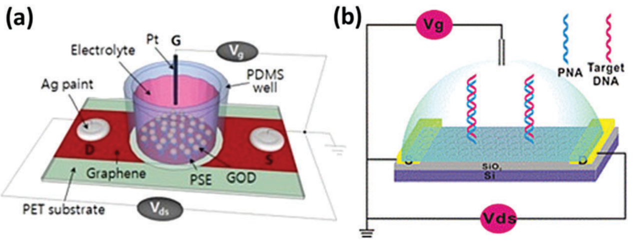

Fig. 22 Schematic representation: (a) graphene top gate FET sensor. Adopted from ref. 446 with permission of the American Chemical Society. (b) Graphene oxide back-gate FET sensor. Adapted from ref. 449 with permission of Elsevier.

4.1.3 (Bio)molecular fluorescence sensors. The use of fluorescence as the readout in the detection of chemical species and biomolecules holds potential for low-cost, effective and highly sensitive device applications. Graphene and graphene oxide are known to be excellent quenching materials; therefore, graphene-based materials became suitable for sensing *via* influence on fluorescence properties.[469] One of the approaches is based on FRET and is useful for quantitative determination of target molecules. Typically, this kind of setup consists of a donor, an acceptor and a bridge. The acceptor (such as GO) can effectively quench the fluorescence of the donor. The addition of specific molecules or surface modification may cause change in the fluorescence intensity and can be utilized as a sensor assuming that the phenomenon is correlated with concentration (Fig. 23a and b).[450,452]

Dong and co-workers reported on the FRET from quantum dots (QDs) to GO.[451] In particular, the authors demonstrated that QDs substituted with molecular beacon (MB) as a recognition unit towards the targeted molecule can strongly interact with the GO surface, to allow the design of novel sensitive and selective platforms for fluorescence-quenching detection of DNA. In general, GO's quenching properties were used to decrease the fluorescence intensity in the presence of QDs – an effective donor supplied with MB that provides efficient energy transfer to GO (Fig. 23c). Fluorescent graphene quantum dots (GQDs) were also applied for detection of aromatic nitro compounds (*e.g.* TNT)

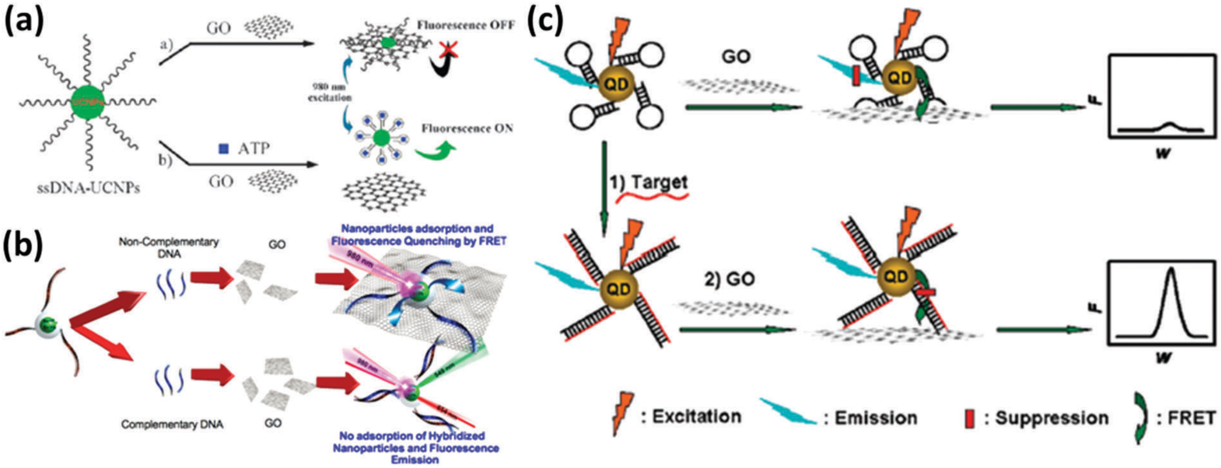

Fig. 23 Schematic representations of different FRET mechanisms used in biomolecule sensing. (a) Schematic representation of the upconversion fluorescence resonance energy transfer used for ATP sensing. Adapted from ref. 452 with permission of the Royal Society of Chemistry. (b) FRET mechanism based on quenching ability of GO applied for complementary DNA detection. Adapted from ref. 450 with permission of American Chemical Society. (c) DNA sensing. Molecular beacon decorated QDs quenched by a GO platform, in the presence of complementary DNA, emission is significantly enhanced. Adapted from ref. 451 with permission of American Chemical Society.

working as quenchers over a wide range, sustaining the linear correlation.[453] Another DNA sensor using FRET between upconversion nanoparticles and GO was reported by Alonso-Cristobal *et al.*[450] The correlation between the concentration of ssDNA (Fig. 24) and luminescence intensity was presented. Its effective detection limit was experimentally shown to be in the picomolar range.

A GO-based platform for DNA and protein sensing reported by Lu and co-workers includes ssDNA supplied with fluorescent organic dye that strongly adsorbs on the GO's surface simultaneously, entailing high quenching efficiency.[455] The addition of a complementary ssDNA sequence causes an efficient fluorescence increase and may be used to determine the desired nucleotide sequences. Experiments also proved the dependence on the concentrations of different proteins. The results revealed that the presence of human thrombin might be determined without the interference of the other proteins.

4.1.4 (Bio)molecular sensing *via* surface enhanced Raman scattering.

Surface enhanced Raman scattering represents the most powerful analytical technique for sensitive chemical sensing, which became an attractive solution for detection of aromatic compounds. Typically, weak Raman signals are intensified through enhancement of the local electromagnetic field, occurring with the charge transfer between adsorbed molecules and the metal surface. Consequently, to observe a SERS signal, molecules must be adsorbed or be placed close to a metal surface. The most common approach is based on modification of a graphene-based material surface with metallic nanoparticles (NPs).[411,459] The optimum size, shape, charge and surface chemistry of NPs are being taken into account to project non-toxic and effective sensors.[104]

Lu *et al.* proposed the use of Ag and Au NP-decorated single-layer rGO films anchored on Si surfaces to detect popular organic dyes rhodamine 6G (R6G), methyl violet (MV), rhodamine B (RB)

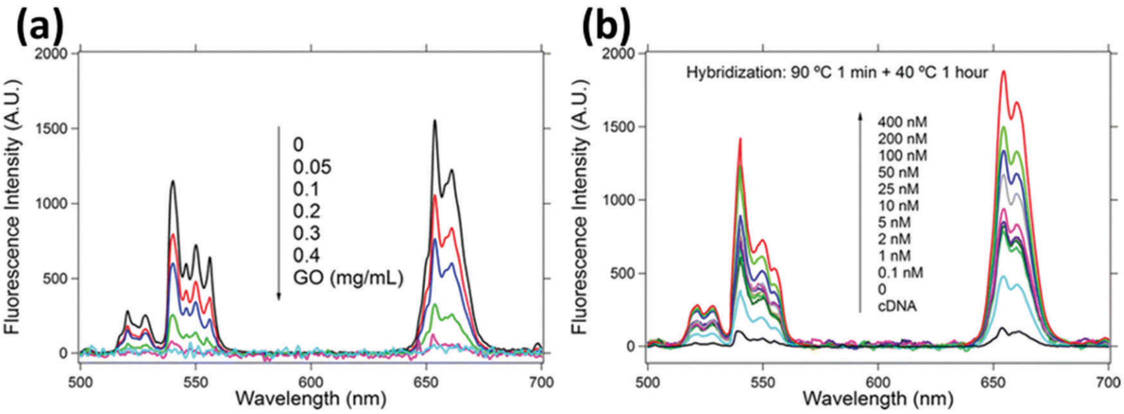

Fig. 24 Up-conversion fluorescence spectra of the UCNPs@SiO_2–ssDNA nanoparticles (0.4 mg mL^{-1}) (a) in the presence of different concentrations of GO, and (b) in the presence of different concentrations of complementary ssDNA and 0.3 mg mL^{-1} of GO. Adapted from ref. 450 with permission of American Chemical Society.

and methylene blue (MB) at nanomolar concentrations.[411] Such molecules easily adsorb on the rGO surface, while Ag and Au nanoparticles provide dramatic enhancement in the Raman intensities of the sample. Moreover, a correlation between NP size and observed signals has been monitored, and it could be controlled through the reaction time. Another modification with Ag NPs for ultrasensitive detection of aromatic molecules was demonstrated by Liu and co-workers.[458] Additional enhancement of the Raman signals was ensured by GO treated with 3-mercaptopropyltrimethoxysilane (MPTMS), further functionalized with Ag-NPs. An effective detection of differently charged molecules was successfully characterized and presented. In particular, experiments with PPh_3 used as the target molecule exhibited limits of detection as low as 10^{-9} M.

Graphene grown on copper foil and Ag NPs anchored on a Si substrate can also be used to prepare a SERS active substrate for detection of TNT by alkaline hydrolysis.[459] High pH values provide efficient hydrolysis of TNT and increase the intensities of Raman spectral signals. Extremely high limits of detection (up to 6.6×10^{-10} M) and an excellent anti-interference ability confirms the perspective potential of SERS sensors. Shanta and Cheng prepared hydrazine reduced GO combined with silver nanoprisms and utilized such a hybrid system for trace detection of tetrachlorobiphenyls (PCBs).[460] The as prepared chip successfully allowed multiplex measurements of several environmentally important aromatic compounds. The proposed SERS sensor provided a low limit of detection (up to 100 nM) and simultaneous analysis of multiple isomers.

Values such as the limit of detection and linearity range for detection of various biomolecules are summarized in Table 9.

4.2 (Bio)molecular sensing with transition metal dichalcogenides

TMDs have been recently used to develop a wide range of chemical sensors including electrochemical,[132,134,486–500] fluorescent[99,133,501–503] and field-effect transistor sensors.[504–506] MoS_2 and its analogues like tungsten disulphide (WS_2), tantalum disulphide (TaS_2), tungsten diselenide (WSe_2) and ternary chalcogenides have been widely investigated with promising results in chemical sensing applications.[132,500–502,507]

Among various TMDs, MoS_2 is the most studied material. The interaction of the 2D lattice of MoS_2 with charged molecules efficiently influences its electrochemical properties, which can be measured directly with voltammetric measurements.[490,492,493] Furthermore, MoS_2 nanosheets used for electrode preparation exhibit significant electrocatalytic activity toward a range of important analytes, including glucose,[493,497] H_2O_2,[488] dopamine,[494,495,508] ascorbic acid,[508] tryptophan[509] and DNA.[489,503,506] Another advantage of MoS_2 is its feasibility to form composites with a wide range of properties, extending its application potential.[509,510] Remarkably, the presence of noble metal nanostructures effectively enhances electrochemical detection of target molecules. Mixing MoS_2 with NPs (*e.g.* Pt, Ag, Au) improves electron transfer and allows achieving lower limits of analyte detection.[495,508,509] MoS_2 is also an excellent quenching material, and thus can be applied for highly

Table 9 Comparison of the sensing properties of different graphene-based sensors

Material	Type of sensor	Analyte	Limit of detection	Linearity range	Ref.
DMF-exfoliated graphene	Electrochemical	AA	0.12 mM	0.4–6.0 mM	477
Pt-NPs–graphene		H_2O_2	80 nM	1–500 μM	478
		TNT	0.3 ppm	0.5–40 ppm	
Cu-NPs–graphene		Glucose	0.5 μM	0–4.5 mM	421
rGO		H_2O_2	0.05 μM	0.05–1500 μM	72
		NADH	10 μM	40–800 μM	
Hydroxyapatite-rGO		NH_2NH_2	0.43 μM	2.5 μM–1.16 mM	472
N-Doped graphene		Glucose	0.01 mM	0.1–1.1 mM	415
N-Doped graphene		AA	2.2 μM	5.0–1300 μM	413
		DA	0.25 μM	0.5–170 μM	
		UA	4.5×10^{-8} M	0.1–20 μM	
CVD-grown graphene	FET	Glucose	0.1 mM	—	445
		Glutamate	5 μM	5–1200 μM	
CVD-grown graphene		Glucose	—	3.3–10.9 mM	446
CVD-grown graphene		DNA	2 pm	—	447
rGO		DNA	100 fM	10 fM–1 nM	449
QDs–GO	Fluorescent	DNA	12 nM	50–1500 nM	451
Graphene QDs		TNT	2.2 μM	4.95×10^{-4}–1.82×10^{-1} g L^{-1}	453
NPs–GO		DNA	5 pm	—	450
Au/Ag-NPs–rGO	SERS	R6G MV RB MB	nm	—	411
Ag NPs–GO		PPh_3	1 nM	5×10^{-6}–1×10^{-9} M	458
Ag NPs–graphene		TNT	0.66 nM	1–100 nM	459
rGO–NP		R6G	100 pM	0–1000 nM	460
		PCB	100 nM	100 μM–100 nM	

List of abbreviations. DMF: dimethylformamide, AA: ascorbic acid, NPs: nanoparticles, TNT: 2,4,6-trinitrotoluene, NADH: β-nicotinamide adenine dinucleotide, NH_2NH_2: hydrazine, DA: dopamine, UA: uric acid, QDs: quantum dots, SERS: surface enhanced Raman scattering, R6G: rhodamine 6G, MV: methyl violet, RB: rhodamine B, MB: methylene blue, PPh_3: triphenylphosphine, PCB: 2,2′,3,3′-tetrachlorobiphenyl.

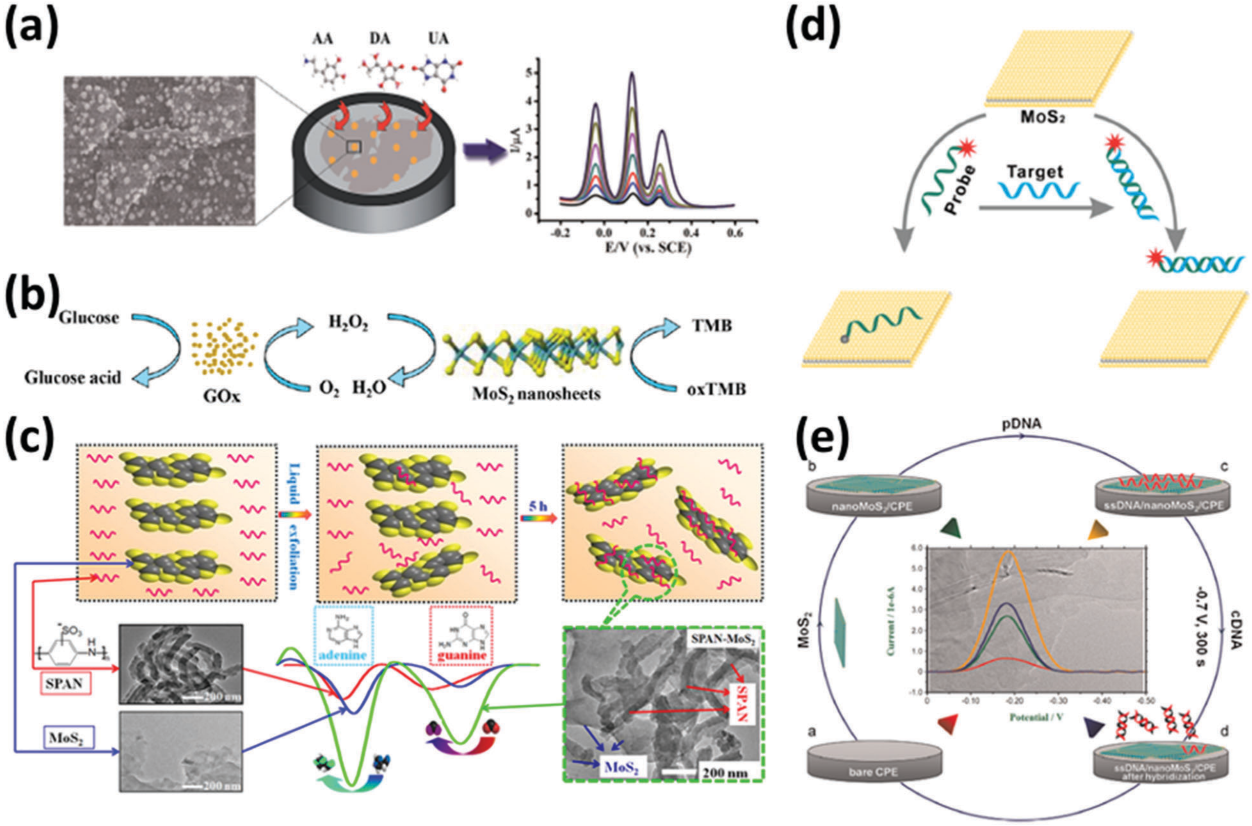

Fig. 25 Representation of different mechanisms used for chemical detection utilizing MoS_2-based materials. (a) Electrochemical sensing of ascorbic acid (AA), dopamine (DA) and uric acid (UA) with gold nanoparticle–MoS_2 nanosheets. Reproduced with permission.[508] Copyright 2014, Royal Society of Chemistry. (b) Sketch of catalytic reactions while colorimetric detection of glucose. Adapted from ref. 499 with permission of the Royal Society of Chemistry. (c) SPAN-MoS_2 for electrochemical detection of adenine and guanine. Adapted from ref. 134 with permission of the American Chemical Society. (d) Fluorescence detection of complementary ssDNA. Adapted from ref. 99 with permission of the American Chemical Society. (e) Label-free electrochemical sensing of DNA. Adapted from ref. 489 with permission of Elsevier.

sensitive detection of biomolecules *via* a fluorescence phenomenon.[99,511] Moreover, MoS_2 shows high affinity toward ssDNA, which is supported by van der Waals interactions, while double stranded DNA (dsDNA) formed in the presence of a complementary sequence hardly interacts with its two-dimensional surface. Different mechanisms of molecular detection utilizing TMD based materials are presented in Fig. 25.

Wu and co-workers presented the controllable lithiation process of MoS_2 and subsequent liquid-phase exfoliation of the intercalated structure in water or ethanol. An electrochemical study of the as-prepared MoS_2 nanosheets revealed a reduction peak in the CV in NaCl aqueous solution. The reduced MoS_2 displayed good conductivity and a fast electron transfer rate in the most common redox systems applicable in electrochemical sensing of glucose and dopamine (DA) in the presence of ascorbic acid (AA) and uric acid (UA).[486] A GCE was covered with MoS_2 using 3-aminopropyltriethoxysilane (APTES) as the linking molecule. The electrode provided good peak separation and allowed to detect dopamine with linearity in the 1–50 μM range in the presence of such interferents as AA and UA. Additional functionalization of the electrode with glucose oxidase enables effective glucose detection.

Another approach for molecular detection was introduced by Huang *et al.*[497] MoS_2 nanosheets obtained *via* liquid-phase exfoliation in ethanol/water mixed with Ni NPs were drop-cast onto a GCE and Nafion copolymer. The as-prepared sensor exhibited amperometric response toward glucose with a detection limit as low as 0.31 μM. Such a GCE/Ni–MoS_2/Nafion electrode allowed nonenzymatic detection of glucose with good reproducibility and long-term storage stability. The simultaneous detection of DA, AA and UA investigated by Sun *et al.* using a MoS_2–Au NP decorated electrode to achieve ultrasensitive determination of the aforementioned biologically important molecules.[508] The joint effect of a wide linearity range and effective electrical response yielded a sensing ability with detection limits as low as 100 μM, 0.05 μM and 10 μM for AA, DA and UA, respectively. Zhu and co-workers showed the fluorescence quenching ability of MoS_2.[99] Nanosheets obtained through exfoliation of bulk MoS_2 using the electrochemical lithium-intercalation method were used as nanoprobes for adenosine. MoS_2 supplied with probe molecules exhibits high fluorescence quenching efficiency (up to 98% compared with probe molecule intensity). Presence of adenosine restores fluorescence properties of nanoprobes and can be used for detection up to 5 μM of analyte. Another MoS_2 fluorescent sensor for DNA detection was proposed by Huang *et al.*[503] The nanosheets were prepared using a solution exfoliation method.

The authors presented selective target DNA recognition *via* hybridization chain reactions (HCRs) with a stunning detection limit of 15 pM. Another example of using adsorption of dye-labelled ssDNA on a MoS_2 surface was presented by Huang *et al*. Chemically exfoliated MoS_2 was utilized as a biosensing platform for complementary DNA and allowed detection up to 500 pM.[512] Shan *et al.* exploited a MoS_2-based FET for glucose detection.[513] The device was fabricated on a Si/SiO_2 substrate with Au/Ni drain electrodes. The sensor exhibited a very fast response time (<1 s) and linearity in the 300 nM–30 mM range, which corresponds to the average glucose concentration present in the blood and therefore constitutes a potential candidate for real-time detection of glucose concentration in human blood.

Inspired by the unique device properties offered by MoS_2, other TMDs (including WS_2 TaS_2, Ta_2NiS_5) have been the subject of further studies for sensing applications. The group of layered TMCs, including the chalcogenides with well-defined crystal structures, has been widely explored.[502,514] Since MoS_2 is known for its quenching properties, the entire group of TMDs is being considered as an effective platform for fluorescence sensing of biomolecules.[501,507]

Zhang *et al.* used single-layer TMD nanosheets as fluorescent sensors for DNA detection.[501] To investigate the quenching ability of TiS_2 and TaS_2, the 6-carboxyfluorescein-labeled ssDNA probe and target DNA molecules were used. In both cases the dichalcogenide's fluorescence intensity was effectively quenched. TiS_2 and TaS_2 exhibited fast detection of complementary DNA with low limits of detection of 0.2 nM and 0.05 nM, respectively. Noteworthily, a TaS_2-based nanosensor was found to be even more sensitive than MoS_2 with a detection limit of 0.1 nM. Another fluorescence sensing platform based on WS_2 for T4-polynucleotide kinase and its inhibitors was introduced by Ge and co-workers.[132] dsDNA does not exhibit strong adsorption on WS_2 sheets; yet when phosphorylated and degraded, the ssDNA binds to nanosheets as evidenced by the occurrence of fluorescence quenching. Linearity, a low limit of detection and a low signal-to-background ratio make this material promising for application in monitoring biological processes. Huang *et al.* developed WS_2 ink by sonication-assisted liquid exfoliation in water supported by Au nanoparticles for detection of 17β-estradiol.[496] An electrode was prepared by covering a GCE with WS_2, then Au NPs were anchored and the ssDNA aptamer was applied for selective detection of target molecules. The as prepared electrode allowed determining 17β-estradiol at a concentration as low as 2 pM. Moreover, it was proved that only target molecules may cause such obvious current changes at concentrations in the range of 10^{-10} M. Tan and co-workers prepared single-layer ternary chalcogenides for fluorescence sensing of DNA.[502] Microsized crystalline flakes of Ta_2NiS_5 were obtained *via* a chemical vapour transport technique from their elementary powders. Then high yield exfoliation was performed to produce a single-layered compound. Probe DNA was supplied with Texas red as fluorescent reporter that can be effetely quenched in the presence of TMDCs. Addition of complementary ssDNA results in fluorescence recovery and can be used for target DNA detection. The fluorescence could be recovered when the target ssDNA was added to form dsDNA. The fabricated sensor exhibited high sensitivity (up to 50 pM) and afforded a detection time of 10 min. Ta_2NiS_5 was also used as a "Capture–Release" nanosensor for detection of biological species (Fig. 26).

4.3 (Bio)molecular sensing with TMD–graphene hybrid materials

Both TMDs and graphene exhibit a range of physico-chemical properties suitable for various electronic and sensing applications. In particular, further modifications of MoS_2 and generation of hybrid materials might be used to generate composites with desired properties. The synergistic effects on the electrochemical performance of carbon-based materials with metal or metal oxides have been previously reported,[515] thus suggesting the combinations of MoS_2 with graphene-like structures as excellent candidates for a new class of electrochemical sensors. Electrodes made of TMC–graphene composites exhibit significant enhancement of electron transfer conductivity.[516–518]

Huang *et al.* reported a MoS_2–graphene composite prepared *via* a modified L-cysteine-assisted solution-phase method cast on a GCE to assemble an electrode.[511] The composite displayed a wide electrochemical potential window (~2.9 V in phosphate buffer), which is comparable to those of graphene-based electrodes. The as-prepared electrode was utilized for voltammetric determination of acetaminophen, exhibiting linear response in the 1–100 μM range. Moreover, the hybrid material showed good interference resistance: in the presence of other electrochemically active molecules the value of the oxidation peak current was sustained.

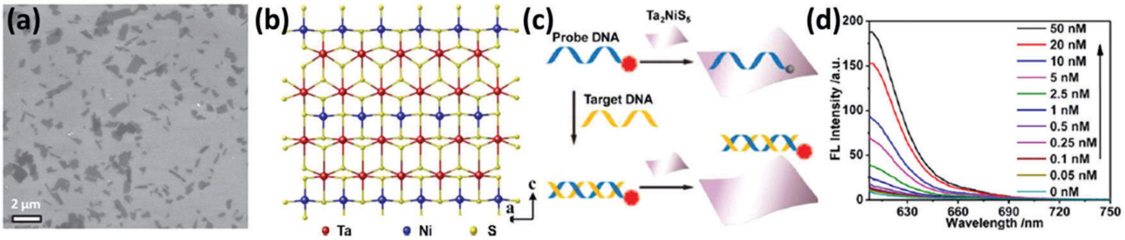

Fig. 26 (a) Scanning electron microscopy (SEM) image of Ta_2NiS_5 nanosheets. (b) Crystal structure of Ta_2NiS_5 along the *b*-axis. (c) Schematic representation of the quenching ability of Ta_2NiS_5 applied for ssDNA detection. (d) Fluorescence detection of different concentrations of target molecules in the presence of probe ssDNA. Adapted from ref. 502 with permission of American Chemical Society.

Table 10 Comparison of the sensing properties of different transition metal chalcogenide based sensors

Material	Type of sensor	Analyte	Limit of detection	Linearity range	Ref.
MoS_2	Electrochemical	H_2O_2	2.5 nM	0.1–100 μM	488
		DNA	0.019 fM	0.1–1 × 10^5 nM	489
	Fluorescent	DNA	15 pM	0–200 pM	503
		DNA	500 pM	0–50 nM	512
	FET	Glucose	300 nM	300 nM–30 mM	513
MoS_2–Pt NPs	Electrochemical	DA	0.17 μM	0.5–150 μM	495
		AA	0.98 μM	5–1000 μM	
		H_2O_2	1.0 μM	4.0–48 500 μM	521
MoS_2–NiNPs		Glucose	0.31 μM	0–4 mM	497
MoS_2–Ag/chitosan		Tryptophan	0.05 μM	0.5–120 μM	509
MoS_2–Au NPs		AA	100 μM	1–70 mM	508
		DA	0.05 μM	0.05–4 × 10^4 μM	
		UA	10 μM	10–10^3 μM	
		DA	80 nM	0.1–200 μM	494
		Glucose	2.8 μM	10–300 μM	493
MoS_2–PANI		Adenine	3 nM	0.05–100 μM	134
		Guanine	5 nM	0.05–100 μM	
		Chloramphenicol	65 nM	0.1–1000 μM	498
WS_2		Glucose	2.9 μM	5–300 μM	500
WS_2–Au NPs		17β-Estradiol	1 pM	0.01–10 nM	496
WS_2–acetylene black		DNA	0.12 fM	0.001–100 pM	522
TaS_2	Fluorescent	DNA	0.05 nM	0–5 nM	501
$TaNiS_5$		DNA	50 pM	0–5 nM	502
MoS_2–graphene	Electrochemical	Acetaminophen	20 nM	0.1–100 μM	511
		Honokiol	0.62 nM	1.0 nM–2.5 μM	519
		H_2O_2	1.25 μM	6.25–225 μM	523
MoS_2–rGO		DA	0.94 μM	1.5–100 μM	520
HPR-MoS_2–graphene		H_2O_2	0.049 μM	0.2 μM–1.1 mM	510

List of abbreviations. NPs: nanoparticles, DA: dopamine, AA: ascorbic acid, UA: uric acid, PANI: polyaniline, TaS_2: tantalum(IV) sulfide, $TaNiS_5$: tantalum nickel sulfide, HPR: horseradish peroxidase.

Another electrochemical sensor composed of a MoS_2–graphene nanohybrid film was developed by Zhao and co-workers.[519] The GCE was embedded in a MoS_2–graphene nanohybrid, resulting in significantly enhanced sensitivity towards honokiol – known in view of its antitumor and antibacterial activity used in western medicine. The electrode revealed high selectivity and stability with a spectacular limit of detection corresponding to 6.2×10^{-10} M. Pramoda *et al.* demonstrated the electrocatalytic activity of MoS_2–rGO/GCE against dopamine and proved its superior nature over a bare rGO-modified electrode.[520] Effective detection of DA in the presence of interferents was established at a level of 0.55 μM.

The most important parameters, including the type of sensor, limit of detection and linearity range, of TMD-based sensors are presented in Table 10.

4.4 (Bio)molecular sensing with other 2DMs

Hexagonal BN is known to be the most stable allotrope among the BN crystalline forms. A few electron transfer reactions toward biomolecule oxidation for commonly used electrodes immobilized with boron nitride have been reported and the results are comparable to those of other 2DM based sensors.[524,525] However, SERS seems to be a more popular technique for the development of hBN-based chemical sensors. Noteworthily, the boron–nitrogen bonds of hBN can be used for further modifications or to facilitate the detection of organic molecules *via* the polarization of B–N bonds.[168] Moreover, the modification of the BN surface, *e.g.* introducing noble metal NPs, allows the enhancement in the Raman signal, thus rendering such material a practical support for SERS. Moreover, BN exhibits a high fluorescence quenching ability and different affinities toward single stranded DNA and double stranded DNA, allowing sensitive detection of complementary DNA fragments.[526]

Khan *et al.* reported the electrocatalytic behaviour of hBN toward the detection of dopamine.[524] The electrode was prepared by drop-casting an ethanolic solution of crystalline hexagonal boron nitride on a screen-printed graphitic electrode (SPE) and found to determine dopamine in the presence of common interference molecules ascorbic acid (AA) and uric acid (UA). The obtained sensor exhibited a limit of detection of 0.65 μM, which is comparable to those of other 2D-based dopamine sensors. Zhan and co-workers exploited the quenching ability of boron nitride for DNA detection.[526] The experiment revealed an effective fluorescence decrease of labelled ss-DNA in the presence of boron nitride nanosheets (BNNS), reaching up to 85%. This sensor exhibited a low limit of detection toward target DNA molecules (104 pM) and linearity in the 0.6–20 nM range. Lin *et al.* assembled a SERS-based sensor for rhodamine 6G (R6G) detection with high reusability.[168] Silver-decorated boron nitride nanosheets, prepared *via* reduction of Ag salt in the presence of BNNS, were deposited on quartz substrates using substrate transfer techniques, resulting in a thermal-oxidation resistant material, which facilitates the removal of any residual analyte. Another SERS sensor for aromatic molecules was prepared by introduction of Au NPs onto BN nanosheets obtained using the Scotch tape technique. Cai *et al.* proposed substrates tested toward R6G detection, with signals greatly enhanced in the presence of 10^{-6} M solutions of analyte.[527] The fabricated sensor also allows the effective removal of detected molecules by thermal treatment.

MXene-based sensors exhibit good electrochemical activity toward a range of biologically important molecules like glucose,[528] H_2O_2[178,529] and nitrites.[179] Wang and co-workers presented a nanocomposite of TiO_2 modified with Ti_3C_2MXene encapsulating haemoglobin with effective activity toward H_2O_2 detection.[529] TiO_2–Ti_3C_2 was synthesized in an autoclave, then a mixture consisting of a suspension of the nanocomposite, haemoglobin in phosphate buffered saline (PBS) and Nafion were applied on a GCE by a simple casting method. The obtained MXene enzyme-based sensor exhibited efficient electrochemical performance, allowing determination of hydrogen peroxide with a low limit of detection of 14 nM and a wide linear range of 0.1–380 μM. Another Ti_3C_2-based electrochemical sensor supplied with haemoglobin to provide direct electron transfer was realized by Liu *et al.*[179] This sensor, due to its large surface area and high conductivity, displayed good electrochemical performance, allowing detection of sodium nitrite ($NaNO_2$) with a linear range of 0.5–11 800 μM and a limit of detection equal to 0.12 μM. Rakhi and co-workers used the synergistic effect of Au NPs and MXenes on glucose oxidation.[528] Two-dimensional titanium carbide was obtained *via* exfoliation of Ti_3AlC_2. Further sonication of MXenes with Au NPs resulted in Au/MXene composites used to prepare electrodes together with glucose oxidase (GOx) by casting the obtained mixtures onto GCEs. These sensors displayed a detection limit of glucose up to 5.9 μM and amperometric response with linearity in the 0.1 mM to 18 mM range.

Two-dimensional nanosheets of black phosphorus have gained attention as an analogue of other widely explored layered materials. BP exhibits impressive opto-electronic properties but it is particularly sensitive to water and oxygen; thus during the preparation of BP-based chemical sensors, particular precautions have to be taken.[530,531] Yan and co-workers proposed a nonenzymatic sensor based on solvent exfoliated BP for determination of H_2O_2.[530] Few-layered black phosphorus, produced *via* a supercritical carbon dioxide-assisted synthesis, was used for electrode preparation by casting an ethanolic solution onto a GCE. The electrochemical impedance was investigated in N_2-saturated phosphate buffered saline (PBS) exhibiting linearity in the 1×10^{-7} M to 1×10^{-5} M range with a limit of detection as low as 1×10^{-7} M. Yew *et al.* used higher affinity of BP NPs toward ssDNA and prepared a fluorescent sensor for nucleic acid detection.[531] This biosensing platform provided linearity in the 4–4000 pM range and a limit of detection equal to 5.9 pM.

The performances of hBN, MXenes and BP-based materials as (bio)molecular sensors are summarized in Table 11.

In this section we have discussed 2DMs and 2DM-based composites for the sensing of (bio)molecular species. A range of unique physico-chemical properties offered by 2DMs allows fabrication of various types of chemical sensors including fluorescent, electrochemical, FET and SERS sensors. The recent literature includes investigations of the most important biological molecules with particular attention to molecules relevant to medical sciences. Among various advantages of 2DM based sensors the extremely low limit of detection (reaching the picomolar level), ultrafast detection (<1 s) and wide linearity of response signals should be emphasized. Moreover, most of the 2DM based sensors exhibit high selectivity and allow determination of multiple target molecules even in the presence of common interferents. The possibility of further modifications of 2DMs allows achieving multicomponent systems, offering better performances in the effective determination of target analytes. Noteworthily, the spectrum of molecules detectable with presented sensors is quite narrow. Also there are a few issues that should be considered while developing new sensing materials such as stability, reusability and biocompatibility. Electrochemical sensing seems to be one of the most widespread approaches applied in chemical sensing, which affirms the superior electrical properties of graphene and TMDs. In the case of TMDs recent investigations seem to be mainly focused on MoS_2 and WS_2, while the other representatives have not gathered much attention so far. Notably, the group of novel 2DMs such as hBN, MXenes and BP holds great potential in molecular sensing. Basing on few recent reports those materials constitute promising fundaments for further investigations in terms of their sensing properties.

5 Conclusions and outlook

Alongside the numerous extraordinary physical and chemical properties exhibited by 2DMs, their high surface area-to-volume

Table 11 Comparison of the sensing properties of hBN, MXenes and BP-based chemical sensors

Material	Type of sensor	Analyte	Limit of detection	Linearity range	Ref.
hBN	Electrochemical	DA	0.65 μM	—	524
Surfactant exfoliated hBN			1.57 μM	—	525
BNNS	Fluorescent	DNA	104 pM	0.6–20 nM	526
Ag–BNNS	SERS	R6G	10 μM	—	168
Au/BN			1 μM	—	527
TiO_2–Ti_3C_2	Electrochemical	H_2O_2	14 nM	0.1–380 μM	529
Ti_3C_2		$NaNO_2$	0.12 μM	0.5–11 800 μM	179
GOx–Au–MXene		Glucose	5.9 μM	0.1–18 mM	528
BP		H_2O_2	0.1 μM	0.1–10 μM	530
BPNPs	Fluorescent	DNA	5.9 pM	4–4000 pM	531

List of abbreviations. DA: dopamine, BNNS: boron nitride nanosheets, SERS: surface enhanced Raman scattering, R6G: rhodamine 6G, GOx: glucose oxidase, BPNPs: black phosphorus nanoparticles.

ratios represent a key additional advantage for applications in sensing. The all-surface-and-volume-free character guarantees the highest sensitivity to any changes in 2DMs' environments, which is an absolute prerequisite for the development of high-performance sensing devices. However, the use of pristine, defect free sheets may result in weak and unspecific interactions with the chosen analytes. Defects hold a pivotal role in 2DMs: they allow the modulation of the (opto)electronic properties, and in particular the engineering of the band gap, which plays a crucial role in improving the sensitivity of the device. Moreover, the presence of dangling groups on the surface can promote analyte absorption, consequently yielding an improvement in the sensing performances. Furthermore, the presence of defects highly increases the chemical reactivity of 2DMs, enabling further chemical functionalization of the reactive sites, which may result in high specificity, enhanced sensitivity and a low detection limit towards the targeted analyte. On the other hand, a lack of control during defect engineering can result in irreproducible properties of 2DMs. In particular, the increased reactivity and the presence of dangling bonds with different chemical structures on the basal plane (or edges) of the 2DM may result in an enhanced, yet, unselective binding of the analytes, ultimately leading to poor selectivity, long response or an even incomplete recovery time of the sensor.

One of the greatest challenges to be tackled in the near future is the controlled introduction of *ad hoc* defects in 2DMs with a precise spatial resolution and concentration. Ideally, the chemical composition of the defects has to be complemented by a chemical functionalization of the reactive sites with the receptor of the analyte of choice. Such a strategy needs to be pursued by mastering the principles of molecular recognitions, *e.g. via* tailoring of supramolecular interactions, which may result not only in ultrasensitive 2DMs but also in superior selectivity and response times – making the actual step towards industrial products. Additionally, chemical programmability, through the generation of multicomponent assemblies based on 2DMs, may enable the future development of multianalyte sensing. Although optical sensors based on the change in the photoluminescence properties of 2DMs upon interaction with analytes have been widely and successfully employed for both metals and biologically relevant molecules, electrochemical sensors seem to be the most promising since they provide a direct electrical response without the need for employing a transducer. By taking advantage not only of the superior electrical properties of graphene and other 2DMs, but also of their excellent mechanical properties such as robustness and flexibility, 2DM based sensors can be supported on flexible foils, for smart wearable technologies for monitoring the human/environment interface. Interestingly, the recent demonstration of the compatibility of 2DMs with ''on-the-skin'' applications opens the door towards their use for the detection of clinically relevant biomarkers. Such 2DM-based tattoos may therefore find application as dry on-the-skin sensors characterized by low susceptibility to motion artefacts, which is one of the biggest drawbacks of conventional dry sensors and electrodes for point-of-care health monitoring.

Conflicts of interest

There are no conflicts to declare.

Acknowledgements

This work was supported by the European Commission through the Graphene Flagship Core 1 project (GA-696656) and the Polish National Science Centre (Grant No. 2015/18/E/ST5/00188). We also are thankful for the support of the Agence Nationale de la Recherche through the LabEx project Chemistry of Complex Systems (ANR-10-LABX-0026_CSC), and the International Center for Frontier Research in Chemistry (icFRC). D. P. acknowledges the support from the Embassy of France in Poland in the form of a scholarship at the Institut de Science et d'Ingénierie Supramoléculaires, University of Strasbourg.

References

1 K. S. Novoselov, A. K. Geim, S. V. Morozov, D. Jiang, M. I. Katsnelson, I. V. Grigorieva, S. V. Dubonos and A. A. Firsov, *Nature*, 2005, **438**, 197.
2 A. C. Ferrari, F. Bonaccorso, V. Fal'ko, K. S. Novoselov, S. Roche, P. Boggild, S. Borini, F. H. L. Koppens, V. Palermo, N. Pugno, J. A. Garrido, R. Sordan, A. Bianco, L. Ballerini, M. Prato, E. Lidorikis, J. Kivioja, C. Marinelli, T. Ryhanen, A. Morpurgo, J. N. Coleman, V. Nicolosi, L. Colombo, A. Fert, M. Garcia-Hernandez, A. Bachtold, G. F. Schneider, F. Guinea, C. Dekker, M. Barbone, Z. Sun, C. Galiotis, A. N. Grigorenko, G. Konstantatos, A. Kis, M. Katsnelson, L. Vandersypen, A. Loiseau, V. Morandi, D. Neumaier, E. Treossi, V. Pellegrini, M. Polini, A. Tredicucci, G. M. Williams, B. Hee Hong, J.-H. Ahn, J. Min Kim, H. Zirath, B. J. van Wees, H. van der Zant, L. Occhipinti, A. Di Matteo, I. A. Kinloch, T. Seyller, E. Quesnel, X. Feng, K. Teo, N. Rupesinghe, P. Hakonen, S. R. T. Neil, Q. Tannock, T. Lofwander and J. Kinaret, *Nanoscale*, 2015, **7**, 4598.
3 Q. H. Wang, K. Kalantar-Zadeh, A. Kis, J. N. Coleman and M. S. Strano, *Nat. Nanotechnol.*, 2012, **7**, 699.
4 M. W. Barsoum, *Prog. Solid State Chem.*, 2000, **28**, 201.
5 L. Li, Y. Yu, G. J. Ye, Q. Ge, X. Ou, H. Wu, D. Feng, X. H. Chen and Y. Zhang, *Nat. Nanotechnol.*, 2014, **9**, 372.
6 S. P. Koenig, R. A. Doganov, H. Schmidt, A. H. Castro Neto and B. Özyilmaz, *Appl. Phys. Lett.*, 2014, **104**, 103106.
7 H. Liu, A. T. Neal, Z. Zhu, Z. Luo, X. Xu, D. Tománek and P. D. Ye, *ACS Nano*, 2014, **8**, 4033.
8 A. Gupta, T. Sakthivel and S. Seal, *Prog. Mater. Sci.*, 2015, **73**, 44.
9 A. S. Mayorov, R. V. Gorbachev, S. V. Morozov, L. Britnell, R. Jalil, L. A. Ponomarenko, P. Blake, K. S. Novoselov, K. Watanabe, T. Taniguchi and A. K. Geim, *Nano Lett.*, 2011, **11**, 2396.
10 D. C. Elias, R. V. Gorbachev, A. S. Mayorov, S. V. Morozov, A. A. Zhukov, P. Blake, L. A. Ponomarenko, I. V. Grigorieva,

K. S. Novoselov, F. Guinea and A. K. Geim, *Nat. Phys.*, 2011, **7**, 701.
11 A. Kuc, N. Zibouche and T. Heine, *Phys. Rev. B: Condens. Matter Mater. Phys.*, 2011, **83**, 245213.
12 A. Splendiani, L. Sun, Y. Zhang, T. Li, J. Kim, C.-Y. Chim, G. Galli and F. Wang, *Nano Lett.*, 2010, **10**, 1271.
13 J.-S. Kim, H.-W. Yoo, H. O. Choi and H.-T. Jung, *Nano Lett.*, 2014, **14**, 5941.
14 D. J. Late, Y.-K. Huang, B. Liu, J. Acharya, S. N. Shirodkar, J. Luo, A. Yan, D. Charles, U. V. Waghmare, V. P. Dravid and C. N. R. Rao, *ACS Nano*, 2013, **7**, 4879.
15 K. Kalantar-zadeh and J. Z. Ou, *ACS Sens.*, 2016, **1**, 5.
16 Y. Song, Y. Luo, C. Zhu, H. Li, D. Du and Y. Lin, *Biosens. Bioelectron.*, 2016, **76**, 195.
17 V. Georgakilas, M. Otyepka, A. B. Bourlinos, V. Chandra, N. Kim, K. C. Kemp, P. Hobza, R. Zboril and K. S. Kim, *Chem. Rev.*, 2012, **112**, 6156.
18 B. Cai, S. Zhang, Z. Yan and H. Zeng, *ChemNanoMat*, 2015, **1**, 542.
19 E. A. Meyer, R. K. Castellano and F. Diederich, *Angew. Chem., Int. Ed.*, 2003, **42**, 1210.
20 S. K. Burley and G. A. Petsko, *FEBS Lett.*, 1986, **203**, 139.
21 P. Tarakeshwar, K. S. Kim, E. Kraka and D. Cremer, *J. Chem. Phys.*, 2001, **115**, 6018.
22 E. C. Lee, B. H. Hong, J. Y. Lee, J. C. Kim, D. Kim, Y. Kim, P. Tarakeshwar and K. S. Kim, *J. Am. Chem. Soc.*, 2005, **127**, 4530.
23 S. J. Grabowski, *J. Phys. Chem. A*, 2001, **105**, 10739.
24 P. Tarakeshwar, H. S. Choi and K. S. Kim, *J. Am. Chem. Soc.*, 2001, **123**, 3323.
25 E.-I. Kim, S. Paliwal and C. S. Wilcox, *J. Am. Chem. Soc.*, 1998, **120**, 11192.
26 K. E. Riley, M. Pitoňák, P. Jurečka and P. Hobza, *Chem. Rev.*, 2010, **110**, 5023.
27 C. A. Hunter and J. K. M. Sanders, *J. Am. Chem. Soc.*, 1990, **112**, 5525.
28 C. A. Hunter, *Chem. Soc. Rev.*, 1994, **23**, 101.
29 E. C. Lee, D. Kim, P. Jurečka, P. Tarakeshwar, P. Hobza and K. S. Kim, *J. Phys. Chem. A*, 2007, **111**, 3446.
30 I. Geronimo, E. C. Lee, N. J. Singh and K. S. Kim, *J. Chem. Theory Comput.*, 2010, **6**, 1931.
31 W. Wang and P. Hobza, *ChemPhysChem*, 2008, **9**, 1003.
32 D. A. Dougherty and D. A. Stauffer, *Science*, 1990, **250**, 1558.
33 D. Kim, S. Hu, P. Tarakeshwar, K. S. Kim and J. M. Lisy, *J. Phys. Chem. A*, 2003, **107**, 1228.
34 S. Tsuzuki, M. Yoshida, T. Uchimaru and M. Mikami, *J. Phys. Chem. A*, 2001, **105**, 769.
35 S. E. Wheeler and K. N. Houk, *J. Am. Chem. Soc.*, 2009, **131**, 3126.
36 M. A. Gebbie, W. Wei, A. M. Schrader, T. R. Cristiani, H. A. Dobbs, M. Idso, B. F. Chmelka, J. H. Waite and J. N. Israelachvili, *Nat. Chem.*, 2017, **9**, 473.
37 A. S. Mahadevi and G. N. Sastry, *Chem. Rev.*, 2013, **113**, 2100.
38 P. B. Crowley and A. Golovin, *Proteins: Struct., Funct., Bioinf.*, 2005, **59**, 231.
39 J. P. Gallivan and D. A. Dougherty, *Proc. Natl. Acad. Sci. U. S. A.*, 1999, **96**, 9459.
40 K. S. Kim, P. Tarakeshwar and J. Y. Lee, *Chem. Rev.*, 2000, **100**, 4145.
41 D. Quiñonero, C. Garau, C. Rotger, A. Frontera, P. Ballester, A. Costa and P. M. Deyà, *Angew. Chem., Int. Ed.*, 2002, **41**, 3389.
42 B. L. Schottel, H. T. Chifotides and K. R. Dunbar, *Chem. Soc. Rev.*, 2008, **37**, 68.
43 Y. S. Rosokha, S. V. Lindeman, S. V. Rosokha and J. K. Kochi, *Angew. Chem., Int. Ed.*, 2004, **43**, 4650.
44 P. De Hoog, P. Gamez, I. Mutikainen, U. Turpeinen and J. Reedijk, *Angew. Chem., Int. Ed.*, 2004, **116**, 5815.
45 R. E. Dawson, A. Hennig, D. P. Weimann, D. Emery, V. Ravikumar, J. Montenegro, T. Takeuchi, S. Gabutti, M. Mayor, J. Mareda, C. A. Schalley and S. Matile, *Nat. Chem.*, 2010, **2**, 533.
46 A. Frontera, P. Gamez, M. Mascal, T. J. Mooibroek and J. Reedijk, *Angew. Chem., Int. Ed.*, 2011, **50**, 9564.
47 B. L. Schottel, H. T. Chifotides, M. Shatruk, A. Chouai, L. M. Pérez, J. Bacsa and K. R. Dunbar, *J. Am. Chem. Soc.*, 2006, **128**, 5895.
48 H. T. Chifotides and K. R. Dunbar, *Acc. Chem. Res.*, 2013, **46**, 894.
49 C. Garau, A. Frontera, D. Quiñonero, P. Ballester, A. Costa and P. M. Deyà, *J. Phys. Chem. A*, 2004, **108**, 9423.
50 D. Kim, P. Tarakeshwar and K. S. Kim, *J. Phys. Chem. A*, 2004, **108**, 1250.
51 P. G. Moses, J. J. Mortensen, B. I. Lundqvist and J. K. Nørskov, *J. Chem. Phys.*, 2009, **130**, 104709.
52 N. Huo, S. Yang, Z. Wei, S. S. Li, J. B. Xia and J. Li, *Sci. Rep.*, 2014, **4**, 5209.
53 A. Hashimoto, K. Suenaga, A. Gloter, K. Urita and S. Iijima, *Nature*, 2004, **430**, 870.
54 W. Zhou, X. Zou, S. Najmaei, Z. Liu, Y. Shi, J. Kong, J. Lou, P. M. Ajayan, B. I. Yakobson and J.-C. Idrobo, *Nano Lett.*, 2013, **13**, 2615.
55 F. Banhart, J. Kotakoski and A. V. Krasheninnikov, *ACS Nano*, 2011, **5**, 26.
56 L. G. Cançado, A. Jorio, E. H. M. Ferreira, F. Stavale, C. A. Achete, R. B. Capaz, M. V. O. Moutinho, A. Lombardo, T. S. Kulmala and A. C. Ferrari, *Nano Lett.*, 2011, **11**, 3190.
57 S. Feng, Z. Lin, X. Gan, R. Lv and M. Terrones, *Nanoscale Horiz.*, 2017, **2**, 72.
58 A. Ambrosi and M. Pumera, *Chem. – Eur. J.*, 2010, **16**, 10946.
59 K. C. Santosh, C. L. Roberto, A. Rafik, M. W. Robert and C. Kyeongjae, *Nanotechnology*, 2014, **25**, 375703.
60 D. Liu, Y. Guo, L. Fang and J. Robertson, *Appl. Phys. Lett.*, 2013, **103**, 183113.
61 S. Tongay, J. Suh, C. Ataca, W. Fan, A. Luce, J. S. Kang, J. Liu, C. Ko, R. Raghunathanan, J. Zhou, F. Ogletree, J. Li, J. C. Grossman and J. Wu, *Sci. Rep.*, 2013, **3**, 2657.
62 H. Nan, Z. Wang, W. Wang, Z. Liang, Y. Lu, Q. Chen, D. He, P. Tan, F. Miao, X. Wang, J. Wang and Z. Ni, *ACS Nano*, 2014, **8**, 5738.

63 J. Xie, H. Zhang, S. Li, R. Wang, X. Sun, M. Zhou, J. Zhou, X. W. Lou and Y. Xie, *Adv. Mater.*, 2013, **25**, 5807.
64 L. Rodriguez-Perez, M. a. A. Herranz and N. Martin, *Chem. Commun.*, 2013, **49**, 3721.
65 G. L. C. Paulus, Q. H. Wang and M. S. Strano, *Acc. Chem. Res.*, 2013, **46**, 160.
66 S. Niyogi, E. Bekyarova, M. E. Itkis, H. Zhang, K. Shepperd, J. Hicks, M. Sprinkle, C. Berger, C. N. Lau, W. A. de Heer, E. H. Conrad and R. C. Haddon, *Nano Lett.*, 2010, **10**, 4061.
67 J. M. Englert, C. Dotzer, G. Yang, M. Schmid, C. Papp, J. M. Gottfried, H.-P. Steinrück, E. Spiecker, F. Hauke and A. Hirsch, *Nat. Chem.*, 2011, **3**, 279.
68 H. Liu, S. Ryu, Z. Chen, M. L. Steigerwald, C. Nuckolls and L. E. Brus, *J. Am. Chem. Soc.*, 2009, **131**, 17099.
69 M. Quintana, K. Spyrou, M. Grzelczak, W. R. Browne, P. Rudolf and M. Prato, *ACS Nano*, 2010, **4**, 3527.
70 D. Chen, H. Feng and J. Li, *Chem. Rev.*, 2012, **112**, 6027.
71 D. R. Dreyer, S. Park, C. W. Bielawski and R. S. Ruoff, *Chem. Soc. Rev.*, 2010, **39**, 228.
72 M. Zhou, Y. Zhai and S. Dong, *Anal. Chem.*, 2009, **81**, 5603.
73 J. T. Robinson, F. K. Perkins, E. S. Snow, Z. Wei and P. E. Sheehan, *Nano Lett.*, 2008, **8**, 3137.
74 S. Wu, Q. He, C. Tan, Y. Wang and H. Zhang, *Small*, 2013, **9**, 1160.
75 W. Yuan and G. Shi, *J. Mater. Chem. A*, 2013, **1**, 10078.
76 Q. He, S. Wu, Z. Yin and H. Zhang, *Chem. Sci.*, 2012, **3**, 1764.
77 G. Zhao, J. Li, X. Ren, C. Chen and X. Wang, *Environ. Sci. Technol.*, 2011, **45**, 10454.
78 R. Sitko, E. Turek, B. Zawisza, E. Malicka, E. Talik, J. Heimann, A. Gagor, B. Feist and R. Wrzalik, *Dalton Trans.*, 2013, **42**, 5682.
79 G. Eda and M. Chhowalla, *Adv. Mater.*, 2010, **22**, 2392.
80 G. Ko, H. Y. Kim, J. Ahn, Y. M. Park, K. Y. Lee and J. Kim, *Curr. Appl. Phys.*, 2010, **10**, 1002.
81 D. R. Dreyer, A. D. Todd and C. W. Bielawski, *Chem. Soc. Rev.*, 2014, **43**, 5288.
82 S. Eigler and A. Hirsch, *Angew. Chem., Int. Ed.*, 2014, **53**, 7720.
83 C. K. Chua and M. Pumera, *Chem. Soc. Rev.*, 2014, **43**, 291.
84 L. Zhou, B. He, Y. Yang and Y. He, *RSC Adv.*, 2014, **4**, 32570.
85 C. Tsai, H. Li, S. Park, J. Park, H. S. Han, J. K. Nørskov, X. Zheng and F. Abild-Pedersen, *Nat. Commun.*, 2017, **8**, 15113.
86 S. Bertolazzi, S. Bonacchi, G. Nan, A. Pershin, D. Beljonne and P. Samorì, *Adv. Mater.*, 2017, **29**, 1606760.
87 K. Cho, M. Min, T.-Y. Kim, H. Jeong, J. Pak, J.-K. Kim, J. Jang, S. J. Yun, Y. H. Lee, W.-K. Hong and T. Lee, *ACS Nano*, 2015, **9**, 8044.
88 E. P. Nguyen, B. J. Carey, J. Z. Ou, J. van Embden, E. D. Gaspera, A. F. Chrimes, M. J. S. Spencer, S. Zhuiykov, K. Kalantar-zadeh and T. Daeneke, *Adv. Mater.*, 2015, **27**, 6225.
89 A. Aliprandi, D. Pakulski, A. Ciesielski and P. Samorì, *ACS Nano*, 2017, **11**, 10654.
90 B. M. Venkatesan and R. Bashir, *Nat. Nanotechnol.*, 2011, **6**, 615.
91 S. Garaj, W. Hubbard, A. Reina, J. Kong, D. Branton and J. A. Golovchenko, *Nature*, 2010, **467**, 190.
92 S. Mao, J. Chang, H. Pu, G. Lu, Q. He, H. Zhang and J. Chen, *Chem. Soc. Rev.*, 2017, **46**, 6872.
93 Y. Liu, X. Dong and P. Chen, *Chem. Soc. Rev.*, 2012, **41**, 2283.
94 D. Chen, L. Tang and J. Li, *Chem. Soc. Rev.*, 2010, **39**, 3157.
95 M. J. Allen, V. C. Tung and R. B. Kaner, *Chem. Rev.*, 2010, **110**, 132.
96 S. Cui, H. Pu, S. A. Wells, Z. Wen, S. Mao, J. Chang, M. C. Hersam and J. Chen, *Nat. Commun.*, 2015, **6**, 8632.
97 Y. Wang, Z. Li, J. Wang, J. Li and Y. Lin, *Trends Biotechnol.*, 2011, **29**, 205.
98 Z. Tang, H. Wu, J. R. Cort, G. W. Buchko, Y. Zhang, Y. Shao, I. A. Aksay, J. Liu and Y. Lin, *Small*, 2010, **6**, 1205.
99 C. Zhu, Z. Zeng, H. Li, F. Li, C. Fan and H. Zhang, *J. Am. Chem. Soc.*, 2013, **135**, 5998.
100 D. Dinda, A. Gupta, B. K. Shaw, S. Sadhu and S. K. Saha, *ACS Appl. Mater. Interfaces*, 2014, **6**, 10722.
101 X. Ling, L. Xie, Y. Fang, H. Xu, H. Zhang, J. Kong, M. S. Dresselhaus, J. Zhang and Z. Liu, *Nano Lett.*, 2010, **10**, 553.
102 X. Ling, W. Fang, Y.-H. Lee, P. T. Araujo, X. Zhang, J. F. Rodriguez-Nieva, Y. Lin, J. Zhang, J. Kong and M. S. Dresselhaus, *Nano Lett.*, 2014, **14**, 3033.
103 S. Schlücker, *Angew. Chem., Int. Ed.*, 2014, **53**, 4756.
104 S. Laing, L. E. Jamieson, K. Faulds and D. Graham, *Nat. Rev. Chem.*, 2017, **1**, 0060.
105 A.-I. Henry, B. Sharma, M. F. Cardinal, D. Kurouski and R. P. Van Duyne, *Anal. Chem.*, 2016, **88**, 6638.
106 M. F. Cardinal, E. Vander Ende, R. A. Hackler, M. O. McAnally, P. C. Stair, G. C. Schatz and R. P. Van Duyne, *Chem. Soc. Rev.*, 2017, **46**, 3886.
107 S. Nie and S. R. Emory, *Science*, 1997, **275**, 1102.
108 K. Kneipp, Y. Wang, H. Kneipp, L. T. Perelman, I. Itzkan, R. R. Dasari and M. S. Feld, *Phys. Rev. Lett.*, 1997, **78**, 1667.
109 L. Sun, H. Hu, D. Zhan, J. Yan, L. Liu, J. S. Teguh, E. K. L. Yeow, P. S. Lee and Z. Shen, *Small*, 2014, **10**, 1090.
110 X. Ling, S. Huang, S. Deng, N. Mao, J. Kong, M. S. Dresselhaus and J. Zhang, *Acc. Chem. Res.*, 2015, **48**, 1862.
111 A. J. Bandodkar, I. Jeerapan and J. Wang, *ACS Sens.*, 2016, **1**, 464.
112 E. Singh, M. Meyyappan and H. S. Nalwa, *ACS Appl. Mater. Interfaces*, 2017, **9**, 34544.
113 H. Lee, T. K. Choi, Y. B. Lee, H. R. Cho, R. Ghaffari, L. Wang, H. J. Choi, T. D. Chung, N. Lu, T. Hyeon, S. H. Choi and D.-H. Kim, *Nat. Nanotechnol.*, 2016, **11**, 566.
114 N. O. Weiss, H. Zhou, L. Liao, Y. Liu, S. Jiang, Y. Huang and X. Duan, *Adv. Mater.*, 2012, **24**, 5782.
115 V. Berry, *Carbon*, 2013, **62**, 1.
116 F. Guo, G. Silverberg, S. Bowers, S.-P. Kim, D. Datta, V. Shenoy and R. H. Hurt, *Environ. Sci. Technol.*, 2012, **46**, 7717.
117 D. Pierleoni, Z. Y. Xia, M. Christian, S. Ligi, M. Minelli, V. Morandi, F. Doghieri and V. Palermo, *Carbon*, 2016, **96**, 503.

118 D. Prasai, J. C. Tuberquia, R. R. Harl, G. K. Jennings and K. I. Bolotin, *ACS Nano*, 2012, **6**, 1102.

119 A. K. Geim, *Science*, 2009, **324**, 1530.

120 X. Li, W. Cai, J. An, S. Kim, J. Nah, D. Yang, R. Piner, A. Velamakanni, I. Jung, E. Tutuc, S. K. Banerjee, L. Colombo and R. S. Ruoff, *Science*, 2009, **324**, 1312.

121 Y. Zhang, L. Zhang and C. Zhou, *Acc. Chem. Res.*, 2013, **46**, 2329.

122 C. Berger, Z. M. Song, T. B. Li, X. B. Li, A. Y. Ogbazghi, R. Feng, Z. T. Dai, A. N. Marchenkov, E. H. Conrad, P. N. First and W. A. de Heer, *J. Phys. Chem. B*, 2004, **108**, 19912.

123 Y. Zhu, S. Murali, W. Cai, X. Li, J. W. Suk, J. R. Potts and R. S. Ruoff, *Adv. Mater.*, 2010, **22**, 3906.

124 S. Basu and P. Bhattacharyya, *Sens. Actuators, B*, 2012, **173**, 1.

125 Y. Hernandez, V. Nicolosi, M. Lotya, F. M. Blighe, Z. Sun, S. De, I. T. McGovern, B. Holland, M. Byrne, Y. K. Gun'Ko, J. J. Boland, P. Niraj, G. S. Duesberg, S. Krishnamurthy, R. Goodhue, J. Hutchison, V. Scardaci, A. C. Ferrari and J. N. Coleman, *Nat. Nanotechnol.*, 2008, **3**, 563.

126 A. Ciesielski and P. Samorì, *Adv. Mater.*, 2016, **28**, 6030.

127 K. R. Paton, E. Varrla, C. Backes, R. J. Smith, U. Khan, A. O'Neill, C. Boland, M. Lotya, O. M. Istrate, P. King, T. Higgins, S. Barwich, P. May, P. Puczkarski, I. Ahmed, M. Moebius, H. Pettersson, E. Long, J. Coelho, S. E. O'Brien, E. K. McGuire, B. M. Sanchez, G. S. Duesberg, N. McEvoy, T. J. Pennycook, C. Downing, A. Crossley, V. Nicolosi and J. N. Coleman, *Nat. Mater.*, 2014, **13**, 624.

128 M. Eredia, S. Bertolazzi, T. Leydecker, M. El Garah, I. Janica, G. Melinte, O. Ersen, A. Ciesielski and P. Samorì, *J. Phys. Chem. Lett.*, 2017, **8**, 3347.

129 Z. Yin, H. Li, H. Li, L. Jiang, Y. Shi, Y. Sun, G. Lu, Q. Zhang, X. Chen and H. Zhang, *ACS Nano*, 2012, **6**, 74.

130 W. Wu, L. Wang, Y. Li, F. Zhang, L. Lin, S. Niu, D. Chenet, X. Zhang, Y. Hao, T. F. Heinz, J. Hone and Z. L. Wang, *Nature*, 2014, **514**, 470.

131 Y. Sun, S. Gao and Y. Xie, *Chem. Soc. Rev.*, 2014, **43**, 530.

132 G. Zhang, G. Proni, S. Zhao, E. C. Constable, C. E. Housecroft, M. Neuburger and J. A. Zampese, *Dalton Trans.*, 2014, **43**, 12313.

133 Kenry, A. Geldert, X. Zhang, H. Zhang and C. T. Lim, *ACS Sens.*, 2016, **1**, 1315.

134 T. Yang, R. Yang, H. Chen, F. Nan, T. Ge and K. Jiao, *ACS Appl. Mater. Interfaces*, 2015, **7**, 2867.

135 M. Chhowalla, H. S. Shin, G. Eda, L.-J. Li, K. P. Loh and H. Zhang, *Nat. Chem.*, 2013, **5**, 263.

136 Y. Li, K.-A. N. Duerloo, K. Wauson and E. J. Reed, *Nat. Commun.*, 2016, **7**, 10671.

137 J. N. Coleman, M. Lotya, A. O'Neill, S. D. Bergin, P. J. King, U. Khan, K. Young, A. Gaucher, S. De, R. J. Smith, I. V. Shvets, S. K. Arora, G. Stanton, H.-Y. Kim, K. Lee, G. T. Kim, G. S. Duesberg, T. Hallam, J. J. Boland, J. J. Wang, J. F. Donegan, J. C. Grunlan, G. Moriarty, A. Shmeliov, R. J. Nicholls, J. M. Perkins, E. M. Grieveson, K. Theuwissen, D. W. McComb, P. D. Nellist and V. Nicolosi, *Science*, 2011, **331**, 568.

138 D. Kong, H. Wang, J. J. Cha, M. Pasta, K. J. Koski, J. Yao and Y. Cui, *Nano Lett.*, 2013, **13**, 1341.

139 J. Shi, D. Ma, G.-F. Han, Y. Zhang, Q. Ji, T. Gao, J. Sun, X. Song, C. Li, Y. Zhang, X.-Y. Lang, Y. Zhang and Z. Liu, *ACS Nano*, 2014, **8**, 10196.

140 H. S. S. Ramakrishna Matte, A. Gomathi, A. K. Manna, D. J. Late, R. Datta, S. K. Pati and C. N. R. Rao, *Angew. Chem., Int. Ed.*, 2010, **49**, 4059.

141 Z. Zeng, Z. Yin, X. Huang, H. Li, Q. He, G. Lu, F. Boey and H. Zhang, *Angew. Chem., Int. Ed.*, 2011, **50**, 11093.

142 V. Nicolosi, M. Chhowalla, M. G. Kanatzidis, M. S. Strano and J. N. Coleman, *Science*, 2013, **340**, 1226419.

143 Y.-H. Lee, X.-Q. Zhang, W. Zhang, M.-T. Chang, C.-T. Lin, K.-D. Chang, Y.-C. Yu, J. T.-W. Wang, C.-S. Chang, L.-J. Li and T.-W. Lin, *Adv. Mater.*, 2012, **24**, 2320.

144 B. Liu, L. Chen, G. Liu, A. N. Abbas, M. Fathi and C. Zhou, *ACS Nano*, 2014, **8**, 5304.

145 K. Lee, R. Gatensby, N. McEvoy, T. Hallam and G. S. Duesberg, *Adv. Mater.*, 2013, **25**, 6699.

146 B. Cho, A. R. Kim, Y. Park, J. Yoon, Y. J. Lee, S. Lee, T. J. Yoo, C. G. Kang, B. H. Lee, H. C. Ko, D. H. Kim and M. G. Hahm, *ACS Appl. Mater. Interfaces*, 2015, **7**, 2952.

147 S.-Y. Cho, S. J. Kim, Y. Lee, J.-S. Kim, W.-B. Jung, H.-W. Yoo, J. Kim and H.-T. Jung, *ACS Nano*, 2015, **9**, 9314.

148 K. F. Mak, C. Lee, J. Hone, J. Shan and T. F. Heinz, *Phys. Rev. Lett.*, 2010, **105**, 136805.

149 T. Wu and H. Zhang, *Angew. Chem., Int. Ed.*, 2015, **54**, 4432.

150 D. M. Sim, H. J. Han, S. Yim, M.-J. Choi, J. Jeon and Y. S. Jung, *ACS Omega*, 2017, **2**, 4678.

151 C. H. Ho and C. E. Huang, *J. Alloys Compd.*, 2004, **383**, 74.

152 Y. Wang, L. Li, W. Yao, S. Song, J. T. Sun, J. Pan, X. Ren, C. Li, E. Okunishi, Y.-Q. Wang, E. Wang, Y. Shao, Y. Y. Zhang, H.-t. Yang, E. F. Schwier, H. Iwasawa, K. Shimada, M. Taniguchi, Z. Cheng, S. Zhou, S. Du, S. J. Pennycook, S. T. Pantelides and H.-J. Gao, *Nano Lett.*, 2015, **15**, 4013.

153 A. Carvalho, M. Wang, X. Zhu, A. S. Rodin, H. Su and A. H. Castro Neto, *Nat. Rev. Mater.*, 2016, **1**, 16061.

154 A. Castellanos-Gomez, L. Vicarelli, E. Prada, J. O. Island, K. L. Narasimha-Acharya, S. I. Blanter, D. J. Groenendijk, M. Buscema, G. A. Steele, J. V. Alvarez, H. W. Zandbergen, J. J. Palacios and H. S. J. van der Zant, *2D Mater.*, 2014, **1**, 25001.

155 M. Buscema, D. J. Groenendijk, G. A. Steele, H. S. J. van der Zant and A. Castellanos-Gomez, *Nat. Commun.*, 2014, **5**, 4651.

156 J. Qiao, X. Kong, Z.-X. Hu, F. Yang and W. Ji, *Nat. Commun.*, 2014, **5**, 4475.

157 C. Backes, R. J. Smith, N. McEvoy, N. C. Berner, D. McCloskey, H. C. Nerl, A. O'Neill, P. J. King, T. Higgins, D. Hanlon, N. Scheuschner, J. Maultzsch, L. Houben, G. S. Duesberg, J. F. Donegan, V. Nicolosi and J. N. Coleman, *Nat. Commun.*, 2014, **5**, 4576.

158 A. N. Abbas, B. Liu, L. Chen, Y. Ma, S. Cong, N. Aroonyadet, M. Köpf, T. Nilges and C. Zhou, *ACS Nano*, 2015, **9**, 5618.

159 Y. Cai, Q. Ke, G. Zhang and Y.-W. Zhang, *J. Phys. Chem. C*, 2015, **119**, 3102.

160 C. C. Mayorga-Martinez, Z. Sofer and M. Pumera, *Angew. Chem., Int. Ed.*, 2015, **127**, 14317.

161 L. Kou, T. Frauenheim and C. Chen, *J. Phys. Chem. Lett.*, 2014, **5**, 2675.

162 J. O. Island, G. A. Steele, H. S. J. van der Zant and A. Castellanos-Gomez, *2D Mater.*, 2015, **2**, 11002.

163 V. L. Solozhenko, A. G. Lazarenko, J. P. Petitet and A. V. Kanaev, *J. Phys. Chem. Solids*, 2001, **62**, 1331.

164 K. Watanabe, T. Taniguchi and H. Kanda, *Nat. Mater.*, 2004, **3**, 404.

165 A. Nag, K. Raidongia, K. P. S. S. Hembram, R. Datta, U. V. Waghmare and C. N. R. Rao, *ACS Nano*, 2010, **4**, 1539.

166 L. Liu, Y. P. Feng and Z. X. Shen, *Phys. Rev. B: Condens. Matter Mater. Phys.*, 2003, **68**, 104102.

167 D. Pacilé, J. C. Meyer, Ç. Ö. Girit and A. Zettl, *Appl. Phys. Lett.*, 2008, **92**, 133107.

168 Y. Lin, C. E. Bunker, K. A. S. Fernando and J. W. Connell, *ACS Appl. Mater. Interfaces*, 2012, **4**, 1110.

169 W.-Q. Han, L. Wu, Y. Zhu, K. Watanabe and T. Taniguchi, *Appl. Phys. Lett.*, 2008, **93**, 223103.

170 C. Zhi, Y. Bando, C. Tang, H. Kuwahara and D. Golberg, *Adv. Mater.*, 2009, **21**, 2889.

171 L. Cao, S. Emami and K. Lafdi, *Mater. Express*, 2014, **4**, 165.

172 F. Müller, K. Stöwe and H. Sachdev, *Chem. Mater.*, 2005, **17**, 3464.

173 W. Auwärter, H. U. Suter, H. Sachdev and T. Greber, *Chem. Mater.*, 2004, **16**, 343.

174 Y.-H. Lee, K.-K. Liu, A.-Y. Lu, C.-Y. Wu, C.-T. Lin, W. Zhang, C.-Y. Su, C.-L. Hsu, T.-W. Lin, K.-H. Wei, Y. Shi and L.-J. Li, *RSC Adv.*, 2012, **2**, 111.

175 M. Naguib, O. Mashtalir, J. Carle, V. Presser, J. Lu, L. Hultman, Y. Gogotsi and M. W. Barsoum, *ACS Nano*, 2012, **6**, 1322.

176 O. Mashtalir, M. Naguib, V. N. Mochalin, Y. Dall'Agnese, M. Heon, M. W. Barsoum and Y. Gogotsi, *Nat. Commun.*, 2013, **4**, 1716.

177 M. R. Lukatskaya, O. Mashtalir, C. E. Ren, Y. Dall'Agnese, P. Rozier, P. L. Taberna, M. Naguib, P. Simon, M. W. Barsoum and Y. Gogotsi, *Science*, 2013, **341**, 1502.

178 L. Lorencova, T. Bertok, E. Dosekova, A. Holazova, D. Paprckova, A. Vikartovska, V. Sasinkova, J. Filip, P. Kasak, M. Jerigova, D. Velic, K. A. Mahmoud and J. Tkac, *Electrochim. Acta*, 2017, **235**, 471.

179 H. Liu, C. Duan, C. Yang, W. Shen, F. Wang and Z. Zhu, *Sens. Actuators, B*, 2015, **218**, 60.

180 S. Yang, C. Jiang and S.-H. Wei, *Appl. Phys. Rev.*, 2017, **4**, 21304.

181 G. F. Fine, L. M. Cavanagh, A. Afonja and R. Binions, *Sensors*, 2010, **10**, 5469.

182 Y. Pak, S.-M. Kim, H. Jeong, C. G. Kang, J. S. Park, H. Song, R. Lee, N. Myoung, B. H. Lee, S. Seo, J. T. Kim and G.-Y. Jung, *ACS Appl. Mater. Interfaces*, 2014, **6**, 13293.

183 J. Zhang, X. Liu, G. Neri and N. Pinna, *Adv. Mater.*, 2016, **28**, 795.

184 S. J. Choi, B. H. Jang, S. J. Lee, B. K. Min, A. Rothschild and I. D. Kim, *ACS Appl. Mater. Interfaces*, 2014, **6**, 2588.

185 W. Li, X. Geng, Y. Guo, J. Rong, Y. Gong, L. Wu, X. Zhang, P. Li, J. Xu, G. Cheng, M. Sun and L. Liu, *ACS Nano*, 2011, **5**, 6955.

186 C. Wang, L. Yin, L. Zhang, D. Xiang and R. Gao, *Sensors*, 2010, **10**, 2088.

187 S. A. Waghuley, S. M. Yenorkar, S. S. Yawale and S. P. Yawale, *Sens. Actuators, B*, 2008, **128**, 366.

188 J. Li, Y. Lu, Q. Ye, M. Cinke, J. Han and M. Meyyappan, *Nano Lett.*, 2003, **3**, 929.

189 A. K. Geim and K. S. Novoselov, *Nat. Mater.*, 2007, **6**, 183.

190 H. Li, Z. Yin, Q. He, H. Li, X. Huang, G. Lu, D. W. Fam, A. I. Tok, Q. Zhang and H. Zhang, *Small*, 2012, **8**, 63.

191 Q. Yue, Z. Shao, S. Chang and J. Li, *Nanoscale Res. Lett.*, 2013, **8**, 425.

192 M. Donarelli, S. Prezioso, F. Perrozzi, F. Bisti, M. Nardone, L. Giancaterini, C. Cantalini and L. Ottaviano, *Sens. Actuators, B*, 2015, **207**, 602.

193 F. K. Perkins, A. L. Friedman, E. Cobas, P. M. Campbell, G. G. Jernigan and B. T. Jonker, *Nano Lett.*, 2013, **13**, 668.

194 M. O'Brien, K. Lee, R. Morrish, N. C. Berner, N. McEvoy, C. A. Wolden and G. S. Duesberg, *Chem. Phys. Lett.*, 2014, **615**, 6.

195 C. C. Mayorga-Martinez, A. Ambrosi, A. Y. S. Eng, Z. Sofer and M. Pumera, *Adv. Funct. Mater.*, 2015, **25**, 5611.

196 M. Ferroni, V. Guidi, G. Martinelli, P. Nelli, M. Sacerdoti and G. Sberveglieri, *Thin Solid Films*, 1997, **307**, 148.

197 K. Xu, N. Li, D. Zeng, S. Tian, S. Zhang, D. Hu and C. Xie, *ACS Appl. Mater. Interfaces*, 2015, **7**, 11359.

198 D. Zhang, Y. Sun, P. Li and Y. Zhang, *ACS Appl. Mater. Interfaces*, 2016, **8**, 14142.

199 M. Sajjad, G. Morell and P. Feng, *ACS Appl. Mater. Interfaces*, 2013, **5**, 5051.

200 N. L. Teradal, S. Marx, A. Morag and R. Jelinek, *J. Mater. Chem. C*, 2017, **5**, 1128.

201 F. Schedin, A. K. Geim, S. V. Morozov, E. W. Hill, P. Blake, M. I. Katsnelson and K. S. Novoselov, *Nat. Mater.*, 2007, **6**, 652.

202 X. Huang, X. Y. Qi, F. Boey and H. Zhang, *Chem. Soc. Rev.*, 2012, **41**, 666.

203 O. Leenaerts, B. Partoens and F. M. Peeters, *Phys. Rev. B: Condens. Matter Mater. Phys.*, 2008, **77**, 125416.

204 Y. Dan, Y. Lu, N. J. Kybert, Z. Luo and A. T. C. Johnson, *Nano Lett.*, 2009, **9**, 1472.

205 S. Rumyantsev, G. Liu, M. S. Shur, R. A. Potyrailo and A. A. Balandin, *Nano Lett.*, 2012, **12**, 2294.

206 H. J. Yoon, D. H. Jun, J. H. Yang, Z. Zhou, S. S. Yang and M. M.-C. Cheng, *Sens. Actuators, B*, 2011, **157**, 310.

207 S. Kumar, S. Kaushik, R. Pratap and S. Raghavan, *ACS Appl. Mater. Interfaces*, 2015, **7**, 2189.

208 M. G. Chung, D. H. Kim, H. M. Lee, T. Kim, J. H. Choi, D. k. Seo, J.-B. Yoo, S.-H. Hong, T. J. Kang and Y. H. Kim, *Sens. Actuators, B*, 2012, **166–167**, 172.

209 H. Choi, J. S. Choi, J. S. Kim, J. H. Choe, K. H. Chung, J. W. Shin, J. T. Kim, D. H. Youn, K. C. Kim, J. I. Lee, S. Y. Choi, P. Kim, C. G. Choi and Y. J. Yu, *Small*, 2014, **10**, 3685.

210 Y. H. Kim, S. J. Kim, Y.-J. Kim, Y.-S. Shim, S. Y. Kim, B. H. Hong and H. W. Jang, *ACS Nano*, 2015, **9**, 10453.

211 M. Gautam and A. H. Jayatissa, *Mater. Sci. Eng., C*, 2011, **31**, 1405.

212 F. Yavari, Z. Chen, A. V. Thomas, W. Ren, H.-M. Cheng and N. Koratkar, *Sci. Rep.*, 2011, **1**, 166.

213 A. D. Smith, K. Elgammal, X. Fan, M. C. Lemme, A. Delin, M. Råsander, L. Bergqvist, S. Schröder, A. C. Fischer, F. Niklaus and M. Östling, *RSC Adv.*, 2017, **7**, 22329.

214 M. W. K. Nomani, R. Shishir, M. Qazi, D. Diwan, V. B. Shields, M. G. Spencer, G. S. Tompa, N. M. Sbrockey and G. Koley, *Sens. Actuators, B*, 2010, **150**, 301.

215 F. Varchon, R. Feng, J. Hass, X. Li, B. N. Nguyen, C. Naud, P. Mallet, J. Y. Veuillen, C. Berger, E. H. Conrad and L. Magaud, *Phys. Rev. Lett.*, 2007, **99**, 126805.

216 R. Pearce, T. Iakimov, M. Andersson, L. Hultman, A. L. Spetz and R. Yakimova, *Sens. Actuators, B*, 2011, **155**, 451.

217 Y. R. Choi, Y.-G. Yoon, K. S. Choi, J. H. Kang, Y.-S. Shim, Y. H. Kim, H. J. Chang, J.-H. Lee, C. R. Park, S. Y. Kim and H. W. Jang, *Carbon*, 2015, **91**, 178.

218 A. Salehi-Khojin, D. Estrada, K. Y. Lin, M.-H. Bae, F. Xiong, E. Pop and R. I. Masel, *Adv. Mater.*, 2012, **24**, 53.

219 S. Prezioso, F. Perrozzi, L. Giancaterini, C. Cantalini, E. Treossi, V. Palermo, M. Nardone, S. Santucci and L. Ottaviano, *J. Phys. Chem. C*, 2013, **117**, 10683.

220 L. Guo, H.-B. Jiang, R.-Q. Shao, Y.-L. Zhang, S.-Y. Xie, J.-N. Wang, X.-B. Li, F. Jiang, Q.-D. Chen, T. Zhang and H.-B. Sun, *Carbon*, 2012, **50**, 1667.

221 D. Zhang, J. Tong and B. Xia, *Sens. Actuators, B*, 2014, **197**, 66.

222 A. Lipatov, A. Varezhnikov, P. Wilson, V. Sysoev, A. Kolmakov and A. Sinitskii, *Nanoscale*, 2013, **5**, 5426.

223 N. Hu, Y. Wang, J. Chai, R. Gao, Z. Yang, E. S.-W. Kong and Y. Zhang, *Sens. Actuators, B*, 2012, **163**, 107.

224 V. Dua, S. P. Surwade, S. Ammu, S. R. Agnihotra, S. Jain, K. E. Roberts, S. Park, R. S. Ruoff and S. K. Manohar, *Angew. Chem., Int. Ed.*, 2010, **49**, 2154.

225 V. Strong, S. Dubin, M. F. El-Kady, A. Lech, Y. Wang, B. H. Weiller and R. B. Kaner, *ACS Nano*, 2012, **6**, 1395.

226 M. Donarelli, S. Prezioso, F. Perrozzi, L. Giancaterini, C. Cantalini, E. Treossi, V. Palermo, S. Santucci and L. Ottaviano, *2D Mater.*, 2015, **2**, 35018.

227 S. Borini, R. White, D. Wei, M. Astley, S. Haque, E. Spigone, N. Harris, J. Kivioja and T. Ryhänen, *ACS Nano*, 2013, **7**, 11166.

228 K. Rathi and K. Pal, *ACS Omega*, 2017, **2**, 842.

229 Y. Tai, T. K. Bera, G. Lubineau and Z. Yang, *J. Mater. Chem. C*, 2017, **5**, 3848.

230 Y. Yao, X. Chen, J. Zhu, B. Zeng, Z. Wu and X. Li, *Nanoscale Res. Lett.*, 2012, **7**, 363.

231 I. Jung, D. Dikin, S. Park, W. Cai, S. L. Mielke and R. S. Ruoff, *J. Phys. Chem. C*, 2008, **112**, 20264.

232 L. Al-Mashat, K. Shin, K. Kalantar-zadeh, J. D. Plessis, S. H. Han, R. W. Kojima, R. B. Kaner, D. Li, X. Gou, S. J. Ippolito and W. Wlodarski, *J. Phys. Chem. C*, 2010, **114**, 16168.

233 X. Huang, N. Hu, R. Gao, Y. Yu, Y. Wang, Z. Yang, E. Siu-Wai Kong, H. Wei and Y. Zhang, *J. Mater. Chem.*, 2012, **22**, 22488.

234 W. Yuan, A. Liu, L. Huang, C. Li and G. Shi, *Adv. Mater.*, 2013, **25**, 766.

235 A. Kaniyoor, R. Imran Jafri, T. Arockiadoss and S. Ramaprabhu, *Nanoscale*, 2009, **1**, 382.

236 H. Conrad, G. Ertl and E. E. Latta, *Surf. Sci.*, 1974, **41**, 435.

237 W. Wu, Z. Liu, L. A. Jauregui, Q. Yu, R. Pillai, H. Cao, J. Bao, Y. P. Chen and S.-S. Pei, *Sens. Actuators, B*, 2010, **150**, 296.

238 M. G. Chung, D.-H. Kim, D. K. Seo, T. Kim, H. U. Im, H. M. Lee, J.-B. Yoo, S.-H. Hong, T. J. Kang and Y. H. Kim, *Sens. Actuators, B*, 2012, **169**, 387.

239 J. Hong, S. Lee, J. Seo, S. Pyo, J. Kim and T. Lee, *ACS Appl. Mater. Interfaces*, 2015, **7**, 3554.

240 B. H. Chu, C. F. Lo, J. Nicolosi, C. Y. Chang, V. Chen, W. Strupinski, S. J. Pearton and F. Ren, *Sens. Actuators, B*, 2011, **157**, 500.

241 U. Lange, T. Hirsch, V. M. Mirsky and O. S. Wolfbeis, *Electrochim. Acta*, 2011, **56**, 3707.

242 L. Huang, Z. Wang, J. Zhang, J. Pu, Y. Lin, S. Xu, L. Shen, Q. Chen and W. Shi, *ACS Appl. Mater. Interfaces*, 2014, **6**, 7426.

243 S. Deng, V. Tjoa, H. M. Fan, H. R. Tan, D. C. Sayle, M. Olivo, S. Mhaisalkar, J. Wei and C. H. Sow, *J. Am. Chem. Soc.*, 2012, **134**, 4905.

244 J. Yi, J. M. Lee and W. I. Park, *Sens. Actuators, B*, 2011, **155**, 264.

245 G. Singh, A. Choudhary, D. Haranath, A. G. Joshi, N. Singh, S. Singh and R. Pasricha, *Carbon*, 2012, **50**, 385.

246 T. V. Cuong, V. H. Pham, J. S. Chung, E. W. Shin, D. H. Yoo, S. H. Hahn, J. S. Huh, G. H. Rue, E. J. Kim, S. H. Hur and P. A. Kohl, *Mater. Lett.*, 2010, **64**, 2479.

247 L. Zhou, F. Shen, X. Tian, D. Wang, T. Zhang and W. Chen, *Nanoscale*, 2013, **5**, 1564.

248 S. Mao, S. Cui, G. Lu, K. Yu, Z. Wen and J. Chen, *J. Mater. Chem. C*, 2012, **22**, 11009.

249 J. Liu, S. Li, B. Zhang, Y. Wang, Y. Gao, X. Liang, Y. Wang and G. Lu, *J. Colloid Interface Sci.*, 2017, **504**, 206.

250 Q. Huang, D. Zeng, H. Li and C. Xie, *Nanoscale*, 2012, **4**, 5651.

251 R. K. Mishra, S. B. Upadhyay, A. Kushwaha, T. H. Kim, G. Murali, R. Verma, M. Srivastava, J. Singh, P. P. Sahay and S. H. Lee, *Nanoscale*, 2015, **7**, 11971.

252 G. Eranna, B. C. Joshi, D. P. Runthala and R. P. Gupta, *Crit. Rev. Solid State Mater. Sci.*, 2004, **29**, 111.

253 Y.-F. Sun, S.-B. Liu, F.-L. Meng, J.-Y. Liu, Z. Jin, L.-T. Kong and J.-H. Liu, *Sensors*, 2012, **12**, 2610.

254 W. Yang, P. Wan, X. Zhou, J. Hu, Y. Guan and L. Feng, *ACS Appl. Mater. Interfaces*, 2014, **6**, 21093.

255 D. Zhang, H. Chang, P. Li and R. Liu, *J. Mater. Sci.: Mater. Electron.*, 2016, **27**, 3723.

256 D. Zhang, N. Yin and B. Xia, *J. Mater. Sci.: Mater. Electron.*, 2015, **26**, 5937.

257 Z. Wu, X. Chen, S. Zhu, Z. Zhou, Y. Yao, W. Quan and B. Liu, *IEEE Sens. J.*, 2013, **13**, 777.

258 H. Bai, K. Sheng, P. Zhang, C. Li and G. Shi, *J. Mater. Chem.*, 2011, **21**, 18653.

259 W. Yuan, L. Huang, Q. Zhou and G. Shi, *ACS Appl. Mater. Interfaces*, 2014, **6**, 17003.

260 Q. Ji, I. Honma, S.-M. Paek, M. Akada, J. P. Hill, A. Vinu and K. Ariga, *Angew. Chem., Int. Ed.*, 2010, **49**, 9737.

261 H. Y. Jeong, D.-S. Lee, H. K. Choi, D. H. Lee, J.-E. Kim, J. Y. Lee, W. J. Lee, S. O. Kim and S.-Y. Choi, *Appl. Phys. Lett.*, 2010, **96**, 213105.

262 S. Tongay, J. Zhou, C. Ataca, J. Liu, J. S. Kang, T. S. Matthews, L. You, J. Li, J. C. Grossman and J. Wu, *Nano Lett.*, 2013, **13**, 2831.

263 B. Cho, J. Yoon, S. K. Lim, A. R. Kim, D. H. Kim, S. G. Park, J. D. Kwon, Y. J. Lee, K. H. Lee, B. H. Lee, H. C. Ko and M. G. Hahm, *ACS Appl. Mater. Interfaces*, 2015, **7**, 16775.

264 Y. H. Kim, K. Y. Kim, Y. R. Choi, Y.-S. Shim, J.-M. Jeon, J.-H. Lee, S. Y. Kim, S. Han and H. W. Jang, *J. Mater. Chem. A*, 2016, **4**, 6070.

265 Y. Yao, L. Tolentino, Z. Yang, X. Song, W. Zhang, Y. Chen and C.-P. Wong, *Adv. Funct. Mater.*, 2013, **23**, 3577.

266 B. Cho, M. G. Hahm, M. Choi, J. Yoon, A. R. Kim, Y.-J. Lee, S.-G. Park, J.-D. Kwon, C. S. Kim, M. Song, Y. Jeong, K.-S. Nam, S. Lee, T. J. Yoo, C. G. Kang, B. H. Lee, H. C. Ko, P. M. Ajayan and D.-H. Kim, *Sci. Rep.*, 2015, **5**, 8052.

267 Q. He, Z. Zeng, Z. Yin, H. Li, S. Wu, X. Huang and H. Zhang, *Small*, 2012, **8**, 2994.

268 C. Kuru, C. Choi, A. Kargar, D. Choi, Y. J. Kim, C. H. Liu, S. Yavuz and S. Jin, *Adv. Sci.*, 2015, **2**, 1500004.

269 D. Sarkar, X. Xie, J. Kang, H. Zhang, W. Liu, J. Navarrete, M. Moskovits and K. Banerjee, *Nano Lett.*, 2015, **15**, 2852.

270 S. Cui, Z. Wen, X. Huang, J. Chang and J. Chen, *Small*, 2015, **11**, 2305.

271 H. Yan, P. Song, S. Zhang, Z. Yang and Q. Wang, *RSC Adv.*, 2015, **5**, 79593.

272 S. S. Chou, M. De, J. Kim, S. Byun, C. Dykstra, J. Yu, J. Huang and V. P. Dravid, *J. Am. Chem. Soc.*, 2013, **135**, 4584.

273 D. J. Late, T. Doneux and M. Bougouma, *Appl. Phys. Lett.*, 2014, **105**, 233103.

274 Y. Luo, C. Chen, K. Xia, S. Peng, H. Guan, J. Tang, H. Lu, J. Yu, J. Zhang, Y. Xiao and Z. Chen, *Opt. Express*, 2016, **24**, 8956.

275 H. Fang, S. Chuang, T. C. Chang, K. Takei, T. Takahashi and A. Javey, *Nano Lett.*, 2012, **12**, 3788.

276 S. Yang, J. Kang, Q. Yue, J. M. D. Coey and C. Jiang, *Adv. Mater. Interfaces*, 2016, **3**, 1500707.

277 S. Yang, S. Tongay, Q. Yue, Y. Li, B. Li and F. Lu, *Sci. Rep.*, 2014, **4**, 5442.

278 S. Yang, S. Tongay, Y. Li, Q. Yue, J.-B. Xia, S.-S. Li, J. Li and S.-H. Wei, *Nanoscale*, 2014, **6**, 7226.

279 C. Yim, K. Lee, N. McEvoy, M. O'Brien, S. Riazimehr, N. C. Berner, C. P. Cullen, J. Kotakoski, J. C. Meyer, M. C. Lemme and G. S. Duesberg, *ACS Nano*, 2016, **10**, 9550.

280 J. Z. Ou, W. Ge, B. J. Carey, T. Daeneke, A. Rotbart, W. Shan, Y. Wang, Z. Fu, A. F. Chrimes, W. Wlodarski, S. P. Russo, Y. X. Li and K. Kalantar-zadeh, *ACS Nano*, 2015, **9**, 10313.

281 S. Weidong, H. Lihua, W. Haishui, Z. Hongjie, Y. Jianhui and W. Pinghui, *Nanotechnology*, 2006, **17**, 2918.

282 P. Yasaei, A. Behranginia, T. Foroozan, M. Asadi, K. Kim, F. Khalili-Araghi and A. Salehi-Khojin, *ACS Nano*, 2015, **9**, 9898.

283 Y.-H. Zhang, K.-G. Zhou, X.-C. Gou, K.-F. Xie, H.-L. Zhang and Y. Peng, *Chem. Phys. Lett.*, 2010, **484**, 266.

284 M. Sajjad and P. Feng, *Mater. Res. Bull.*, 2014, **49**, 35.

285 S. Chowdhury and R. Balasubramanian, *Adv. Colloid Interface Sci.*, 2014, **204**, 35.

286 L. Fan, C. Luo, M. Sun and H. Qiu, *J. Mater. Chem.*, 2012, **22**, 24577.

287 H. Wang, X. Yuan, Y. Wu, H. Huang, X. Peng, G. Zeng, H. Zhong, J. Liang and M. Ren, *Adv. Colloid Interface Sci.*, 2013, **195-196**, 19.

288 D. S. Sholl and R. P. Lively, *Nature*, 2016, **532**, 435.

289 I. Ali, *Chem. Rev.*, 2012, **112**, 5073.

290 T. Zhang, Z. Cheng, Y. Wang, Z. Li, C. Wang, Y. Li and Y. Fang, *Nano Lett.*, 2010, **10**, 4738.

291 H. G. Sudibya, Q. He, H. Zhang and P. Chen, *ACS Nano*, 2011, **5**, 1990.

292 G. Zhou, J. Chang, S. Cui, H. Pu, Z. Wen and J. Chen, *ACS Appl. Mater. Interfaces*, 2014, **6**, 19235.

293 J. H. An, S. J. Park, O. S. Kwon, J. Bae and J. Jang, *ACS Nano*, 2013, **7**, 10563.

294 W. Fu, C. Nef, A. Tarasov, M. Wipf, R. Stoop, O. Knopfmacher, M. Weiss, M. Calame and C. Schonenberger, *Nanoscale*, 2013, **5**, 12104.

295 K. Maehashi, Y. Sofue, S. Okamoto, Y. Ohno, K. Inoue and K. Matsumoto, *Sens. Actuators, B*, 2013, **187**, 45.

296 S. Jiang, R. Cheng, R. Ng, Y. Huang and X. Duan, *Nano Res.*, 2015, **8**, 257.

297 G. Zhou, J. Chang, H. Pu, K. Shi, S. Mao, X. Sui, R. Ren, S. Cui and J. Chen, *ACS Sens.*, 2016, **1**, 295.

298 P. Li, D. Zhang, C. Jiang, X. Zong and Y. Cao, *Biosens. Bioelectron.*, 2017, **98**, 68.

299 Z.-Q. Zhao, X. Chen, Q. Yang, J.-H. Liu and X.-J. Huang, *Chem. Commun.*, 2012, **48**, 2180.

300 P. K. Sahoo, B. Panigrahy, S. Sahoo, A. K. Satpati, D. Li and D. Bahadur, *Biosens. Bioelectron.*, 2013, **43**, 293.

301 Y. Wei, C. Gao, F.-L. Meng, H.-H. Li, L. Wang, J.-H. Liu and X.-J. Huang, *J. Phys. Chem. C*, 2012, **116**, 1034.

302 J. Li, S. Guo, Y. Zhai and E. Wang, *Electrochem. Commun.*, 2009, **11**, 1085.

303 S. Chaiyo, E. Mehmeti, K. Žagar, W. Siangproh, O. Chailapakul and K. Kalcher, *Anal. Chim. Acta*, 2016, **918**, 26.

304 R. Seenivasan, W.-J. Chang and S. Gunasekaran, *ACS Appl. Mater. Interfaces*, 2015, **7**, 15935.

305 J. Cui, S. Xu and L. Wang, *Sci. China Mater.*, 2017, **60**, 352.

306 Z. S. Qian, X. Y. Shan, L. J. Chai, J. R. Chen and H. Feng, *Biosens. Bioelectron.*, 2015, **68**, 225.

307 M. Li, X. Zhou, W. Ding, S. Guo and N. Wu, *Biosens. Bioelectron.*, 2013, **41**, 889.

308 Y. Wen, F. Xing, S. He, S. Song, L. Wang, Y. Long, D. Li and C. Fan, *Chem. Commun.*, 2010, **46**, 2596.

309 K. Mao, Z. Wu, Y. Chen, X. Zhou, A. Shen and J. Hu, *Talanta*, 2015, **132**, 658.

310 Y. Yang, T. Liu, L. Cheng, G. Song, Z. Liu and M. Chen, *ACS Appl. Mater. Interfaces*, 2015, **7**, 7526.

311 X. Liu, L. Li, Y. Wei, Y. Zheng, Q. Xiao and B. Feng, *Analyst*, 2015, **140**, 4654.

312 Y. Wang, J. Hu, Q. Zhuang and Y. Ni, *ACS Sustainable Chem. Eng.*, 2016, **4**, 2535.

313 X. Zuo, H. Zhang, Q. Zhu, W. Wang, J. Feng and X. Chen, *Biosens. Bioelectron.*, 2016, **85**, 464.

314 B. L. Li, J. Wang, H. L. Zou, S. Garaj, C. T. Lim, J. Xie, N. B. Li and D. T. Leong, *Adv. Funct. Mater.*, 2016, **26**, 7034.

315 C. Liu, Z. Sun, L. Zhang, J. Lv, X. F. Yu, L. Zhang and X. Chen, *Sens. Actuators, B*, 2018, **257**, 1093.

316 P. Li, D. Zhang, J. Liu, H. Chang, Y. e. Sun and N. Yin, *ACS Appl. Mater. Interfaces*, 2015, **7**, 24396.

317 W. Gu, X. Pei, Y. Cheng, C. Zhang, J. Zhang, Y. Yan, C. Ding and Y. Xian, *ACS Sens.*, 2017, **2**, 576.

318 K. C. Kemp, H. Seema, M. Saleh, N. H. Le, K. Mahesh, V. Chandra and K. S. Kim, *Nanoscale*, 2013, **5**, 3149.

319 K. A. Mahmoud, B. Mansoor, A. Mansour and M. Khraisheh, *Desalination*, 2015, **356**, 208.

320 S. Wang, H. Sun, H. M. Ang and M. O. Tadé, *Chem. Eng. J.*, 2013, **226**, 336.

321 H. M. Hegab and L. Zou, *J. Membr. Sci.*, 2015, **484**, 95.

322 G. Zhao, X. Ren, X. Gao, X. Tan, J. Li, C. Chen, Y. Huang and X. Wang, *Dalton Trans.*, 2011, **40**, 10945.

323 W. Peng, H. Li, Y. Liu and S. Song, *J. Mol. Liq.*, 2017, **230**, 496.

324 İ. Duru, D. Ege and A. R. Kamali, *J. Mater. Sci.*, 2016, **51**, 6097.

325 S. Wang, X. Li, Y. Liu, C. Zhang, X. Tan, G. Zeng, B. Song and L. Jiang, *J. Hazard. Mater.*, 2018, **342**, 177.

326 R. Sitko, P. Janik, B. Feist, E. Talik and A. Gagor, *ACS Appl. Mater. Interfaces*, 2014, **6**, 20144.

327 F. Zhang, B. Wang, S. He and R. Man, *J. Chem. Eng. Data*, 2014, **59**, 1719.

328 Y. Yang, Y. Xie, L. Pang, M. Li, X. Song, J. Wen and H. Zhao, *Langmuir*, 2013, **29**, 10727.

329 Y. L. F. Musico, C. M. Santos, M. L. P. Dalida and D. F. Rodrigues, *J. Mater. Chem. A*, 2013, **1**, 3789.

330 L. Hu, Z. Yang, L. Cui, Y. Li, H. H. Ngo, Y. Wang, Q. Wei, H. Ma, L. Yan and B. Du, *Chem. Eng. J.*, 2016, **287**, 545.

331 Z. Xu, Y. Zhang, X. Qian, J. Shi, L. Chen, B. Li, J. Niu and L. Liu, *Appl. Surf. Sci.*, 2014, **316**, 308.

332 W. Jia and S. Lu, *Korean J. Chem. Eng.*, 2014, **31**, 1265.

333 S. Kumar, R. R. Nair, P. B. Pillai, S. N. Gupta, M. A. R. Iyengar and A. K. Sood, *ACS Appl. Mater. Interfaces*, 2014, **6**, 17426.

334 X. Yang, C. Chen, J. Li, G. Zhao, X. Ren and X. Wang, *RSC Adv.*, 2012, **2**, 8821.

335 L. Cui, Y. Wang, L. Gao, L. Hu, L. Yan, Q. Wei and B. Du, *Chem. Eng. J.*, 2015, **281**, 1.

336 C. J. Madadrang, H. Y. Kim, G. Gao, N. Wang, J. Zhu, H. Feng, M. Gorring, M. L. Kasner and S. Hou, *ACS Appl. Mater. Interfaces*, 2012, **4**, 1186.

337 H. Hadi Najafabadi, M. Irani, L. Roshanfekr Rad, A. Heydari Haratameh and I. Haririan, *RSC Adv.*, 2015, **5**, 16532.

338 X. Zou, Y. Yin, Y. Zhao, D. Chen and S. Dong, *Mater. Lett.*, 2015, **150**, 59.

339 X. Li, H. Zhou, W. Wu, S. Wei, Y. Xu and Y. Kuang, *J. Colloid Interface Sci.*, 2015, **448**, 389.

340 C. Cheng, S. Li, J. Zhao, X. Li, Z. Liu, L. Ma, X. Zhang, S. Sun and C. Zhao, *Chem. Eng. J.*, 2013, **228**, 468.

341 S. Luo, X. Xu, G. Zhou, C. Liu, Y. Tang and Y. Liu, *J. Hazard. Mater.*, 2014, **274**, 145.

342 Y. Wang, S. Liang, B. Chen, F. Guo, S. Yu and Y. Tang, *PLoS One*, 2013, **8**, e65634.

343 V. R. Dandu Kamakshi Gari and M. Kim, *Monatsh. Chem.*, 2015, **146**, 1445.

344 L. Cui, Y. Wang, L. Hu, L. Gao, B. Du and Q. Wei, *RSC Adv.*, 2015, **5**, 9759.

345 G. Zhou, C. Liu, Y. Tang, S. Luo, Z. Zeng, Y. Liu, R. Xu and L. Chu, *Chem. Eng. J.*, 2015, **280**, 275.

346 L. Yang, Z. Li, G. Nie, Z. Zhang, X. Lu and C. Wang, *Appl. Surf. Sci.*, 2014, **307**, 601.

347 M. Tan, X. Liu, W. Li and H. Li, *J. Chem. Eng. Data*, 2015, **60**, 1469.

348 J. Yang, J.-X. Wu, Q.-F. Lü and T.-T. Lin, *ACS Sustainable Chem. Eng.*, 2014, **2**, 1203.

349 Z. Dong, F. Zhang, D. Wang, X. Liu and J. Jin, *J. Solid State Chem.*, 2015, **224**, 88.

350 S. Sheshmani, M. Akhundi Nematzadeh, S. Shokrollahzadeh and A. Ashori, *Int. J. Biol. Macromol.*, 2015, **80**, 475.

351 R. Sitko, P. Janik, B. Zawisza, E. Talik, E. Margui and I. Queralt, *Anal. Chem.*, 2015, **87**, 3535.

352 Y. Q. He, N. N. Zhang and X. D. Wang, *Chin. Chem. Lett.*, 2011, **22**, 859.

353 Y. Wang, T. Yan, L. Gao, L. Cui, L. Hu, L. Yan, B. Du and Q. Wei, *Desalin. Water Treat.*, 2016, **57**, 3975.

354 L. Fan, C. Luo, M. Sun, X. Li and H. Qiu, *Colloids Surf., B*, 2013, **103**, 523.

355 X. Guo, B. Du, Q. Wei, J. Yang, L. Hu, L. Yan and W. Xu, *J. Hazard. Mater.*, 2014, **278**, 211.

356 R. Sitko, B. Zawisza, E. Talik, P. Janik, G. Osoba, B. Feist and E. Malicka, *Anal. Chim. Acta*, 2014, **834**, 22.

357 H. T. Xing, J. H. Chen, X. Sun, Y. H. Huang, Z. B. Su, S. R. Hu, W. Weng, S. X. Li, H. X. Guo, W. B. Wu, Y. S. He, F. M. Li and Y. Huang, *Chem. Eng. J.*, 2015, **263**, 280.

358 Y. Yang, W.-Q. Wu, H.-H. Zhou, Z.-Y. Huang, T.-T. Ye, R. Liu and Y.-F. Kuang, *J. Cent. South Univ.*, 2014, **21**, 2826.

359 L. Li, Z. Wang, P. Ma, H. Bai, W. Dong and M. Chen, *J. Polym. Res.*, 2015, **22**, 150.

360 T. Jiang, W. Liu, Y. Mao, L. Zhang, J. Cheng, M. Gong, H. Zhao, L. Dai, S. Zhang and Q. Zhao, *Chem. Eng. J.*, 2015, **259**, 603.

361 W. Wu, Y. Yang, H. Zhou, T. Ye, Z. Huang, R. Liu and Y. Kuang, *Water, Air, Soil Pollut.*, 2012, **224**, 1372.

362 I. E. Mejias Carpio, J. D. Mangadlao, H. N. Nguyen, R. C. Advincula and D. F. Rodrigues, *Carbon*, 2014, **77**, 289.

363 D. Chen, H. Zhang, K. Yang and H. Wang, *J. Hazard. Mater.*, 2016, **310**, 179.

364 X.-J. Hu, Y.-G. Liu, H. Wang, A.-W. Chen, G.-M. Zeng, S.-M. Liu, Y.-M. Guo, X. Hu, T.-T. Li, Y.-Q. Wang, L. Zhou and S.-H. Liu, *Sep. Purif. Technol.*, 2013, **108**, 189.

365 W. M. Algothmi, N. M. Bandaru, Y. Yu, J. G. Shapter and A. V. Ellis, *J. Colloid Interface Sci.*, 2013, **397**, 32.

366 Y. Wang, X. Liu, H. Wang, G. Xia, W. Huang and R. Song, *J. Colloid Interface Sci.*, 2014, **416**, 243.

367 V. P. Chauke, A. Maity and A. Chetty, *J. Mol. Liq.*, 2015, **211**, 71.

368 S. Li, X. Lu, Y. Xue, J. Lei, T. Zheng and C. Wang, *PLoS One*, 2012, **7**, e43328.

369 Y. Lei, F. Chen, Y. Luo and L. Zhang, *J. Mater. Sci.*, 2014, **49**, 4236.

370 A. S. K. Kumar, S. S. Kakan and N. Rajesh, *Chem. Eng. J.*, 2013, **230**, 328.

371 H. Ge and Z. Ma, *Carbohydr. Polym.*, 2015, **131**, 280.

372 X. Yuan, Y. Wang, J. Wang, C. Zhou, Q. Tang and X. Rao, *Chem. Eng. J.*, 2013, **221**, 204.

373 H. Jabeen, V. Chandra, S. Jung, J. W. Lee, K. S. Kim and S. B. Kim, *Nanoscale*, 2011, **3**, 3583.

374 L. Li, C. Luo, X. Li, H. Duan and X. Wang, *Int. J. Biol. Macromol.*, 2014, **66**, 172.

375 L. Li, H. Duan, X. Wang and C. Luo, *New J. Chem.*, 2014, **38**, 6008.

376 L. Li, F. Liu, H. Duan, X. Wang, J. Li, Y. Wang and C. Luo, *Colloids Surf., B*, 2016, **141**, 253.

377 F.-Y. Guo, Y.-G. Liu, H. Wang, G.-M. Zeng, X.-J. Hu, B.-H. Zheng, T.-T. Li, X.-F. Tan, S.-F. Wang and M.-M. Zhang, *RSC Adv.*, 2015, **5**, 45384.

378 V. Chandra and K. S. Kim, *Chem. Commun.*, 2011, **47**, 3942.

379 Y. Zhang, T. Yan, L. Yan, X. Guo, L. Cui, Q. Wei and B. Du, *J. Mol. Liq.*, 2014, **198**, 381.

380 F. Najafi, O. Moradi, M. Rajabi, M. Asif, I. Tyagi, S. Agarwal and V. K. Gupta, *J. Mol. Liq.*, 2015, **208**, 106.

381 F. Fang, L. Kong, J. Huang, S. Wu, K. Zhang, X. Wang, B. Sun, Z. Jin, J. Wang, X.-J. Huang and J. Liu, *J. Hazard. Mater.*, 2014, **270**, 1.

382 L. Liu, C. Li, C. Bao, Q. Jia, P. Xiao, X. Liu and Q. Zhang, *Talanta*, 2012, **93**, 350.

383 H. Qi, H. Liu and Y. Gao, *J. Mol. Liq.*, 2015, **208**, 394.

384 F. Peng, T. Luo, L. Qiu and Y. Yuan, *Mater. Res. Bull.*, 2013, **48**, 2180.

385 S. Chen, J. Hong, H. Yang and J. Yang, *J. Environ. Radioact.*, 2013, **126**, 253.

386 H. Cheng, K. Zeng and J. Yu, *J. Radioanal. Nucl. Chem.*, 2013, **298**, 599.

387 L. Chen, D. Zhao, S. Chen, X. Wang and C. Chen, *J. Colloid Interface Sci.*, 2016, **472**, 99.

388 M. Zambianchi, M. Durso, A. Liscio, E. Treossi, C. Bettini, M. L. Capobianco, A. Aluigi, A. Kovtun, G. Ruani, F. Corticelli, M. Brucale, V. Palermo, M. L. Navacchia and M. Melucci, *Chem. Eng. J.*, 2017, **326**, 130.

389 H. Gu, S. B. Rapole, Y. Huang, D. Cao, Z. Luo, S. Wei and Z. Guo, *J. Mater. Chem. A*, 2013, **1**, 2011.

390 M. Bhaumik, A. Maity, V. V. Srinivasu and M. S. Onyango, *J. Hazard. Mater.*, 2011, **190**, 381.

391 Y. Wang, B. Zou, T. Gao, X. Wu, S. Lou and S. Zhou, *J. Mater. Chem.*, 2012, **22**, 9034.

392 G. Chillemi, G. Mancini, N. Sanna, V. Barone, S. Della Longa, M. Benfatto, N. V. Pavel and P. D'Angelo, *J. Am. Chem. Soc.*, 2007, **129**, 5430.

393 M.-R. Gao, M. K. Y. Chan and Y. Sun, *Nat. Commun.*, 2015, **6**, 7493.

394 J. Zheng, H. Zhang, S. Dong, Y. Liu, C. Tai Nai, H. Suk Shin, H. Young Jeong, B. Liu and K. Ping Loh, *Nat. Commun.*, 2014, **5**, 2995.

395 K. Ai, C. Ruan, M. Shen and L. Lu, *Adv. Funct. Mater.*, 2016, **26**, 5542.

396 B. Li, Y. Zhang, D. Ma, Z. Shi and S. Ma, *Nat. Commun.*, 2014, **5**, 5537.

397 X. Feng, G. E. Fryxell, L. Q. Wang, A. Y. Kim, J. Liu and K. M. Kemner, *Science*, 1997, **276**, 923.

398 S. Bag, P. N. Trikalitis, P. J. Chupas, G. S. Armatas and M. G. Kanatzidis, *Science*, 2007, **317**, 490.

399 C. Liu, F. Jia, Q. Wang, B. Yang and S. Song, *Appl. Mater. Today*, 2017, **9**, 220.

400 J. Wang, W. Zhang, X. Yue, Q. Yang, F. Liu, Y. Wang, D. Zhang, Z. Li and J. Wang, *J. Mater. Chem. A*, 2016, **4**, 3893.

401 F. Jia, Q. Wang, J. Wu, Y. Li and S. Song, *ACS Sustainable Chem. Eng.*, 2017, **5**, 7410.

402 L. Zhi, W. Zuo, F. Chen and B. Wang, *ACS Sustainable Chem. Eng.*, 2016, **4**, 3398.

403 K. P. Carter, A. M. Young and A. E. Palmer, *Chem. Rev.*, 2014, **114**, 4564.

404 C. Zhu, D. Du and Y. Lin, *2D Mater.*, 2015, **2**, 32004.

405 E. Treossi, M. Melucci, A. Liscio, M. Gazzano, P. Samorì and V. Palermo, *J. Am. Chem. Soc.*, 2009, **131**, 15576.

406 K. Chen, G. Lu, J. Chang, S. Mao, K. Yu, S. Cui and J. Chen, *Anal. Chem.*, 2012, **84**, 4057.

407 T. H. Kim, J. Lee and S. Hong, *J. Phys. Chem. C*, 2009, **113**, 19393.

408 Y. Huang, J. Guo, Y. Kang, Y. Ai and C. M. Li, *Nanoscale*, 2015, **7**, 19358.

409 C. M. Willemse, K. Tlhomelang, N. Jahed, P. G. Baker and E. I. Iwuoha, *Sensors*, 2011, **11**, 3970.

410 J. Gong, T. Zhou, D. Song and L. Zhang, *Sens. Actuators, B*, 2010, **150**, 491.

411 G. Lu, H. Li, C. Liusman, Z. Yin, S. Wu and H. Zhang, *Chem. Sci.*, 2011, **2**, 1817.

412 M. Zhang, C. Liao, Y. Yao, Z. Liu, F. Gong and F. Yan, *Adv. Funct. Mater.*, 2014, **24**, 1036.

413 Z.-H. Sheng, X.-Q. Zheng, J.-Y. Xu, W.-J. Bao, F.-B. Wang and X.-H. Xia, *Biosens. Bioelectron.*, 2012, **34**, 125.

414 F. Yan, M. Zhang and J. Li, *Adv. Healthcare Mater.*, 2014, **3**, 313.

415 Y. Wang, Y. Shao, D. W. Matson, J. Li and Y. Lin, *ACS Nano*, 2010, **4**, 1790.

416 C. Shan, H. Yang, J. Song, D. Han, A. Ivaska and L. Niu, *Anal. Chem.*, 2009, **81**, 2378.

417 X. Kang, J. Wang, H. Wu, I. A. Aksay, J. Liu and Y. Lin, *Biosens. Bioelectron.*, 2009, **25**, 901.

418 C. Shan, H. Yang, D. Han, Q. Zhang, A. Ivaska and L. Niu, *Biosens. Bioelectron.*, 2010, **25**, 1070.

419 Z. Wang, X. Zhou, J. Zhang, F. Boey and H. Zhang, *J. Phys. Chem. C*, 2009, **113**, 14071.

420 Y. Liu, D. Yu, C. Zeng, Z. Miao and L. Dai, *Langmuir*, 2010, **26**, 6158.

421 J. Luo, S. Jiang, H. Zhang, J. Jiang and X. Liu, *Anal. Chim. Acta*, 2012, **709**, 47.

422 H. Wu, J. Wang, X. Kang, C. Wang, D. Wang, J. Liu, I. A. Aksay and Y. Lin, *Talanta*, 2009, **80**, 403.

423 T. T. Baby, S. S. J. Aravind, T. Arockiadoss, R. B. Rakhi and S. Ramaprabhu, *Sens. Actuators, B*, 2010, **145**, 71.

424 S. Alwarappan, A. Erdem, C. Liu and C.-Z. Li, *J. Phys. Chem. C*, 2009, **113**, 8853.

425 G. Zeng, Y. Xing, J. Gao, Z. Wang and X. Zhang, *Langmuir*, 2010, **26**, 15022.

426 K. Zhou, Y. Zhu, X. Yang and C. Li, *Electroanalysis*, 2010, **22**, 259.

427 N. Q. Dung, D. Patil, T. T. Duong, H. Jung, D. Kim and S.-G. Yoon, *Sens. Actuators, B*, 2012, **166**, 103.

428 X. Dong, Y. Shi, W. Huang, P. Chen and L.-J. Li, *Adv. Mater.*, 2010, **22**, 1649.

429 M. Du, T. Yang and K. Jiao, *J. Mater. Chem.*, 2010, **20**, 9253.

430 O. Niwa, J. Jia, Y. Sato, D. Kato, R. Kurita, K. Maruyama, K. Suzuki and S. Hirono, *J. Am. Chem. Soc.*, 2006, **128**, 7144.

431 C. Wang, L. Zhang, Z. Guo, J. Xu, H. Wang, K. Zhai and X. Zhuo, *Microchim. Acta*, 2010, **169**, 1.

432 N. G. Shang, P. Papakonstantinou, M. McMullan, M. Chu, A. Stamboulis, A. Potenza, S. S. Dhesi and H. Marchetto, *Adv. Funct. Mater.*, 2008, **18**, 3506.

433 Y.-R. Kim, S. Bong, Y.-J. Kang, Y. Yang, R. K. Mahajan, J. S. Kim and H. Kim, *Biosens. Bioelectron.*, 2010, **25**, 2366.

434 C.-L. Sun, H.-H. Lee, J.-M. Yang and C.-C. Wu, *Biosens. Bioelectron.*, 2011, **26**, 3450.

435 C. X. Lim, H. Y. Hoh, P. K. Ang and K. P. Loh, *Anal. Chem.*, 2010, **82**, 7387.

436 S. Hou, M. L. Kasner, S. Su, K. Patel and R. Cuellari, *J. Phys. Chem. C*, 2010, **114**, 14915.

437 L. Wu, L. Feng, J. Ren and X. Qu, *Biosens. Bioelectron.*, 2012, **34**, 57.

438 L. Tan, K.-G. Zhou, Y.-H. Zhang, H.-X. Wang, X.-D. Wang, Y.-F. Guo and H.-L. Zhang, *Electrochem. Commun.*, 2010, **12**, 557.

439 F. Li, J. Chai, H. Yang, D. Han and L. Niu, *Talanta*, 2010, **81**, 1063.

440 Y. Fan, H.-T. Lu, J.-H. Liu, C.-P. Yang, Q.-S. Jing, Y.-X. Zhang, X.-K. Yang and K.-J. Huang, *Colloids Surf., B*, 2011, **83**, 78.

441 T. Peik-See, A. Pandikumar, H. Nay-Ming, L. Hong-Ngee and Y. Sulaiman, *Sensors*, 2014, **14**, 15227.

442 G. P. Keeley, A. O'Neill, M. Holzinger, S. Cosnier, J. N. Coleman and G. S. Duesberg, *Phys. Chem. Chem. Phys.*, 2011, **13**, 7747.

443 Y. Fang, S. Guo, C. Zhu, Y. Zhai and E. Wang, *Langmuir*, 2010, **26**, 11277.

444 S. Karapetis, S. Bratakou, G.-P. Nikoleli, C. Siontorou, D. Nikolelis and N. Tzamtzis, *Electroanalysis*, 2016, **28**, 2171.

445 Y. Huang, X. Dong, Y. Shi, C. M. Li, L.-J. Li and P. Chen, *Nanoscale*, 2010, **2**, 1485.

446 Y. H. Kwak, D. S. Choi, Y. N. Kim, H. Kim, D. H. Yoon, S.-S. Ahn, J.-W. Yang, W. S. Yang and S. Seo, *Biosens. Bioelectron.*, 2012, **37**, 82.

447 W. Fu, L. Feng, G. Panaitov, D. Kireev, D. Mayer, A. Offenhäusser and H.-J. Krause, *Sci. Adv.*, 2017, **3**, 1701247.

448 G. Liu, S. Rumyantsev, M. S. Shur and A. A. Balandin, *Appl. Phys. Lett.*, 2013, **102**, 93111.

449 B. Cai, S. Wang, L. Huang, Y. Ning, Z. Zhang and G.-J. Zhang, *ACS Nano*, 2014, **8**, 2632.

450 P. Alonso-Cristobal, P. Vilela, A. El-Sagheer, E. Lopez-Cabarcos, T. Brown, O. L. Muskens, J. Rubio-Retama and A. G. Kanaras, *ACS Appl. Mater. Interfaces*, 2015, **7**, 12422.

451 H. Dong, W. Gao, F. Yan, H. Ji and H. Ju, *Anal. Chem.*, 2010, **82**, 5511.

452 C. Liu, Z. Wang, H. Jia and Z. Li, *Chem. Commun.*, 2011, **47**, 4661.

453 L. Fan, Y. Hu, X. Wang, L. Zhang, F. Li, D. Han, Z. Li, Q. Zhang, Z. Wang and L. Niu, *Talanta*, 2012, **101**, 192.

454 J.-L. Chen, X.-P. Yan, K. Meng and S.-F. Wang, *Anal. Chem.*, 2011, **83**, 8787.

455 C.-H. Lu, H.-H. Yang, C.-L. Zhu, X. Chen and G.-N. Chen, *Angew. Chem., Int. Ed.*, 2009, **48**, 4785.

456 Y. Lin, Y. Tao, F. Pu, J. Ren and X. Qu, *Adv. Funct. Mater.*, 2011, **21**, 4565.

457 F. Li, Y. Huang, Q. Yang, Z. Zhong, D. Li, L. Wang, S. Song and C. Fan, *Nanoscale*, 2010, **2**, 1021.

458 X. Liu, L. Cao, W. Song, K. Ai and L. Lu, *ACS Appl. Mater. Interfaces*, 2011, **3**, 2944.

459 Z. Chen, L. Qiu, Y. Tian, Y.-I. Lee, X. Hou and L. Wu, *Anal. Methods*, 2017, **9**, 3105.

460 P. V. Shanta and Q. Cheng, *ACS Sens.*, 2017, **2**, 817.

461 Y. Song, K. Qu, C. Zhao, J. Ren and X. Qu, *Adv. Mater.*, 2010, **22**, 2206.

462 S. Alwarappan, C. Liu, A. Kumar and C.-Z. Li, *J. Phys. Chem. C*, 2010, **114**, 12920.

463 P. Wu, Q. Shao, Y. Hu, J. Jin, Y. Yin, H. Zhang and C. Cai, *Electrochim. Acta*, 2010, **55**, 8606.

464 Y. Zhang, Y. Wang, J. Jia and J. Wang, *Sens. Actuators, B*, 2012, **171**, 580.

465 M. Zhang, C. Liao, C. H. Mak, P. You, C. L. Mak and F. Yan, *Sci. Rep.*, 2015, **5**, 8311.

466 S. He, B. Song, D. Li, C. Zhu, W. Qi, Y. Wen, L. Wang, S. Song, H. Fang and C. Fan, *Adv. Funct. Mater.*, 2010, **20**, 453.

467 J. Balapanuru, J.-X. Yang, S. Xiao, Q. Bao, M. Jahan, L. Polavarapu, J. Wei, Q.-H. Xu and K. P. Loh, *Angew. Chem., Int. Ed.*, 2010, **49**, 6549.

468 Z. Wang, J. Zhang, P. Chen, X. Zhou, Y. Yang, S. Wu, L. Niu, Y. Han, L. Wang, P. Chen, F. Boey, Q. Zhang, B. Liedberg and H. Zhang, *Biosens. Bioelectron.*, 2011, **26**, 3881.

469 C.-H. Lu, J. Li, J.-J. Liu, H.-H. Yang, X. Chen and G.-N. Chen, *Chem. – Eur. J.*, 2010, **16**, 4889.

470 R. Devasenathipathy, V. Mani and S.-M. Chen, *Talanta*, 2014, **124**, 43.

471 J. Ding, S. Zhu, T. Zhu, W. Sun, Q. Li, G. Wei and Z. Su, *RSC Adv.*, 2015, **5**, 22935.

472 F. Gao, Q. Wang, N. Gao, Y. Yang, F. Cai, M. Yamane, F. Gao and H. Tanaka, *Biosens. Bioelectron.*, 2017, **97**, 238.

473 Z. Yang, Q. Sheng, S. Zhang, X. Zheng and J. Zheng, *Microchim. Acta*, 2017, **184**, 2219.

474 Y. Wang, Y. Li, L. Tang, J. Lu and J. Li, *Electrochem. Commun.*, 2009, **11**, 889.

475 J. Du, R. Yue, F. Ren, Z. Yao, F. Jiang, P. Yang and Y. Du, *Gold Bull.*, 2013, **46**, 137.

476 J. Ping, J. Wu, Y. Wang and Y. Ying, *Biosens. Bioelectron.*, 2012, **34**, 70.

477 G. P. Keeley, A. O'Neill, N. McEvoy, N. Peltekis, J. N. Coleman and G. S. Duesberg, *J. Mater. Chem.*, 2010, **20**, 7864.

478 S. Guo, D. Wen, Y. Zhai, S. Guo and E. Wang, *ACS Nano*, 2010, **4**, 3959.

479 K. Zhou, Y. Zhu, X. Yang, J. Luo, C. Li and S. Luan, *Electrochim. Acta*, 2010, **55**, 3055.

480 L. Li, Z. Du, S. Liu, Q. Hao, Y. Wang, Q. Li and T. Wang, *Talanta*, 2010, **82**, 1637.

481 A. Ciesielski and P. Samorì, *Chem. Soc. Rev.*, 2014, **43**, 381.

482 J. N. Coleman, *Acc. Chem. Res.*, 2013, **46**, 14.

483 F. Bonaccorso, A. Lombardo, T. Hasan, Z. Sun, L. Colombo and A. C. Ferrari, *Mater. Today*, 2012, **15**, 564.

484 J. Wang, *Chem. Rev.*, 2008, **108**, 814.

485 L. Tang, Y. Wang, Y. Li, H. Feng, J. Lu and J. Li, *Adv. Funct. Mater.*, 2009, **19**, 2782.

486 S. Wu, Z. Zeng, Q. He, Z. Wang, S. J. Wang, Y. Du, Z. Yin, X. Sun, W. Chen and H. Zhang, *Small*, 2012, **8**, 2264.

487 N. N. Thrangattu, S. R. V. Chiranjeevi and A. Subbiah, *Nanotechnology*, 2014, **25**, 409601.

488 T. Wang, H. Zhu, J. Zhuo, Z. Zhu, P. Papakonstantinou, G. Lubarsky, J. Lin and M. Li, *Anal. Chem.*, 2013, **85**, 10289.

489 X. Wang, F. Nan, J. Zhao, T. Yang, T. Ge and K. Jiao, *Biosens. Bioelectron.*, 2015, **64**, 386.

490 G.-X. Wang, W.-J. Bao, J. Wang, Q.-Q. Lu and X.-H. Xia, *Electrochem. Commun.*, 2013, **35**, 146.

491 J. Tang, Y. Quan, Y. Zhang, M. Jiang, A. M. Al-Enizi, B. Kong, T. An, W. Wang, L. Xia, X. Gong and G. Zheng, *Nanoscale*, 2016, **8**, 5786.

492 M. Kukkar, A. Sharma, P. Kumar, K.-H. Kim and A. Deep, *Anal. Chim. Acta*, 2016, **939**, 101.

493 S. Su, H. Sun, F. Xu, L. Yuwen, C. Fan and L. Wang, *Microchim. Acta*, 2014, **181**, 1497.

494 S. Su, H. Sun, F. Xu, L. Yuwen and L. Wang, *Electroanalysis*, 2013, **25**, 2523.

495 J. Chao, X. Han, H. Sun, S. Su, L. Weng and L. Wang, *Sci. China: Chem.*, 2016, **59**, 332.

496 K.-J. Huang, Y.-J. Liu, J.-Z. Zhang and Y.-M. Liu, *Anal. Methods*, 2014, **6**, 8011.

497 J. Huang, Y. He, J. Jin, Y. Li, Z. Dong and R. Li, *Electrochim. Acta*, 2014, **136**, 41.

498 R. Yang, J. Zhao, M. Chen, T. Yang, S. Luo and K. Jiao, *Talanta*, 2015, **131**, 619.

499 T. Lin, L. Zhong, L. Guo, F. Fu and G. Chen, *Nanoscale*, 2014, **6**, 11856.

500 T. Lin, L. Zhong, Z. Song, L. Guo, H. Wu, Q. Guo, Y. Chen, F. Fu and G. Chen, *Biosens. Bioelectron.*, 2014, **62**, 302.

501 Y. Zhang, B. Zheng, C. Zhu, X. Zhang, C. Tan, H. Li, B. Chen, J. Yang, J. Chen, Y. Huang, L. Wang and H. Zhang, *Adv. Mater.*, 2015, **27**, 935.

502 C. Tan, P. Yu, Y. Hu, J. Chen, Y. Huang, Y. Cai, Z. Luo, B. Li, Q. Lu, L. Wang, Z. Liu and H. Zhang, *J. Am. Chem. Soc.*, 2015, **137**, 10430.

503 J. Huang, L. Ye, X. Gao, H. Li, J. Xu and Z. Li, *J. Mater. Chem. B*, 2015, **3**, 2395.

504 J. Lee, P. Dak, Y. Lee, H. Park, W. Choi, M. A. Alam and S. Kim, *Sci. Rep.*, 2014, **4**, 7352.

505 H.-Y. Park, S. R. Dugasani, D.-H. Kang, G. Yoo, J. Kim, B. Gnapareddy, J. Jeon, M. Kim, Y. J. Song, S. Lee, J. Heo, Y. J. Jeon, S. H. Park and J.-H. Park, *Sci. Rep.*, 2016, **6**, 35733.

506 D.-W. Lee, J. Lee, I. Y. Sohn, B.-Y. Kim, Y. M. Son, H. Bark, J. Jung, M. Choi, T. H. Kim, C. Lee and N.-E. Lee, *Nano Res.*, 2015, **8**, 2340.

507 Kenry, A. Geldert, Z. Lai, Y. Huang, P. Yu, C. Tan, Z. Liu, H. Zhang and C. T. Lim, *Small*, 2017, **13**, 1601925.

508 H. Sun, J. Chao, X. Zuo, S. Su, X. Liu, L. Yuwen, C. Fan and L. Wang, *RSC Adv.*, 2014, **4**, 27625.

509 X. Xia, Z. Zheng, Y. Zhang, X. Zhao and C. Wang, *Sens. Actuators, B*, 2014, **192**, 42.

510 H. Song, Y. Ni and S. Kokot, *Biosens. Bioelectron.*, 2014, **56**, 137.

511 K.-J. Huang, L. Wang, J. Li and Y.-M. Liu, *Sens. Actuators, B*, 2013, **178**, 671.

512 Y. Huang, Y. Shi, H. Y. Yang and Y. Ai, *Nanoscale*, 2015, **7**, 2245.

513 J. Shan, J. Li, X. Chu, M. Xu, F. Jin, X. Wang, L. Ma, X. Fang, Z. Wei and X. Wang, *RSC Adv.*, 2018, **8**, 7942.

514 X. Hu, W. Shao, X. Hang, X. Zhang, W. Zhu and Y. Xie, *Angew. Chem., Int. Ed.*, 2016, **55**, 5733.

515 J. Lu, *Carbon*, 2007, **45**, 1599.

516 K. Chang and W. Chen, *Chem. Commun.*, 2011, **47**, 4252.

517 K. Chang and W. Chen, *ACS Nano*, 2011, **5**, 4720.

518 E. G. Da Silveira Firmiano, A. C. Rabelo, C. J. Dalmaschio, A. N. Pinheiro, E. C. Pereira, W. H. Schreiner and E. R. Leite, *Adv. Energy Mater.*, 2014, **4**, 1301380.

519 X. Zhao, X. Xia, S. Yu and C. Wang, *Anal. Methods*, 2014, **6**, 9375.

520 K. Pramoda, K. Moses, U. Maitra and C. N. R. Rao, *Electroanalysis*, 2015, **27**, 1892.

521 K. Duan, Y. Du, Q. Feng, X. Ye, H. Xie, M. Xue and C. Wang, *ChemCatChem*, 2014, **6**, 1873.

522 H.-L. Shuai, K.-J. Huang and Y.-X. Chen, *J. Mater. Chem. B*, 2016, **4**, 1186.

523 K. Zhang, H. Sun and S. Hou, *Anal. Methods*, 2016, **8**, 3780.

524 A. F. Khan, D. A. C. Brownson, E. P. Randviir, G. C. Smith and C. E. Banks, *Anal. Chem.*, 2016, **88**, 9729.

525 A. F. Khan, D. A. C. Brownson, C. W. Foster, G. C. Smith and C. E. Banks, *Analyst*, 2017, **142**, 1756.

526 Y. Zhan, J. Yan, M. Wu, L. Guo, Z. Lin, B. Qiu, G. Chen and K.-Y. Wong, *Talanta*, 2017, **174**, 365.

527 Q. Cai, L. H. Li, Y. Yu, Y. Liu, S. Huang, Y. Chen, K. Watanabe and T. Taniguchi, *Phys. Chem. Chem. Phys.*, 2015, **17**, 7761.

528 R. B. Rakhi, P. Nayak, C. Xia and H. N. Alshareef, *Sci. Rep.*, 2016, **6**, 36422.

529 F. Wang, C. Yang, M. Duan, Y. Tang and J. Zhu, *Biosens. Bioelectron.*, 2015, **74**, 1022.

530 S. Yan, B. Wang, Z. Wang, D. Hu, X. Xu, J. Wang and Y. Shi, *Biosens. Bioelectron.*, 2016, **80**, 34.

531 Y. T. Yew, Z. Sofer, C. C. Mayorga-Martinez and M. Pumera, *Mater. Chem. Front.*, 2017, **1**, 1130.

Nanoscale

PAPER

View Article Online
View Journal | View Issue

Cite this: *Nanoscale*, 2020, **12**, 18733

Reduced graphene oxide–silsesquioxane hybrid as a novel supercapacitor electrode†

Włodzimierz Czepa,*[a,b] Samanta Witomska,[a,b] Artur Ciesielski *[b,c] and Paolo Samorì *[c]

Received 13th July 2020,
Accepted 12th August 2020

DOI: 10.1039/d0nr05226d

rsc.li/nanoscale

Supercapacitor energy storage devices recently garnered considerable attention due to their cost-effectiveness, eco-friendly nature, high power density, moderate energy density, and long-term cycling stability. Such figures of merit render supercapacitors unique energy sources to power portable electronic devices. Among various energy storage materials, graphene-related materials have established themselves as ideal electrodes for the development of elite supercapacitors because of their excellent electrical conductivity, high surface area, outstanding mechanical properties combined with the possibility to tailor various physical and chemical properties *via* chemical functionalization. Increasing the surface area is a powerful strategy to improve the performance of supercapacitors. Here, modified polyhedral oligosilsesquioxane (POSS) is used to improve the electrochemical performance of reduced graphene oxide (rGO) through the enhancement of porosity and the extension of interlayer space between the sheets allowing efficient electrolyte transport. rGO–POSS hybrids exhibited a high specific capacitance of 174 F g^{-1}, power density reaching 2.25 W cm^{-3}, and high energy density of 41.4 mW h cm^{-3} endowed by the introduction of POSS spacers. Moreover, these electrode materials display excellent durability reaching >98% retention after 5000 cycles.

1. Introduction

The ever-increasing energy demand has triggered an intensive search for sustainable and renewable power sources which has led to the emergence of multiple technological solutions including clean energy conversion and storage devices. In fact, nowadays the most employed energy sources such as fossil fuels, coal, oil, and natural gasses are neither ecofriendly nor everlasting. Fossil fuel burning releases harmful gasses, resulting in continuous deterioration of the global environment. During the past decades, renewable energy sources have become extremely important because of their sustainability and efficiency combined with their pollution-free processability. Among them, supercapacitors (SCs) have received considerable attention as modern portable energy storage devices featuring high power density, ultrafast charge–discharge, long cycling life, high operating durability, and low maintenance.[1,2] Since the first demonstration of SC in 1957 by Becker using porous carbon electrodes, much progress has been made in this research area. Albeit a vast number of electrode materials have been reported so far, carbon nanomaterials have attracted the greatest attention due to their unique physicochemical and electrochemical properties. In particular, the use of graphitic carbon nanomaterials yielded an increase in the overall performance of SCs. Moreover, carbonaceous electrodes represent an ecologically friendly alternative for traditional energy storage devices such as batteries.[3,4] Considering the mechanism of charge storage, supercapacitors can be classified as electrical double layer capacitors (EDLCs) based on electrostatic adsorption of electrolyte ions onto the surface of electrodes and pseudocapacitors (PCs), additionally supported by faradaic redox reactions. Notably, EDLCs are beneficial especially in terms of higher power density and longer cyclic stability but they exhibit lower power density than PCs.[5,6]

Among all carbon-related materials that can be used as electrodes for EDLCs, graphene possesses the largest surface area (up to 2700 m^2 g^{-1}). However, graphene-based supercapacitors exhibit significant quasi-rectangular curves at lower scan rates (1–10 mV s^{-1}) due to their densely packed layered structure, kinetically limiting electrolyte ion penetration at higher scan rates, thereby resulting in overall electrochemical performance decrease.[7]

---

[a] *Faculty of Chemistry, Adam Mickiewicz University, ul. Uniwersytetu Poznańskiego 8, 61614 Poznań, Poland*
[b] *Center for Advanced Technologies, Adam Mickiewicz University, Uniwersytetu Poznańskiego 10, 61614 Poznań, Poland*
[c] *Université de Strasbourg, CNRS, ISIS, 8 alleé Gaspard Monge, 67000 Strasbourg, France. E-mail: ciesielski@unistra.fr, samori@unistra.fr*

† Electronic supplementary information (ESI) available: SEM/EDX picture, FT-IR spectra, XRD patterns, BET isotherms, charge–discharge curves, stability investigations, and comparison of rGO-based electrode properties. See DOI: 10.1039/d0nr05226d

Three-dimensional (3D) graphene-based architectures have gathered remarkable attention for EDLC applications owing to their highly accessible surface area, low density, structural interconnectivity (micro-, meso- and macro-interconnected pores), excellent electrical conductivity, and good mechanical features. Overall, the supercapacitance performance of 3D graphene-based SCs has been correlated to the enhanced accessibility of the electrode surface to electrolyte ions, which also provides conductive channels for electron transfer. Such an increase in the dimensionality can be beneficial in terms of the physicochemical properties of hybrid materials.[8–10] Therefore, the use of porous scaffolds can be an asset, especially in terms of specific surface area, the presence of the pores with controllable size, and effective charge transport.

Graphene-based materials, which are popular because of their exceptional electrical and mechanical properties, can be produced either *via* bottom-up or top-down strategies.[11–14] Among the various GRMs, graphene oxide (GO) offers multiple advantageous features including good dispersibility in aqueous media and easy chemical functionalization.[15,16] Notably, GO exhibits modest electrical properties compared to pristine graphene due to the existence of multiple structural defects in the sp^2 lattice combined with the presence of various oxygen-containing groups.[17,18] However, GO can be reduced leading to reduced graphene oxide (rGO). The latter, which can have a sheet resistance of a few $\Omega\ \square^{-1}$, can be efficiently used as an electrode in different device types.[19] In a simplistic model, the conductivity of graphene-based materials is proportional to the carbon to oxygen ratio. However, other parameters such as geometrical aspects, including sheet orientation and percolation effects, also play a non-negligible role.[20–22] A plethora of reduction pathways to restore to a great extent the π-conjugated electronic structure were proposed and widely applied, including chemical, thermal, electrochemical, and microwave-assisted processes.[20,23–26] Reduction is a viable approach to generate large quantities of high-quality rGO with moderate oxygen content, while the use of structural scaffolding might support electrochemical processes that require effective ion penetration.[27] Chemically reduced GO was previously investigated as a neat component for energy storage applications reaching a moderate capacitance ranging from 67 to 100 F g^{-1}, mainly due to the limited accessibility for electrolyte molecules. The more effective rGO-based electrodes usually exhibit lower cyclability and durability while tested in aqueous media or even require the use of organic electrolytes.[28,29]

Notably, chemically or thermally reduced graphene oxide sheets, which combine high electrical conductivity and electrochemical stability, are unfortunately prone to undergo a substantial restacking when producing macroscopic assemblies from a liquid suspension. This restacking drastically reduces the material's surface area leading to dramatic decreases in the energy density of the graphene film-based supercapacitors. However, the inhibition of the restacking of graphene sheets can be achieved by the use of molecular spacers to guarantee high specific surface porosity which is required for effective electrolyte penetration.[30] A vast number of approaches using the covalent and non-covalent functionalizations of graphene-based materials have been explored leading to superior electrochemical performance.[31–33] It was demonstrated that the appropriate selection of functional molecules allows fine-tuning the interlaminar distance between rGO sheets and might result in higher capacitance and improved durability of electrodes.[34]

Polyhedral oligomeric silsesquioxanes (POSSs) are inorganic molecules comprising a Si–O cage-like core surrounded by organic sites exposing the functional groups.[35] By exploiting their well-defined structure, high stability and good solubility, POSSs have been used as attractive functional building blocks to develop nanohybrid materials, in particular when combined with porous carbon structures.[36,37] The introduction of silsesquioxanes makes it possible to endow the materials with enhanced durability, rigidity, and higher specific surface area. Moreover, the presence of POSSs can enhance the electrochemical performance of graphene-based materials due to the pseudocapacitive co-contribution and expansion of the interlayer space of tightly packed nanosheets.

Here, we report the modification of GO with OctaAmmonium-POSS followed by the chemical reduction of the hybrid to generate rGO–POSS electrodes for supercapacitors. The latter device exhibited an enhanced specific capacitance of 173 F g^{-1}, thus comparable to the state-of-the-art chemical rGO materials. The introduction of POSS resulted in a porous structure with a specific surface area of 180 $m^2\ g^{-1}$, with a moderate pore size of 4 nm allowing effective electrolyte penetration and thereby ensuring effective electrochemical performance and exceptional cyclability. The prepared electrodes exhibited high durability and excellent capacitance retention (>98%) after 5000 cycles. Moreover, the use of molecular spacers provided a high volumetric energy density of 41.4 mW h cm^{-3}. These results provide clear evidence regarding the beneficial role of POSS in improving the electrochemical performance *via* simple chemical functionalization of rGO.

2. Results and discussion

2.1 Synthesis and characterizations

The synthesis of rGO–POSS was performed by using the condensation reaction between primary amine moieties, which are generated upon the hydrolysis of ammonium chloride on the termini of OctaAmmonium POSS and epoxides present on the GO surface, mainly *via* the nucleophilic ring opening reaction yielding covalent cross-links of the two components (Fig. 1). Subsequently, the isolated product was chemically reduced with hydrazine to get rid of the excess of oxygen species and non-covalently attached POSS molecules.

Scanning electron microscopy (SEM) and energy-dispersive X-ray spectroscopy (EDS) analysis made it possible to gain insight into the morphology and elemental distribution in the final material. Fig. 2a reveals that rGO–POSS possesses a

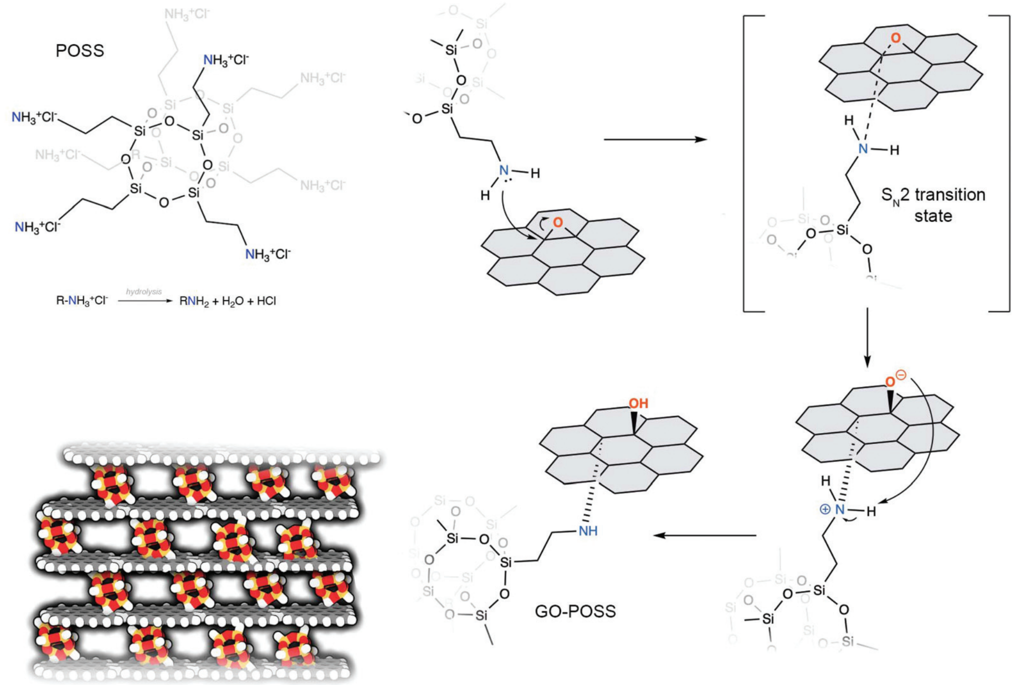

Fig. 1 Scheme representing the mechanism of functionalization of GO with OctaAmmonium POSS.

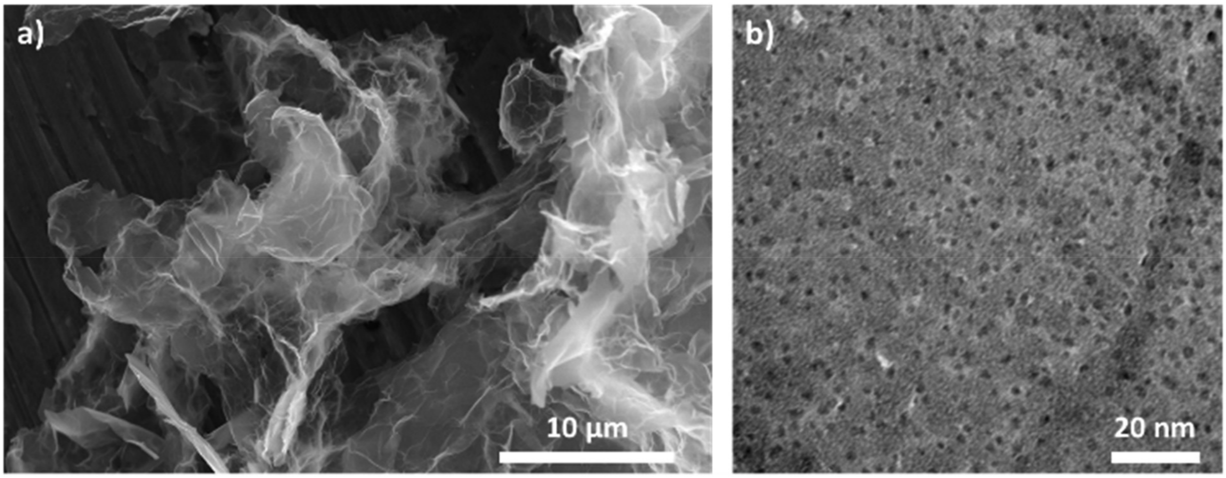

Fig. 2 (a) SEM picture of rGO–POSS and (b) HR-TEM investigation of rGO–POSS hybrid material.

folded structure typical of graphene oxide-based hybrids.[38–40] Elemental mapping confirms the homogeneous distribution of the elements in the final material *i.e.* silicon atoms dispersed in the matrix of rGO, thereby excluding the formation of aggregates (Fig. S1†). High-resolution transmission electron microscopy (HR-TEM) was performed to reveal the porosity provided by the evenly spread POSS cages in the matrix of reduced graphene oxide (Fig. 2b). The estimated average POSS loading amounts to 1 POSS for each 10 nm^2. The Fourier transform infrared spectroscopy (FT-IR) spectra of GO, POSS, GO–POSS, and rGO–POSS portrayed in Fig. S2† provide evidences for the covalent functionalization of rGO with POSS. The spectra of pristine GO displays typical peaks associated with C=O stretching at 1724 cm^{-1}, C=C stretching at 1624 cm^{-1}, C–O stretching of epoxy groups at 1216 and 1054 cm^{-1}, and a broad peak between 3000 and 3500 cm^{-1} corresponding to hydroxyl species stretching. The functionalization with POSS molecules determined the appearance of a strong absorption peak at 1573 cm^{-1} corresponding to N–H stretching vibration, and a broad peak at 3276 cm^{-1} corresponding to N–H vibration of secondary amines suggesting that most of the $-NH_2$ groups took part in covalent bonding to the surface of graphene oxide.[41] Moreover, due to hydrazine reduction, we can observe a significant decrease in hydroxyl species around

3500 cm^{-1}. Notably, the decreased intensity of the peaks corresponding to the C–O bonds results from the functionalization and chemical reduction of the final material and was previously reported while cross-linking GO with amine-based functional molecules.[42,43] In addition, the asymmetric peaks at 2937 and 2870 cm^{-1} are assigned to the C–H stretching vibrations of the alkyl group –CH_2. The formation of the rGO–POSS composite was further evidenced by the appearance of bands characteristic of siloxane groups *i.e.* Si–O–Si (1130 cm^{-1}) and Si–C (908 cm^{-1}) coming from the core of the POSS cage.

X-ray photoelectron spectroscopy (XPS) was exploited to obtain information on the chemical composition of materials by identifying the relevant chemical elements and bonds present in the neat and functionalized GO (see Fig. 3). The C 1s spectra of GO show peaks corresponding to the C–C (284.6 eV), C–O (286.4 eV), C═O (287.5 eV), and COOH (288.3 eV) bonds. Comparably, the C 1s spectra of the functionalized GO–POSS appear differently and feature peaks at 284.6 eV, 285.5 eV, 286.4 eV, and 287.5 eV, which can be assigned to C–C, C–N, C–O, and C═O bonds, respectively. However, the C 1s spectra of rGO–POSS exhibit a significant decrease of C–O bonds indicating the successful reduction of unreacted oxygen group on the surface of GO-POSS (Fig. 3c). As expected, the high-resolution N 1s spectra of the GO sample does not show the presence of a nitrogen signal. Conversely, signals observed in the GO-POSS sample can be deconvoluted into two peaks, *i.e.* at 398.9 eV and 401.2 eV, which can be attributed to the secondary (N-sp^3 bonds) and protonated primary amines, respectively.[27] Notably, the existence of the external –NH_3^+ groups suggests that only the majority of amines undergo covalent grafting onto GO sheets with the coexistence of electrostatic interactions mostly at the edges of the GO surface and form the ammonium-carboxylate species. Interestingly, the non-covalent grafted molecules were easily removed from the GO-POSS during the reduction step, which was previously reported in the case of functionalization and reduction of graphene-based materials.[44] Moreover, the N 1s spectra of rGO–POSS reveal a decrease in the signal corresponding to the protonated primary amines (401.2 eV). In addition, a new peak at

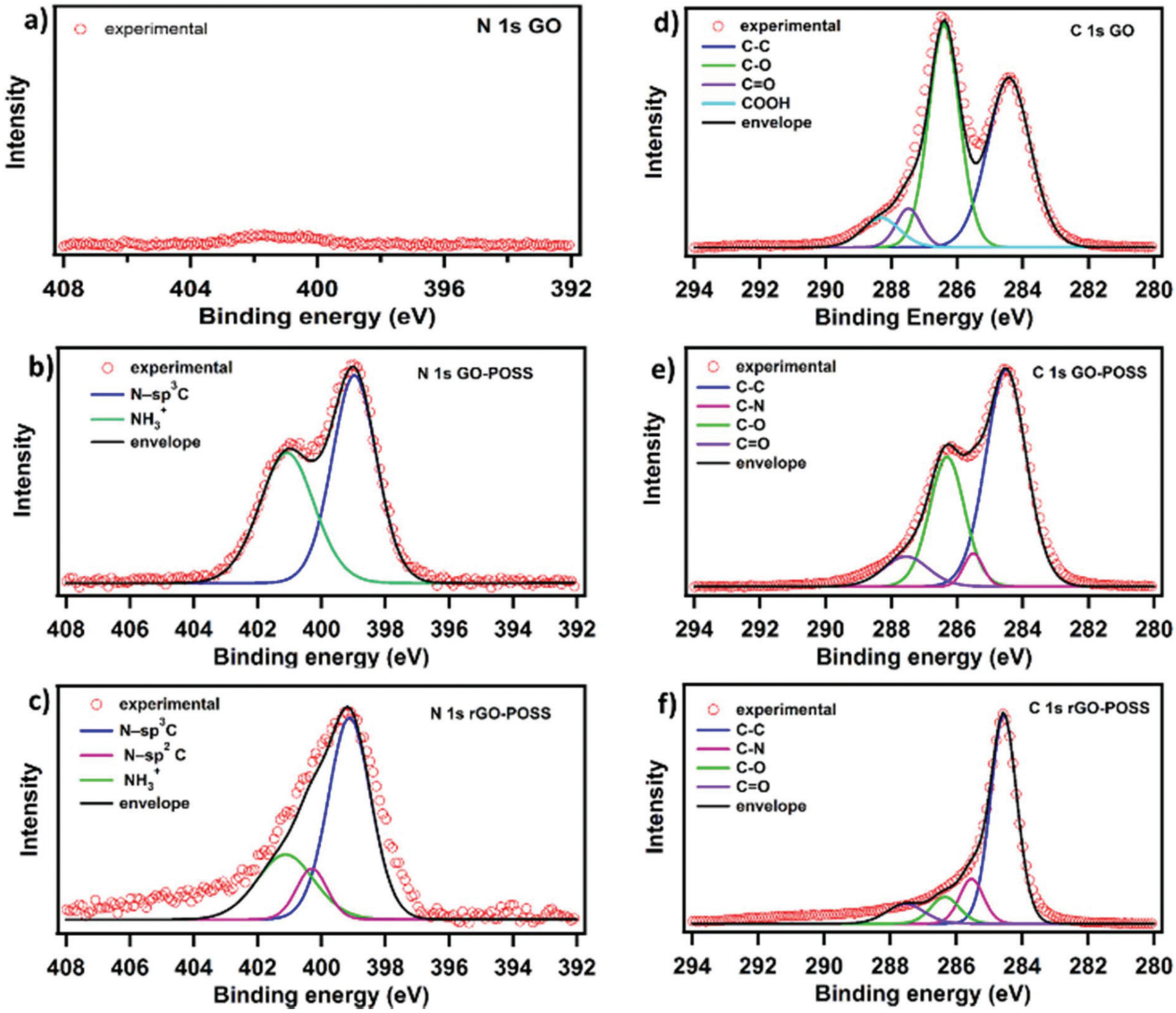

Fig. 3 Comparison of XPS high-resolution C 1s and N 1s spectra of (a and d) GO, (b and e) GO–POSS, and (c and f) rGO–POSS.

400.2 eV on the N 1s spectra of GO–POSS after hydrazine treatment indicates minor nitrogen inclusion mostly on the edges of the GO sheets forming N-sp^2 species.[45] Furthermore, determination of the C/N ratio, which amounts to 10.2 and 25.4 for GO–POSS and rGO–POSS, respectively, confirms the removal of non-covalently attached POSS molecules.[44]

Thermogravimetric analysis was performed to investigate the thermal stability and composition of GO, POSS, and rGO–POSS. The GO curve displays about 45% weight loss in the range of 150–300 °C due to oxygen functional group degradation. POSS exhibits good thermal stability up to 340° when the organic aminopropyl-species start to decompose with increasing temperature leading to the formation of amorphous SiO_2.[46,47] The rGO–POSS curve shows similar mass drops corresponding to organic functional group degradation with the 20% mass residue coming from the POSS Si–O core.

Powder X-ray diffraction investigations were performed to study POSS intercalation into the 3D structure and the structural orientation changes due to functionalization. Wide-angle X-ray scattering (WAXS) results of the pristine GO display only a typical sharp peak at ≈10.01° (see Fig. S3†), corresponding to an interlayer spacing of 0.87 nm due to the (002) reflection of the stacked GO sheets, in accordance with the previously reported value.[48,49] Interestingly, after functionalization with POSS, a significant shift of the peak towards lower angle values (7.65°) was observed, the latter corresponding to an increased interlayer spacing of 1.15 nm. The latter can be assigned to the intercalation of POSS particles with sizes of *ca.* 0.5 nm (core–shell), which vary depending on the substituents.[50] Moreover, due to functionalization, a new broad peak at 21.03° coming from POSS is observed. After reduction with hydrazine, a new peak at 27.96° appears suggesting the presence of new crystalline domains, which corresponds to the partially restored graphitic domains and π–π interactions with a significant shift compared to rGO that resulted from the presence of POSS species.[44] Moreover, chemical reduction provides the removal of non-covalently attached POSS cages in accordance with XPS results. The irregular intercalation of POSS between graphene sheets results in broadening of the peak towards the 2Θ range of 6–11° and broad signals around 20° and 30° corresponding to the high-intensity peaks of crystalline POSS itself (Fig. S4†).

Further insights into the morphologies of rGO–POSS were obtained by quantifying the specific surface area (SSA), pore size, and pore distribution with the Brunauer–Emmett–Teller (BET) model, which relies on N_2 adsorption desorption. Our hybrid material exhibited a large SSA reaching 180 m^2 g^{-1}, which is roughly twice the accessible surface area of pristine GO (Fig. S5†). Notably, the material was finally reduced, a reaction which typically is accompanied by a decrease in the surface area. However, in our case, the presence of mesopores during the functionalization made it possible to maintain the porous structure. The type IV hysteresis loop (Fig. S5b†) confirms the presence of capillary condensation occurring in mesopores with new types of pores of size 4 nm and an average pore volume of 0.54 cm^3 g^{-1}, which clearly differ morphologically from the materials used for the synthesis (Table S1†), enabling effective electrolyte transport during the electrochemical measurements.[51–53]

2.2 Electrochemical study

Cyclic voltammetry (CV) was employed to probe the electrochemical behaviour of the rGO–POSS electrode in aqueous H_2SO_4 (1 M) electrolyte at a potential window from 0 to 1 V. The working electrode was investigated at scan rates ranging from 1 mV s^{-1} to 1000 mV s^{-1} as shown on Fig. 4. At lower

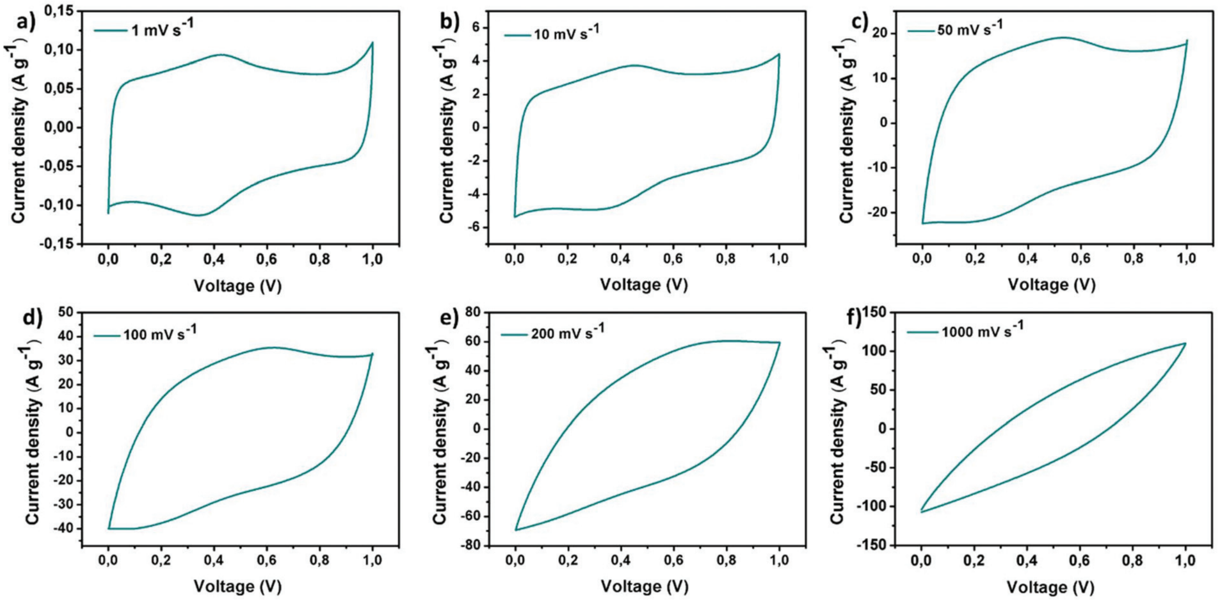

Fig. 4 Cyclic voltammetry curves of rGO–POSS electrode at different scan rates (1–1000 mV s^{-1}).

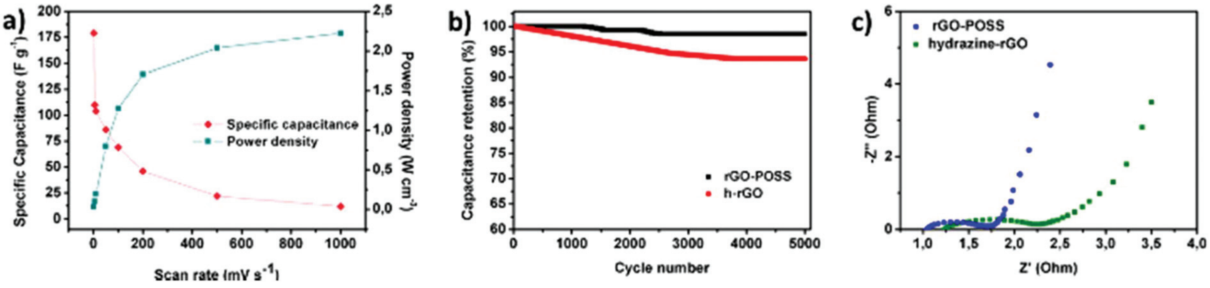

Fig. 5 (a) The dependence of specific capacitance and power density at various scan rates for rGO–POSS. (b) Cyclic stability of electrodes at 100 mV s^{-1} for rGO–POSS and h-rGO. (c) Comparison of Nyquist plots for rGO–POSS and hydrazine-reduced graphene oxide.

scan rate values (1–100 mV s^{-1}), the CV curves display a quasi-rectangular shape confirming effective electrolyte ion transport resulting in good electrochemical performance. This phenomenon can be attributed to the presence of the stable porous structure provided by POSS scaffolding which allows achieving effective capacitance at higher scan rates, which usually drastically drops over 20 mV s^{-1} for graphene-based materials.[54,55] A specific capacitance of 179 F g^{-1} was obtained at a scan rate of 1 mV s^{-1} and represents a relatively high result considering that chemically reduced graphene oxide-based materials, including the reference hydrazine-reduced graphene oxide, reach 94 F g^{-1} (Fig. S10†). In addition, voltamperograms recorded at low scan rates revealed peaks around 0.4 V suggesting the slight co-participation of pseudocapacitance in the electrochemical behaviour of electrode which might be due to the presence of heteroatoms (such as nitrogen, oxygen, and silicon).[56,57] With the scan rate increase, an obvious drop in specific capacitance was observed, *e.g.* 86 F g^{-1} at 50 mV s^{-1}, sustaining good electrochemical performance (Fig. 5a). Further experiments show a significant drop in specific capacitance comparable to the pristine rGO electrode. Notably, the prepared electrode also exhibited good areal capacitance of 350 mF cm^{-2} and volumetric capacitance reaching 115 F cm^{-3}.

The prepared electrode displayed a power density of 2.25 W cm^{-3} at an operating voltage of 1 V s^{-1} (Fig. 5a). Notably, the prepared electrode revealed excellent cyclability: its electrochemical capacitance remains at level over 98% of initial capacitance after 5000 cycles while tested at a scan rate of 100 mV s^{-1} in aqueous media which is superior when compared to the reference rGO material, which drops to 95% under the same conditions (Fig. 5b, Fig. S9†). Galvanostatic charge–discharge curves at the current density of 1 A g^{-1} reveal a significant difference in the cycle time for rGO–POSS (290 s) when compared to reference rGO (190 s). Electrochemical impedance spectroscopy (EIS) was employed to gain kinetic information of the electrode materials wherein the data was obtained in the form of Nyquist plots where the real part of impedance was plotted against the imaginary part of the impedance. The Warburg resistance (a slope of 45° region of the plots) of the rGO–POSS electrode was estimated as 1.75 Ohm, indicating fast charge transfer during the energy storage process and good conductivity and better ion transfer between the electrolyte–electrode than that of hydrazine-reduced graphene oxide (Fig. 5c). The volumetric energy density (E) constitutes an important parameter, especially for real applications in electric vehicles and mobile devices. Our electrodes exhibited energy density as high as 41.4 mW h cm^{-3}.

3. Experimental

3.1 Materials

A 4 mg mL^{-1} aqueous dispersion of graphene oxide (GO) was acquired from Graphenea. Hydrazine monohydrate and absolute ethanol (Sigma Aldrich) were used as received without purification. OctaAmmonium POSS (AM0285) was purchased from Hybrid Plastics Inc. Carbon Black Super P (H30253) was acquired from Alfa Aesar. All the solutions were prepared using Milli-Q water.

3.2 Preparation of rGO–POSS hybrid

A batch of rGO–POSS was prepared as follows: a mixture of ethanol (100 ml) and GO (100 ml, 4 mg mL^{-1}) was sonicated for 15 min and added to a solution of POSS (1 g in 200 mL of DI water). The mixture was vigorously stirred overnight under reflux. After 24 hours, the precipitate was filtrated, rinsed several times with water and ethanol and then the obtained GO–POSS was dried under vacuum. 570 mg of GO-POSS was dispersed in water and 570 μL of hydrazine was added and stirred for another 6 hours. The precipitate was then filtered and rinsed with a large amount of water and ethanol. The resulting black powder was then freeze-dried for 24 h under vacuum.

3.3 Characterization techniques

FT-IR spectra were studied within the mid-IR range (400–4000 cm^{-1}) using a PerkinElmer spectrometer (Spectrum Two) equipped with an ATR Diamond. X-ray photoelectron spectroscopy (XPS) analyses were carried out using a Thermo Scientific K-Alpha X-ray photoelectron spectrometer with a basic chamber pressure of ~10^{-9} mbar and an Al anode as the X-ray source (X-ray radiation of 1486 eV). X-ray powder diffraction (XRD) experiments were conducted on powder specimens using a Bruker ASX D8 Advanced diffractometer equipped with

Cu anode and Kα radiation (λ = 1.5418 Å). Diffraction patterns were collected at room temperature in the scattered angular range between 6° and 40° with an angular resolution of 0.02° per step and a typical counting time 4 of 10 s per step. The specific surface area was measured using a Micromeritics ASAP 2050 surface area and porosity analyzer. Prior to the BET measurements, the samples were outgassed for 12 hours at 100 °C. Adsorption isotherms were calculated for nitrogen adsorption at 77 K and pressures up to 1 bar. Scanning electron microscopy (SEM) characterization was carried out by means of an FEI Quanta 250 FEG instrument using energy-dispersive X-ray (EDX) analyses. High-resolution transmission electron microscopy (HR-TEM) was performed with a Hitachi HT7700 transmission electron microscope.

3.4 Electrochemical measurements

The working electrode (disc with a diameter of 0.7 cm and a thickness of 30 μm) was prepared by vacuum filtration of rGO–POSS dispersed in ethanol and carbon black (as a conducting additive, 10 wt% ratio of the total mass of the film). After drying, a free-standing pastille was deposited on Au-covered polyethylene terephthalate (PET) substrate by pressing under a pressure of 10 MPa for 24 hours (Fig. S5†). A platinum wire was employed as the counter electrode and an Ag/AgCl electrode in KCl was used as the reference electrode. 1 M H_2SO_4 aqueous solution was used as the electrolyte for CV measurements. The CV curves were performed under a potential window from 0 to 1 V at different scan rates ranging from 1 to 1000 mV s^{-1}. The capacitance was calculated from the CV curves using the eqn (1):[58]

$$C = \frac{1}{m \times \Delta v \times s} \int_{v_0}^{v} i\mathrm{d}v + \int_{v}^{v_0} i\mathrm{d}v \tag{1}$$

where C is the capacitance (F g^{-1}), m is the mass loading of active material, Δv is the voltage window in the measurement, and s is the scan speed for each CV measurement. The energy density (eqn (2)) and power density (eqn (3)) were calculated as given:[59]

$$E = \frac{1}{2} \times C \times \frac{\Delta V}{3600} \tag{2}$$

$$P = \frac{E}{\Delta t} \times 3600 \tag{3}$$

where E is the energy density (W h cm^{-3}), C is the volumetric capacitance, ΔV is the discharge voltage range, P is the power density (in W cm^{-3}), E is the volumetric energy, and Δt is the discharge time. CV, galvanostatic charge/discharge and electrochemical impedance spectra were measured with EC-LAB VMP3 (BioLogic Science Instruments).

4. Conclusions

In conclusion, we have demonstrated a facile approach for covalent functionalization of graphene oxide with silsesquioxane (POSS) followed by chemical reduction and exploited the hybrid structure as an electrode for supercapacitors. Due to the introduction of POSS cages and optimization of oxygen content, the final material exhibited a three-dimensional porous structure that was fully characterized in terms of morphology, chemical composition, and electrochemical behaviour. The prepared electrode exhibited high specific, areal, and volumetric capacitances (171 F g^{-1}, 350 mF cm^{-2}, and 115 F cm^{-3}, respectively). The introduction of POSS molecules provided optimal pores allowing efficient electrolyte penetration while the electrochemical processes resulted in excellent performance over a wide range of scan rates. Moreover, the electrode revealed excellent durability and cyclability maintaining >98% capacitance retention after 5000 cycles showing superior electrochemical performance when compared to rGO. This work enriches the current family of modern molecularly engineered graphene-based energy storage materials. Such an approach enables the tuning of a variety of physicochemical properties of the hybrid system towards the generation of high-performing multifunctional electrode materials exhibiting enhanced stability.

Conflicts of interest

There are no conflicts to declare.

Acknowledgements

This work was financially supported by the National Science Center (Grant No. 2019/35/B/ST5/01568 and Grant No. 2019/33/N/ST5/00052), co-financed by the European Union through the European Social Fund under the Operational Program Knowledge Education Development (Grant No. POWR.03.02.00-00-I026/16) and the EC–Graphene Flagship Core 3 project (GA-881603), the Agence Nationale de la Recherche through the Labex project CSC (ANR-10-LABX-0026 CSC) within the Investissement d'Avenir program (ANR-10-120 IDEX-0002-02) and the International Center for Frontier Research in Chemistry (icFRC). S.W. acknowledges the support from the Foundation for Polish Science (FNP) in the form of a scholarship.

Notes and references

1 F. X. Wang, X. W. Wu, X. H. Yuan, Z. C. Liu, Y. Zhang, L. J. Fu, Y. S. Zhu, Q. M. Zhou, Y. P. Wu and W. Huang, *Chem. Soc. Rev.*, 2017, **46**, 6816–6854.
2 N. Choudhary, C. Li, J. Moore, N. Nagaiah, L. Zhai, Y. Jung and J. Thomas, *Adv. Mater.*, 2017, **29**, 30.
3 Z. Liu, H. Zhang, M. Eredia, H. Qiu, W. Baaziz, O. Ersen, A. Ciesielski, M. Bonn, H. I. Wang and P. Samorì, *ACS Nano*, 2019, **13**, 9431–9441.
4 Z. P. Song and H. S. Zhou, *Energy Environ. Sci.*, 2013, **6**, 2280–2301.

5 Z. N. Yu, L. Tetard, L. Zhai and J. Thomas, *Energy Environ. Sci.*, 2015, **8**, 702–730.

6 C. Zhong, Y. D. Deng, W. B. Hu, J. L. Qiao, L. Zhang and J. J. Zhang, *Chem. Soc. Rev.*, 2015, **44**, 7484–7539.

7 Z. B. Lei, L. Lu and X. S. Zhao, *Energy Environ. Sci.*, 2012, **5**, 6391–6399.

8 H. Ren, H. Tian, C. L. Gardner, T.-L. Ren and J. Chae, *Nanoscale*, 2016, **8**, 3539–3547.

9 J. Y. Chen, P. Xie and Z. P. Zhang, *Chem. Eng. J.*, 2019, **361**, 615–624.

10 F. Wang, Z. Hu, L. Mao and J. Mao, *J. Power Sources*, 2020, **450**, 227692.

11 C. Moreno, M. Vilas-Varela, B. Kretz, A. Garcia-Lekue, M. V. Costache, M. Paradinas, M. Panighel, G. Ceballos, S. O. Valenzuela, D. Pena and A. Mugarza, *Science*, 2018, **360**, 199–203.

12 H. J. Jiang, *Small*, 2011, **7**, 2413–2427.

13 A. Ciesielski and P. Samori, *Chem. Soc. Rev.*, 2014, **43**, 381–398.

14 V. Eswaraiah, S. S. J. Aravind and S. Ramaprabhu, *J. Mater. Chem.*, 2011, **21**, 6800–6803.

15 D. R. Dreyer, S. Park, C. W. Bielawski and R. S. Ruoff, *Chem. Soc. Rev.*, 2010, **39**, 228–240.

16 Y. Zhu, S. Murali, W. Cai, X. Li, J. W. Suk, J. R. Potts and R. S. Ruoff, *Adv. Mater.*, 2010, **22**, 3906–3924.

17 S. H. Dave, C. Gong, A. W. Robertson, J. H. Warner and J. C. Grossman, *ACS Nano*, 2016, **10**, 7515–7522.

18 C. Punckt, F. Muckel, S. Wolff, I. A. Aksay, C. A. Chavarin, G. Bacher and W. Mertin, *Appl. Phys. Lett.*, 2013, **102**, 023114.

19 S. J. Rowley-Neale, E. P. Randviir, A. S. Abo Dena and C. E. Banks, *Appl. Mater. Today*, 2018, **10**, 218–226.

20 C. K. Chua and M. Pumera, *Chem. Soc. Rev.*, 2014, **43**, 291–312.

21 S. Eigler, S. Grimm, M. Enzelberger-Heim, P. Müller and A. Hirsch, *Chem. Commun.*, 2013, **49**, 7391–7393.

22 M. J. Fernández-Merino, L. Guardia, J. I. Paredes, S. Villar-Rodil, P. Solís-Fernández, A. Martínez-Alonso and J. M. D. Tascón, *J. Phys. Chem. C*, 2010, **114**, 6426–6432.

23 S. Pei and H.-M. Cheng, *Carbon*, 2012, **50**, 3210–3228.

24 X. Gao, J. Jang and S. Nagase, *J. Phys. Chem. C*, 2010, **114**, 832–842.

25 D. Voiry, J. Yang, J. Kupferberg, R. Fullon, C. Lee, H. Y. Jeong, H. S. Shin and M. Chhowalla, *Science*, 2016, **353**, 1413–1416.

26 L. G. Guex, B. Sacchi, K. F. Peuvot, R. L. Andersson, A. M. Pourrahimi, V. Ström, S. Farris and R. T. Olsson, *Nanoscale*, 2017, **9**, 9562–9571.

27 S. Park, J. An, J. R. Potts, A. Velamakanni, S. Murali and R. S. Ruoff, *Carbon*, 2011, **49**, 3019–3023.

28 P. K. Jha, S. K. Singh, V. Kumar, S. Rana, S. Kurungot and N. Ballav, *Chem*, 2017, **3**, 846–860.

29 C. Zhao, K. Shu, C. Wang, S. Gambhir and G. G. Wallace, *Electrochim. Acta*, 2015, **172**, 12–19.

30 H. J. Kim, S.-Y. Lee, L. H. Sinh, C. S. Yeo, Y. R. Son, K. R. Cho, Y. Song, S. Ju, M. K. Shin, S.-J. Park and S. Park, *J. Power Sources*, 2017, **346**, 113–119.

31 H. H. Shi, S. Jang, A. Reza-Ugalde and H. E. Naguib, *ACS Appl. Energy Mater.*, 2020, **3**, 987–997.

32 Z. Lei, N. Christov and X. S. Zhao, *Energy Environ. Sci.*, 2011, **4**, 1866–1873.

33 V. H. Luan, H. N. Tien, L. T. Hoa, N. T. M. Hien, E.-S. Oh, J. Chung, E. J. Kim, W. M. Choi, B.-S. Kong and S. H. Hur, *J. Mater. Chem. A*, 2013, **1**, 208–211.

34 H. Kang, C. Zhang, Y. Xu, W. Zhang, J. Jiao, Z. Li, L. Zhu and X. Liu, *RSC Adv.*, 2020, **10**, 1507–1513.

35 K. Tanaka and Y. Chujo, *J. Mater. Chem.*, 2012, **22**, 1733–1746.

36 S. K. Yadav, S. S. Mahapatra, H. J. Yoo and J. W. Cho, *Nanoscale Res. Lett.*, 2011, **6**, 122.

37 Y. Xue, Y. Liu, F. Lu, J. Qu, H. Chen and L. Dai, *J. Phys. Chem. Lett.*, 2012, **3**, 1607–1612.

38 D. Pakulski, W. Czepa, S. Witomska, A. Aliprandi, P. Pawluć, V. Patroniak, A. Ciesielski and P. Samorì, *J. Mater. Chem. A*, 2018, **6**, 9384–9390.

39 P. M. Sudeep, T. N. Narayanan, A. Ganesan, M. M. Shaijumon, H. Yang, S. Ozden, P. K. Patra, M. Pasquali, R. Vajtai, S. Ganguli, A. K. Roy, M. R. Anantharaman and P. M. Ajayan, *ACS Nano*, 2013, **7**, 7034–7040.

40 Y. Qin, J. Yuan, J. Li, D. Chen, Y. Kong, F. Chu, Y. Tao and M. Liu, *Adv. Mater.*, 2015, **27**, 5171–5175.

41 T. Kolev, M. Spiteller and B. Koleva, *Amino Acids*, 2010, **38**, 45–50.

42 D. M. El-Gendy, N. A. A. Ghany, E. E. F. El Sherbini and N. K. Allam, *Sci. Rep.*, 2017, **7**, 43104.

43 H.-L. Ma, H.-B. Zhang, Q.-H. Hu, W.-J. Li, Z.-G. Jiang, Z.-Z. Yu and A. Dasari, *ACS Appl. Mater. Interfaces*, 2012, **4**, 1948–1953.

44 C.-B. Huang, S. Witomska, A. Aliprandi, M.-A. Stoeckel, M. Bonini, A. Ciesielski and P. Samorì, *Adv. Mater.*, 2019, **31**, 1804600.

45 S. Park, Y. Hu, J. O. Hwang, E.-S. Lee, L. B. Casabianca, W. Cai, J. R. Potts, H.-W. Ha, S. Chen, J. Oh, S. O. Kim, Y.-H. Kim, Y. Ishii and R. S. Ruoff, *Nat. Commun.*, 2012, **3**, 638.

46 O. Bianchi, G. B. Repenning, L. B. Canto, R. S. Mauler and R. V. B. Oliveira, *Polym. Test.*, 2013, **32**, 794–801.

47 I. Penso, E. A. Cechinatto, G. Machado, C. Luvison, C. H. Wanke, O. Bianchi and M. R. F. Soares, *J. Non-Cryst. Solids*, 2015, **428**, 82–89.

48 S. Chen, J. Zhu, X. Wu, Q. Han and X. Wang, *ACS Nano*, 2010, **4**, 2822–2830.

49 S. Witomska, Z. Liu, W. Czepa, A. Aliprandi, D. Pakulski, P. Pawluć, A. Ciesielski and P. Samorì, *J. Am. Chem. Soc.*, 2019, **141**, 482–487.

50 A. Strąkowska, S. Członka and K. Strzelec, *Polymers*, 2019, **11**, 1092.

51 J. H. Bae, J.-H. Han and T. D. Chung, *Phys. Chem. Chem. Phys.*, 2012, **14**, 448–463.

52 B. Moyo, D. Momodu, O. Fasakin, A. Bello, J. Dangbegnon and N. Manyala, *J. Mater. Sci.*, 2018, **53**, 5229–5241.

53 H. Lu, K. Kim, Y. Kwon, X. Sun, R. Ryoo and X. S. Zhao, *J. Mater. Chem. A*, 2018, **6**, 10388–10394.

54 A. Sumboja, C. Y. Foo, X. Wang and P. S. Lee, *Adv. Mater.*, 2013, **25**, 2809–2815.

55 Z. Lei, L. Lu and X. S. Zhao, *Energy Environ. Sci.*, 2012, **5**, 6391–6399.

56 C. Romanitan, P. Varasteanu, I. Mihalache, D. Culita, S. Somacescu, R. Pascu, E. Tanasa, S. A. V. Eremia, A. Boldeiu, M. Simion, A. Radoi and M. Kusko, *Sci. Rep.*, 2018, **8**, 9654.

57 Y. J. Oh, J. J. Yoo, Y. I. Kim, J. K. Yoon, H. N. Yoon, J.-H. Kim and S. B. Park, *Electrochim. Acta*, 2014, **116**, 118–128.

58 M. D. Stoller, S. Park, Y. Zhu, J. An and R. S. Ruoff, *Nano Lett.*, 2008, **8**, 3498–3502.

59 Z. S. Wu, K. Parvez, X. Feng and K. Müllen, *Nat. Commun.*, 2013, **4**, 2487.

Electronic Supplementary Material (ESI) for Nanoscale.

Reduced graphene oxide - silsesquioxane hybrid as novel supercapacitor electrode

Włodzimierz Czepa,[a,b] Samanta Witomska,[a,b] Artur Ciesielski*[b,c] and Paolo Samorì*[c]

[a] Faculty of Chemistry, Adam Mickiewicz University Uniwersytetu Poznańskiego 8, 61614 Poznań, Poland

[b] Center for Advanced Technologies, Adam Mickiewicz University, Uniwersytetu Poznańskiego 10, 61614 Poznań, Poland

[c] Université de Strasbourg, CNRS, ISIS, 8 alleé Gaspard Monge, 67000 Strasbourg, France

E-mail: samori@unistra.fr , ciesielski@unistra.fr

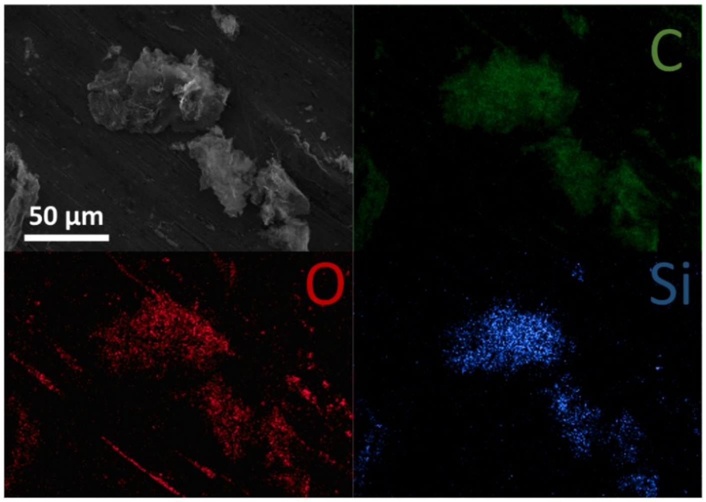

Fig. S1 Scanning Electron Microscopy (SEM) pictures of rGO-POSS.

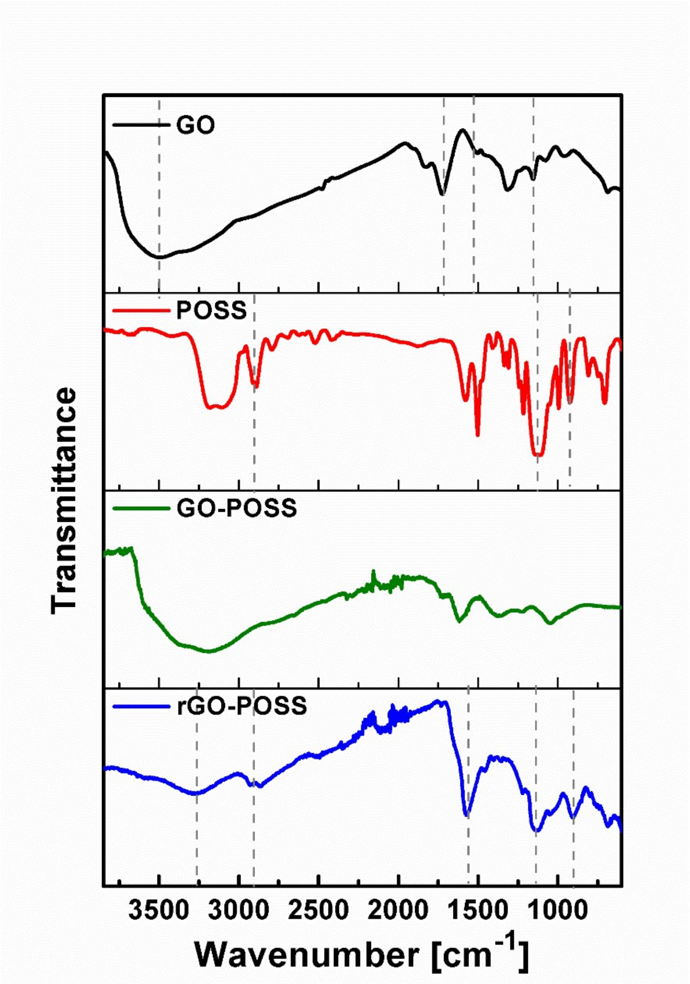

Fig. S2 FT-IR spectra of graphene oxide (black curve), POSS (red), GO-POSS (green) rGO-POSS composite (blue).

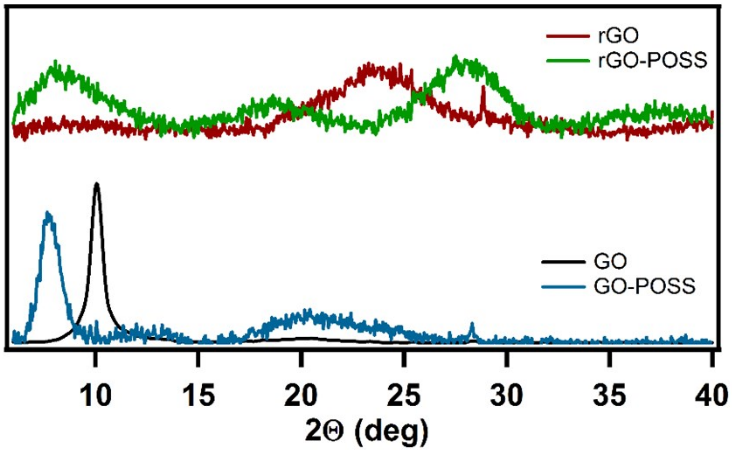

Fig. S3 X-ray diffraction spectra of graphene oxide (GO), chemically reduced graphene oxide (rGO), and its composites with silsesquioxane (GO-POSS, rGO-POSS).

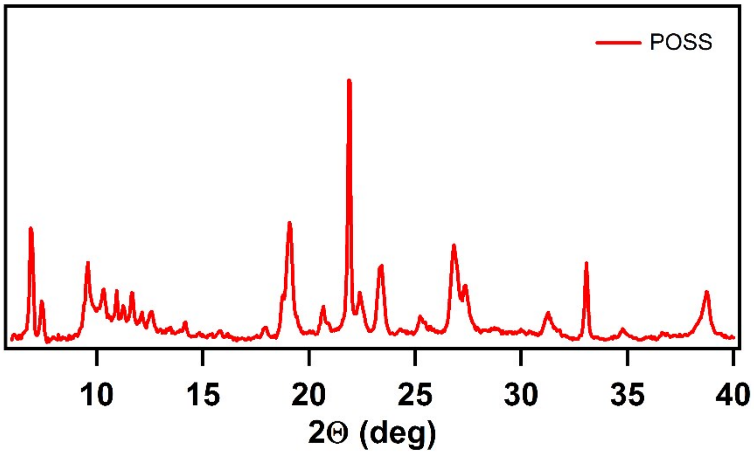

Fig. S4 X-ray diffraction spectra of POSS.

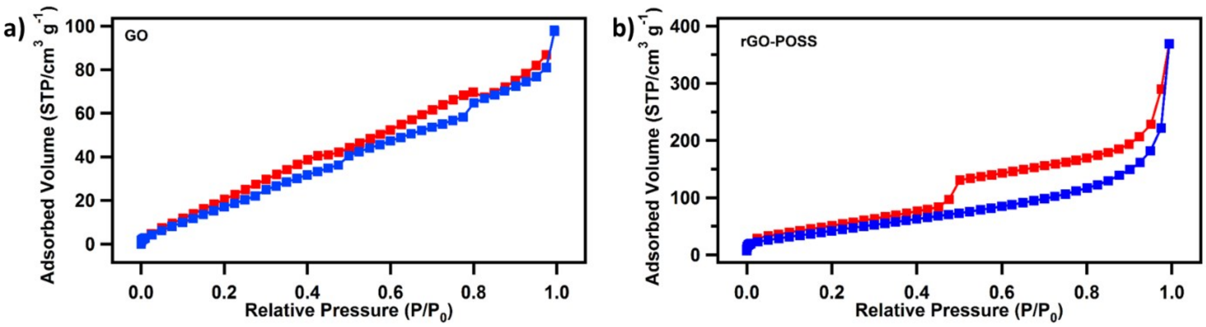

Fig. S5 Adsorption-desorption N_2 isotherm for a) graphene oxide (GO) b) rGO-POSS composite.

Tab. S1 BET surface area analysis of GO, POSS, rGO and rGO-POSS.

	BET Surface area (m^2g^{-1})	Pore volume ($cm^3\ g^{-1}$)	Average pore size (nm)
GO	108	0.15	5.6
POSS	13	0.025	3.3
rGO	9	0.018	1.5
rGO-POSS	180	0.54	4

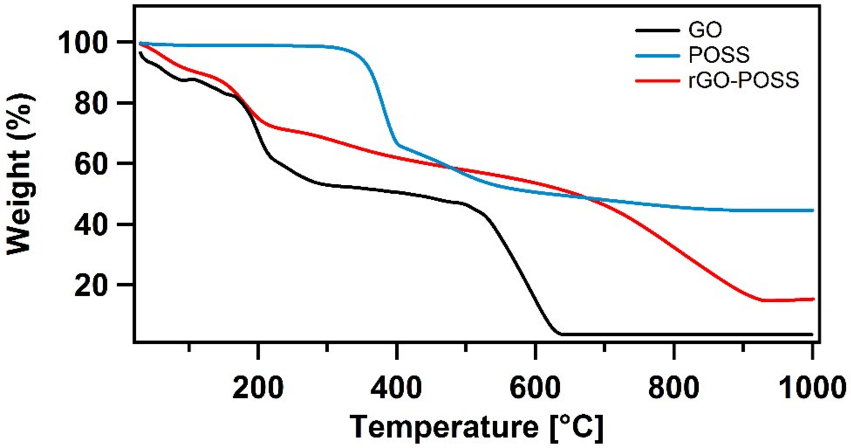

Fig. S6 Thermogravimetric analysis of GO, POSS and rGO-POSS.

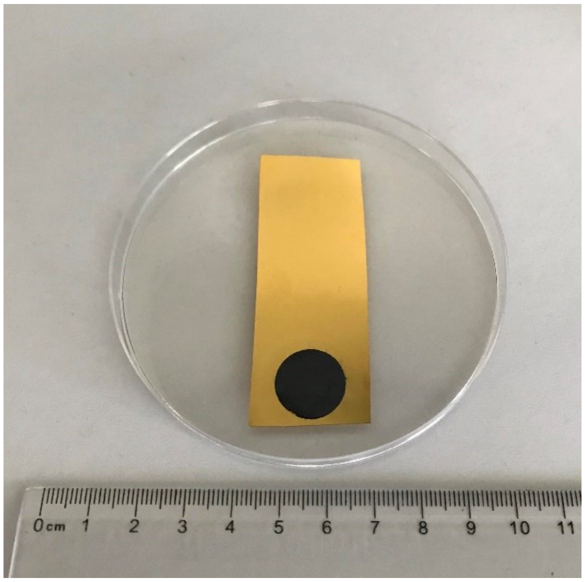

Fig. S7 rGO-POSS electrode deposited on Au-covered polyethylene terephthalate (PET).

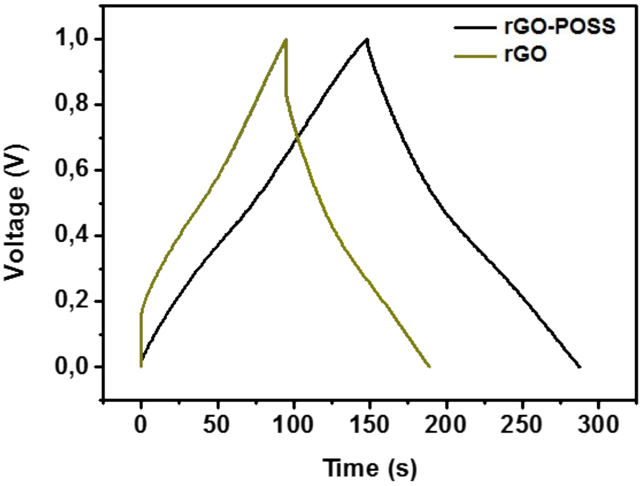

Fig. S8 Charge-discharge curves for rGO-POSS and rGO at current density of 1 A g^{-1}.

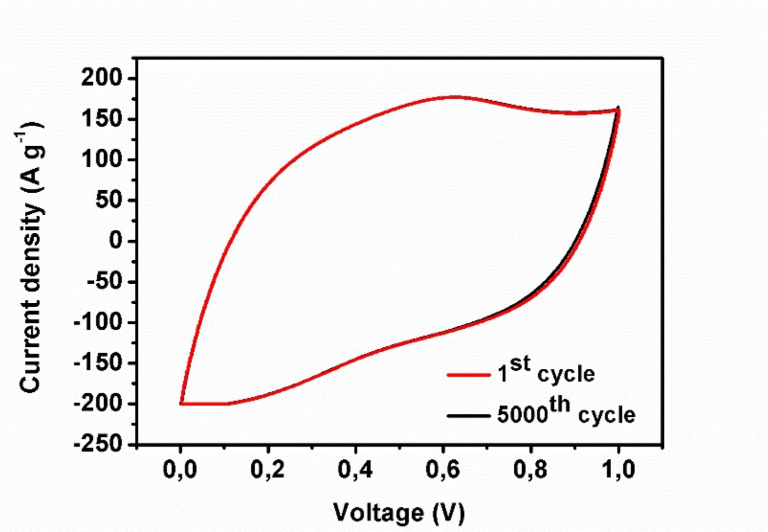

Fig. S9 CV curves showing cyclability of rGO-POSS electrode after 5000 cycles at scan rate of 100 mV s^{-1}.

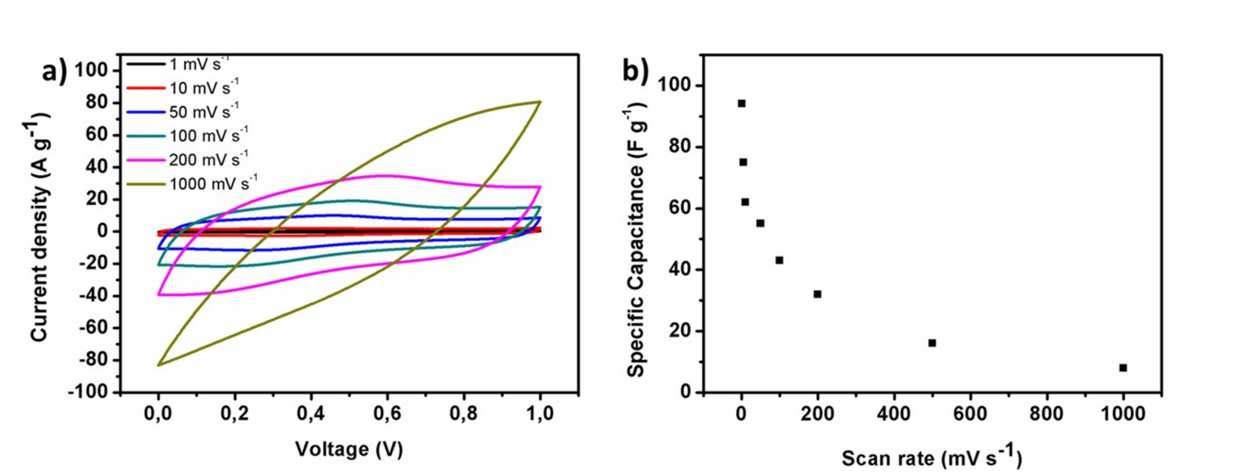

Fig. S10 Electrochemical measurements for hydrazine-reduced graphene oxide used as reference material a) circular voltammetry curves in the range of 1-1000 mV $\mathrm{s^{-1}}$ b) specific capacitance at different scan rates for hydrazine-reduced graphene oxide.

Tab. S2 Comparison of most common characteristics of reduced graphene-based electrodes.

Material	Electrolyte	Scan Rate/ current density	Specific Capacitance	Cycle no. (retention)	Ref.
rGO	2M KOH	2 mV $\mathrm{s^{-1}}$	44 F $\mathrm{g^{-1}}$	-	1
rGO	1M H_2SO_4	1 mA $\mathrm{cm^{-2}}$	areal: 33.8 mF $\mathrm{cm^{-2}}$	-	2
rGO	2M H_2SO_4	0.2 A $\mathrm{g^{-1}}$	141 F $\mathrm{g^{-1}}$	-	3
rGO	PVA-H_2SO_4	1.1 A $\mathrm{g^{-1}}$	171 F $\mathrm{g^{-1}}$	100000(80%)	4
rGO-powder rGO-paper	6M KOH	0.5 A $\mathrm{g^{-1}}$	255 F $\mathrm{g^{-1}}$ 196 F $\mathrm{g^{-1}}$	1200 (~93%) 1200 (~94%)	5
rGO	1M Na_2SO_4	50 mA $\mathrm{g^{-1}}$	67 F $\mathrm{g^{-1}}$	-	6
rGO-MnO_2	1M Na_2SO_4	50 mA $\mathrm{g^{-1}}$	897 mF $\mathrm{cm^{-2}}$	6450 (83%)	6
rGO-biochar	0.5 M H_2SO_4	0.5 A $\mathrm{g^{-1}}$	167 F $\mathrm{g^{-1}}$	10000 (90%)	7
Ap-rGO	6M KOH	5 mV $\mathrm{s^{-1}}$	160 F $\mathrm{g^{-1}}$	5000 (80%)	8
TiO_2-rGO	1M $LiPF_6$	0.4 A $\mathrm{g^{-1}}$	150 F $\mathrm{g^{-1}}$	100 (80%)	9
rGO-PVA		1 A $\mathrm{g^{-1}}$	122.7 F $\mathrm{g^{-1}}$	1000 (87.4%)	10
rGO-melamine		1 A $\mathrm{g^{-1}}$	101 F $\mathrm{g^{-1}}$	-	10
rGO-PU		1 A $\mathrm{g^{-1}}$	55.56 F $\mathrm{g^{-1}}$	-	10
rGO-POSS	1M H_2SO_4	1 mV $\mathrm{s^{-1}}$	174 F $\mathrm{g^{-1}}$ 350 mF $\mathrm{cm^{-2}}$ 115 F $\mathrm{cm^{-3}}$	5000 (>98%)	This work

Ap- aminopyrole, PVA- polyvinyl alcohol; PU- polyurethane

References:

1. C. Xiang, M. Li, M. Zhi, A. Manivannan and N. Wu, *Journal of Power Sources*, 2013, **226**, 65-70.
2. U. N. Maiti, J. Lim, K. E. Lee, W. J. Lee and S. O. Kim, *Advanced Materials*, 2014, **26**, 615-619.
3. B. Rajagopalan and J. S. Chung, *Nanoscale research letters*, 2014, **9**, 535-535.
4. P. K. Jha, S. K. Singh, V. Kumar, S. Rana, S. Kurungot and N. Ballav, *Chem*, 2017, **3**, 846-860.
5. Z. Lei, L. Lu and X. S. Zhao, *Energy & Environmental Science*, 2012, **5**, 6391-6399.
6. A. Sumboja, C. Y. Foo, X. Wang and P. S. Lee, *Advanced Materials*, 2013, **25**, 2809-2815.
7. B. Rui, M. Yang, L. Zhang, Y. Jia, Y. Shi, R. Histed, Y. Liao, J. Xie, F. Lei and L. Fan, *Journal of Applied Electrochemistry*, 2020, **50**, 407-420.
8. E. Y. L. Teo, H. N. Lim, R. Jose and K. F. Chong, *RSC Advances*, 2015, **5**, 38111-38116.
9. H. Kim, M. Y. Cho, M. H. Kim, K. Y. Park, H. Gwon, Y. Lee, K. C. Roh and K. Kang, *Adv. Energy Mater.*, 2013, **3**, 1500-1506.
10. D. Choi and K. Kim, *Carbon Lett.*, 2016, **18**, 71-75.

A Graphene Oxide–Thioamide Polymer Hybrid for High-Performance Supercapacitor Electrodes

Włodzimierz Czepa, Samanta Witomska, Paolo Samorì, and Artur Ciesielski**

The controlled chemical functionalization of graphene oxide (GO) represents a powerful strategy to finely tune its physical and chemical properties toward applications in energy storage. Herein, an unprecedented approach for the GO modification with thioamide-based polymers featuring numerous heteroatoms (S,N,O) is reported, which is instrumental for achieving superior electrochemical performance in symmetric supercapacitors. While the electrochemical investigations in aqueous electrolytes reveal specific capacitance of 221 F g^{-1} at 1 A g^{-1}, the use of organic media allows the specific capacitance to be boosted up to 340 F g^{-1}. Additionally, the increase of operating window yields energy densities as high as 94.4 Wh kg^{-1}, thereby exceeding state-of-the-art performances of GO-based supercapacitors. Furthermore, the symmetric devices exhibit great robustness in both aqueous and organic electrolytes as evidenced by an excellent stability after 5000 working cycles (>98% in H_2SO_4 and >90% in $TEABF_4$/ACN).

1. Introduction

The ever-growing energy needs call for the development of new power sources and sustainable energy storage systems. Supercapacitors (SCs) represent an attractive portable energy storage alternative to state-of-the-art devices, e.g., batteries, as they combine very high cycling stability, ultrafast charging, high range of operating temperatures and improved durability, and most importantly high power density.[1–3] However, several obstacles need to be overcome to render SCs ready for being used in daily applications, e.g., to power portable electronic devices. The existing major problems to be solved include: 1) the lack of industrial standardization such as general specifications, electrodes, and electrolyte specifications; 2) low rated voltages, which require preparation of stack of connected SC components for practical applications; 3) relative low energy densities, which result in the need of constructing bulky, noncompact, and relatively heavy devices.[4,5] Various types of materials have been investigated for application in energy storage devices exploiting either their electrochemical double-layer (ECDL) formation or pseudocapacitance (PS) provided by Faradic reactions taking place on redox active sides on electrode–electrolyte interface.[6–9] In this context, different forms of carbon-based materials including activated carbon, carbon nanotubes, and graphene-based materials have been studied in the last decade.[10–12] To enhance their electrochemical characteristics, these materials have been modified by increasing their porosity, which rules the electrolyte penetration within the electrode material and therefore it allows control over the kinetics of charge/discharge processes. Moreover, to provide additional pseudocapacitative behaviors, heteroatoms such as N, P, S, and O have been introduced.[13–15] During the last few years, numerous studies have been reported on the exploration of 2D materials toward enhanced efficiency in energy storage density, mainly achieved by increasing their specific surface areas, taking advantage of their high electrical conductivity, and by developing synthetic protocols that can be potentially upscaled.[16,17]

Among 2D materials, graphene oxide (GO) can be produced in large scale at moderate costs, and it is known to exhibit unique physical and chemical properties including high mechanical strengths and ease of processability. Furthermore, the presence of oxygen containing groups (carboxyls, alcohols, and epoxides) on the surface and rim of GO's sheets enables the use of different synthetic pathways for its covalent and noncovalent modification.[18–23] The chemical functionalization of GO was amply demonstrated to be a powerful strategy to tune its properties toward desired application in (electro)chemical sensing, energy storage, water and gas purification as well as biomedical technologies.[24–28] However, GO exhibits poor electrical characteristics when compared to pristine graphene due to the presence of multiple structural defects and the aforementioned oxygen-containing groups acting as traps and scattering sites for efficient

W. Czepa, S. Witomska
Faculty of Chemistry
Adam Mickiewicz University
Uniwersytetu Poznańskiego 8, 61614 Poznań, Poland

W. Czepa, S. Witomska, A. Ciesielski
Center for Advanced Technologies
Adam Mickiewicz University
Uniwersytetu Poznańskiego 10, 61614 Poznań, Poland

P. Samorì, A. Ciesielski
Nanochemistry Laboratory
Institut de Science et d'Ingénierie Supramoléculaires (I.S.I.S.)
Université de Strasbourg, CNRS, ISIS
8 alleé Gaspard Monge, 67000 Strasbourg, France
E-mail: samori@unistra.fr; ciesielski@unistra.fr

The ORCID identification number(s) for the author(s) of this article can be found under https://doi.org/10.1002/smsc.202300013.

DOI: 10.1002/smsc.202300013

charge transport. Moreover, the GO itself is highly hydrophilic and it can be easily penetrated by solvents molecules causing swelling of the material.[29] The phenomena significantly influence the structure and result in worsening of long-cycle performance of the electrode causing low stability.[30] Nonetheless, various chemical and physical methods for the GO reduction can be used to restore the conjugation between carbon atoms within GO yielding reduced graphene oxide (rGO). The latter is electrically conducting and it can be used both as electrode or semiconductor for the fabrication of optoelectronics devices.[31] Interestingly, the reduction and functionalization of GO can be accomplished simultaneously when molecules bearing primary amines are employed to covalently modify GO via condensation between the oxygen functional groups of GO (mainly epoxides) and NH_2 units of ad hoc molecules. This results in the dramatic decrease of oxygen content and restoration of GO conductivity.[32,33] Noteworthy, a moderate amount of oxygen is also desired in carbon-based materials when employed as SC's electrode material, as they provide pseudocapacitative characteristics.[34,35] Previous works have been focussed on the influence of oxygen content on SC performance in GO/rGO-based electrodes. Harsh reduction conditions might cause drastic decrease in specific capacitance due to lowered pseudocapacity effect.[36] The today's performance of most GO/polymer hybrid materials employed as electrodes in SCs, as quantified by its specific capacitance, amounts typically in the range of 100–300 F g^{-1}.[37–39] Importantly, the crucial obstacle hampering the practical application of GO-based hybrids in SCs is the low energy density, being usually two orders of magnitudes lower than in case of Li-ion batteries and typically reaching values up to 5–15 Wh kg^{-1} in case of aqueous electrolytes.[40] Notably, Song and co-workers showed that the use of 1-butyl-3-methyl-imidazolium tetrafluoroborate electrolyte allows a high energy density of 51 Wh kg^{-1} to be obtained, demostrating the high potential of organic electrolytes for widening of the potential window.[41] Most of reported examples of GO-based SCs comprise aqueous electrolytes, which are relatively cheap, easily available, and provide good ion conductivity. However, the operating voltage windows of such SCs are limited by the thermodynamic water decomposition at 1.23 V.[42] According to theoretical predictions, the use of higher voltage windows, which might be modulated by the choice of the electrolyte, represents appealing strategy toward increased energy density and power density performance of SCs.[43,44] In particular, organic electrolytes, including ionic liquids, represent attractive solutions when employed in carbonaceous-based SCs.[45,46] Among them, tetraethylammonium tetrafluoroborate ($TEABF_4$) exhibits very high conductivity (10.55 mS cm^{-1}) and very high oxidation and reduction limiting potentials defining an operative voltage window in the range of −3.0 to 3.6 V.[47] Hence, organic electrolytes are particularly suitable for the development of hybrid SCs with excellent performance by mastering both ECDL and PS mechanisms of energy storage.[48] To generate new electrode materials mastering both mechanisms, we exploited a supramolecular approach comprising the synthesis of a new thioamide-based polymer (THA) and its grafting to GO yielding GO-THA porous hybrids. The latter have been used as electrode material in symmetric SC devices, displaying gravimetric capacitance as high as 221 and 340 F g^{-1} at 1 A g^{-1} in 1 M aqueous H_2SO_4 and 1M $TEABF_4$ in ACN, respectively. Moreover, the enlarged operating potential window allowed the achievement of energy density of 94.4 Wh kg^{-1}, being several times greater than typical values for carbonaceous SCs (Table S6, Supporting Information).

2. Results and Discussions

2.1. Synthesis

The thioamide polymer (THA) was synthesized in a three-step reaction. First, modified Hofmann rearrangement was employed to substitute terminal primary amines of 2,2′-(ethylenedioxy) bis(ethylamine) with dithiocarbamide salt by reacting the former with carbon disulfide in basic conditions. Subsequently, dithiocarbamide salt was transformed into diisothiocyanate.[48] Finally, the condensation of diisothiocyanate and 2,2′-(ethylenedioxy) bis(ethylamine) yielded the thioamide (THA) polymer. The condensation reaction time was set to 1 h to avoid complete polymerization and therefore insoluble polymer precipitation (**Figure 1**). The as-prepared THA was used to modify GO through the ring opening reaction of GO's epoxide-driven nucleophilic attack of THA's terminal primary amines, as well as the esterification of carboxyl moieties located mainly on the GO sheet edges. The former reaction is accomplished thanks to the tautomerization of active sulfides (thioamide grouping).[49] The ratio GO:THA 1:10 (w/w) was applied to maximize the functionalization degree of GO and to avoid formation of nonhomogeneous product.

2.2. Characterization

^1H and ^{13}C NMR analysis was carried out to attain qualitative information on the chemical structure of THA (Figure S1, Supporting Information). ^1H spectra revealed the presence of signals at δ 7.54 (s, 2 H), 3.68–3.44 (*m*, 12 H), and 2.67 (*t*, NH_2) which are assigned to secondary amine, ethylene units, and terminal amines hydrogens of THA, respectively. The average molecular weight of the polymer size was estimated as 1958 g mol^{-1} by MALDI-TOF with MS detector (Figure S2, Supporting Information). Scanning electron microscopy (SEM) and transmission electron microscopy (TEM) studies of the GO-THA hybrid material revealed a dense, homogeneous, wrinkled, porous morphology (**Figure 2** and S3, Supporting Information). Such porosity is especially beneficial for the subsequent electrochemical experiments, as it is one of the factors enabling efficient electrolyte ion transportation. Moreover, the energy-dispersive X-Ray (EDX) mapping (Figure S4, Supporting Information) showed an even distribution of the heteroatoms (S, N) introduced upon functionalization with the THA polymer.

X-ray photoelectron spectroscopy (XPS) measurements of pristine GO, THA, and GO-THA hybrid were performed to cast further light onto the chemical composition of the materials. The survey spectra confirm the presence of introduced heteroatoms (N, S) into the GO structure (Figure S5, Supporting Information) High-resolution C 1s spectrum of GO (**Figure 3**a) exhibited typical peaks at 284.6, 286.4, 287.5, and 288.3 eV corresponding to the C–C, C–O, C=O, and COOH groups, respectively. N 1s and S 2p spectra of THA displayed characteristic peaks confirming its structure along with the emergence of resonance effect according

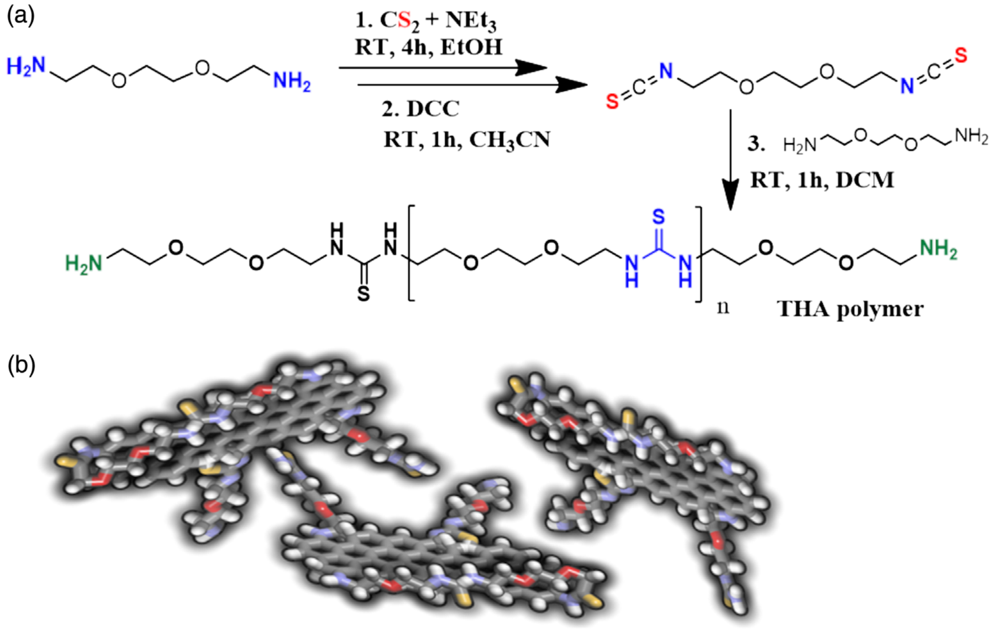

Figure 1. a) Scheme of the synthesis of the THA polymer. b) Model of the GO-THA composite.

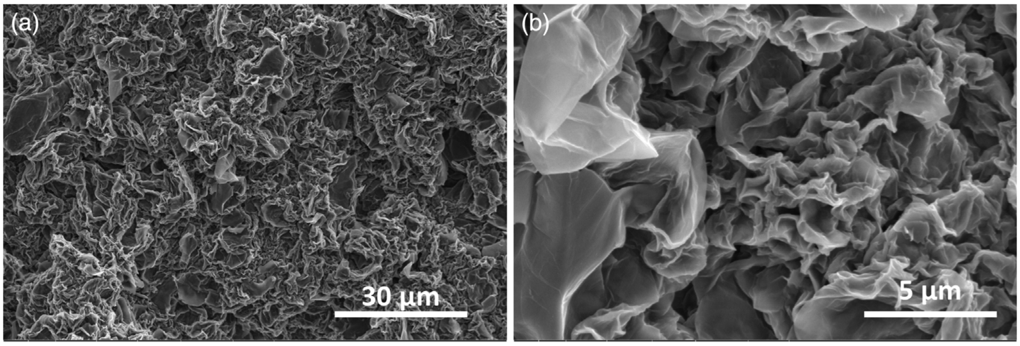

Figure 2. SEM images of GO-THA hybrid.

to S 2p high-resolution spectra featuring C=S and C–SH peaks at 161.5 and 163 eV, respectively. (Figure S6, Supporting Information). The C 1s spectra of pristine GO and GO-THA hybrid evidenced major differences. In particular, in the latter two new peaks appeared: the C–N bond (287.3 eV) arising from the covalent attachment of terminal primary amines of THA to GO's epoxides, and the band at 285.5 eV which is assigned to C–S bond and whose presence has confirmed the formation of thioamide.[50,51] On the other hand, the N 1s spectra of GO-THA provided valuable insight into the composition of obtained material. While the major peak at 399.5 eV (Figure 3c) can be ascribed to N–C bond of thioamide and secondary amine grouping, the existence of a peak at 398.1 eV is indicative of a resonance effect taking place in the thioamide moiety [R1–NH–C(=S)–NH–R2]↔[R1–HN–C(SH)=N–R2].[52] The S 2p spectra of GO-THA revealed characteristic sulfur–carbon bonds (at 161.0, 162.1, and 164 eV). Moreover, partial oxidation of sulfides to sulfones was monitored (167.0 and 168.5 eV), occurring simultaneously while functionalizing the GO. This phenomenon is beneficial especially in view of electrochemical properties of GO-THA, as redox reversible reactions allow the introduction of an additional PS effect and improved the SCs' performance. Notably, the chemical composition of GO-THA hybrid displayed significant degree of functionalization as revealed by a nitrogen and sulfur content amounting to 9.23% and 3.93%, respectively, according to XPS data. Such values are in good agreement with elemental analysis (Table S1, Supporting Information).

Fourier transform infrared spectroscopy (FTIR) spectra of GO and GO-THA are shown in Figure S7, Supporting Information. The GO spectrum displayed the well-known bands at 1731 cm^{-1} (C=O stretching), 1620 cm^{-1} (C=C), and stretching of epoxy moieties C–O–C at 1047 cm^{-1}. Moreover, one can observe the broadband between 3000 and 3500 cm^{-1}, due to the stretching vibration of the hydroxyl groups. As a result of the functionalization, a strong peak appeared at 1568 cm^{-1} that can be ascribed to C=N–H stretching vibrations which is characteristic for thiourea resonance structure. Moreover, one can observe

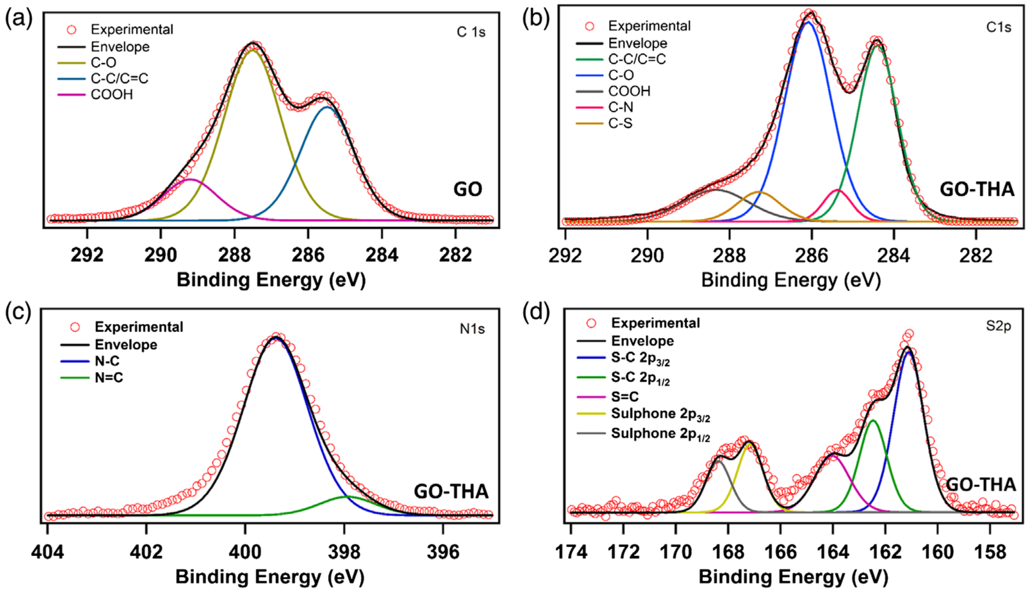

Figure 3. High-resolution XPS spectra of GO: a) C 1s, and GO-THA: b) C 1s, c) N 1s, and d) S 2p.

typical $-CH_2-$symmetric and asymmetric stretching at 2864 and 2923 cm^{-1}, respectively, arising from ethylene grouping present in the polymer.

The functionalization of GO with THA yielded a threefold increase in the specific surface area of 371 $m^2 g^{-1}$ according to Brunauer–Emmett–Teller (BET) N_2 adsorption–desorption investigations (Table S2, Supporting Information). The hysteresis of type H3 (Figure S8, Supporting Information) indicates the slit-like mesopores being present in the material, which is in correlation with an average pore diameter of 3.1 nm. Powder X-ray diffraction (XRD) investigations were performed to study the crystallinity of the materials. Wide-angle X-ray scattering (WAXS) of the pristine GO displayed only the (002) reflection of stacked GO sheets which appears as a typical sharp peak at ≈10.01° (see Figure S9, Supporting Information), indicating an interlayer spacing of 0.87 nm, in accordance with previously reported values.[53,54] Conversely, the THA polymer exhibited two broad peaks at ≈22° and a secondary peak at ≈8.3°. Interestingly, GO-THA hybrid featured a peak at ≈8.15°, suggesting an increased interlayer spacing between adjacent GO sheets up to 1.05 nm. Moreover, due to functionalization a new broad peak at 23.4° originating from an amorphous THA phase can be identified. Raman spectroscopy provided useful information on the quality and degree of functionalization of GO within GO-THA hybrid. The relative ratio between D and G peaks of GO and GO-THA (Figure S10, Supporting Information), which are located around 1350 and 1600 cm^{-1} respectively, confirms the highly efficient functionalization. In particular, the increase in the I_D/I_G ratio from 0.87 to 1.14 in GO-THA reflects the enhancement in structural and electronic disorder after grafting THA polymer, which is due to the enhancement in the sp^3 carbon atoms content in the hybrid, in line with previous reports on GO functionalization.[55,56] Thermogravimetric analysis was performed to investigate thermal stability of GO, THA polymer, and GO-THA. The GO curve displayed ≈45% weight loss in the range of 150–300 °C due to the degradation of oxygen functional groups. THA exhibited an average thermal stability up to 210 °C, typical for organic compounds, with a rapid decomposition and weight loss of 60%. The GO-THA curve revealed a slight mass decrease over 100 °C associated with surface water removal, along with a slow degradation over 150 °C eventually up to 48% mass loss. Overall, based on the thermal gravimetric analysis (TGA) analysis the relative mass composition of GO-THA is estimated as 80:20 GO:THA (Figure S11, Supporting Information).

2.3. Electrochemical Studies

The electrochemical performance of the developed material when integrated in 2-electrodes SC devices was investigated in solid state symmetric setup embedded in CR2030 coin cell. The use of aqueous electrolyte (1M H_2SO_4) provided excellent wettability mainly due to presence of numerous electronegative atoms (O, N, S) in GO-THA hybrid. The electrolyte–material interface displayed a good conductivity, reaching values of 140 $S cm^{-1}$ (Figure S12a, Supporting Information). The most important electrochemical characteristic is portrayed in **Figure 4**: the displayed cyclic voltammetry (CV) profile exhibits very good electrode performance. The quasirectangular shape of CV, characterized by small peaks at around 0.4 and 0.5 V, provides evidence for the slight coparticipation of a redox reaction in the energy storage mechanism. The nearly triangular galvanostatic charge–discharge (GCD) curves indicate excellent reversibility and effective charging and discharging of the electrodes. Notably, the electrode does not show any IR drop, which might indicate internal resistance, confirming a negligible charge loss due to resistance effect. Such feature is also confirmed by Nyquist plot revealing solution resistance (R_S) and charge resistance transfer (R_{CT}) factors of 0.9 and 6.0 Ω, respectively (Figure 4c). Interestingly, the GO-THA-based device exhibited high specific capacitance of 221 $F g^{-1}$ at current density of 1 $A g^{-1}$ combined with a great capacitance retention

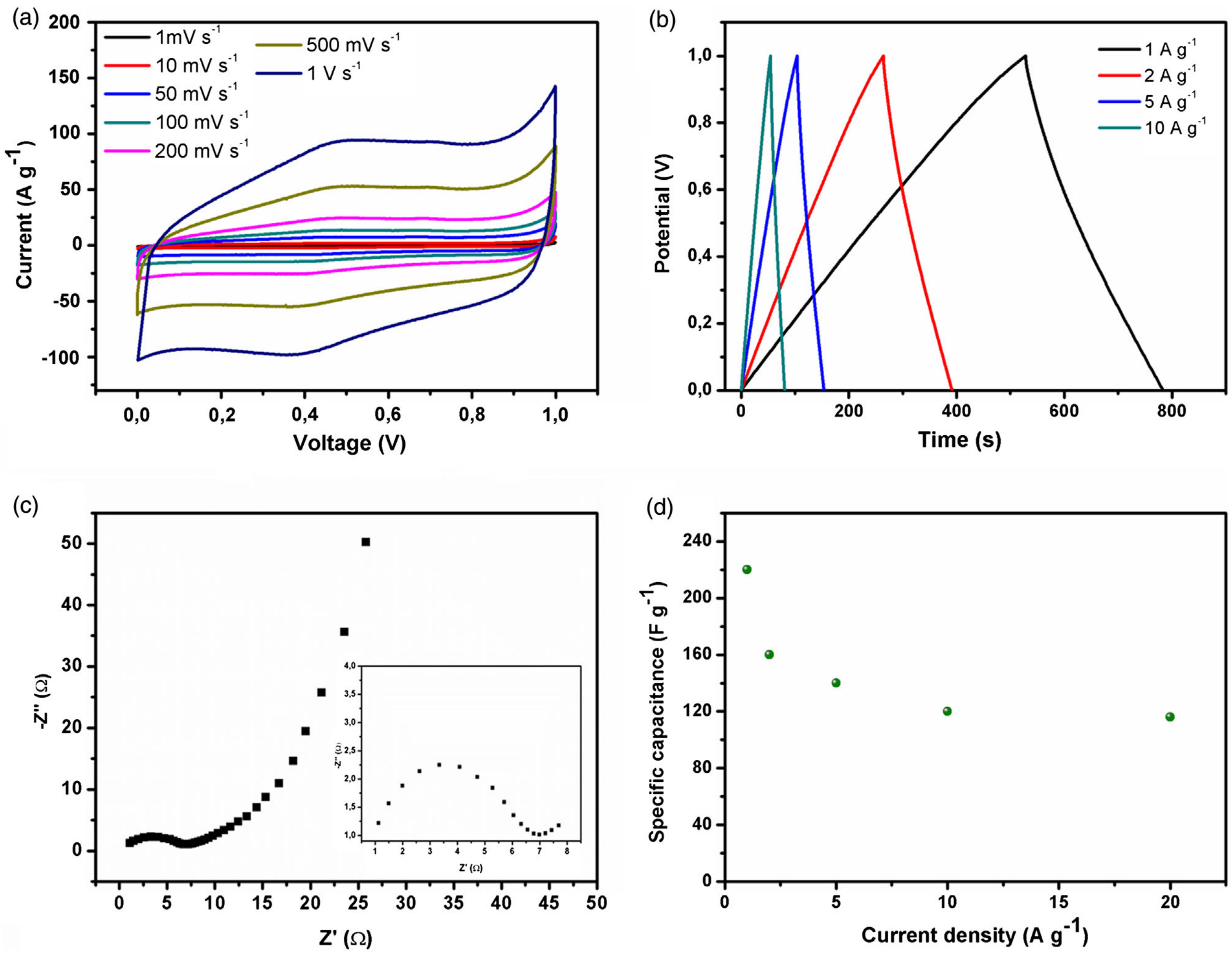

Figure 4. Electrochemical characterizations of symmetric SC in 1 M aqueous H_2SO_4: a) CV, b) GCD curves, c) electrochemical impedance spectroscopy, and d) specific capacitance at different current densities.

while increased current density up to 20 A g^{-1} (120 F g^{-1}). Moreover, the stability tests confirmed outstanding performance even after 5000 cycles, with a decrease in the initial capacitance limited to ≈2% (Figure S12b,c, Supporting Information). In general, the operating potential window determines the performance of energy storage devices (Equation (2)). It has been shown that its widening allows both energy density and power density to be boosted. Toward this end, we have employed 1 M $TEABF_4$ in acetonitrile as the electrolyte which made it possible to increase the potential window up to 2 V. The CV profiles in **Figure 5**a show excellent performance, especially in the range of 2–500 mV s^{-1}, as the last curve (500 mV s^{-1}). Notably, the electrode exhibits

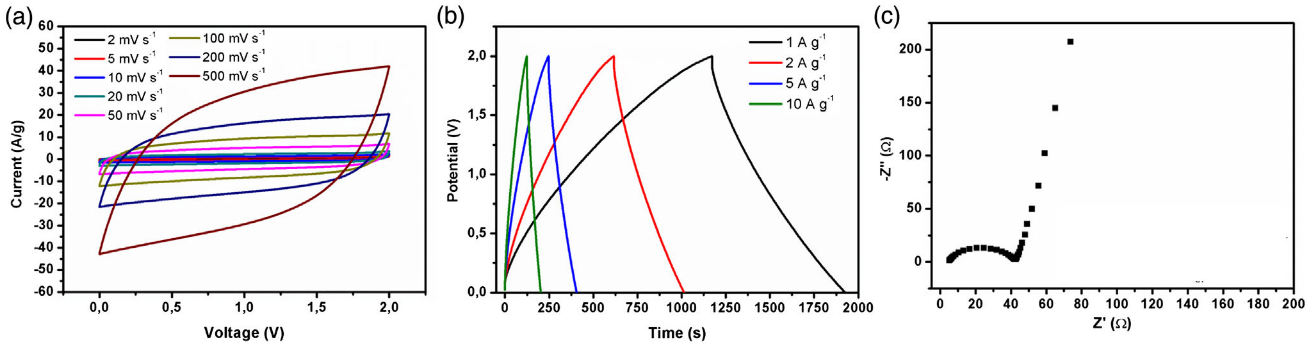

Figure 5. Electrochemical characteristics of GO-THA electrodes in 1 M $TEABF_4$ in ACN: a) CV, b) GCD curves, and c) electrochemical impedance spectroscopy and proposed electrical circuit.

great pseudocapatitative behavior, which can be only observed for low scan rates value (Figure S13, Supporting Information), as the Faradic peaks flatten with subsequent scan rates increment.

The specific capacitance of device calculated from GCD exceeds the value obtained in aqueous media and reaches 371 F g^{-1} at current density of 1 A g^{-1}, standing out among other GO-related materials (Figure 5b). The electrode also exhibits great capacitance retention at higher current densities reaching 250 F g^{-1} at 20 A g^{-1}(Figure S14, Supporting Information). Significantly, the increase in the operating window allowed notable increase of the energy density up to values as high as 94.4 Wh kg^{-1} with the power density reaching 333 mWh cm^{-3}, being exceptional performance for energy storage applications. Moreover, the GO-THA electrodes exhibited high areal and volumetric capacitance of 556.5 mF cm^{-2} and 85.6 F cm^{-3}, respectively (Table S3, Supporting Information). According to Nyquist plot, R_S and R_{CT} factors can be evaluated by fitting the electrochemical impedance spectroscopy (EIS) spectra on the equivalent circuit proposed on Figure S15, Supporting Information. The charge transfer resistance reached values as low as 32 Ω, thereby providing excellent kinetics of electrochemical processes (Figure 5c). Notably, the attained conductivities of the electrode material correspond to 48 S cm^{-1} (Figure S15a, Supporting Information).

3. Conclusions

We have demonstrated the covalent functionalization of GO with thioamide-based polymer, as an efficient route to decorate in a robust fashion the surface of GO with different heteroatoms. The multiscale characterization of GO-THA by means of XPS, SEM-EDX, Raman, XRD, and FTIR analysis revealed significant amount of polymer present in the hybrid with high nitrogen and sulfur content. The GO-THA hybrid was employed as electrode material in symmetric SCs that were investigated in both aqueous (1 M H_2SO_4) and organic electrolyte (1 M $TEABF_4$ in ACN). In both cases the electrodes exhibited excellent conductivity and very good specific capacitance amounting to 221 and 340 F g^{-1}, respectively. Notably, the use of organic electrolyte made it possible to widen the potential window resulting in very high volumetric capacitances of 85.6 F cm^{-3} and energy density of 94.4 Wh kg^{-1}, being several times higher than typical energy densities of other carbonaceous materials.

4. Experimental Section

Materials: All the compounds and components required for the synthesis including triethylamine, carbon disulfide, 2,2′-(ethylenedioxy)bis(ethylamine), dicyclohexylcarbodiimide, electrolyte components tetraethylammonium tetrafluoroborate, acetonitrile (electronic grade), separators Whatman glass microfiber filters, binder poly(tetrafluoroethylene), and 1-methyl-2-pyrrolidinone were purchased from Sigma–Aldrich. Conductive carbon black Super P (H30253) was acquired from Alfa Aesar and carbon AvCarb P75 substrate was obtained from FuelCellStore. The GO was acquired from Graphenea (4 mg mL^{-1} solution).

Synthesis of Polymer THA: A 4 mL of ethanol was poured into a round bottom glass placed in ice cooled bath and subsequently 3.9 mL of triethylamine (4 eq, 28 mmol) and 4.2 mL of carbon disulfide (10 eq, 70 mmol) were added. Then, 1.04 g of 2,2′-(ethylenedioxy)bis(ethylamine) dissolved in 2 mL of ethanol was droplet added while the reaction mixture was intensively stirred. After 5 min the round bottom glass was taken out from the ice cooled bath and stored at room temperature for 4 h. Following, a pale-yellow precipitate was filtrated and rinsed with cooled ethanol to yield the final product (yield = 97%). To the solution of 0.496 × g *N*,*N*′-dicyclohexylcarbodiimide (2 eq, 2.4 mmol) in acetonitrile, 0.68 g of triethylammonium ((ethane-1,2diylbis(oxy))bis(ethane- 2,1-diyl))dicarbamodithiolate (1 eq, 1.2 mmol) dissolved in 5 mL of acetonitrile was added dropwise. The reaction was carried out for 1 h at RT. Subsequently, the white precipitate was filtered, and 10 mL of water was added to the yellow solution, followed by three times extraction with DCM. The combined organic fractions were washed with brine, dried over anhydrous Na_2SO_4, and evaporated till fully exsiccated. The crude product was dissolved in a small volume of cold ethyl acetate and placed in the ice bath for 1 h to enable the precipitation of the residual dicyclohexylurea (DCU). After filtration, the solution was evaporated under the vacuum to give the isothiocyanate product as a yellow oil (60% yield). 0.68 × g of 1,2-bis(2-isothiocyanatoethoxy)ethane (1 eq, 2.9 mmol) was dissolved in 10 mL of DCM and added dropwise 0.42 mL of 2,2′-(ethylenedioxy)bis(ethylamine) (1 eq, 2.8 mmol) mixed with constant stirring in RT. After 2 h, additional amount of 2,2′-(ethylenedioxy)bis(ethylamine) (0.1 mL) was added and stirred for 15 min. The precipitate was filtered and dried to yield product (30% yield).

Preparation of GO-THA Hybrid Material: A mixture of DMF (10 mL) and aqueous GO (10 mL, 4 mg mL^{-1}) was sonicated for 15 min and then 10 mL of THA polymer in DMF (40 mg mL^{-1}) was added. The mixture was rigorously stirred overnight and heated at 90 °C. The resulting powder was then filtered and washed several times with DMF and copious amount of water to remove the unreacted THA polymer. The product was then freeze-dried for 24 h under vacuum to obtain black solid foam-like material.

Characterization Techniques: FTIR spectra were recorded in the mid-IR range (400–4000 cm^{-1}) by using a Perkin Elmer Spectrometer (Spectrum Two) equipped with ATR Diamond. XPS analyses were carried out on a Thermo Scientific KAlpha X-ray photoelectron spectrometer with a basic chamber pressure of ≈10–9 mbar and an Al anode as the X-ray source (X-ray radiation of 1486 eV). X-ray powder diffraction (XRD) experiments were conducted on powder specimens using Bruker ASX D8 Advanced equipped with Cu anode with Kα radiation ($\lambda = 1.5418$ Å). Diffraction patterns were collected at room temperature in the scattered angular range between 6° and 40° with an angular resolution of 0.02° per step and a typical counting time 4 of 10 s per step. The specific surface area was measured by using a Micromeritics ASAP 2050 surface area and porosity analyzer. Prior to the BET measurements, the samples were outgassed for 12 h at 100 °C. Adsorption isotherms were calculated for nitrogen adsorption at 77 K and pressures up to 1 bar. SEM characterization was carried out by means of a FEI Quanta 250 FEG instrument with EDX analyses. High-resolution transmission electron microscopy (HR-TEM) was performed with a Hitachi HT7700 transmission electron microscope. TGA decomposition curves are recorded in the range 25–700 °C operating under nitrogen atmosphere, with a thermal step of 10 °C min^{-1} on a Mettler Toledo TGA/SDTA851e system. Raman spectra were recorded by a Renishaw microscope with a 100× objective, laser excitation wavelength of 532 nm, and laser power of 0.05%. The silicon peak at 520.3 cm^{-1} was taken as reference for wavenumber calibration. Point of zero charge of adsorbent was determined following previously reported method. Mass spectra were collected on MALDI-TOF mass spectra Ultrafle Xtreme Bruker.

Preparation of SCs: The working electrodes were prepared by mixing of GO-THA hybrid (80 wt%, 8 mg), carbon black (10 wt%, 1 mg), and poly(tetrafluoroethylene) (PTFE) (10 wt%, 1 mg) in a probe with 1 mL of *N*-methylpyrrolidone (NMP) and sonicated for 15 min to achieve homogeneous suspension. Consequently, the material was deposited on carbon substrate providing 2 mg of active material per electrode (AvCarb-P75) and dried under vacuum (80 °C). The electrodes were assembled in CR2032 coin cell using Whatman glass microfiber filters as a separator and several drops of the given electrolyte, i.e., 1 M aqueous H_2SO_4 or 1 M tetraethylammonium tetrafluoroborate in acetonitrile.

Electrochemical Measurements: The CV study was performed in the range of 0-2 V with scan rates spanning from 2 to 1000 mV s^{-1}. GCD curves were recorded from 0–2 V at different current densities

(1–20 A g^{-1}) and used to calculate specific capacitance using following formula[49]

$$E = \frac{2 \times I \times \Delta t}{m \times \Delta V} \quad (1)$$

where I is a current density, Δt is the discharge time, m is a mass of the electrode, and ΔV is a potential window. EIS and conductivity of electrodes were taken in the frequency range from 200 kHz to 1 mHz with an amplitude of 10 mV. The energy density (Equation (2)) and power density (Equation (3)) were calculated as given

$$E = \frac{C \times \Delta V^2}{3.6 \times 2} \quad (2)$$

$$P = \frac{E'}{\Delta t} \times 3600 \quad (3)$$

where E is the energy density (Wh kg^{-1}), C is the gravimetric capacitance, ΔV is the discharge voltage range, P is the power density (in mWh cm^{-3}), E' is the volumetric energy density, and Δt is the discharge time. CVs, GCD curves, and EIS were recorded using EC-LAB VMP3 (BioLogic Science Instrument).

Supporting Information

Supporting Information is available from the Wiley Online Library or from the author.

Acknowledgements

This work was financially supported by the National Science Center (grant nos. 2019/33/N/ST5/00052 and 2019/35/B/ST5/01568). Grant no. POWR.03.02.00-00-I026/16 co-financed by the European Union through the European Social Fund under the Operational Program Knowledge Education Development. The authors also acknowledge support from the Interdisciplinary Thematic Institute SysChem via the IdEx Unistra (ANR-10-IDEX-0002) within the program Investissement d'Avenir program, the Fundation Jean-Marie Lehn, and the Institut Universitaire de France (IUF).

Conflict of Interest

The authors declare no conflict of interest.

Data Availability Statement

The data that support the findings of this study are available from the corresponding author upon reasonable request.

Keywords

energy storage, graphene oxide, supercapacitors, thioamide polymer

Received: February 6, 2023
Revised: March 16, 2023
Published online:

---

[1] C. Couly, M. Alhabeb, K. L. Van Aken, N. Kurra, L. Gomes, A. M. Navarro-Suárez, B. Anasori, H. N. Alshareef, Y. Gogotsi, *Adv. Electron. Mater.* **2018**, *4*, 1700339.
[2] J. Sun, B. Luo, H. Li, *Adv. Energy Sustain. Res.* **2022**, *3*, 2100191.
[3] L. Wang, X. Feng, L. Ren, Q. Piao, J. Zhong, Y. Wang, H. Li, Y. Chen, B. Wang, *J. Am. Chem. Soc.* **2015**, *137*, 4920.
[4] S. Huang, X. Zhu, S. Sarkar, Y. Zhao, *APL Mater.* **2019**, *7*, 100901.
[5] C. Lethien, J. Le Bideau, T. Brousse, *Energy Environ. Sci.* **2019**, *12*, 96.
[6] E. Frackowiak, Q. Abbas, F. Béguin, *J. Energy Chem.* **2013**, *22*, 226.
[7] R. Guo, L. Li, B. Wang, Y. Xiang, G. Zou, Y. Zhu, H. Hou, X. Ji, *Energy Storage Mater.* **2021**, *37*, 8.
[8] H. Wu, Y. Zhang, L. Cheng, L. Zheng, Y. Li, W. Yuan, X. Yuan. *Energy Storage Mater.* **2016**, *5*, 8.
[9] J. Zhu, L. Wang, X. Gan, T. Tang, F. Qin, W. Luo, Q. Li, N. Guo, S. Zhang, D. Jia, H. Song, *Energy Storage Mater.* **2022**, *47*, 158.
[10] R. Kumar, S. Sahoo, E. Joanni, R. K. Singh, K. Maegawa, W. K. Tan, G. Kawamura, K. K. Kar, A. Matsuda, *Mater. Today* **2020**, *39*, 47.
[11] S. Kumar, G. Saeed, L. Zhu, K. N. Hui, N. H. Kim, J. H. Lee, *Chem. Eng. J.* **2021**, *403*, 126352.
[12] H. Pan, J. Y. Li, Y. P. Feng, *Nanoscale Res. Lett.* **2010**, *5*, 654.
[13] S. Ghosh, S. Barg, S. M. Jeong, K. Ostrikov, *Adv. Energy Mater.* **2020**, *10*, 2001239.
[14] Z.-H. Huang, T.-Y. Liu, Y. Song, Y. Li, X.-X. Liu, *Nanoscale* **2017**, *9*, 13119.
[15] J.-S. M. Lee, M. E. Briggs, C.-C. Hu, A. I. Cooper, *Nano Energy* **2018**, *46*, 277.
[16] Y. M. Volfkovich, V. E. Sosenkin, A. Y. Rychagov, A. V. Melezhik, A. G. Tkachev, E. N. Kabachkov, V. I. Korepanov, I. I. Khodos, A. Michtchenko, Y. M. Shulga, *Microporous Mesoporous Mater.* **2021**, *319*, 111063.
[17] R. Zhou, Y. Li, K. H. Lam, *J. Mater. Chem. A* **2021**, *9*, 21302.
[18] D. R. Dreyer, S. Park, C. W. Bielawski, R. S. Ruoff, *Chem. Soc. Rev.* **2010**, *39*, 228.
[19] S. Eigler, A. Hirsch, *Angew. Chem. Int. Ed.* **2014**, *53*, 7720.
[20] A. T. Lawal, *Biosens. Bioelectron.* **2019**, *141*, 111384.
[21] K. Parvez, S. Yang, Y. Hernandez, A. Winter, A. Turchanin, X. Feng, K. Müllen, *ACS Nano* **2012**, *6*, 9541.
[22] A. Razaq, F. Bibi, X. Zheng, R. Papadakis, S. H. M. Jafri, H. Li, *Materials* **2022**, *15*, 1012.
[23] F. Bonaccorso, L. Colombo, G. Yu, M. Stoller, V. Tozzini, A. C. Ferrari, R. S. Ruoff, V. Pellegrini, *Science* **2015**, *347*, 1246501.
[24] H. Guo, T. Jiao, Q. Zhang, W. Guo, Q. Peng, X. Yan, *Nanoscale Res. Lett.* **2015**, *10*, 272.
[25] F. Li, X. Jiang, J. Zhao, S. Zhang, *Nano Energy* **2015**, *16*, 488.
[26] X. Liu, J. Li, X. Wang, C. Chen, X. Wang, *J. Nucl. Mater.* **2015**, *466*, 56.
[27] D. Pakulski, W. Czepa, S. Witomska, A. Aliprandi, P. Pawluć, V. Patroniak, A. Ciesielski, P. Samorì, *J. Mater. Chem. A* **2018**, *6*, 9384.
[28] J. Xu, Y. Wang, S. Hu, *Microchim. Acta* **2017**, *184*, 1.
[29] A. Iakunkov, A. V. Talyzin, *Nanoscale* **2020**, *12*, 21060.
[30] W. Czepa, S. Witomska, A. Ciesielski, P. Samorì, *Nanoscale* **2020**, *12*, 18733.
[31] V. Agarwal, P. B. Zetterlund, *Chem. Eng. J.* **2021**, *405*, 127018.
[32] A. O. E. Abdelhalim, V. V. Sharoyko, A. A. Meshcheriakov, S. D. Martynova, S. V. Ageev, G. O. Iurev, H. Al Mulla, A. V. Petrov, I. L. Solovtsova, L. V. Vasina, I. V. Murin, K. N. Semenov, *Nanomed.: Nanotechnol. Biol. Med.* **2020**, *29*, 102284.
[33] V. Belessi, D. Petridis, T. Steriotis, K. Spyrou, G. K. Manolis, V. Psycharis, V. Georgakilas, *SN Appl. Sci.* **2018**, *1*, 77.
[34] K. Gross, J. J. P. Barragán, S. Sangiao, J. M. De Teresa, L. Lajaunie, R. Arenal, H. A. Calderón, P. Prieto, *Nanotechnology* **2016**, *27*, 365708.
[35] X. Zheng, S. S. Mofarah, A. Cen, C. Cazorla, E. Haque, E. Y. Chen, A. J. Atanacio, M. Manohar, C. Vutukuri, J. L. Abraham, P. Koshy, C. C. Sorrell, *ACS Appl. Mater. Interfaces* **2021**, *13*, 59820.
[36] Y. J. Oh, J. J. Yoo, Y. I. Kim, J. K. Yoon, H. N. Yoon, J.-H. Kim, S. B. Park, *Electrochim. Acta* **2014**, *116*, 118.
[37] W. Ge, Q. L. Ma, W. Wang, F. F. Jia, S. X. Song, *Chem. Phys.* **2021**, *543*, 111096.

[38] M. Hwang, H. W. Kim, J. U. Jin, H. Yoo, J. Yu, B. C. Ku, N. H. You, *Int. J. Energy Res.* **2021**, *45*, 21209.
[39] B. Rajagopalan, J. S. Chung, *Nanoscale Res. Lett.* **2014**, *9*, 535.
[40] X. Gao, H. Zhang, E. Guo, F. Yao, Z. Wang, H. Yue, *Microchem. J.* **2021**, *164*, 105979.
[41] B. Song, J. Zhao, M. Wang, J. Myllavey, Y. Zhu, Z. Geng, D. Chen, Y. Ding, K. Moon, M. Liu, C.-P. Wong, *Nano Energy* **2017**, *31*, 183.
[42] P. J. McHugh, A. D. Stergiou, M. D. Symes, *Adv. Energy Mater.* **2020**, *10*, 2002453.
[43] T.-W. Lin, C.-S. Dai, K.-C. Hung, *Sci. Rep.* **2014**, *4*, 7274.
[44] C. Liu, Z. Yu, D. Neff, A. Zhamu, B. Z. Jang, *Nano Lett.* **2010**, *10*, 4863.
[45] Q. Wang, J. Yan, Z. Fan, *Energy Environ. Sci.* **2016**, *9*, 729.
[46] Z. Yang, J. Tian, Z. Yin, C. Cui, W. Qian, F. Wei, *Carbon* **2019**, *141*, 467.
[47] C. Zhong, Y. Deng, W. Hu, J. Qiao, L. Zhang, J. Zhang, *Chem. Soc. Rev.* **2015**, *44*, 7484.
[48] X. Wang, Y. Li, F. Lou, M. E. Melandsø Buan, E. Sheridan, D. Chen, *RSC Adv.* **2017**, *7*, 23859.
[49] X. Shi, S. Zhang, X. Chen, T. Tang, E. Mijowska, *Carbon* **2020**, *157*, 55.
[50] E. S. Wallis, J. F. Lane, *Org. React.* **2011**, 267.
[51] Y. Zu, C. He, D. Liu, L. Chen, *Dyes Pigm.* **2020**, *173*, 107841.
[52] D. Chen, C. Gan, X. Fan, L. Zhang, W. Li, M. Zhu, X. Quan, *Materials* **2019**, *12*, 2800.
[53] S. Witomska, Z. Liu, W. Czepa, A. Aliprandi, D. Pakulski, P. Pawluć, A. Ciesielski, P. Samorì, *J. Am. Chem. Soc.* **2019**, *141*, 482.
[54] Y. He, Z. Shan, T. Tan, Z. Chen,Y. Zhang, *Polymers* **2018**, *10*, 930.
[55] J. Zhang, H. Zhao, G. Li, X. Zhu, L. Shang, Y. He, X. Liu, Y. Ma, M. Szostak, *Org. Biomol. Chem.* **2022**, *20*, 5981.
[56] S. Chen, J. Zhu, X. Wu, Q. Han, X. Wang, *ACS Nano* **2010**, *4*, 2822.

Supporting Information

A graphene oxide – thioamide polymer hybrid for high performance supercapacitor electrode

Włodzimierz Czepa, Samanta Witomska, Paolo Samorì and Artur Ciesielski**

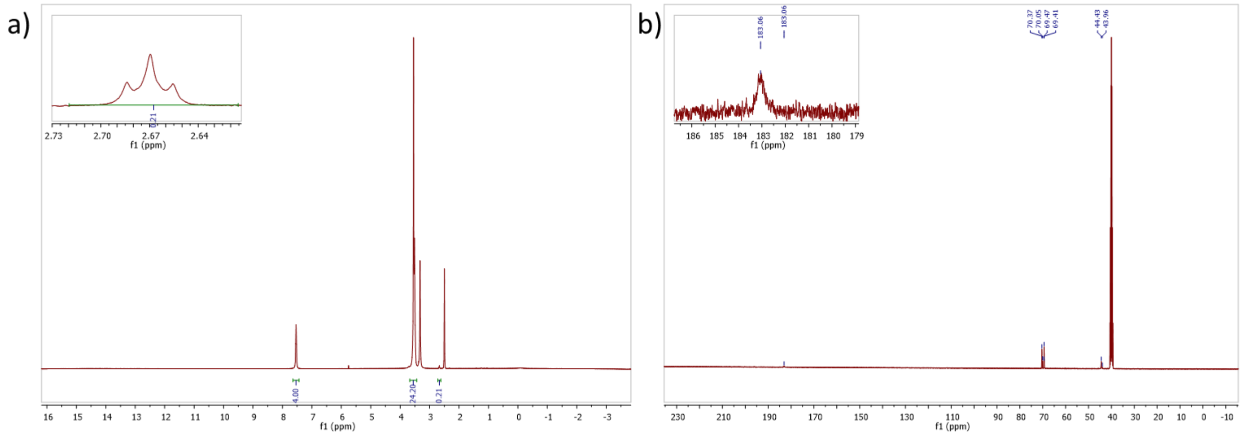

Figure S1 Nuclear Magnetic Resonance spectra of THA polymer: a) ^{1}H NMR, b) ^{13}C NMR.

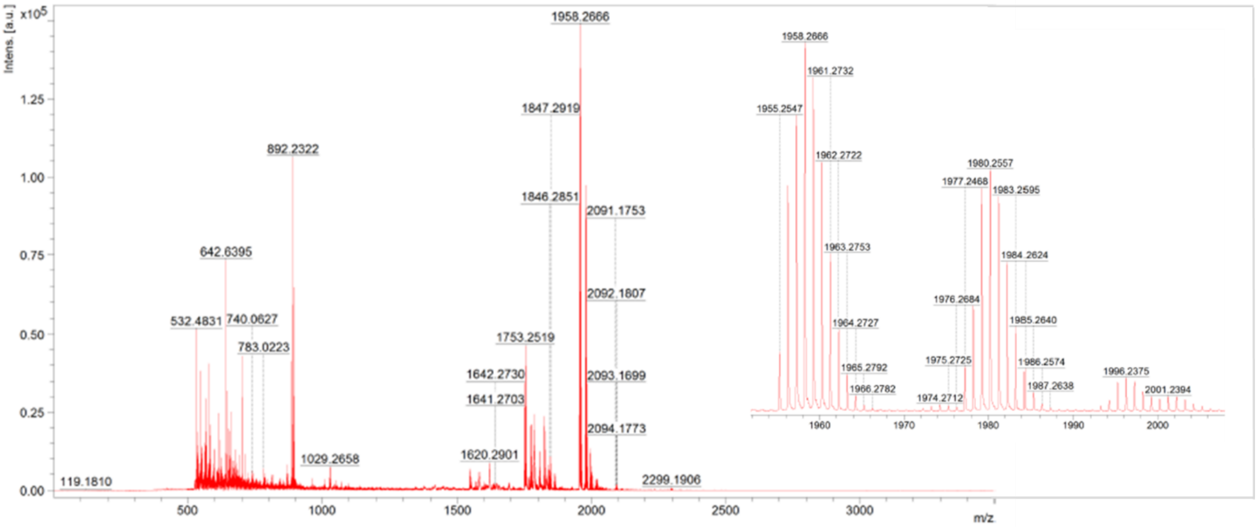

Figure S2 MALDI-TOF spectra of THA polymer.

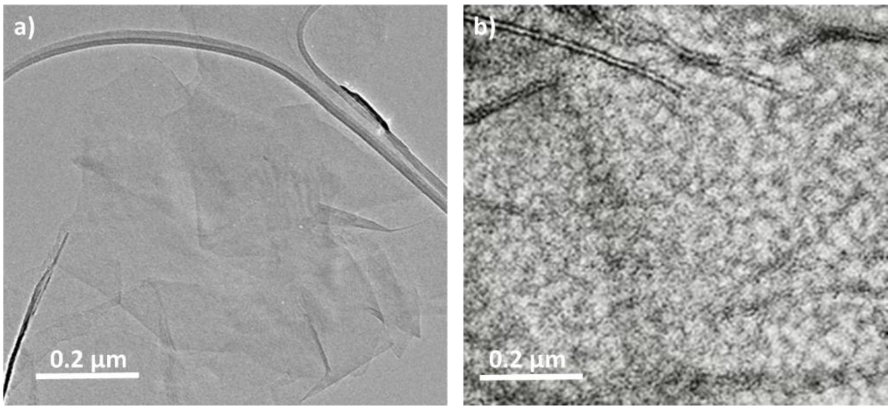

Figure S3 TEM pictures of (a) GO (b) GO-THA.

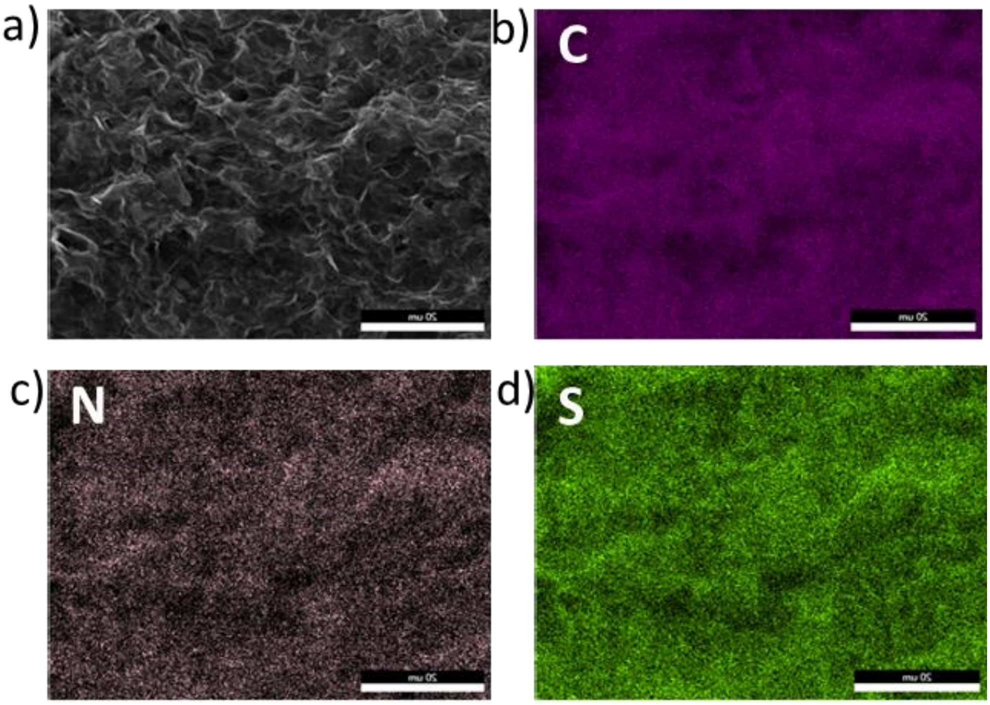

Figure S4 (a) SEM and (b-d) EDX element mapping spectra of GO-THA hybrid's (b) carbon, (c) nitrogen, and (d) sulfur.

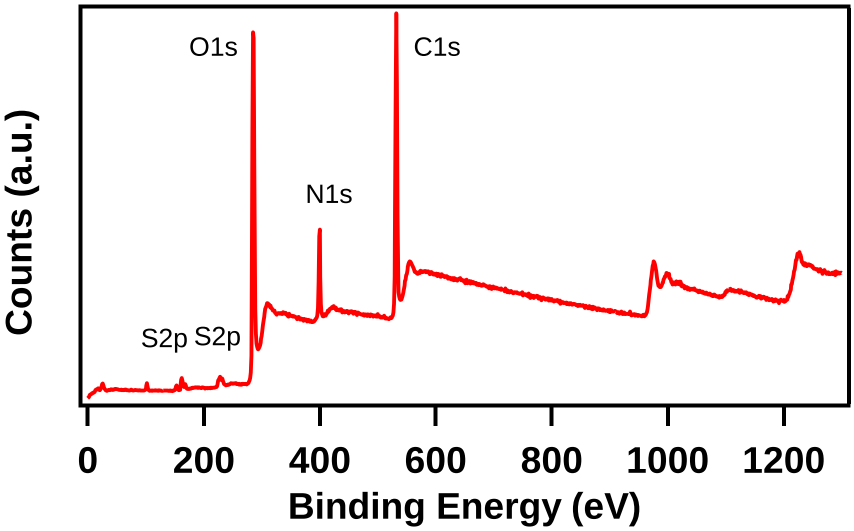

Figure S5 X-ray Photoelectron Spectroscopy survey spectra of GO-THA composite.

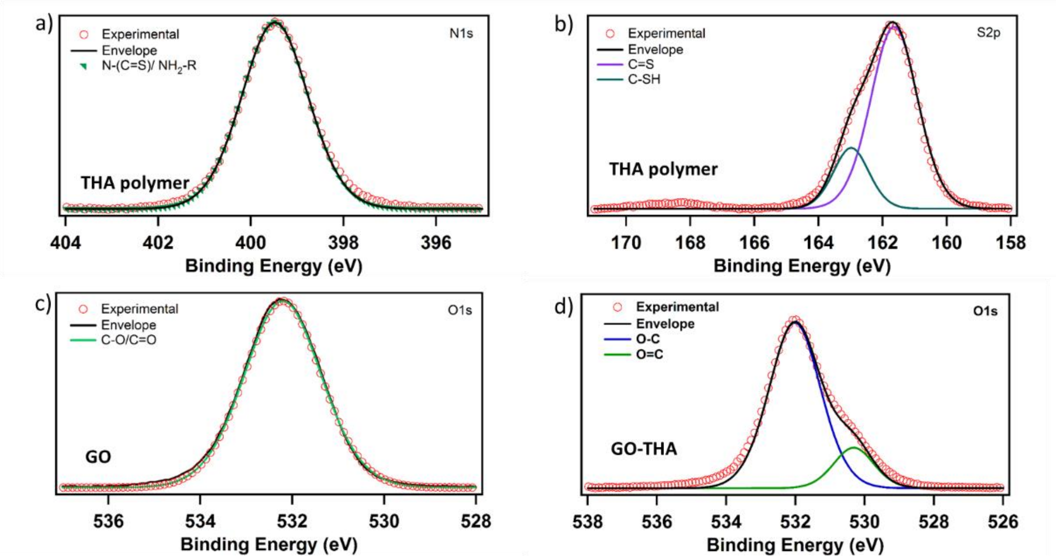

Figure S6 X-ray Photoelectron Spectroscopy of THA polymer: a) N1s, b) S2p, GO: c) O1s and GO-THA: d) O1s: d) O1s; GO-THA hybrid: e) O1s.

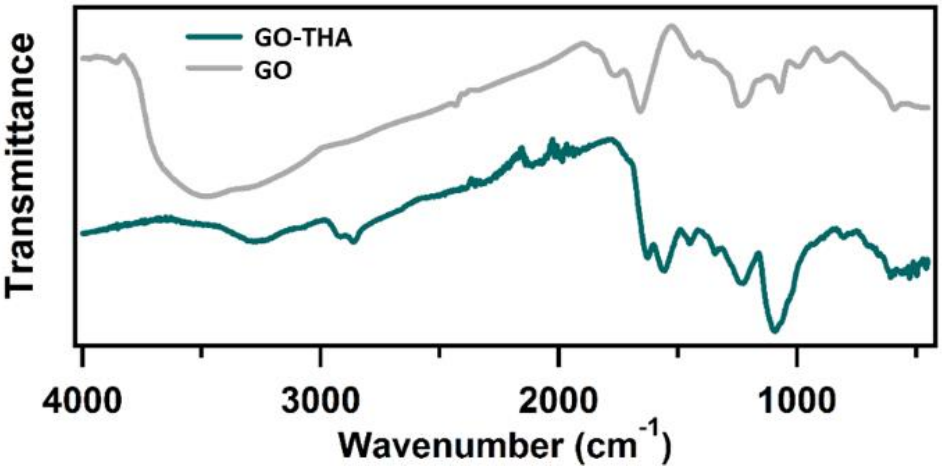

Figure S7 FT-IR spectra of GO (gray) and GO-THA hybrid (black).

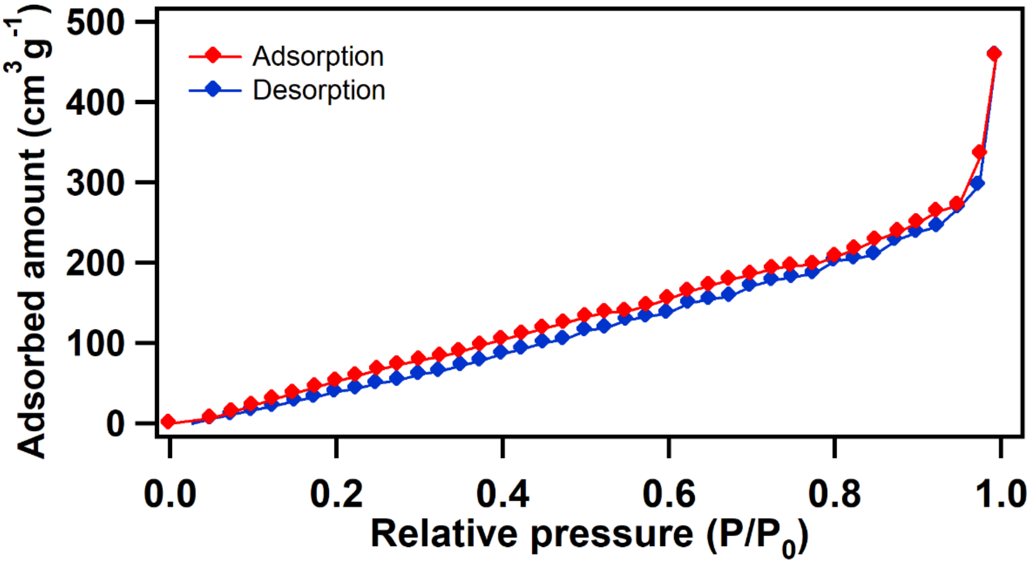

Figure S8 Adsorption-desorption N_2 isotherm of GO-THA hybrid.

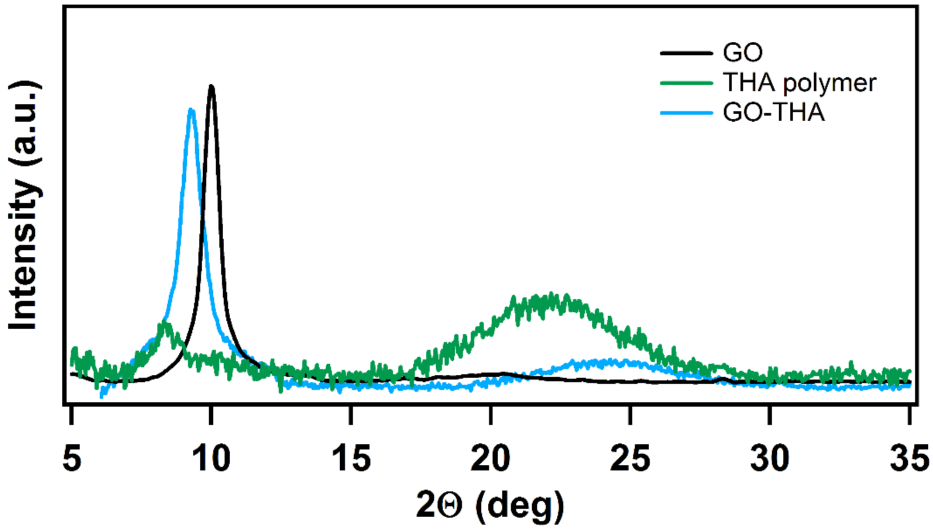

Figure S9 XRD patterns of GO, THA and GO-THA hybrid.

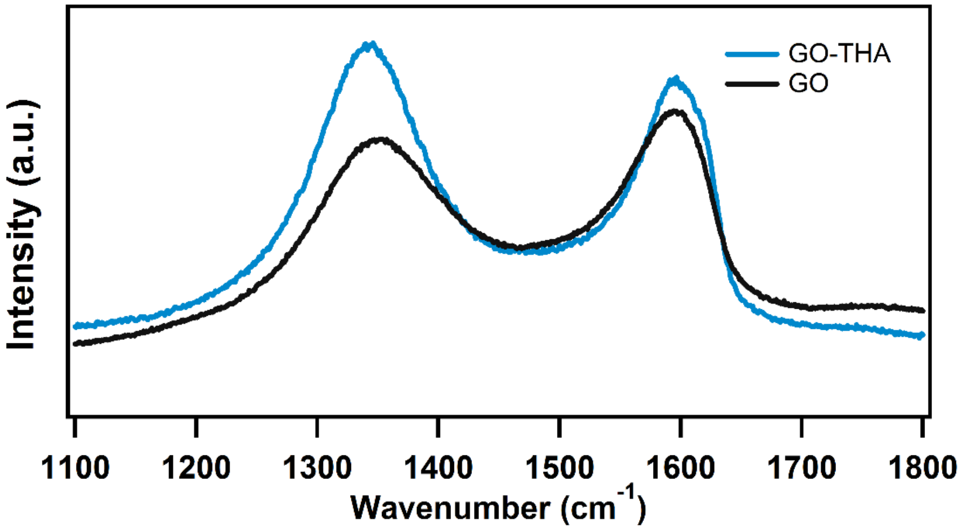

Figure S10 Raman spectra of GO and GO-THA hybrid.

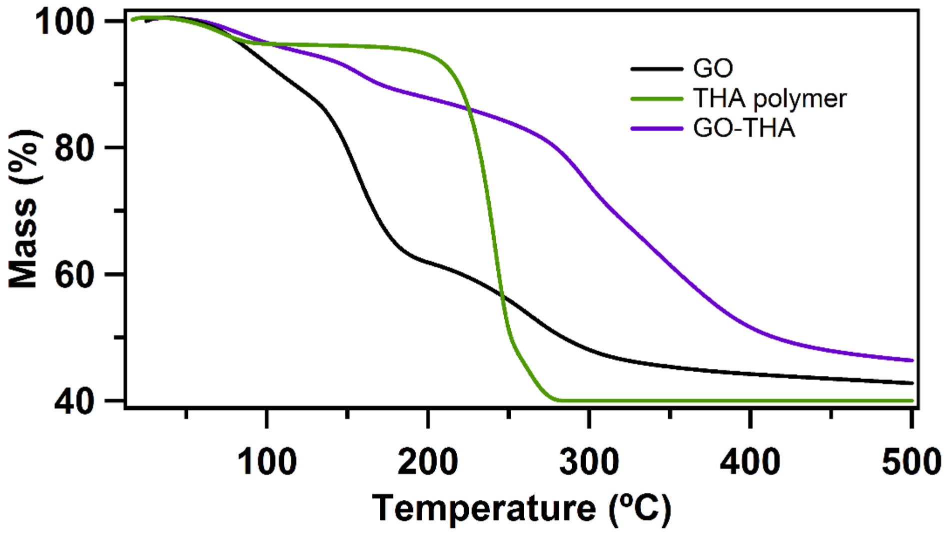

Figure S11 Thermogravimetric analysis of GO, THA and GO-THA hybrid.

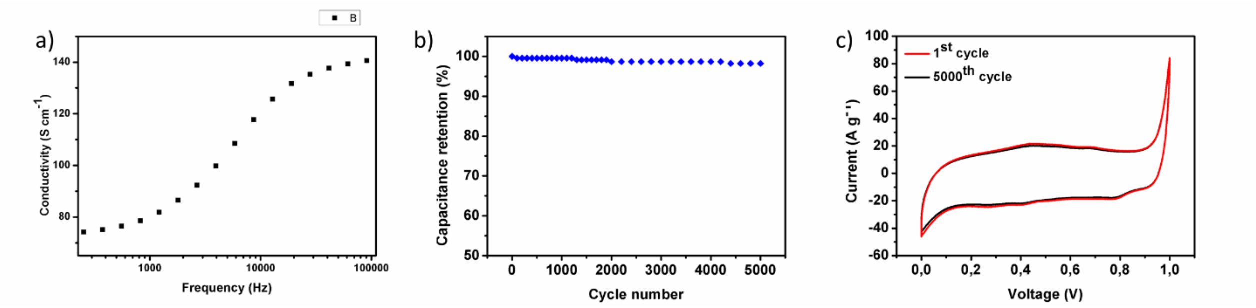

Figure S12 Electrochemical characteristics of GO-THA supercapacitor device in 1 M H_2SO_4: a) conductivity; b) stability of device over 5000 cycles; c) CV collected while 1st and 5000th cycle at 100 mV s^{-1}.

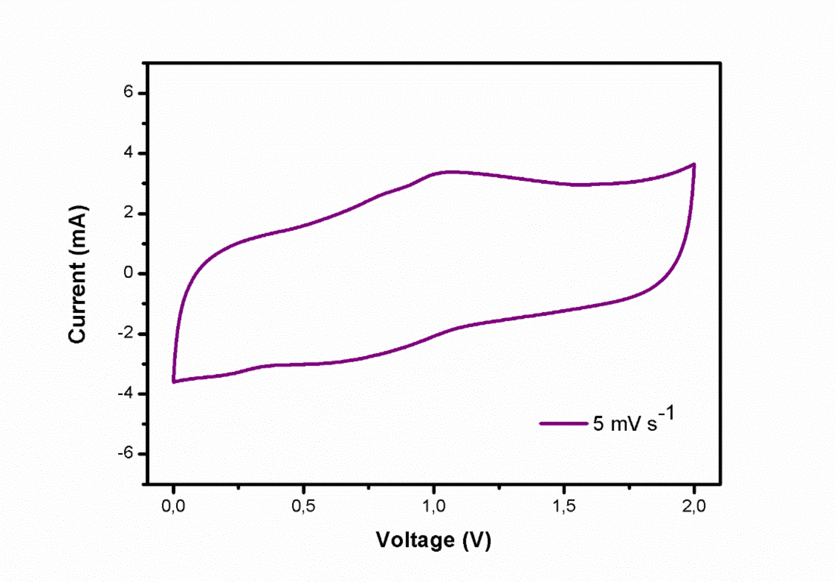

Figure S13 CV curve of GO-THA prepared device in $TEABF_4$ in ACN at 5 mV s^{-1}.

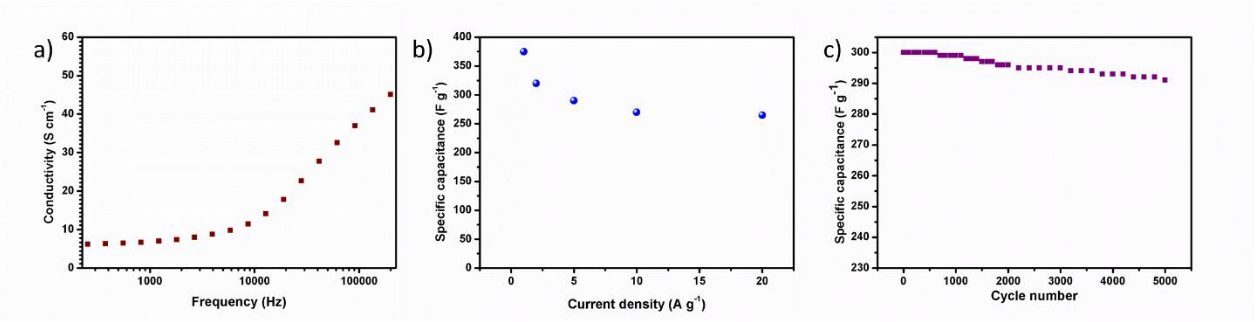

Figure S14 Electrochemical characteristics of GO-THA supercapacitor device in 1 M $TEABF_4$ in acetonitrile: a) conductivity; b) specific capacitance over different current density values; c) stability of the sample over 5000 cycles.

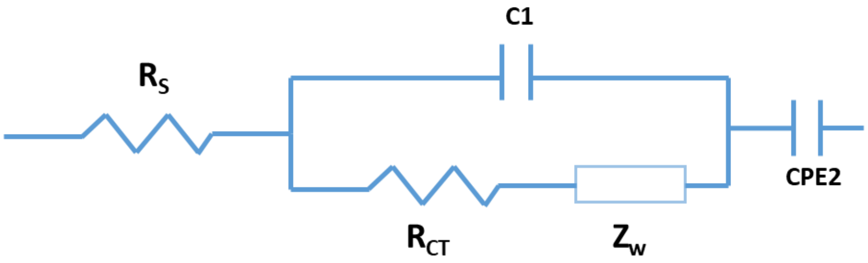

Figure S15 Proposed equivalent electrical circuit. Rs

Table S1 Chemical composition of GO-THA hybrid based on elemental analysis and XPS survey.

Table S2 BET surface area analysis of GO, POSS, rGO and rGO-POSS.

Analysis	**%C**	**%N**	**%S**
Elemental analysis	**55.07**	**9.17**	**4.02**
XPS survey composition	66.8	9.23	3.93

	BET Surface area (m^2g^{-1})	**Pore volume (cm^3 g^{-1})**	**Average pore size (nm)**
GO	108	0.15	5.6
THA polymer	62	0.013	2.0
GO-THA	371	0.0524	3.3

Table S3 Circuit parameters for the EIS measurements of GO-THA in 1M H_2SO_4.

Element	**Parameter**	**Value**	**Estimated Error (%)**
R_S	R	0.9	2.21

R$_{CT}$	R	6.0	3.54
C1	C	7.9 µF	7.12
Z$_{W}$	Y0	0.00596	12.5
CPE2	Y0	0.0036	6.84

Table S4 Circuit parameters for the EIS measurements of GO-THA in 1M TEABF$_4$ in ACN.

Element	Parameter	Value	Estimated Error (%)
R$_{S}$	**R**	4.6	2.17
R$_{CT}$	**R**	32	4.22
C1	**C**	12.9 µF	6.15
Z$_{W}$	**Y0**	0.00812	10.78
CPE2	**Y0**	0.00391	7.65

Table S5 The most important electrochemical parameters calculated for symmetric GO-THA device in 1M TEABF$_4$ in acetonitrile.

Current density (A g^{-1})	Gravimetric capacitance (F g^{-1})	Areal capacitance (mF cm^{-2})	Volumetric capacitance (F cm^{-3})	Energy density (Wh kg^{-1})	Power density (mWh cm^{-3})
1	371	556.5	85.6	94.4	24.1
2	324	486	74.8	90	41.5
5	289	433.5	66.7	80.3	92.6
10	275	412.5	63.5	76.4	176.3
20	260	390	60	72.2	333

Table S6 Comparison of most common characteristics of GO-polymer based electrodes.

Material	Specific capacitance	Scan rates/ Current density	Electrolyte	Energy density	Ref.
GO/polythiophene	201 F g^{-1}	10 mVs^{-1}	1M H$_2$SO$_4$	-	[1]
GO/PANI	320 F g^{-1}	0.1 A g^{-1}	2M H$_2$SO$_4$	-	[2]
GO	121.7 F g^{-1} 423 F g^{-1}	- -	1M H$_2$SO$_4$ C$_4$MIM BF$_4$	3.08 kW kg^{-1} 11.6 Wh kg^{-1}	[3]
C-Sr-GO	260 F g^{-1}	1 A g^{-1}	6M KOH	36.3 Wh kg^{-1}	[4]
N-rGO	223.5 F g^{-1}	1 mVs^{-1}	6M KOH	-	[5]
NSG	176.5 F g^{-1}	1 A g^{-1}	6M KOH	-	[6]
GP	361.9 F g^{-1}	1 A g^{-1}	2M H$_2$SO$_4$	-	[7]
N/O-doped porous carbon	522 F g^{-1} (3-electrode)	0.5 A g^{-1}	6M KOH	18.04 Wh kg^{-1}	[8]
Graphene/polyrrole	285 F g^{-1}	0.5 A g^{-1}	0.5M Na$_2$SO$_4$	-	[9]
N/S co-doped rGO	180.5 F g^{-1}	1 A g^{-1}	EMIMBF$_4$	33 Wh kg^{-1}	[10]
tris/rGO	119 F g^{-1}	10 mVs^{-1}	BMIMBF$_4$	51 Wh kg^{-1}	[11]

	131 F g^{-1} 189 F g^{-1}	2 mVs^{-1} 2 mVs^{-1}	$TEABF_4$/ACN 1M H_2SO_4	- -	
pErGO	81 F g^{-1}	0.5 A g^{-1}	Polivinyl H_3PO_4 gel	11.25 Wh kg^{-1}	[12]
Sulfonated graphene PPy	310 F g^{-1}	0.3 A g^{-1}	1M KCl	4.3 Wh kg^{-1}	[13]
GO-THA	221 F g^{-1} 340 F g^{-1}	1 A g^{-1} 1 A g^{-1}	1M H_2SO_4 1M $TEABF_4$ ACN	27 Wh kg^{-1} 94.4 Wh kg^{-1}	This work

List of abbreviations: GO - graphene oxide; PANI- polyaniline; C-Sr-GO – crumpled sulfur-assisted reduced graphene oxide; N-rGO – nitrogen enriched reduced graphene oxide; NSG-nitrogen and sulfur co-doped graphene; GP- graphene-polyaniline, Tris/rGO- tris(2-aminoethyl) amine/ reduced graphene oxide, pErGO- growing porous electrochemically reduced graphene oxide, PPy- polypyrole.

References:

[1] N. A. Kumar, H. J. Choi, A. Bund, J. B. Baek, Y. T. Jeong, Journal of Materials Chemistry. **2012**, 22, 12268;
[2] K, Zhang, L. L. Zhang, X. S. Zhao, J. Wu, Chem. Mater. **2010**, 22,1392;
[3] M. P. Down, S. J. Rowley-Neale, G. C. Smith, C. E. Banks, ACS Appl. Energy Mater. **2018**, 1, 707;
[4] M. Hwang, H.-W. Kim, J.-U. Jin, H. Yoo, J. Yu, B.-C. Ku, N.-H. You, Int. J. Energy Res. **2021**, 45, 21209;
[5] L. Chen, X. Chen, Y. Q. Wen, B. X. Wang, Y. C. Wu, Z. T. Sheng, J. Nanosci. Nanotechnol. **2020**, 20, 4854;
[6] F. Pogacean,C. Varodi, M. Coros, I. Kacso, T. Radu, B. I. Cozar, V. Mirel, S. Pruneanu Biosensors, **2021**,11, 36;
[7] L. Jianhua, A. Junwei, Z. Yecheng, M. Yuxiao, L. Mengliu, Y. Mei, et al. ACS Appl. Mater. Interfaces, **2012**, 4, 2870;
[8] J. Lao, Y. Lu, S. Fang, F. Xu, L. Sun, et al. Nanomaterials, 2022, 12, 2186.
[9] P. Si, S. Ding, X. –W. Lou, D. –H. Kim, RSC Adv. **2011,** *1* (7), 1271.

[10] Y. Chen, L. Sun, Z. Liu, Y. Jiang, K. Zhuo, Mater. Chem. Phys. 2019, 238, 121932.

[11] B. Song, J. Zhao, M. Wang, J. Myllavey, Y. Zhu, et al. Nano Energy, 2017, 31, 183.

[12] T. Purkait, G. Singh, D. Kumar, M. Singh, R. S. Dey, Sci. Rep., 2018, 8, 640.

[13] X. Zuo, Y. Zhang, L. Si, B. Zhou, B. Zhao, L. Zhu, et al. J. Alloys Comp. 2016, 688, 140.

Journal of
Materials Chemistry C

ROYAL SOCIETY OF CHEMISTRY

PAPER

View Article Online
View Journal | View Issue

Check for updates

Cite this: *J. Mater. Chem. C*, 2021, 9, 12133

Synthesis and characterization of ultralong copper sulfide nanowires and their electrical properties†

Cosimo Anichini,[a] Włodzimierz Czepa,[bc] Alessandro Aliprandi,[a] Valentina Girelli Consolaro,[d] Ovidiu Ersen,[d] Artur Ciesielski *[ab] and Paolo Samorì *[a]

Received 28th June 2021,
Accepted 20th July 2021

DOI: 10.1039/d1tc03004c

rsc.li/materials-c

We report the synthesis of ultralong copper sulfide nanowires (Cu_{2-x}SNWs) through the sulphidation reaction of metallic copper nanowires (CuNWs) by thiourea under mild conditions. The multiscale characterization of Cu_{2-x}SNWs revealed the presence of a core shell structure made up of an external covellite layer coating a roxbyite core. The Cu_{2-x}SNWs, exhibiting lengths as high as 200 μm, can be easily dispersed in ethanol and deposited onto arbitrary substrates such as glass or plastic. The resulting films are readily conducting without the need for post-treatments and exhibit a sheet resistance of 4.1 kΩ sq^{-1} at 73.7% transmittance (at 550 nm), by virtue of the high aspect ratio of the Cu_{2-x}SNWs. The multiscale electrical characterization down to the single Cu_{2-x}SNWs revealed a low resistivity of 6.9×10^{-6} Ω m and perfect Ohmic conductivity. Interestingly, the conductivity of Cu_{2-x}SNW films supported on polyethylene naphthalate sheets remained almost unaltered (4% decrease) after 10 000 bending cycles. In addition, Cu_{2-x}SNWs have shown excellent chemical stability towards a strong oxidant like $FeCl_3$ as well as in an acidic environment. Finally, Cu_{2-x}SNWs have been employed as active materials in symmetric supercapacitors revealing good pseudocapacitive behaviour, with specific capacity as high as 324 F g^{-1} (at 5 mV s^{-1}) and 70% retention of the initial capacitance after 5000 cycles (at 100 mV s^{-1}).

Introduction

The ever-growing flexible, wearable electronics markets require a constant supply of conducting materials that can be processed at low-cost, over a large area and on various flexible substrates. Furthermore, for opto-electronic applications, transparency of thin conductive films is a coveted feature, *e.g.* due to the widespread demand for curved/foldable screens. Beyond carbon-based nanomaterials such as carbon nanotubes[1] or graphene,[2] metal nanowires have been considered as the next generation of flexible transparent conductors.[3] Indeed, the high aspect ratio of metal nanowires allows them to exhibit a relatively low percolation threshold, which is beneficial for the fabrication of thin film conductive layers and devices for transparent electronics[4] with enhanced mechanical properties. Among them, copper nanowires (CuNWs) have gained increasing attention in the last decade as they can be readily synthesized at extremely low cost and exhibit high processability.[5] Furthermore, in view of the high transparency of the obtained CuNW films, performance comparable to commercially available transparent conductive oxides such as indium tin oxide (ITO) can be reached. Regrettably, CuNWs are prone to oxidation, which limits their technological applications. In particular, the as-synthesized CuNWs exhibit a native insulating oxide layer that needs to be removed to allow efficient charge percolation through CuNW films and networks. Many efforts have been devoted to improving the electrochemical stability of copper through the formation of alloys,[6] or by coating with protective shells.[7] Unfortunately, such strategies require a post-processing of the material that not only increases the production cost, but could be incompatible with chemically fragile substrates such as paper or plastic. Therefore, it is of interest to obtain a material that can be used as an ink to be readily deposited onto an arbitrary substrate without any further treatment. In this regard copper sulfide, which has the general formula $Cu_{2-x}S$, appears particularly appealing as it displays a remarkable chemical stability, while its electronic properties not only depend on the Cu : S ratio, but also on its morphology at the nanoscale.[8] Currently, $Cu_{2-x}S$ is explored in a wide range of applications including solar cells,

---

[a] *Université de Strasbourg, CNRS, ISIS 8 allée Gaspard Monge, 67000 Strasbourg, France. E-mail: ciesielski@unistra.fr, samori@unistra.fr*
[b] *Centre for Advanced Technologies, Adam Mickiewicz University, Uniwersytetu Poznańskiego 10, 61-614 Poznań, Poland*
[c] *Faculty of Chemistry, Adam Mickiewicz University, Uniwersytetu Poznańskiego 8, 61-614 Poznań, Poland*
[d] *Université de Strasbourg, CNRS, IPCMS, 23 rue du Loess, BP 43, 67034 Strasbourg Cedex 2, France*

† Electronic supplementary information (ESI) available. See DOI: 10.1039/d1tc03004c

photocatalysis, biosensors, optoelectronics and is employed as a cathode material in lithium rechargeable batteries.[9]

Herein, we investigate the possibility of converting the native oxide layer (Cu_xO_y) present on the CuNW surface to copper sulfide ($Cu_{2-x}S$) while keeping the same high aspect ratio of the unmodified CuNWs to obtain a stable material that can be disperse and directly deposited onto a substrate without the need for any post-deposition treatment. The resulting Cu_{2-x}SNWs have been characterized in-depth with a wide range of physicochemical techniques to determine their composition and properties. The conductivity of the Cu_{2-x}SNW films has been correlated with the optical transparency, to evaluate their possible use as transparent conductors, and through bending test experiments to verify their adequacy in flexible electronics. The chemical stability of Cu_{2-x}SNWs has been verified against known copper etchants such as $FeCl_3$, HCl and NaOH. Finally, the Cu_{2-x}SNWs have been exploited as active materials in a solid-state symmetric supercapacitor revealing pseudocapacitive behavior and promising electrochemical performances.

Materials and methods

$Cu_{2-x}S$ nanowire (NW) synthesis

First, CuNWs were synthesized following a modification of an existing method.[10] To this end 380 mg of $CuCl_2 \cdot 2H_2O$ and 2.6 g of octadecylamine were dissolved in 110 mL of deionized water. The suspension was sonicated until a light blue emulsion was obtained. Then 850 mg of glucose were added and the emulsion was stirred at 60 °C for 3 hours to homogenize the emulsion. Finally, the emulsion was transferred to a steel autoclave and heated to 115 °C for 16 hours. The resulting CuNWs were isolated from the reaction suspension by centrifugation firstly with water, then with the ethanol/water mixture 1/1, and finally with pure ethanol (4500 rpm, 8 min).

To synthesize the Cu_{2-x}SNWs, thiourea (137 mg) and $CuCl_2 \cdot 2H_2O$ (0.0 or 1.0 mg) were dissolved in 55 mL of ethanol (or 55 mL of water). Then, 5 mL of CuNW ethanolic suspension (1.2 mg mL^{-1}) were added to the solution and this was sonicated for 2 min to obtain a homogenous dispersion. Finally, the solution was heated at 80 °C without stirring for 2 hours. The obtained Cu_{2-x}SNWs were then washed several times by centrifugation from ethanol to remove the excess of thiourea (5000 rpm, 10 min) and finally dispersed in 40 mL ethanol.

Preparation of transparent conductive substrates based on Cu_{2-x}SNWs

The Cu_{2-x}SNW ethanolic dispersion was further diluted 20 times in ethanol, sonicated for 2 min and finally spray-coated with a commercial airbrush onto freshly cleaned soda lime glass slides, polyethylene terephthalate (PET) and polyethylene naphthalate (PEN) substrates (125 μm thick). To assess the transparency of the film as a function of its sheet resistance, increasing amounts of NW dispersion were coated onto the substrates.

Single $Cu_{2-x}S$ nanowire device fabrication

A diluted suspension of Cu_{2-x}SNWs in ethanol was sonicated for 5 min and then drop-cast onto a freshly cleaned Si/SiO_2 substrate with patterned gold markers. Then, the single Cu_{2-x}SNW devices were patterned by direct laser lithography (AZ1505 photoresist and MIF726 developer, Micro Chemicals GmbH, Italy) using a laser writer LW405B (Microtech srl, Italy). Afterwards, a uniform gold layer (60 nm) was deposited on top by vacuum thermal evaporation, followed by a lift-off process in warm acetone (50 °C) to remove the unexposed photoresist and obtain the final source and drain electrodes.

Assembly of the supercapacitor

The working electrodes were prepared by mixing Cu_{2-x}SNWs (80% wt%, 8 mg), carbon black (10 wt%, 1 mg) and poly(tetrafluoroethylene) (PTFE) (10 wt%, 1 mg) in 2–3 drops

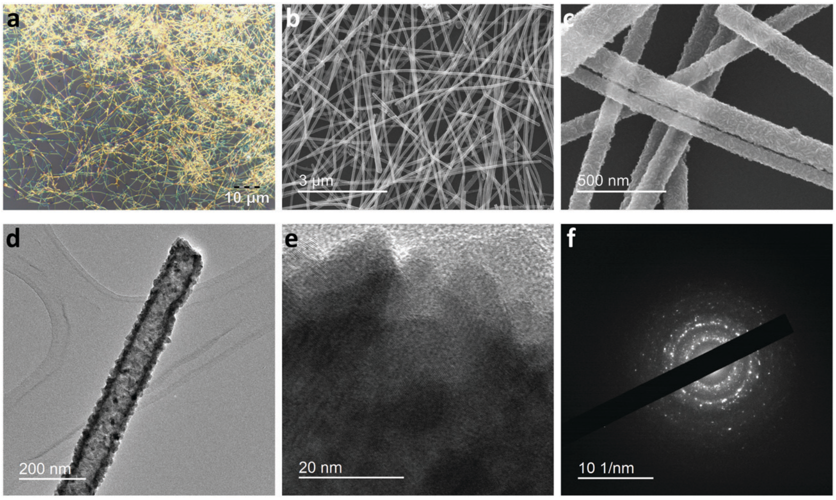

Fig. 1 (a) Optical micrograph, (b and c) SEM, (d) TEM, (e) HRTEM images of the synthesized Cu_{2-x}SNWs. (f) SAED pattern of the area in (e), highlighting the presence of crystallized grains and the polycrystalline feature of the chosen area.

of *N*-methyl-2-pyrrolidone. The paste was then deposited on carbon foil substrate and dried under vacuum (80 °C). The electrodes were assembled in a coin cell (CR2032) using Whatman® glass microfiber filters as a separator using a drop of electrolyte 1-ethyl-3-methylimidazolium bis(trifluoromethylsulfonyl)imide in polycarbonate 1 M.

Results

The copper sulfide nanowires (Cu_{2-x}SNWs) were synthesized by sulphidation of high-quality CuNWs. We employed a facile procedure in which thiourea was used as a source of sulfur, instead of the more toxic and reactive Na_2S. In particular, the CuNWs were treated with a diluted ethanolic solution of thiourea heated at 80 °C for two hours. Heating is necessary to activate the reaction with thiourea,[11] the conversion of the CuNWs into Cu_{2-x}SNWs is made possible by the thin layer of CuO which coats the synthesized CuNWs.[10] Fig. 1a and b displays optical micrograph and scanning electron microscopy (SEM) images of the nanowires. They reveal that the NWs preserve a high aspect ratio, with lengths in the range of 20–200 μm and an average diameter of 98 ± 17 nm as determined on 105 individual wires. Interestingly, when the reaction was conducted in water instead of ethanol, the fragmentation of the nanowires, with the consequent reduction of the aspect-ratio, was observed (Fig. S1 of the ESI†). Magnified SEM image (Fig. 1c) depicts that the surface of the nanowire is covered by nanoplates of copper sulfide. The transmission electron microscopy (TEM) image shows that the nanowires present a core–shell structure, with a darker contrast in the outer shell and brighter one in the center (Fig. 1d). In addition, the high-resolution TEM (HRTEM) image (Fig. 1e) displays characteristic lattice fringes that demonstrate the presence of crystallized structures associated with grains of various morphologies and orientations and sizes of 10–20 nm. The polycrystalline composition of the Cu_{2-x}SNWs is confirmed also by selected area electron diffraction (SAED) pattern (Fig. 1f), which exhibits the combination of discrete spots and concentric rings.

The chemical composition of the nanowires was investigated using both energy dispersive X-ray (EDX) mapping and X-ray photoelectron spectroscopy. The EDX mapping provided evidence for the presence of both copper and sulfur on all the nanowire section, with no appreciable differences between the outer and inner part (Fig. S2a of the ESI†) while the EDX spectrum shows the presence of copper and sulfur, in addition to small quantities of carbon, nitrogen and oxygen, with a Cu : S ratio of 1.57 (Fig. S2 b of the ESI†). The fitting of the survey spectra of XPS analysis (Fig. S3 of the ESI†) provides a similar Cu : S ratio of 1.55. Fig. 2a portrays a high-resolution spectrum

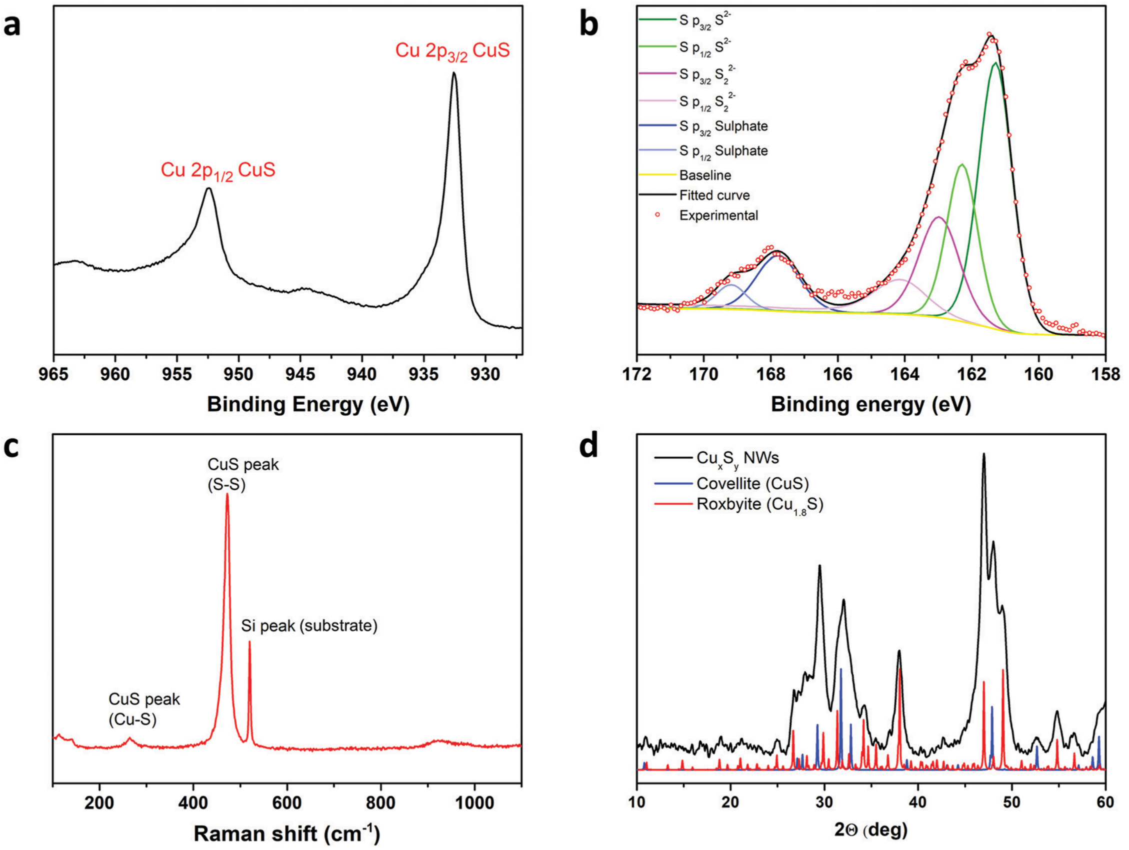

Fig. 2 Characterization of the chemical composition. XPS spectra of (a) Cu 2p and (b) S p of Cu_{2-x}SNWs. (c) Raman spectrum, and (d) XRD powder diffractogram of Cu_{2-x}SNWs.

of Cu 2p peak of the copper sulfide nanowires. The Cu $2p_{3/2}$ peak has a chemical shift of 932.4 eV, which is representative of Cu(I) of both CuS and Cu_2S.[12,13] The broad peaks at 945 and 963 eV are weak satellite peaks, which can be likely ascribed to some Cu^{2+} surface impurities, while the pronounced tails of Cu $2p_{3/2}$ and $2p_{1/2}$ are due to the metallic properties of copper sulphides.[13] The Cu LMM Auger peak (Fig. S4 of the ESI†) falls at 568.7 eV, which is a typical value for CuS.[14] Fig. 2b depicts the deconvoluted peak of Sp. Each component of the spectrum is split into two peaks ($p_{3/2}$ and $p_{1/2}$) for the spin–orbit coupling ($\Delta e = 1.16$ eV). The components at 161.3 and 162.8 eV belong to the species S^{2-} and $S_2{}^{2-}$ which can be found in all copper sulphides.[15,16] Another split component is visible at 167.9 eV and is due to some sulfate (probably from decomposition of thiourea) present on the surface of the nanowires. The Raman spectrum (Fig. 2c) further confirms the composition of the nanowires; in fact, the intense peak at 473 cm^{-1} is due to S–S stretching and the weaker peak at 264 cm^{-1} is attributed to Cu–S vibrations.[17,18] In particular, the peak shifts are characteristic of the covellite (CuS) structure.[19] The presence of the covellite phase is confirmed also by X-ray powder diffraction (XRD). Moreover, the diffractograms of the nanowires evidence the presence of another crystalline phase, which can be identified as roxbyite ($Cu_{1.8}S$).[20,21] The presence of two crystalline phases would also explain why the stoichiometric ratio Cu : S measured was 1.55. Furthermore, the absence of the Cu(111) peak at $2\theta = 43.3°$ and Cu(200) peak at 50.4°, which are typical of metallic CuNWs, indicates a total conversion of the copper(0) in $Cu_{2-x}S$.[22,23] To confirm the core–shell structure of the Cu_{2-x}SNWs, we acquired the XPS spectra of the nanowires while etching their surface with an argon ion beam. It is possible to see that the peaks belonging to sulfate at 168 eV in the S 2p spectra (Fig. S5a of the ESI†) and the satellite peaks due to Cu^{2+} in the Cu 2p spectra (Fig. S5b of the ESI†) disappear already after the first etching cycle, thus confirming that the contamination involves just a thin layer of the surface. Similarly, the foreign elements C, N and O also disappear after the first etching cycles (Fig. S5c of the ESI†). Moreover, the atomic abundance ratio between Cu and S increases from 1.04 to 1.72 with increasing etching time (Fig. S5d of the ESI†), thus supporting the hypothesis of core–shell nanowires composed by an outer core of covellite and an inner core of roxbyite.

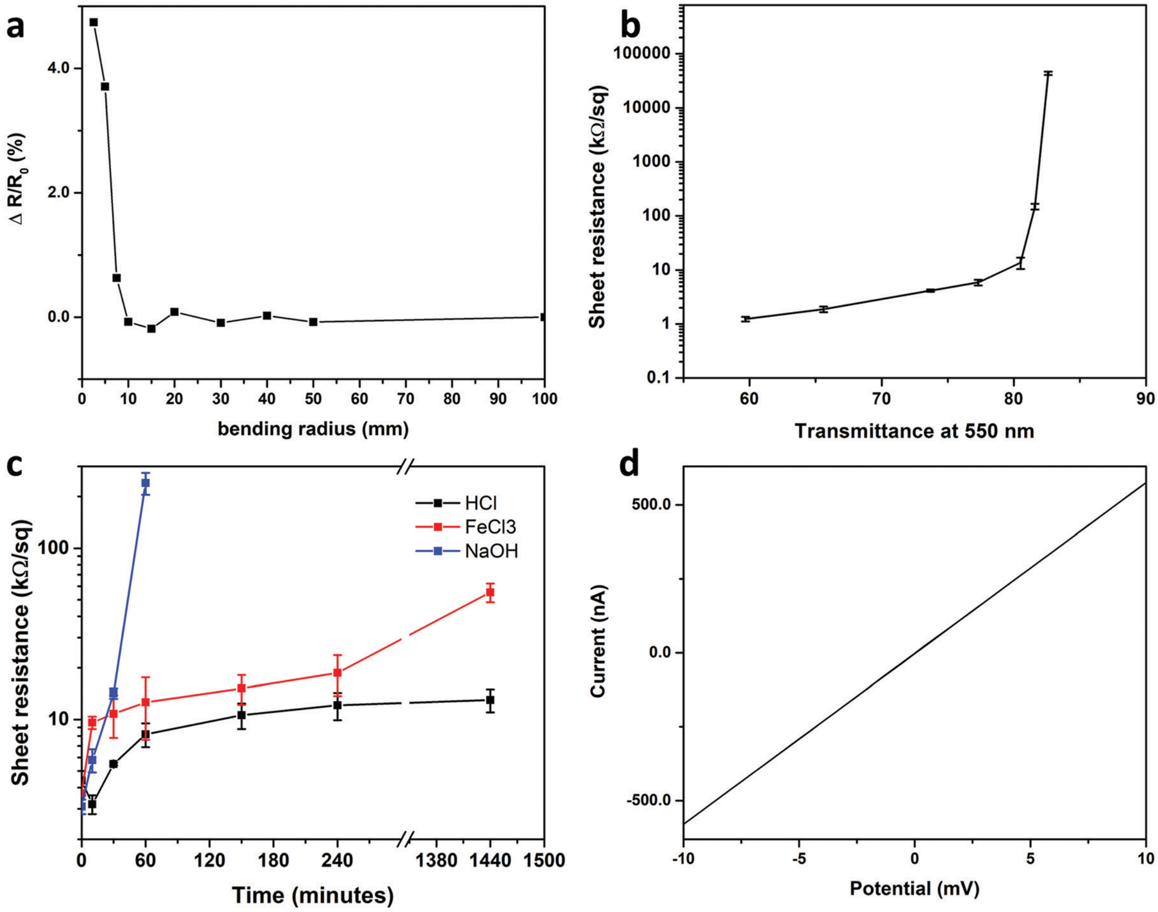

Fig. 3 (a) Change in sheet resistance of a 5 × 1.5 cm^2 conductive film of spray-coated Cu_{2-x}SNWs on PEN (125 μm) as a function of the bending radius. (b) Sheet resistance of spray-coated Cu_{2-x}SNWs on glass as a function of their transmittance at 550 nm. (c) Sheet resistance of 3 different films of spray-coated Cu_{2-x}SNWs on glass as function of soaking time into water solutions of HCl 1 M (black curve), $FeCl_3$ 50 mM (red curve) and NaOH 1 M (blue curve). (d) Current as a function of the potential applied to a single Cu_{2-x}SNW.

The absorption spectra of the Cu_{2-x}SNWs dispersed in ethanol was used to evaluate the optical bandgap (Fig. S6 of the ESI†). The nanowires exhibit the maximum absorbance at 397 nm. The energy of the optical direct and indirect bandgaps, computed from the Tauc plot (Fig. S7 of the ESI†) amount to 2.0 eV and 1.27 eV respectively, in line with the reported values for CuS and $Cu_{1.8}S$.[24,25] We also measured the ionization potential (IP) of the Cu_{2-x}SNWs deposited on a Si/SiO_2 substrate by photoemission spectroscopy in air (Fig. S8 of the ESI†) which was 4.80 ± 0.02.

The Cu_{2-x}SNWs were then tested as transparent conductive films. The nanowires could be uniformly deposited onto glass, plastic, and paper substrates readily *via* ethanolic dispersion by using a commercial airbrush. Interestingly, the films were already conductive, immediately after the spray-deposition, and did not need any post-treatment such as annealing under a reducing atmosphere or chemical reduction. We tested the *I–V* characteristics of a conductive Cu_{2-x}SNWs film deposited on a $5 \times 1.5\ cm^2$ foil of polyethylene naphthalate (PEN) 125 μm thick by connecting two electrodes made of copper tape. The film presented perfect Ohmic conductivity, with a resistance of 3.8 kΩ (Fig. S9 of the ESI†). Then, we tested the flexibility of the film, by performing 10 000 bending cycles with a bending radius of 8 mm (Fig. S10 of the ESI†). The resistance of the film revealed an increase of only 4.4% after 10 000 bending cycles. We also manually tested the static bending of the film with different radii (Fig. 3a). No appreciable changes in the resistance were detected up to 1 cm of bending radius, followed by an increase of the resistance, which reaches 4.7% at a bending radius of 2.5 mm.

Subsequently, we spray-coated different amounts of Cu_{2-x}SNWs dispersed in ethanol onto glass substrates, and we measured the sheet resistance and transmittance of the films. The measured sheet resistance of the films as a function of their transmittance at 550 nm is reported in Fig. 3b. The corresponding transmittance spectra, photos and microphotographs of the conductive films are reported in Fig. S11 of the ESI.† The sheet resistance decreases by several orders of magnitude passing from 90% transmittance to 80%. At 73.7% of transmittance (at 550 nm) the sheet resistance of the film is $4.1\ k\Omega\ sq^{-1}$, hence being around 50–100 times higher than for films of CuNWs after annealing or chemical reduction.[5,10,26] Thick films made by filtration (34 ± 4 μm thick) presented a sheet resistance of $15 \pm 2\ \Omega\ sq^{-1}$ which corresponds to a bulk resistivity of $5 \times 10^{-4}\ \Omega$ m. However, compared to CuNWs, these copper sulfide nanowires display a much higher chemical stability, in particular to acid and oxidative environments. Spray coated films of Cu_{2-x}SNWs onto glass substrates were soaked into a $FeCl_3$ 50 mM, HCl 1 M and NaOH 1 M solutions for 24 hours at room temperature (Fig. 3c). The sheet resistance of the film exposed to the oxidizing $FeCl_3$ increased by 15 times over 24 hours, while the sheet resistance of the film exposed to acidic environment presented a 3-fold increase over 24 hours. In both cases the transmittance (at 465 nm) of the films after 24 h increased by *ca.* 6% because of the corrosion (Fig. S12a–c of the ESI†). In comparison, films of CuNWs on glass were completely dissolved by $FeCl_3$ and HCl in less than 30 seconds and 5 min of exposure, respectively. Nevertheless, the stability of the Cu_{2-x}SNWs to NaOH 1 M was lower, with complete loss of the conductivity and dissolution of the film after 4 hours of exposure (Fig. S12d of the ESI†).

We have annealed the film under nitrogen at different temperatures to evaluate the effect of the annealing on the conductivity of the film. We noticed a 2-fold decrease of the sheet resistance of the film (from $1.24 \pm 0.07\ k\Omega\ sq^{-1}$ to $632 \pm 28\ \Omega\ sq^{-1}$) after 30 min of annealing at 190 °C. To check if this decrease in resistance was due to a crystal phase transition, we performed differential scanning calorimetry (DSC) analysis on the Cu_{2-x}SNWs under nitrogen flux (Fig. S13a of the ESI†). We found an endothermic peak at 189 °C, which can be ascribed to the crystal phase transition. However, XPS analysis performed after the annealing suggests that the increase in conductivity may be due to desorption of the contaminants and removal of the surface oxidized layer (Fig. S14 of the ESI†). The thermogravimetric analysis of the nanowires made it possible to assess their thermal stability in air (Fig. S13b of the ESI†). The Cu_{2-x}SNWs present a steep mass loss at 275 °C, probably determined by the conversion of the external CuS into Cu_2S and release of SO_2, followed by a first increase of mass (+23%) at 305 °C, due to oxidation to copper sulfate, and a second increase of mass (+6%) at 480 °C, due to formation of CuO $CuSO_4$. Finally, at 550 °C the mass starts to decrease because of the conversion to CuO and release of SO_2.[27]

The electrical characterization was performed also on a single Cu_{2-x}SNW. We evaporated two gold top electrodes on a single Cu_{2-x}SNW by direct laser lithography (Fig. S15 of the ESI†). Also in this case, the conduction was perfectly Ohmic (Fig. 3d). The measured resistance of the single wire amounted to 16.9 ± 0.1 kΩ. The length and diameter of the nanowire were measured by SEM and resulted in 18.1 ± 0.3 μm and 97.6 ± 3.3 nm. This made it possible to calculate the resistivity of the single nanowire, which was resulted $6.9 \times 10^{-6}\ \Omega$ m. The lower value compared to the bulk resistivity can be attributed to the absence of the contact resistance between nanowires in the single nanowire measurement. For comparison, a single CuNW of a similar aspect ratio has been reported having a 43 times lower resistivity.[28]

Copper sulfide nanostructures were found being promising electrode materials for supercapacitors.[29] Since Cu_{2-x}SNWs could benefit from their large specific surface area, we tested them as electrode materials for supercapacitors. The Cu_{2-x}SNWs were deposited on a carbon foil substrate and used as electrodes in a solid-state symmetric supercapacitor in which 1-ethyl-3-methylimidazolium bis(trifluoromethylsulfonyl)imide 1 M in polycarbonate was used as the electrolyte. The use of an organic electrolyte and of an aprotic ionic liquid allowed to extend the potential window up to 2.5 V. We performed cyclic voltammetry (CV) analyses between 0 and 2.5 V at different scan rates, ranging from $5\ mV\ s^{-1}$ to $2000\ mV\ s^{-1}$ (Fig. 4a and Fig. S16 of the ESI†). The analysis of curves at lower scan rates clearly depicts pseudocapacitive behaviour indicating a significant contribution of faradaic reactions in the storage

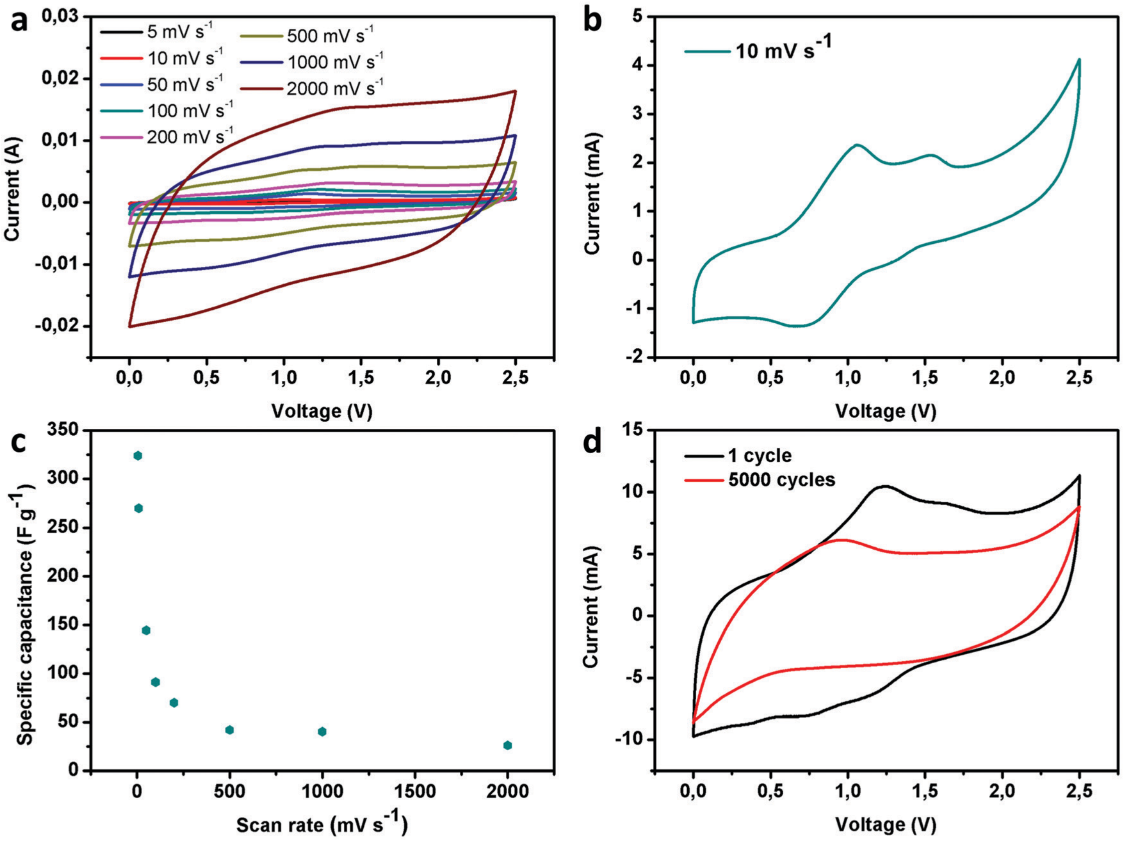

Fig. 4 (a) Cyclic voltammetry (CV) curves of the Cu_{2-x}SNWs based supercapacitor at different scan rates (from 5 mV s^{-1} to 2000 mV s^{-1}) and (b) details of the CV performed at 10 mV s^{-1}. (c) Calculated specific capacitance of the supercapacitor at different scan rates. (d) CV of the supercapacitor at the 1st and 5000th cycle (scan rate: 100 mV s^{-1}).

mechanism (Fig. 4b). The presence of peaks around 1.0 and 1.5 V can be attributed to oxidation between $Cu_{1.8}S$ and CuS, followed by the oxidation of S^- to S^0.[30–32] At higher scan rates the redox peaks become less pronounced and the curves acquire a quasi-rectangular shape, indicating that the capacitance of the pseudocapacitor becomes dominated by the double-layer effect, due to the fast polarization of electrolyte ions on electrodes surfaces. The slow diffusion of the large electrolyte ions into the nanostructured electrode is responsible of the diminished faradaic component. The highest specific capacitance of 324 F g^{-1} was obtained at scan rates of 5 mV s^{-1}, which is similar to the one of a previously reported solid state supercapacitor based on Cu_7S_4 NWs.[33] The volumetric capacitance and energy density of the electrode were estimated at 60.5 F cm^{-3} and 52.5 mWh cm^{-3}, respectively (at scan rates of 5 mV s^{-1}). To the best of our knowledge these values are the highest reported for supercapacitors based on copper sulfide nanostructures.[34–36] However, due to the slow diffusion of the electrolyte, the material shows an important drop of the specific capacity at higher scan rates (40.3 F g^{-1} at 1000 mV s^{-1}) (Fig. 4c and Table S1 of the ESI†). Notably, the material exhibited moderate capacitance retention of 70% of initial capacitance, dropping from 91.3 F g^{-1} to 64 F g^{-1} after 5000 cycles while tested at 100 mV s^{-1} (Fig. 4d and Fig. S17a of the ESI†), which is comparable to similar copper sulfide nanostructures.[30,31] Such a drop mainly occurs during the first 1000 cycles, and it is followed by a stabilization of the capacitance, thus suggesting the formation of an irreversibly oxidized passivation layer which protects the rest of the active material. The distorted shape of GCD curves (Fig. S17b of the ESI†) also confirms pseudocapacitive behavior which can be additionally supported by redox active electrolyte which was previously reported for bis(trifluoromethylsulfonyl)imide anion.[37] The Nyquist plot (Fig. S17c of the ESI†) revealed a solution resistance of 5.8 Ω, comparable with other ionic liquid electrolyte-based devices[38,39] and the Warburg resistance of 25 Ω corresponding to ion transfer on the electrolyte–Cu_{2-x}SNWs electrode interface and suggests that dense packing of nanowires might slightly restrict easy ion migration through the electrode.[30]

Conclusions

In summary, we have demonstrated that ultralong copper nanowires (CuNWs) can be converted into copper sulfide nanowires (Cu_{2-x}SNWs) maintaining the high aspect ratio by sulphidation in ethanolic solution employing thiourea as the sulfur source. The multiscale characterization of Cu_{2-x}SNWs by means of XRD, TEM, EDX and XPS revealed that after sulphidation a core shell structure is obtained with the outer core being composed of covellite and the inner core composed of roxbyite. The obtained Cu_{2-x}SNWs could be readily dispersed in ethanol and be directly deposited by spray-coating onto glass or plastic substrate resulting in conductive films without the need for any post-deposition process. Because of the high aspect ratio of the synthesized Cu_{2-x}SNWs, films deposited on glass revealed a sheet resistance as low as 4.1 kΩ sq^{-1} at 73.7% transmittance (measured at 550 nm), which can be further halved after annealing of the film at 190 °C for 30 min. The film possesses an improved chemical stability in the presence of copper etchants such as $FeCl_3$, as well as under acidic conditions. Bending tests have also shown a remarkable stability with an increase of the resistance of only 4.4% after 10 000 bending cycles. The electronic conductivity of the material has been determined not only on the film as a function of light transmission, but also in the bulk and at a single nanowire level. The latter exhibited perfect Ohmic conductivity with a resistivity of 6.9×10^{-6} Ω m. Finally, the performance of the material in a symmetric supercapacitor has been evaluated. The Cu_{2-x}SNWs presented a pseudocapacitive behavior, with a high specific capacity of 324 F g^{-1} and an ultrahigh volumetric capacity of 60.5 F cm^{-3} at scan rates of 5 mV s^{-1}. The supercapacitor also revealed a moderate capacity retention after 5000 cycles of operation at 100 mV s^{-1} (70% of the original capacitance). Our results suggest that Cu_{2-x}SNWs can be used for printed, flexible electronics while their use as transparent electrodes still require an improvement of the conductivity to be comparable with metallic CuNWs.

Conflicts of interest

The authors declare no competing financial interest.

Acknowledgements

We acknowledge financial support from the European Commission through the H2020 project DECOCHROM (GA-760973), the ERC project SUPRA2DMAT (GA-833707), the Agence Nationale de la Recherche through the Labex project CSC (ANR-10-LABX-0026 CSC) within the Investissement d'Avenir program (ANR-10-120 IDEX-0002-02), the International Center for Frontier Research in Chemistry (icFRC) as well as the Institut Universitaire de France (IUF) and the National Science Center (Grant No. 2019/35/B/ST5/01568 and Grant No. 2019/33/N/ST5/00052).

References

1 Z. Wu, Z. Chen, X. Du, J. M. Logan, J. Sippel, M. Nikolou, K. Kamaras, J. R. Reynolds, D. B. Tanner, A. F. Hebard and A. G. Rinzler, Transparent, Conductive Carbon Nanotube Films, *Science*, 2004, **305**(5688), 1273–1276.

2 V. H. R. Souza, S. Husmann, E. G. C. Neiva, F. S. Lisboa, L. C. Lopes, R. V. Salvatierra and A. J. G. Zarbin, Flexible, Transparent and Thin Films of Carbon Nanomaterials as Electrodes for Electrochemical Applications, *Electrochim. Acta*, 2016, **197**, 200–209.

3 S. Ye, A. R. Rathmell, Z. Chen, I. E. Stewart and B. J. Wiley, Metal Nanowire Networks: The Next Generation of Transparent Conductors, *Adv. Mater.*, 2014, **26**(39), 6670–6687.

4 T. Zhang, M. Zhao, F. Daneshvar, F. Xia and H.-J. Sue, Solution-Processable Oxidation-Resistant Copper Nanowires Decorated with Alkyl Ligands, *ACS Appl. Nano Mater.*, 2019, **2**(12), 7775–7784.

5 V. B. Nam and D. Lee, Copper Nanowires and Their Applications for Flexible, Transparent Conducting Films: A Review, *Nanomaterials*, 2016, **6**, 3.

6 A. R. Rathmell, M. Nguyen, M. Chi and B. J. Wiley, Synthesis of Oxidation-Resistant Cupronickel Nanowires for Transparent Conducting Nanowire Networks, *Nano Lett.*, 2012, **12**(6), 3193–3199.

7 Z. F. Chen, S. R. Ye, I. E. Stewart and B. J. Wiley, Copper Nanowire Networks with Transparent Oxide Shells That Prevent Oxidation without Reducing Transmittance, *ACS Nano*, 2014, **8**(9), 9673–9679.

8 U. Shamraiz, R. A. Hussain and A. Badshah, Fabrication and applications of copper sulfide (CuS) nanostructures, *J. Solid State Chem.*, 2016, **238**, 25–40.

9 J. S. Chung and H. J. Sohn, Electrochemical behaviors of CuS as a cathode material for lithium secondary batteries, *J. Power Sources*, 2002, **108**(1–2), 226–231.

10 A. Aliprandi, T. Moreira, C. Anichini, M.-A. Stoeckel, M. Eredia, U. Sassi, M. Bruna, C. Pinheiro, C. A. T. Laia, S. Bonacchi and P. Samorì, Hybrid Copper-Nanowire–Reduced-Graphene-Oxide Coatings: A "Green Solution" Toward Highly Transparent, Highly Conductive, and Flexible Electrodes for (Opto)Electronics, *Adv. Mater.*, 2017, **29**(41), 1703225.

11 M. P. Hendricks, M. P. Campos, G. T. Cleveland, I. Jen-La Plante and J. S. Owen, A tunable library of substituted thiourea precursors to metal sulfide nanocrystals, *Science*, 2015, **348**(6240), 1226–1230.

12 S. W. Goh, A. N. Buckley and R. N. Lamb, Copper(II) sulfide?, *Miner. Eng.*, 2006, **19**(2), 204–208.

13 J. C. W. Folmer and F. Jellinek, The valence of copper in sulphides and selenides: An X-ray photoelectron spectroscopy study, *J. Less-Common Met.*, 1980, **76**(1–2), 153–162.

14 V. Krylova and M. Andrulevičius, Optical, XPS and XRD Studies of Semiconducting Copper Sulfide Layers on a Polyamide Film, *Int. J. Photoenergy*, 2009, **2009**, 1–8.

15 N. Karikalan, R. Karthik, S.-M. Chen, C. Karuppiah and A. Elangovan, Sonochemical Synthesis of Sulfur Doped Reduced Graphene Oxide Supported CuS Nanoparticles for the Non-Enzymatic Glucose Sensor Applications, *Sci. Rep.*, 2017, **7**, 1–10.

16 A. C. Estrada, F. M. Silva, S. F. Soares, J. A. P. Coutinho and T. Trindade, An ionic liquid route to prepare copper sulphide nanocrystals aiming at photocatalytic applications, *RSC Adv.*, 2016, **6**(41), 34521–34528.

17 T. Thongtem, A. Phuruangrat and S. Thongtem, Characterization of copper sulfide nanostructured spheres and

nanotubes synthesized by microwave-assisted solvothermal method, *Mater. Lett.*, 2010, **64**(2), 136–139.

18 S. H. Chaki, J. P. Tailor and M. P. Deshpande, Covellite CuS – Single crystal growth by chemical vapour transport (CVT) technique and characterization, *Mater. Sci. Semicond. Process.*, 2014, **27**, 577–585.

19 M. Ishii, K. Shibata and H. Nozaki, Anion Distributions and Phase Transitions in $CuS_{1-x}Se_x(x = 0 - 1)$ Studied by Raman Spectroscopy, *J. Solid State Chem.*, 1993, **105**(2), 504–511.

20 W. G. Mumme, R. W. Gable and V. Petricek, THE CRYSTAL STRUCTURE OF ROXBYITE, $Cu_{58}S_{32}$, *Can. Mineral.*, 2012, **50**(2), 423–430.

21 K. Tezuka, W. C. Sheets, R. Kurihara, Y. J. Shan, H. Imoto, T. J. Marks and K. R. Poeppelmeier, Synthesis of covellite (CuS) from the elements, *Solid State Sci.*, 2007, **9**(1), 95–99.

22 M. Mohl, P. Pusztai, A. Kukovecz, Z. Konya, J. Kukkola, K. Kordas, R. Vajtai and P. M. Ajayan, Low-Temperature Large-Scale Synthesis and Electrical Testing of Ultralong Copper Nanowires, *Langmuir*, 2010, **26**(21), 16496–16502.

23 T. Zhang, W.-Y. Hsieh, F. Daneshvar, C. Liu, S.-P. Rwei and H.-J. Sue, Copper(I)–alkylamine mediated synthesis of copper nanowires, *Nanoscale*, 2020, **12**(33), 17437–17449.

24 T. Safrani, J. Jopp and Y. Golan, A comparative study of the structure and optical properties of copper sulfide thin films chemically deposited on various substrates, *RSC Adv.*, 2013, 3(45), 23066.

25 P. V. Quintana-Ramirez, M. C. Arenas-Arrocena, J. Santos-Cruz, M. Vega-González, O. Martínez-Alvarez, V. M. Castaño-Meneses, L. S. Acosta-Torres and J. de la Fuente-Hernández, Growth evolution and phase transition from chalcocite to digenite in nanocrystalline copper sulfide: Morphological, optical and electrical properties, *Beilstein J. Nanotechnol.*, 2014, **5**, 1542–1552.

26 A. R. Rathmell, S. M. Bergin, Y.-L. Hua, Z.-Y. Li and B. J. Wiley, The Growth Mechanism of Copper Nanowires and Their Properties in Flexible, Transparent Conducting Films, *Adv. Mater.*, 2010, **22**(32), 3558–3563.

27 M. Nafees, S. Ali, K. Rasheed and S. Idrees, The novel and economical way to synthesize CuS nanomaterial of different morphologies by aqueous medium employing microwaves irradiation, *Appl. Nanosci.*, 2011, **2**(2), 157–162.

28 B. Luo, Y. Fang, J. Li, Z. Huang, B. Hu and J. Zhou, Improved Stability of Metal Nanowires *via* Electron Beam Irradiation Induced Surface Passivation, *ACS Appl. Mater. Interfaces*, 2019, **11**(13), 12195–12201.

29 S. Sun, P. Li, S. Liang and Z. Yang, Diversified copper sulfide (Cu_2–*x*S) micro-/nanostructures: a comprehensive review on synthesis, modifications and applications, *Nanoscale*, 2017, **9**(32), 11357–11404.

30 C. Justin Raj, B. C. Kim, W.-J. Cho, W.-G. Lee, Y. Seo and K.-H. Yu, Electrochemical capacitor behavior of copper sulfide (CuS) nanoplatelets, *J. Alloys Compd.*, 2014, **586**, 191–196.

31 Y.-K. Hsu, Y.-C. Chen and Y.-G. Lin, Synthesis of copper sulfide nanowire arrays for high-performance supercapacitors, *Electrochim. Acta*, 2014, **139**, 401–407.

32 Z. Stević and M. Rajčić-Vujasinović, Chalcocite as a potential material for supercapacitors, *J. Power Sources*, 2006, **160**(2), 1511–1517.

33 M. S. Javed, S. Dai, M. Wang, Y. Xi, Q. Lang, D. Guo and C. Hu, faradaic redox active material of Cu_7S_4 nanowires with a high conductance for flexible solid state supercapacitors, *Nanoscale*, 2015, **7**(32), 13610–13618.

34 D. Majumdar, Recent progress in copper sulfide based nanomaterials for high energy supercapacitor applications, *J. Electroanal. Chem.*, 2021, **880**, 114825.

35 Y.-W. Lee, B.-S. Kim, J. Hong, J. Lee, S. Pak, H.-S. Jang, D. Whang, S. Cha, J. I. Sohn and J. M. Kim, A pseudo-capacitive chalcogenide-based electrode with dense 1-dimensional nanoarrays for enhanced energy density in asymmetric supercapacitors, *J. Mater. Chem. A*, 2016, **4**(26), 10084–10090.

36 D. Ranjith Kumar, S. Kesavan, M. L. Baynosa and J.-J. Shim, Flower-like Cu1.8S nanostructures for high-performance flexible solid-state supercapacitors, *Appl. Surf. Sci.*, 2018, **448**, 547–558.

37 P. Navalpotro, J. Palma, M. Anderson and R. Marcilla, High performance hybrid supercapacitors by using para-Benzoquinone ionic liquid redox electrolyte, *J. Power Sources*, 2016, **306**, 711–717.

38 S. Maiti, A. Pramanik, S. Chattopadhyay, G. De and S. Mahanty, Electrochemical energy storage in montmorillonite K10 clay based composite as supercapacitor using ionic liquid electrolyte, *J. Colloid Interface Sci.*, 2016, **464**, 73–82.

39 G. A. Tiruye, D. Muñoz-Torrero, J. Palma, M. Anderson and R. Marcilla, Performance of solid state supercapacitors based on polymer electrolytes containing different ionic liquids, *J. Power Sources*, 2016, **326**, 560–568.

Electronic Supplementary Material (ESI) for Journal of Materials Chemistry C.

Supporting Information

Synthesis and Characterization of Ultralong Copper Sulfide Nanowires and their Electrical Properties

Cosimo Anichini, [a] *Włodzimierz Czepa* [b,c] *Alessandro Aliprandi,* [a] *Valentina Girelli Consolaro,* [d] *Ovidiu Ersen,* [d]

Artur Ciesielski [a,b,*] *Paolo Samorì* [a*]

[a] *Université de Strasbourg, CNRS, ISIS 8 allée Gaspard Monge, 67000 Strasbourg, France.*

E-mail : ciesielski@unistra.fr, samori@unistra.fr

[b] *Centre for Advanced Technologies, Adam Mickiewicz University, 61-614 Poznań, Uniwersytetu Poznańskiego 10, Poland.*

[c] *Faculty of Chemistry, Adam Mickiewicz University, Uniwersytetu Poznańskiego 8, 61-614 Poznań, Poland.*

[d] *Université de Strasbourg,CNRS, IPCMS, 23 rue du Loess, BP 43 67034 Strasbourg Cedex 2, France*

Table of Contents

Instrumental methods

For X-Ray Photoelectron Spectroscopy (XPS) measurements Cu2-xSNWs were deposited by drop-casting onto silicon substrates. The X-Ray Photoelectron Spectroscopy (XPS) measurements were carried out using a Thermo Scientific KAlpha X-ray Photoelectron Spectrometer system equipped with an Al Kα X-Ray source (photon energy Eph = 1486.6 eV, beam spot size ~100 µm). The depth profiling was done by etching the Cu2-xSNWs with a rastered Argon ions beam (2 kV). Transmittance UV-Vis spectra of the substrates were recorded on the Jasco V-670 spectrophotometer. Raman spectra were recorded by a Renishaw microscope with a 50x objective, laser excitation wavelength of 532 nm and laser power of 1% on Cu2-xS NWs deposited on Si substrate. The silicon peak at 520.3 cm^{-1} was taken as reference for wavenumber calibration. TGA was conducted using a Mettler Toledo TGA/DSC 2 system, with a heating rate of 10 °C min^{-1} from 25 °C to 800 °C under air atmosphere. The X-Ray Diffraction (XRD) measurements were performed in specular geometry using a SmartLab-Rigaku diffractometer equipped with a rotating anode (Cu Kα, $\lambda = 1.54180$ Å), followed by a parabolic mirror to collimate the incident beam, and a series of variable slits (placed before and after the sample position). Scanning Electron Microscopy (SEM) was performed with a FEI Quanta 250 FEG instrument, operated in high vacuum mode (pressure in 10^{-4} Pa range). Conventional transmission electron microscopy (TEM), high resolution TEM (HRTEM) imaging, electron diffraction (ED) and Energy-Dispersive X-Rays Spectroscopy (EDX) were performed a JEOL2100F microscope operating at 200 kV and equipped with a probe corrector for spherical aberrations. Photoemission spectroscopy in air (PESA) measurements were performed on Cu2-xSNWs drop-casted on a Si/SiO_2 substrate (230 nm) with an AC-2 Photoelectron Spectrometer (Riken-Keiki Co.). A UV light intensity of 40 nW and a counting time of 10 seconds per point were used for the measurement. All the electrical measurements were performed with a Keithley 2636A source meter, except the measurements of sheet resistance, which were performed with a Jandel RM3000 test unit equipped with a four-point probe.

Results and Discussion

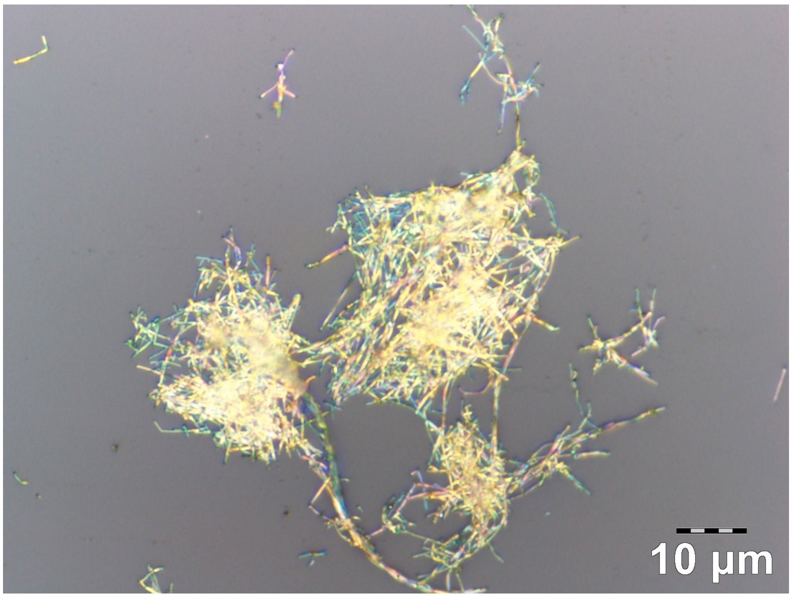

Figure S1. Optical micrograph of Cu NWs treated with a 30mM water solution of thiourea at 90 °C for 30 min.

Energy-dispersive X-ray spectroscopy (EDX)

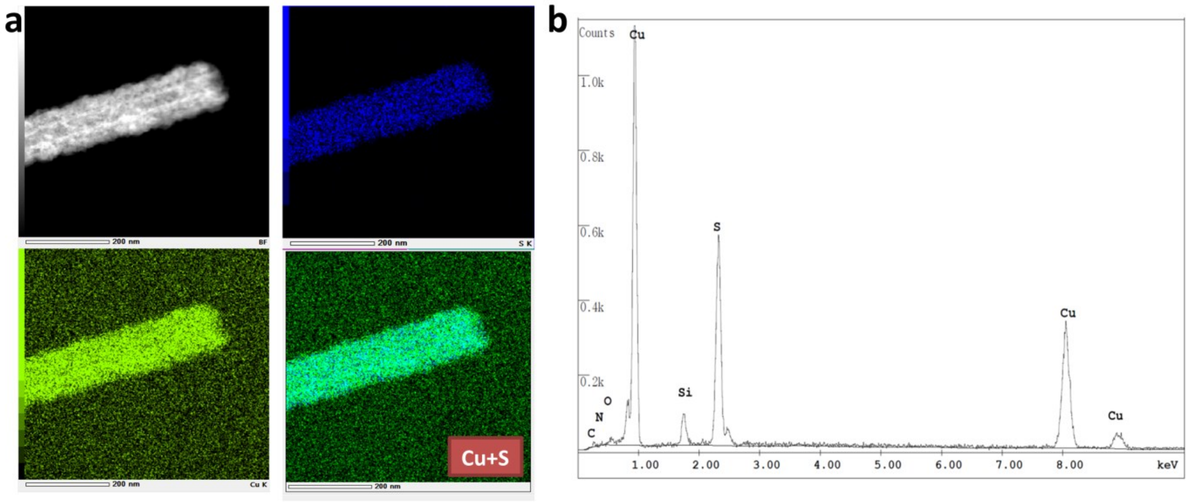

Figure S2. (a) EDX mapping of a Cu$_{2-x}$S NW (gray, the high angle annular dark field image, blue: S chemical map, green: Cu chemical map). (b) Representative EDX spectrum of Cu$_{2-x}$S NWs.

X-ray photoelectron spectroscopy (XPS)

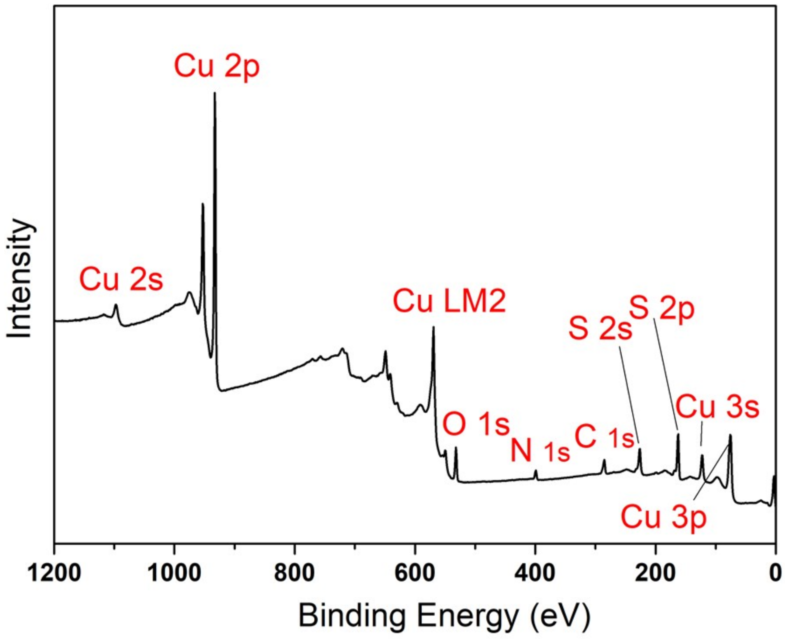

Figure S3. XPS survey spectrum of Cu$_{2-x}$SNWs.

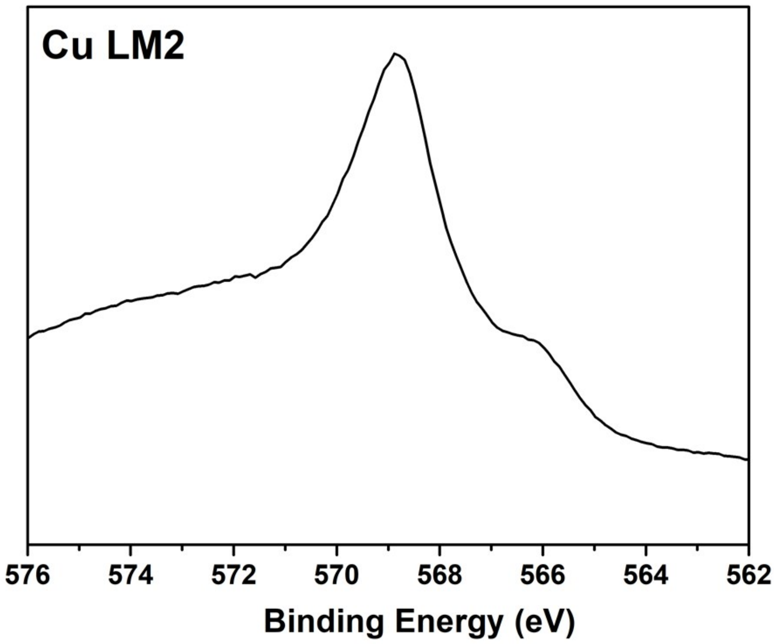

Figure S4. XPS spectrum of Cu LM2 peak of $Cu_{2-x}S$NWs.

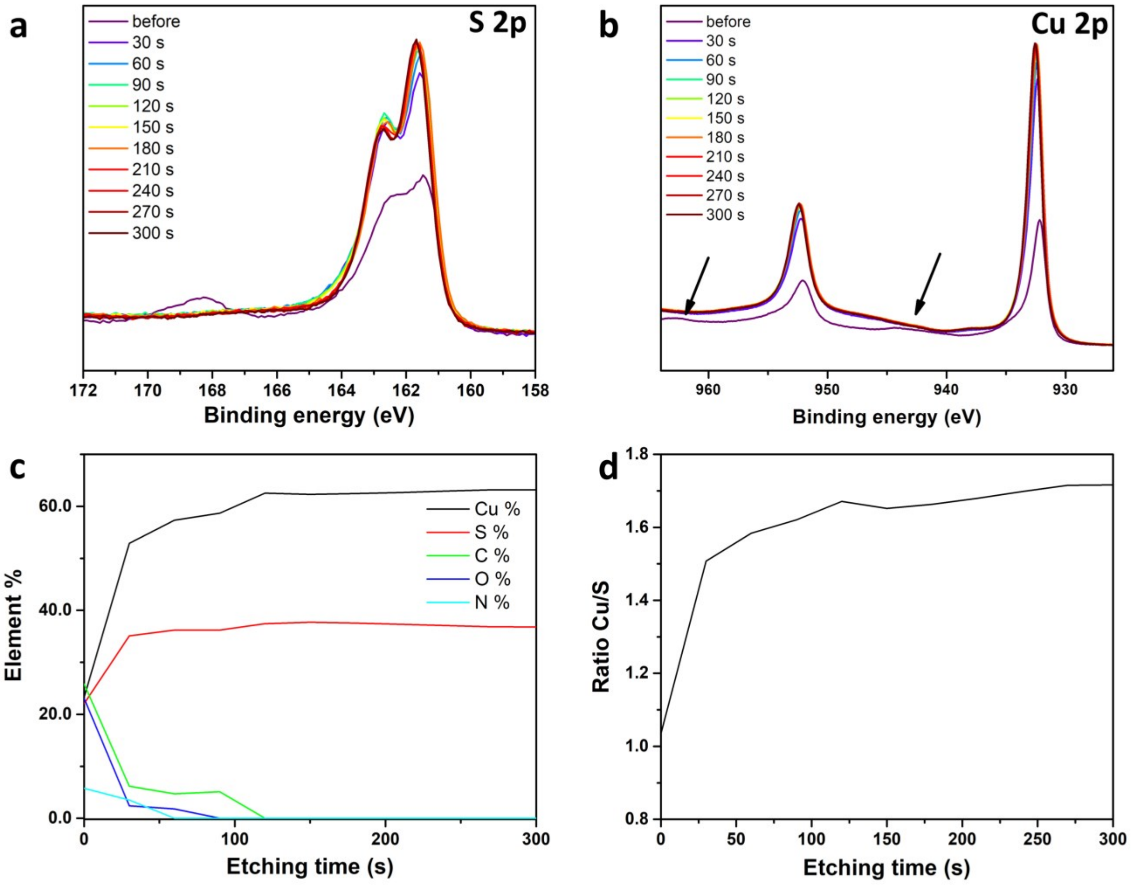

Figure S5. S 2p spectra (a) and Cu 2p spectra (b) of Cu_{2-x}SNWs before and after increasing times of exposure (30-300 s) to an accelerated Argon ions beam. Element abundance (%) computed from the Survey spectra (c) and elemental ratio Cu/S (d) as a function of the Ar^+ etching time.

UV-Vis Absorbance

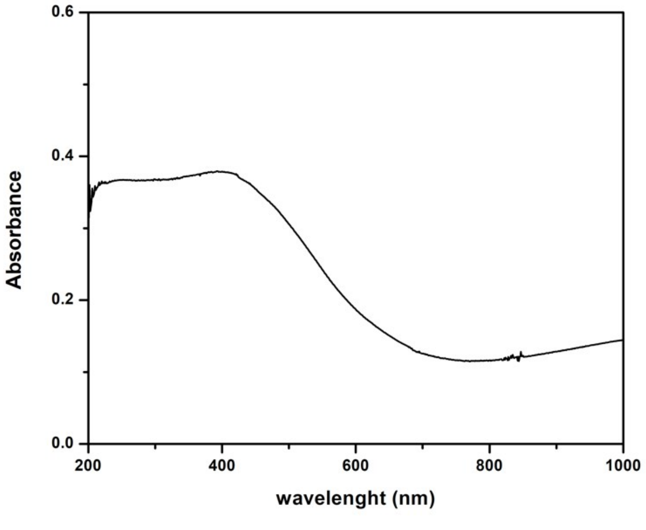

Figure S6. Absorbance spectrum of Cu_{2-x}SNWs dispersed in ethanol.

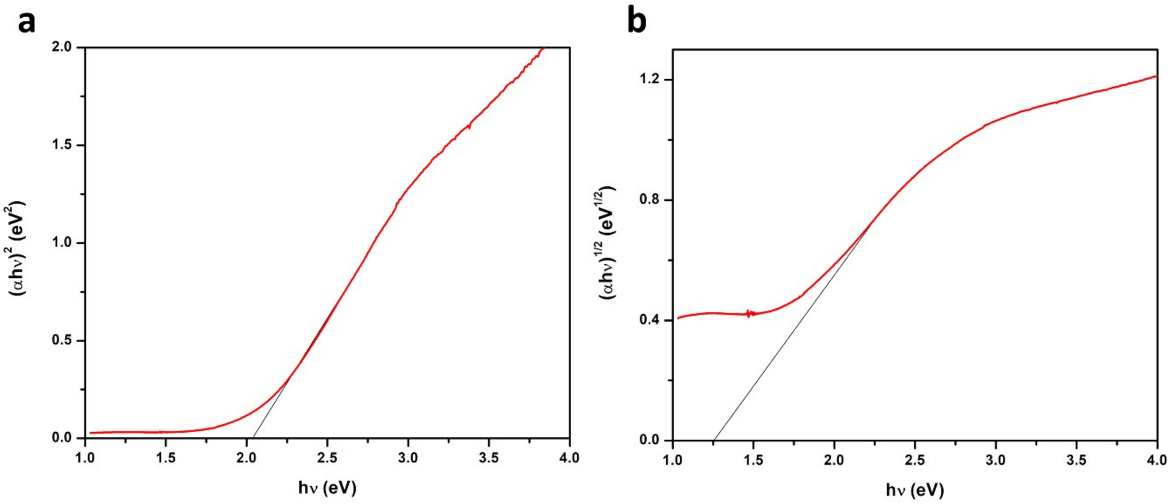

Figure S7. Tauc plots for direct (a) and indirect (b) band-gaps of $Cu_{2-x}S$NWs dispersed in ethanol.

Photoelectron spectroscopy in air (PESA)

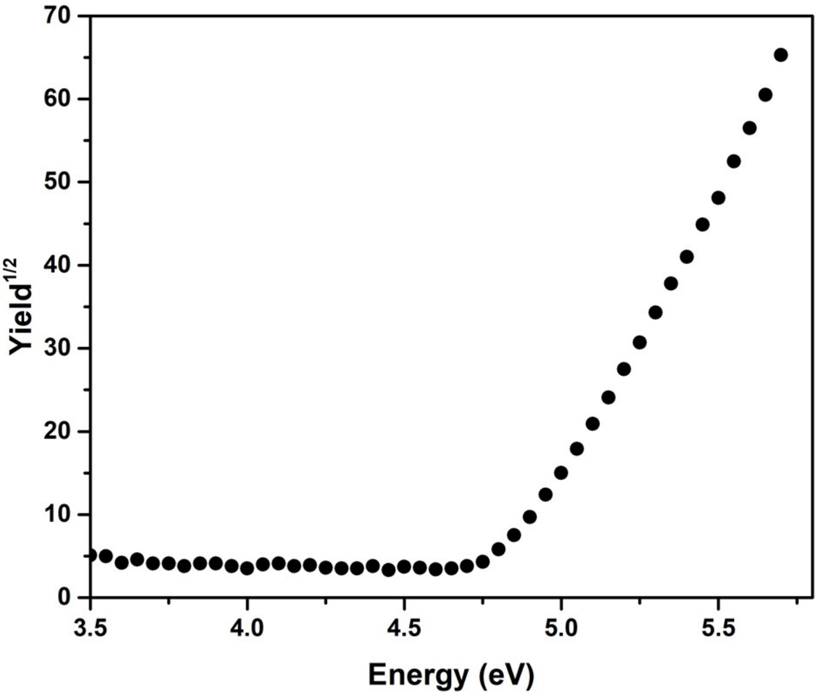

Figure S8. Measurements of the ionization energy of $Cu_{2-x}S$ NWs by photoemission spectroscopy in air (PESA)

Bending tests

First, $Cu_{2-x}S$ NWs were spray coated onto PEN substrates (1.5x5.0 cm^2, 125 µm thick) and the film was contacted electrically with conductive copper tape and Ag paste. The sheet resistance of the films was 2.4 kΩ/sq. The stability of the film to the bending was first characterized by performing sheet resistance measurements under different bending radii, using 3D printing molds with different well-defined diameters. The electrical resistivity was measured in situ with the film kept at the desired bending radius. The stability of the $Cu_{2-x}S$ NWs conductive film to fatigue bending has been carried out by performing 10000 bending cycles using a digital force gauge (Mark-10, M7-025E, ~25 N) equipped with a motorized test stand (Mark-10, ESM-

303E). In each bending cycle the gauge was extended of 5 mm (Figure S10). The corresponding bending radius was measured with a caliper and was equal to 8 mm. All the above-mentioned tests were performed by applying a bias voltage of 0.1 V.

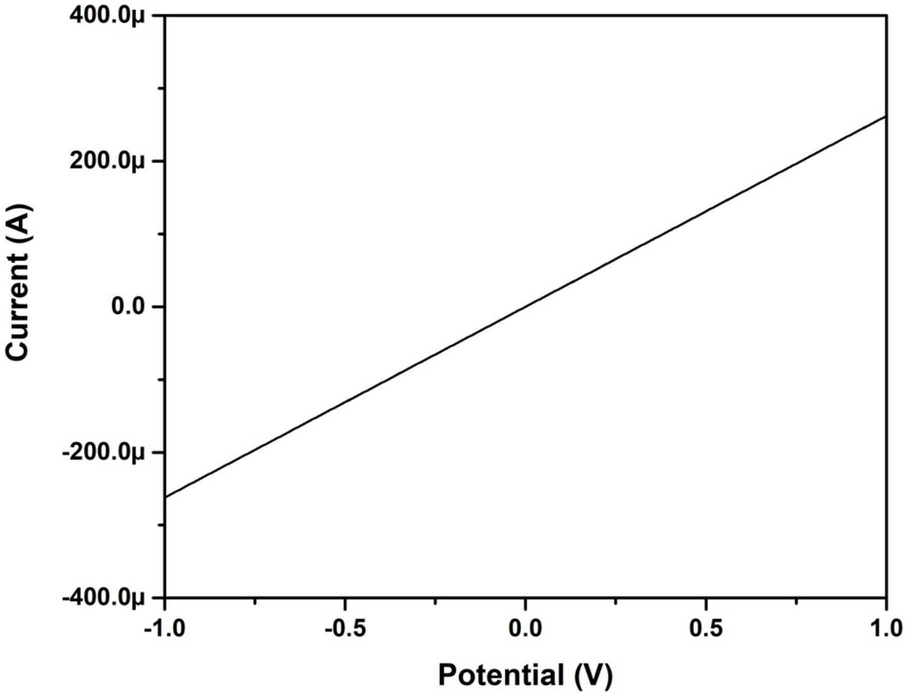

Figure S9. I-V characteristic of a $Cu_{2-x}S$NWs spray-coated film on PEN

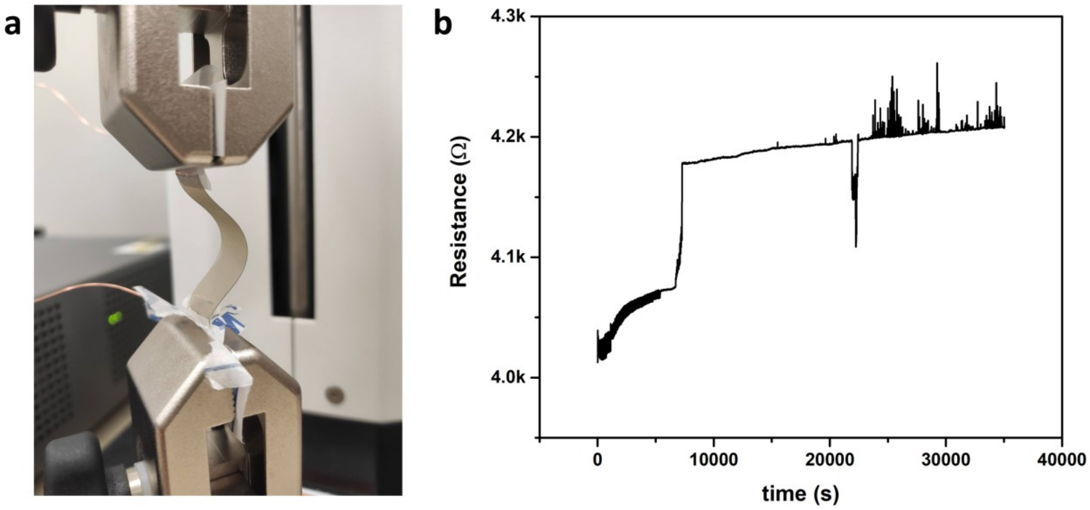

Figure S10. a) Photo of the 5x1.5 cm^2 conductive film of spray-coated $Cu_{2-x}S$NWs on PEN (125μm) in the bent position (8 mm radius). (b) Resistance of the film as a function of time during the application of 10000 bending cycles with a bending radius of 8 mm.

Sheet resistance as a function of transmittance

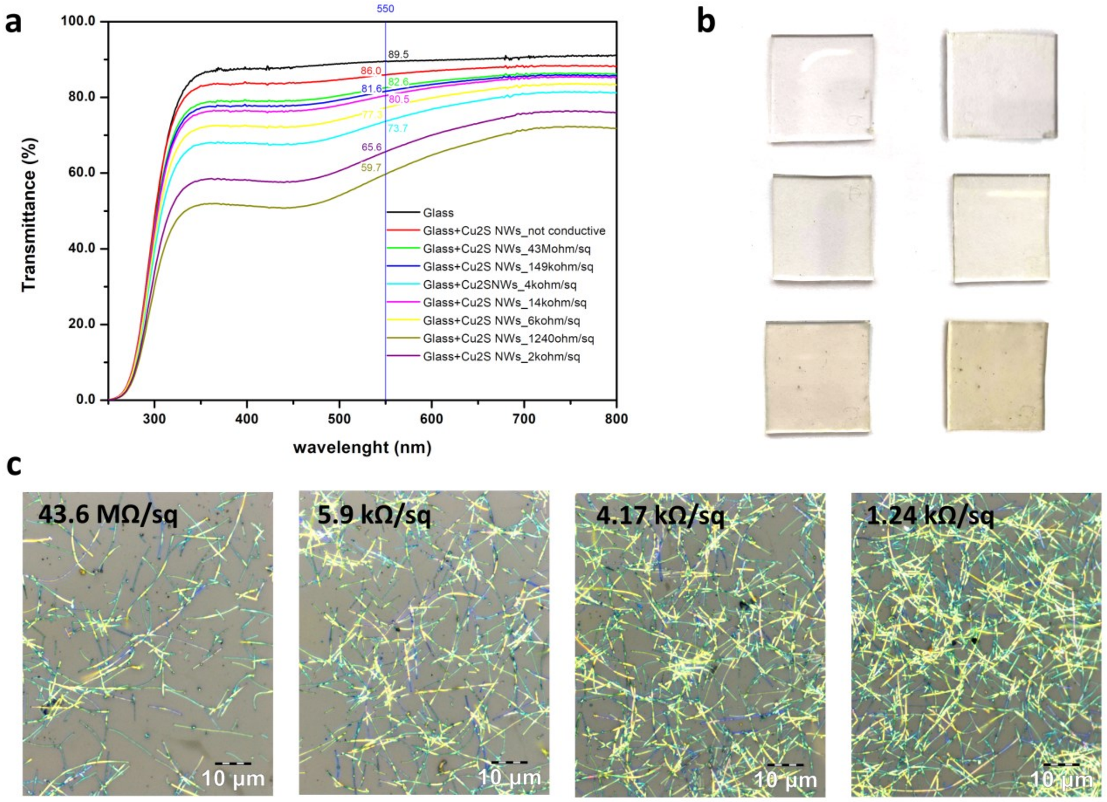

Figure S11. Transmittance spectra (a), photos (b) and microphotographs (c) of the glass substrate with increasing amounts of spray-coated $Cu_{2-x}S$ NWs.

Corrosion resistance

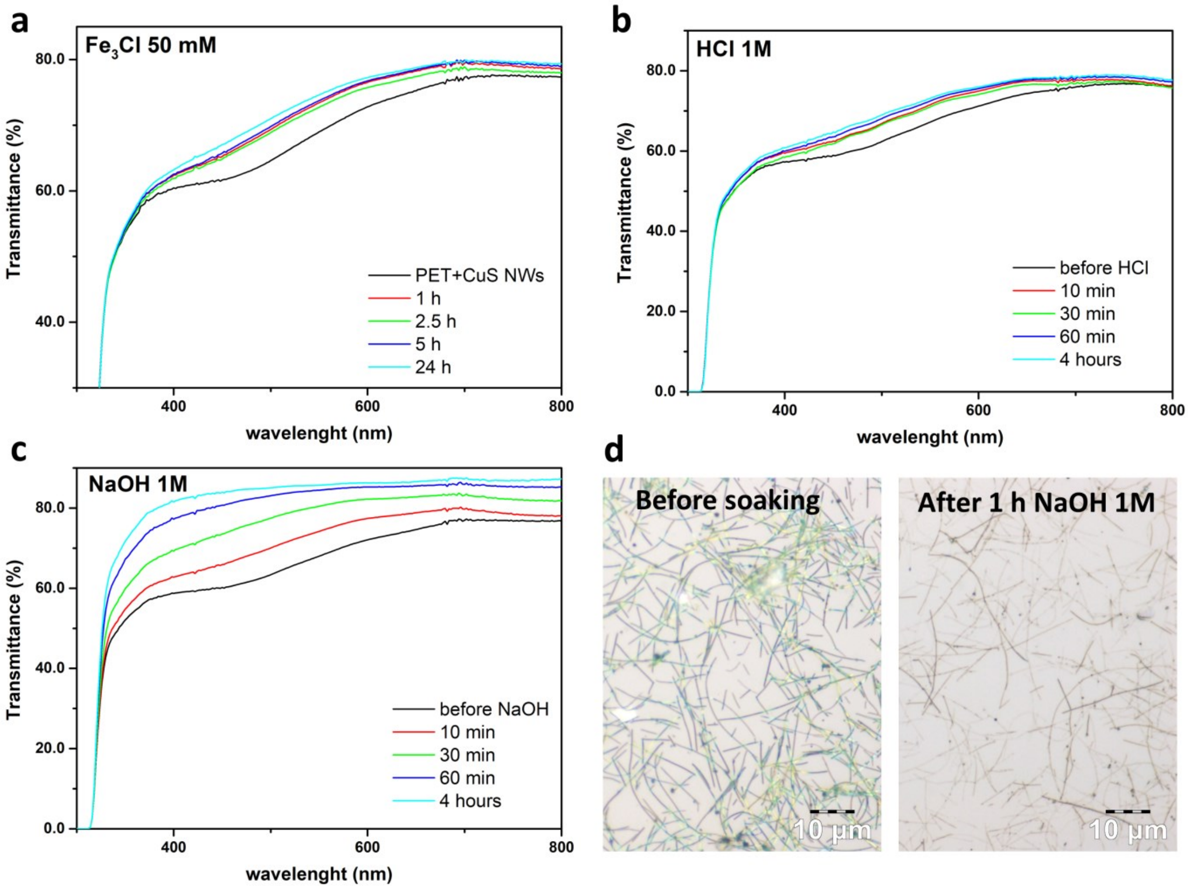

Figure S12. Transmittance spectra of spray-coated $Cu_{2-x}S$NWs on glass before and after increasing exposure times to water solutions of $FeCl_3$ 50 mM (a), HCl 1M (b), NaOH (c). (d) Micrograph of spray-coated $Cu_{2-x}S$NWs on glass before and after 1h of exposure to a 1 M water solution of NaOH.

DSC and TGA

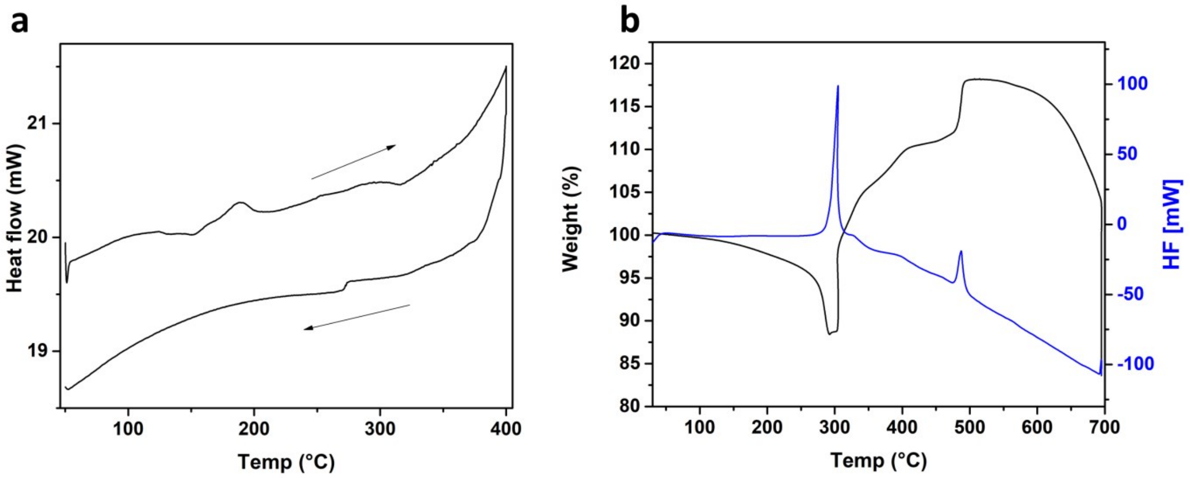

Figure S13. (a) DSC performed under Nitrogen flux (heating and cooling, 5 °C/min) ands (b) TGA-DSC performed under air (heating, 10 °C/min) of $Cu_{2-x}S$NWs.

XPS before and after annealing under N2 at 190°C for 30 min

In Figure S14a-b are reported the Cu 2p peak and S 2p peak of Cu_{2-x}SNWs before and after the annealing at 190 °C. It is possible to notice that after the annealing the two weak satellites peaks at 944 and 963 eV due to the presence of Cu^{2+} disappear completely, indicating a removal of the surface oxidized layer after the annealing. Similarly, also the peak at 168.3 eV in the S 2p region, due to the presence of sulfate, disappears completely after the annealing. Furthermore, the elemental abundance calculated from the fitting of XPS survey spectra of the Cu_{2-x}SNWs before and after the annealing (Figure S 14c) shows an important reduction of C and O after the annealing, which indicates a desorption of the organic contaminants (thiourea byproducts and solvent) and a reduction of the surface oxidized layer.

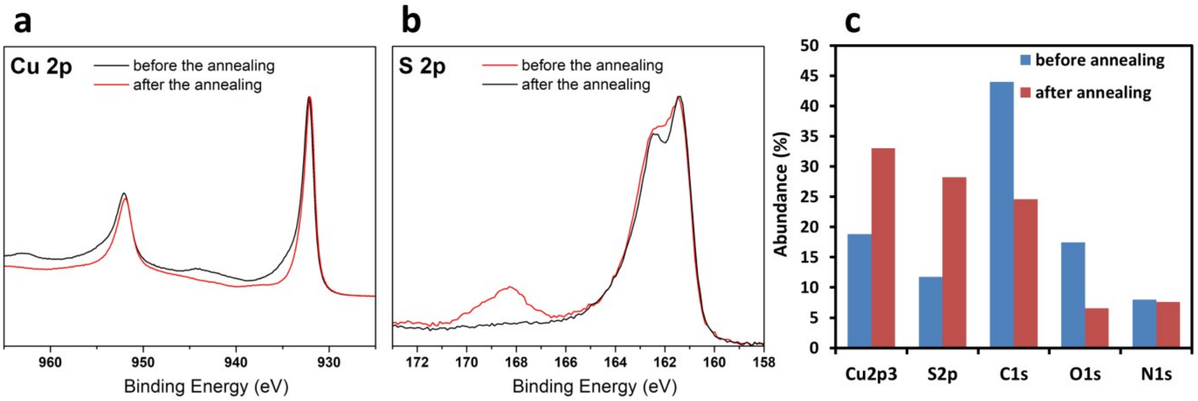

Figure S14. XPS spectra of Cu 2p (a) and S 2p (b) regions of Cu_{2-x}SNWs before (red) and after (black) annealing under nitrogen (190 °C, 30 min). (c) Abundance of the elements Cu, S, C, O and N, computed from the fitting of XPS survey spectra, in the Cu_{2-x}SNWs sample before and after the annealing.

Single nanowire device

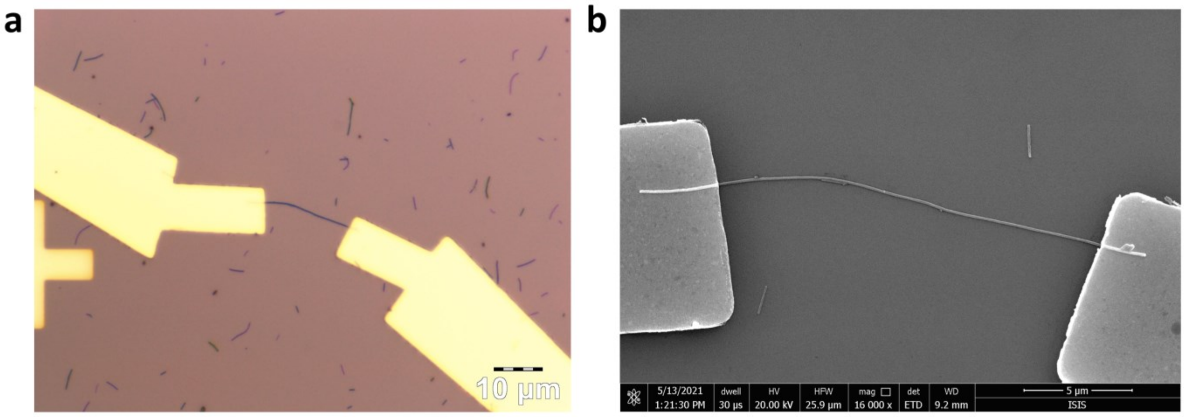

Figure S15. Optical micrograph (a) and SEM image (b) of the single $Cu_{2-x}S$ NW device, showing the two gold electrodes.

Electrochemical characterization of the $Cu_{2-x}S$ NWs based supercapacitor

Cyclic voltammetry (CV) was performed in the range of 0-2.5 V in the range of scan rates ranging from 5 mV s^{-1} to 2000 mV s^{-1}. The specific and volumetric capacitance were calculated from the CV curves using following equation[1]:

$$C = \frac{\int ivdv}{2\mu k\Delta V}$$

where, i and v are current and potential in the CV tests, μ is the scan rate of measurement (V/s), k is either the mass of active material (for specific capacitance) or its volume (for volumetric capacitance) and ΔV is the potential window. The volume of the electrode was calculated from its area and average thickness, which were, respectively, 350 µm and 1.53 cm^2. The average thickness of the electrode was measured with a KLA-Tencor Alpha-Step IQ profilometer.

The energy density was calculated according to the following equation:

$$E = \frac{1}{2} \times C \times \frac{\Delta V}{3600}$$

where *E* is the energy density (Wh cm^{-3}), *C* is the volumetric capacitance, *ΔV* is the discharge voltage range.

Galvanostatic charge-discharge curves (GCD) were recorded from 0-2.5 V at different current densities (1-10 A g^{-1}). Electrochemical Impedance Spectroscopy was taken in the frequency range from 100 kHz to 1 mHz with an amplitude of 10 mV. CV, GCD curves and EIS were recorded using EC-LAB VMP3 (BioLogic Science Instrument).

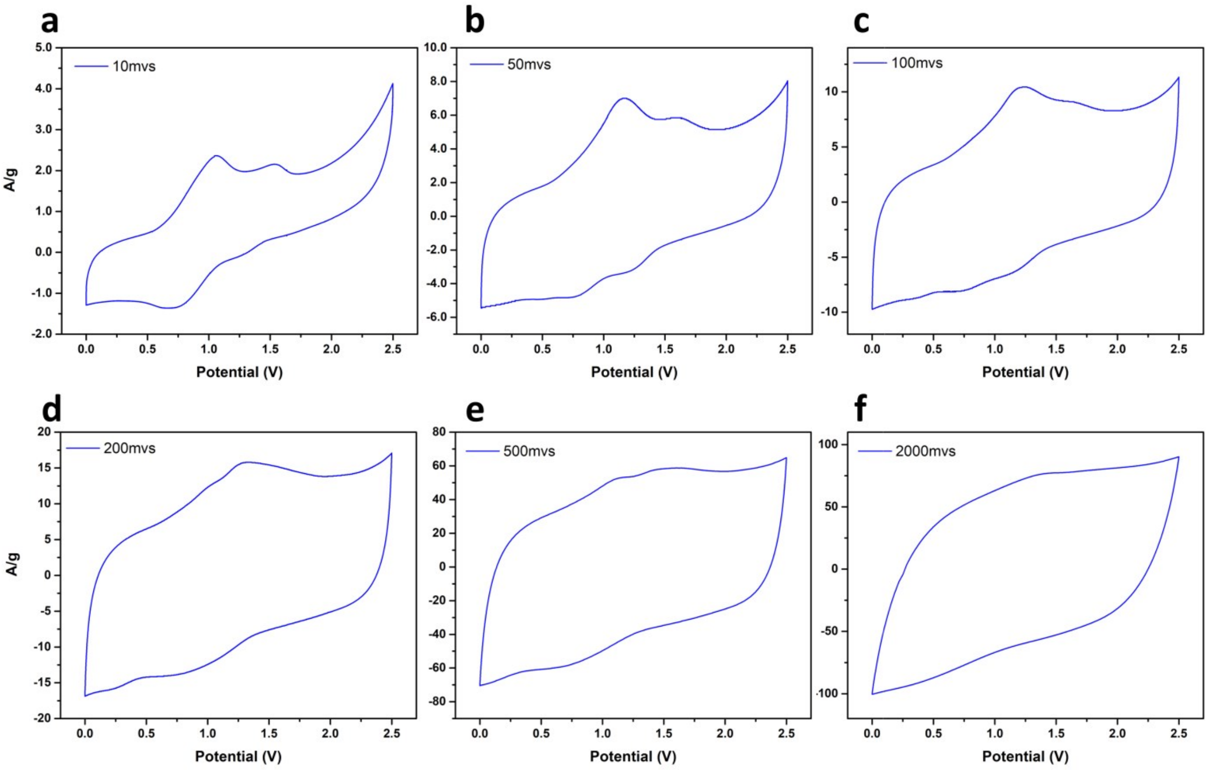

Figure S16. Cyclic voltammetry (CV) curves of the $Cu_{2-x}S$ NWs based supercapacitor at different scan rates: 10 mV/s (a), 50 mV/s (b), 100 mV/s (c), 200 mV/s (d), 500 mV/s (e) and 2000 mV/s (f).

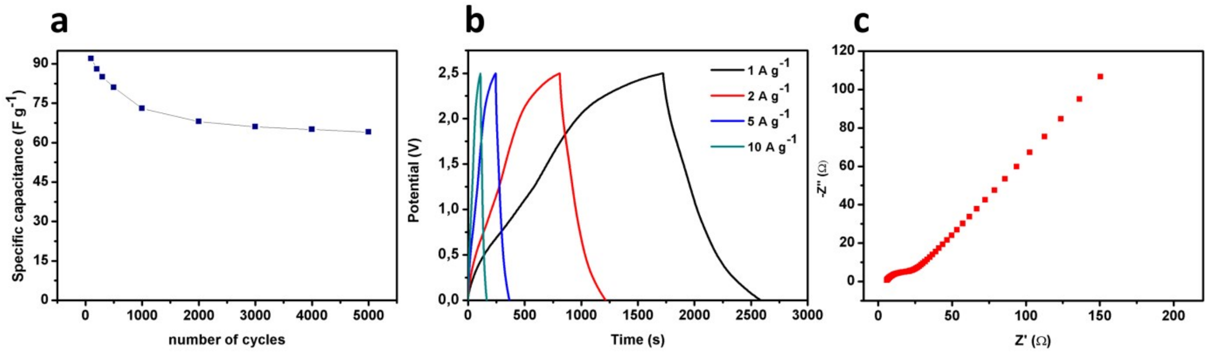

Figure S17. (a) Specific capacitance of the $Cu_{2-x}S$ NWs based supercapacitor as a function of the number of CV cycles (scan rate 100 mV/s). (b) Galvanostatic charge-discharge (GCD) curves of the supercapacitor at 1, 2, 5 and 10 A/g. (c) Electrochemical impedance spectroscopy (EIS) Nyquist plot of the supercapacitor.

Table S1. Specific and volumetric capacitance of the electrode at different scan rates

Scan Rate [mV s^{-1}]	Specific Capacitance [F g^{-1}]	Volumetric Capacitance [F cm^{-3}]
5	324	60,5
10	270	50,4
50	144	26,9
100	91	17,0
200	70	13,1
500	42	7,8
1000	40	7,5

References

1. Zhang, L.; Gong, H. Improvement in flexibility and volumetric performance for supercapacitor application and the effect of Ni–Fe ratio on electrode behaviour. *Journal of Materials Chemistry A* **2015,** *3* (14), 7607-7615.